

PRODUCTION OF HIGGS BOSON IN ASSOCIATION WITH ANOTHER TWO BOSONS AT THE HADRON COLLIDERS

By

DEBASHIS SAHA

PHYS07201304008

Institute of Physics, Bhubaneswar

A thesis submitted to the

Board of Studies in Physical Sciences

In partial fulfillment of requirements

for the Degree of

DOCTOR OF PHILOSOPHY

of

HOMI BHABHA NATIONAL INSTITUTE





JULY, 2019

Homi Bhabha National Institute


Recommendations of the Viva Voce Committee

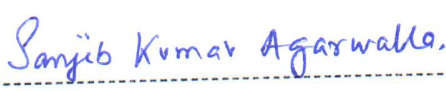
As members of the Viva Voce Committee, we certify that we have read the dissertation prepared by *Debashis Saha* entitled "*Production of Higgs boson in association with another two bosons at the hadron colliders*", and recommend that it may be accepted as fulfilling the dissertation requirement for the Degree of Doctor of Philosophy.

 25-6-20
Chairman - **Prof. Ajit M. Srivastava** Date: 25/06/2020

 25-6-20
Guide - **Prof. Pankaj Agrawal** Date: 25/06/2020

Co-guide (if any) Date:
 25/06/2020
Examiner - **Prof. Sudhir K. Vempati** Date: 25/06/2020

 25/06/2020
Member 1 - **Prof. Suresh K. Patra** Date: 25/06/2020

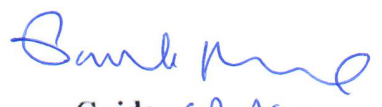
 25/06/2020
Member 2 - **Prof. Sanjib K. Agarwalla** Date: 25/06/2020

Final approval and acceptance of this thesis is contingent upon the candidate's submission of the final copies of the dissertation to HBNI.

I hereby certify that I have read this thesis prepared under my direction and recommend that it may be accepted as fulfilling the thesis requirement.

Date: 25-6-20

Place: Bhubaneswar


Guide (P. AGRAWAL)

STATEMENT BY AUTHOR

This dissertation has been submitted in partial fulfillment of requirements for an advanced degree at Homi Bhabha National Institute (HBNI) and is deposited in the Library to be made available to borrowers under rules of the HBNI.

Brief quotations from this dissertation are allowable without special permission, provided that accurate acknowledgement of source is made. Requests for permission for extended quotation from or reproduction of this manuscript in whole or in part may be granted by the Competent Authority of HBNI when in his or her judgement the proposed use of the material is in the interests of scholarship. In all other instances, however, permission must be obtained from the author.

Debashis Saha
DEBASHIS SAHA

DECLARATION

I hereby declare that the investigation presented in the thesis has been carried out by me. The work is original and has not been submitted earlier as a whole or in part for a degree / diploma at this or any other Institution / University.

Debashis Saha.

DEBASHIS SAHA

To the memory of my mother

ACKNOWLEDGEMENTS

First and foremost, I would like to express my gratitude to my advisor Prof. Pankaj Agrawal for his continued guidance and encouragement, as well as for his effort to bring me back in the right track whenever I got lost in unnecessary stuffs or because of my personal problems. Moreover, the special courses offered by him have been extremely useful in carrying out my research and will be so in future as well. Whether it is the classroom or his office, he has always welcomed questions, which made studying various topics quite easy and helped overcome numerous stumbling blocks during the research.

I am especially grateful to my senior Ambresh Kumar Shivaji, with whom I have done two works, both of which are part of this thesis. Besides research works, in non-research things also, his advice has been extremely helpful. I would also like to thank my other collaborators Prof. C.-P. Yuan, Prof. Jiang Hao Yu, and Ling-Xiao. With them I have done one work, which is part of this thesis. I have learned a lot from them about physics, in general and how to organize a paper.

I would like to express my special thanks to faculties of Institute of Physics (IOP) who took various courses during this period. Some of the classes were really beneficial to me. I would like to thank all the organizers of various schools and conferences that I attended during my Ph.D tenure. Special mention should be made about SERC school. I would also like to take this opportunity to express my gratitude to my college teachers for encouraging to ask questions and creating an environment open for discussion. Besides others, I especially want to thank Dr. Bidhan Chandra Roy for clearing many of my doubts, and for encouraging to critically think on various points after raising doubts about them.

I am also grateful to the doctoral committee members. I am further thankful to all the academic, non-academic, computer center, and temporary staff of IOP. Further, I would like to thank all the people responsible for bringing the HPC cluster facility in IOP.

I would like to express my gratitude to my family and relatives for their enduring encouragement and support, which have helped me complete this thesis. Besides parents, I am particularly grateful to my elder brothers for taking all the responsibilities of family during this period.

I am grateful to all the IOP friends who stood beside me during my tough times. I have met here people from various regions and backgrounds. Spending time with them for last few years gave me an opportunity to have a better understanding and improved perspective on many things such as religion, politics, social problems, psyche of human beings. I would like to convey my special thanks to some of my college friends who stood beside me during all my ups and downs. Their continuous supports and encouragements meant a lot, especially in difficult times. Mentions should also be made about some of my M.Sc. days friends who encouraged me to do research. Physics discussion with them at that time have surely helped me a lot in my research work. I would like to thank Taushif Ahmed (IMSC), my senior Ambresh Shivaji, and others whose theses inspired the format of this thesis.

Special mention should be made about Zaariya Kids and wonderful time I had spent with them there. Their innocent faces and smile can reduce stress and anxiety of any person.

Last but not least, I would like to acknowledge the funding agencies for providing the fellowship and contingency during the tenure of my Ph.D.

DEBASHIS SAHA

Publications arising from the thesis

Journal:

- Production of HHH and HHV ($V = \gamma, Z$) at the hadron colliders, P. Agrawal, D. Saha, and A. Shivaji, Phys. Rev. D 97, no. 3, 036006 (2018) [arXiv:1708.03580].
- Shape of Higgs Potential at Future Colliders, P. Agrawal, D. Saha, L. X. Xu, J. H. Yu and C. P. Yuan, Phys. Rev. D 101 no.7, 075023 (2020) [arXiv:1907.02078]

Preprint:

- Di-vector boson production in association with a Higgs boson at hadron colliders, P. Agrawal, D. Saha, and A. Shivaji, arXiv:1907.13168

Talks Delivered in Conferences/Workshop

- Presented a talk titled “**Production of HHH and HHZ at one loop via gluon fusion channel, and anomalous couplings**” at **XXI DAE-BRNS High Energy Physics Symposium**, University of Delhi, Delhi, India, 12-16 December, 2016
- Presented a talk titled “**Production of HHH and HHV ($V = \gamma, Z$) at the hadron colliders**” at **First International High Energy Physics School in Western China**, Lanzhou University, Lanzhou, Gansu, China, 1-10 August, 2018

Debashis Saha
DEBASHIS SAHA

Contents

Summary	xix
List of Figures	xxi
List of Tables	xxxi
1 Introduction	1
2 Standard Model and Effective field theories	13
2.1 SM	14
2.2 SMEFT	22
2.2.1 Warsaw basis	24
2.2.2 SILH basis	27
2.2.3 Effective Lagrangian of mass eigenstates	29
2.2.4 Higgs basis	30
2.2.5 Other frameworks	30
2.3 HEFT	31
3 One loop calculation	35
3.1 Scalar Integrals	37
3.2 Tensor Reduction	43
3.2.1 Passarino Veltman Technique	44
3.2.2 Oldenborg Vermaseren Technique	46

3.2.3	OPP Technique	48
3.3	Rational terms	51
3.4	Tools for one loop calculation	52
4	Production of hhh and hhV ($V = \gamma, Z$) at the hadron colliders	53
4.1	Processes	57
4.2	Anomalous couplings	60
4.2.1	Anomalous $t\bar{t}h$ coupling	60
4.2.2	Anomalous hhh and $hhhh$ couplings	61
4.2.3	Anomalous hZZ and $hhZZ$ couplings	62
4.3	Techniques and Checks	64
4.4	Numerical Results	67
4.4.1	The process $pp \rightarrow hhh$	67
4.4.2	The process $pp \rightarrow hhZ$	73
4.5	Conclusion	82
5	Production of VVh ($V = \gamma, Z, W$) at the hadron colliders	85
5.1	Gluon fusion diagrams for VVh	89
5.2	BSM Parametrization	93
5.3	Calculation and Checks	95
5.4	Numerical Results	97
5.4.1	The process $pp \rightarrow ZZh$	98
5.4.2	The process $pp \rightarrow WW h$	107
5.4.3	The process $pp \rightarrow \gamma Zh$	114

5.4.4	The process $pp \rightarrow \gamma\gamma h$	119
5.5	Conclusion	123
6	Phenomenology of Higgs Potential at Future Colliders	125
6.1	Various scenarios and relevant couplings	130
6.2	Double Higgs production	132
6.2.1	Cross Section and Distributions	133
6.2.2	Interference Effects	138
6.2.3	constraints on d_3 in various models	143
6.3	Triple Higgs production	145
6.3.1	Cross Section and Distributions	146
6.3.2	Interference Effects	152
6.3.3	Constraints on d_4 in various models	155
6.4	Conclusion	158
7	Conclusions	161
	Appendix A	167
A.1	Tensor reductions in Passarino-Veltman technique	167
A.1.1	Bubble integral	167
A.1.2	Triangle integrals	171
A.1.3	Box integrals	181
A.2	van Neerven-Vermaseren basis	186
A.3	Tensor integral reduction using Oldenborg-Vermaseren Technique	191

A.3.1	Box integrals	191
A.4	Reduction of five point and higher point functions	205
Appendix B	Miscellaneous	211
B.1	Loop Integrations	211
B.2	Running of QCD coupling constant	213
B.3	Hadronic Cross-section	214
B.4	Polarization	215
Appendix C		217
C.1	Feynman Rules for Chapter-IV	217
Bibliography		219

Summary

After the discovery of the scalar particle in 2012 at the LHC, measuring its various properties and couplings with other fermions, gauge bosons and itself have been one of the major goals of the particle physics community. So far all these measurements are at par with the predictions for the Standard Model Higgs boson within experimental uncertainty. In this thesis, we have considered the production of various multiparticle final states with at least one Higgs boson. To study the effect of new physics lying at some high-energy scale at comparatively low energy scale, one often relies on the effective field theory (EFT) frameworks. We have briefly reviewed linearly and non-linearly realized EFTs. As the processes considered in this thesis have production channels which occur at one loop, we have reviewed techniques for reduction of one loop tensor integral to scalar integrals. We have discussed various sources of divergences in the scalar integrals. Interference effect between various classes of diagrams have been explored which facilitates a better understanding of various features of cross sections and distributions. Uncertainty due to scale variation has been studied. Effects of various anomalous couplings have been studied both on the inclusive and differential cross sections.

In particular, in one of the chapters, we have studied the processes — $pp \rightarrow hhh, hh\gamma$, and hhZ , where focus was on the gluon-gluon (gg) fusion channel contribution, mediated by heavy quarks in one loop. This channel occurs at NNLO in QCD coupling, α_s . To $pp \rightarrow hhh$, the main contribution comes from $gg \rightarrow hhh$, as the contribution of $q\bar{q} \rightarrow hhh$ is negligible because of tiny Yukawa couplings of light quarks. The $gg \rightarrow hhh$ channel is

specially sensitive to anomalous trilinear Higgs coupling. Unlike $pp \rightarrow hhh$, for $pp \rightarrow hhZ$ production, $q\bar{q}$ initiated tree level channel is not suppressed. At the LHC, $q\bar{q}$ initiated channel contributes much more than gg fusion channel. However, with increasing center-of-mass energy, gluon flux at the colliders increases. At 100 TeV collider, the contribution to hhZ production cross section from gg fusion channel becomes comparable to that from $q\bar{q}$ initiated channel. The $gg \rightarrow hhZ$ shows some modest dependence on anomalous hZZ coupling. Also, $pp \rightarrow hhZ$ is important as it is background to $pp \rightarrow hhh$. The overall amplitude for $gg \rightarrow hh\gamma$ is zero, owing to Furry's theorem. Next we consider $pp \rightarrow VVh$ processes, ($V = \gamma, Z, W$). Here also we compare gg fusion channel to $q\bar{q}$ initiated channel contribution. We find that for some of the processes gg fusion channel is comparable to NLO QCD correction to $q\bar{q}$ initiated channel. Effect of various anomalous couplings on these processes both at the cross section and distribution level have been considered. Next, we consider hh and hhh production to explore the shape of the Higgs potential. We show various salient features of different Higgs potentials models. We further find the constraints on the trilinear and quartic Higgs boson couplings in these models assuming some benchmark uncertainties in the cross section measurement.

List of Figures

3.1	Collinear divergence. The lines with Q are parts of loop. The line with only p is external line. A dashed line signifies masslessness for lines in the loop and zero virtuality ($p^2 = 0$) for external lines.	40
3.2	Soft divergence. The lines with Q are parts of loop. The lines with only p 's are external lines. A dashed line signifies masslessness.	41
4.1	Prototype Feynman diagram for $gg \rightarrow hhh$ production.	58
4.2	Prototype Feynman diagram for $gg \rightarrow hhZ$ production.	59
4.3	SM contribution of pentagon (blue), box (green), and triangle (violet) diagrams to leading $p_T(h)$ distribution in $gg \rightarrow hhh$ at 13 TeV (left) and 100 TeV (right) colliders.	69
4.4	Kinematic distributions for $gg \rightarrow hhh$ in the SM at 13 TeV collider. These plots are obtained after p_T ordering the Higgs bosons. h_1, h_2 , and h_3 refer to the hardest, second hardest, and third hardest Higgs bosons in p_T , respectively.	70
4.5	$\frac{\sigma_{\text{BSM}}}{\sigma_{\text{SM}}}$ as function of various Higgs anomalous couplings affecting $gg \rightarrow hhh$ at 13 TeV.	71
4.6	Normalized leading $p_T(h)$ distribution in $gg \rightarrow hhh$ at 13 TeV for some benchmark values of anomalous trilinear Higgs boson coupling. In the lower panels R is defined as the ratio of the distributions ($d\sigma/dp_T$) in BSM and in the SM.	72

4.7	SM contribution of pentagon (blue), box (green) and triangle (violet) diagrams to leading $p_T(h)$ distribution in $gg \rightarrow hhZ$ at 13 TeV (left) and 100 TeV (right).	76
4.8	Kinematic distributions for $gg \rightarrow hhZ$ in the SM at 13 TeV. These plots are obtained after p_T ordering the Higgs bosons. h_1 and h_2 refer to the hardest and second hardest Higgs bosons in p_T respectively.	77
4.9	A comparison of normalized distributions for $p_T(h_1)$ and $p_T(Z)$ due to $gg \rightarrow hhZ$ and $q\bar{q} \rightarrow hhZ$ in the SM at 13 TeV.	77
4.10	Combined $gg \rightarrow hhZ(\text{LO}) + q\bar{q} \rightarrow hhZ(\text{NLO})$ contribution to $p_T(h_1)$ and $p_T(Z)$ distributions in the SM at 13 TeV and 100 TeV. Lower panels show the ratio of $q\bar{q}(\text{NLO}) + gg(\text{LO})$ and $q\bar{q}(\text{NLO})$ for each of these distributions. The dashed straight line in the lower panel of each plot refers to the same quantity at inclusive or total cross section level (see R_2 in Table 4.3).	78
4.11	$\frac{\sigma_{\text{BSM}}}{\sigma_{\text{SM}}}$ as a function of anomalous couplings of the Higgs boson in $gg \rightarrow hhZ$ at 13 TeV.	79
4.12	Normalized leading $p_T(h)$ distribution in $gg \rightarrow hhZ$ at 13 TeV for some benchmark values of anomalous top Yukawa couplings.	79
4.13	Normalized leading $p_T(h)$ distribution in $gg \rightarrow hhZ$ at 13 TeV for some benchmark values of hhh anomalous couplings.	80
4.14	Normalized leading $p_T(h)$ distribution in $gg \rightarrow hhZ$ at 13 TeV for some benchmark values of hZZ and $hhZZ$ anomalous couplings.	81

5.1	Different classes of diagrams for $gg \rightarrow VVh$, $V = \gamma, Z$. In diagram (b), q represents all quark flavors. Process $gg \rightarrow \gamma\gamma h$ receives contribution only from (a) type diagrams, while $gg \rightarrow \gamma Zh$ gets contribution from both (a) and (b) type diagrams. In the case of ZZh , all the diagrams contribute; the diagrams (b) and (f) cover the situation in which h is attached to the other Z boson.	90
5.2	Different classes of diagrams contributing to $gg \rightarrow WW h$ process. With respect to ZZh , new classes of box and triangle diagrams appear due to ZWW coupling. In (a) and (b), due to the flavor changing interaction of W with quarks, both the quark flavors of a given generation enter in the loop. The diagrams (b), (g) and (i) cover the case when h is attached to the other W boson.	91
5.3	SM contribution of pentagon (blue), box (green), triangle (gray) diagrams, as well as their squared sum (black), interference (orange) and total (red) contribution to partonic center-of-mass energy and $p_T(h)$ distributions in $gg \rightarrow ZZh$ at 100 TeV collider (FCC-hh). As can be seen, there is a strong destructive interference between the penta, box, and triangle diagrams. . . .	100
5.4	Left: The top-quark contribution to box diagram of Fig. 1(b). Right: The effect of excluding top-quark contribution from Fig. 1(b) to full amplitude. In the lower panel, we have taken ratio of contributions without top and with top quark in Fig 1(b). While the green histogram shows ratio for differential distributions, the black dashed line shows the ratio for the cross sections.	101

5.5	Kinematic distributions for $gg \rightarrow ZZh$ in the SM at the 100 TeV collider. These plots are made with the histogram data obtained after p_T ordering of the Z bosons. Z_1 and Z_2 refer to the hardest, and second hardest in p_T , respectively.	102
5.6	The left figure shows the normalized distribution for $p_T(h)$ in gg and $q\bar{q}$ initiated process. In the top panel of the right figure, we show the distribution of $q\bar{q}$ (NLO) + gg (LO) and $q\bar{q}$ (NLO) production with $p_T(h)$. The lower panel shows the ratio of them.	102
5.7	$t\bar{t}$ threshold effect for ZZh production via gg fusion channel. We have chosen an arbitrary phase space point with $\sqrt{\hat{s}} = 346$ GeV and then vary m_t from 160 GeV to 190 GeV. We see a sudden change in the slope of $ M ^2$ plot around $m_t = 173$ GeV.	103
5.8	Effect of anomalous values of κ_t and κ_V on ZZh production via gg fusion channel. The left column shows normalized distribution, and right column shows distributions and their ratio with the SM value.	105
5.9	Effect of anomalous value of κ_V on NLO QCD ZZh production via $q\bar{q}$ initiated channel. We have not shown the effect of scaling of other couplings as their effect on the total cross section is negligible.	107
5.10	SM contribution of pentagon (blue), box(green), triangle (gray) diagrams, as well as their square sum, interference and total contribution to partonic center-of-mass energy and $p_T(h)$ distributions in $gg \rightarrow WW h$ at 100 TeV FCC-hh collider. As can be seen, there is strong destructive interference between the penta, box, and triangle diagrams.	108

5.11	Left: The third generation quark contribution to box diagram of Fig. 2(b). Right: The effect of excluding third generation quark contribution from Fig. 2(b) to full amplitude.	109
5.12	p_T and $M(WWh)$ distributions for $gg \rightarrow WWh$ in the SM at the 100 TeV collider (FCC-hh). As expected, the p_T distributions for W^+ and W^- fall on each other as the process is a gg fusion one. A small peak can be seen at 350 GeV in the $M(WWh)$ distribution, which occurs due to $t\bar{t}$ threshold effect.	110
5.13	The left figure shows the normalized distribution for $p_T(h)$ in gg and $q\bar{q}$ initiated process. In the top panel of the right figure, we show the distribution of $q\bar{q}$ (NLO)+ gg (LO) and $q\bar{q}$ (NLO) production with $p_T(h)$. The lower panel shows their ratio. Results do not include contribution of $b\bar{b}$ initiated process	110
5.14	$t\bar{t}$ threshold effect for WWh via gg fusion channel. To show this effect, after arbitrarily choosing a phase space point with $\sqrt{\hat{s}} = 346$ GeV, we vary m_t from 160 GeV to 190 GeV. We see a peak around $m_t = 173$ GeV, which happens to be half of $\sqrt{\hat{s}}$ for the chosen phase space point.	111
5.15	Effect of anomalous values of κ_t and κ_V on WWh production via gg fusion channel. The left panel shows normalized distribution, and the right panel shows distributions and the ratio of the distributions to the SM distribution.	113

5.16	SM contribution of pentagon (blue) and box (green) diagrams, as well as their square sum, interference, and total contribution to partonic center-of-mass energy and $p_T(h)$ distributions in $gg \rightarrow \gamma Zh$ at 100 TeV FCC-hh collider. The interference shows an interesting effect. In 300 – 400 GeV range of partonic center-of-mass energy, it is constructive, while it is destructive at energies higher than that. $p_T^\gamma > 50$ GeV has been imposed. . .	116
5.17	Left: The top-quark contribution to box diagram of Fig. 1(b). Right: The effect of excluding top-quark contribution from Fig. 1(b) to full amplitude. .	117
5.18	Kinematic distributions for $gg \rightarrow \gamma Zh$ in the SM at 100 TeV. $p_T^\gamma > 50$ GeV has been imposed.	117
5.19	$t\bar{t}$ threshold effect for γZh production via gg fusion channel at the amplitude level.	118
5.20	Kinematic distributions for $gg \rightarrow \gamma\gamma h$ process in the SM at 100 TeV. These plots have been made using histogram data obtained after p_T ordering of two γ s — γ_1 and γ_2 refer to the hardest and second hardest in p_T , respectively. $p_T^\gamma > 50$ GeV and $\Delta R_{\gamma\gamma} > 0.4$ have been imposed.	121
5.21	$t\bar{t}$ threshold effect for $\gamma\gamma h$ production via gg fusion channel.	122
6.1	Different classes of diagrams for the hh production via gg fusion channel. The third diagram occurs in models having $t\bar{t}hh$ vertex.	134

6.2	Variation of the ratio of the new-physics cross section to that of the SM for hh production with respect to the trilinear Higgs boson coupling d_3 as in the fundamental Higgs, Coleman-Weinberg Higgs and Tadpole-induced Higgs scenarios (upper row), and with respect to the parameter ξ in Nambu-Goldstone Higgs scenario (lower row).	136
6.3	Cross section ratio σ/σ_{SM} as a function of c_2 and d_3 ; (a) without any cut, and (b) with the only kinematic cut $p_T^h > 70$ GeV. The standard model cross sections, at the 27 TeV HE-LHC collider, for the above mentioned two cuts are 73.6 fb and 66.2 fb, respectively. For no cut the cross sections for Tadpole-induced Higgs model and Coleman-Weinberg model are 149.2 fb and 124.1 fb, respectively, while with $p_T^h > 70$ GeV they are 44.2 fb and 40.3 fb, respectively. The magenta, blue, and cyan dots denote the ratios for Tadpole-induced Higgs model, the SM, and Coleman-Weinberg model, respectively.	137
6.4	Normalized distributions for hh production via gg fusion channel against partonic center of mass energy and p_T of either Higgs. The case of $d_3 = 3$ shows an interesting feature, caused by the competition between the triangle and box diagram contributions, as explained in the text, around Fig. 6.5.	138

6.5	Contribution of various classes of diagrams and their interference to the $M(hh)$ distribution of hh production for $d_3 = 1$ and $d_3 = 3$. The triangle diagrams contribution and interference (negative) term get scaled by 9 and 3, respectively, when we go to $d_3 = 3$ from $d_3 = 1$. However, as “bx” does not depend on d_3 , it remains the same. The peak of the total distribution gets shifted to left with increase in d_3 as the triangle diagram, being a s-channel one, contributes significantly near the threshold of hh production.	140
6.6	Variation of different pieces of Eq. 6.3 with ξ in MCH and CTH models at 14 TeV collider. The Magenta line (which shows the effect of $t\bar{t}hh$) crosses the blue line (which shows the effect of $t\bar{t}h$ and hhh coupling) around $\xi = 0.06$.	142
6.7	Constraints on the scaling \tilde{d}_3/d_3 if the cross section can be measured up to 10% and 20% accuracy, respectively. Here, \tilde{d}_3 denotes the scaled d_3 value.	144
6.8	Constraints on \tilde{c}_2/c_2 and \tilde{d}_3/d_3 if the cross section can be measured up to 10% and 20% accuracy, respectively, in the MCH and CTH models. Here, \tilde{c}_2 and \tilde{d}_3 denote the scaled c_2 and d_3 values, respectively.	144
6.9	Different classes of diagrams for hhh production in the SM.	146
6.10	New diagrams for hhh production in the presence of $t\bar{t}hh$ and $t\bar{t}hhh$ vertices.	146

6.11	We summarize the total cross sections of the $pp \rightarrow hh$ and $pp \rightarrow hhh$ for the SM at the 14 TeV LHC, the 27 TeV HE-LHC and the 100 TeV hadron collider, respectively. The blue lines denote the cross sections without cut, and the red lines denote the ones with rudimentary cuts. Here we do not include the QCD K factors, which are known as around 1.7 [1] for $pp \rightarrow hh$ and around 2 [2] for $pp \rightarrow hhh$, respectively.	149
6.12	Cross section ratio σ/σ_{SM} for the scaling of trilinear and quartic Higgs boson couplings for various cuts. At the 100 TeV collider, the standard model cross section for no-cut and $p_T > 70$ GeV cut are 2987 ab and 1710 ab, respectively. The blue, cyan, and magenta dots denote the SM, CW Higgs and Tadpole-induced Higgs model, respectively. The orange dashed line denotes the SMEFT (with non-vanishing O_6) for d_3 in the range of [5/6,2.5].	151
6.13	Cross section ratio with parameter ξ in the Minimal Composite Higgs (MCH) and Composite Twin Higgs (CTH) Models at the 100 TeV collider (FCC-hh).	152
6.14	Distributions with partonic center-of-mass energy $M(hhh)$ for hhh production via gg fusion channel with different benchmark values of d_3 and d_4 at the 100 TeV collider. No cut on p_T of Higgs bosons has been imposed. . . .	152
6.15	Variation of Cross section ratio σ/σ_{SM} with d_3 and d_4 at a 100 TeV collider. In the left figure, we see a band for d_4 in the range [0,10]. In the right figure, variation with d_4 for fixed d_3 is shown. The standard model cross section for no cut and $p_T^h > 70$ GeV cut are 2987 ab and 1710 ab, respectively. . . .	153

6.16	Cross section [in ab] with parameter ξ in the Minimum Composite Higgs Model (MCH) and the Composite Twin Higgs Model (CTH). The magenta line shows the effect of $t\bar{t}hh$ coupling. In MCH model, it exceeds the “SM-like” effect (σ_{Mod}^{SM}) around $\xi = 0.05$. The blue line shows the effect of $t\bar{t}hhhh$ coupling, which includes interference (which is negative for the shown range of ξ) of $t\bar{t}hhhh$ with $t\bar{t}hh$ as well.	154
6.17	Variation of the ratio of cross sections of MCH and CTH models to the SM value with ξ and \tilde{d}_4/d_4 at the 100 TeV proton-proton collider. The bands are obtained by varying \tilde{d}_4/d_4 in the range of [0,10] for the MCH and CTH models. The standard model cross section for no cut and $p_T^h > 70$ GeV cut are 2987 ab and 1710 ab, respectively.	155
6.18	Constraints on \tilde{d}_4/d_4 in various new physics models, when the cross section can be measured up to 10% and 20% accuracy, respectively. The parameter \tilde{d}_4/d_4 scales the quartic Higgs boson coupling in a given model.	157
6.19	Constraints on \tilde{c}_3/c_3 and \tilde{d}_4/d_4 if the cross section can be measured up to 10% and 20% accuracy, respectively, in the MCH and CTH models.	158

List of Tables

2.1	Bosonic CP-even and CP-odd D=6 operators in Warsaw basis. There are 9 bosonic CP-even and 6 CP-odd operators. So, in the Warsaw basis there are 15 bosonic operators. The dual tensor $\tilde{F}_{\mu\nu}$ is defined as $\frac{1}{2}\epsilon_{\mu\nu\rho\sigma}F^{\rho\sigma}$. . .	25
2.2	Two-fermionic operators. Here l, q are left-handed doublet and e, u, d are right handed singlet of SU(2), respectively. There are 19 two-fermionic operators — 8 vertex, 3 Yukawa and 8 dipole operators. Moreover, Hermitian conjugates of Q_{Hud} , all the Yukawa operators, and all the Dipole operators need to be added.	27
2.3	Four-fermionic operators. There are 25 B-conserving four-fermionic operators. Hermitian conjugates of 5 operators in $(\bar{L}R)(\bar{L}R)$ and $(\bar{L}R)(\bar{R}L)$, i.e., the operators in the last column need to be added.	27
2.4	Bosonic CP-even and CP-odd D=6 operators. There are 14 bosonic CP-even and 6 CP odd operators. In the Warsaw basis, however, there are 15 bosonic operators. Extra 5 bosonic operators here in SILH basis are traded off for 2 two-fermionic operator and 3 four-fermionic operators in the Warsaw basis. It is to be noted that first 7 operators and last four operators are also present in the Warsaw basis. Only 4 bosonic operators in Warsaw basis are replaced by 9 bosonic operators in SILH basis.	28
4.1	$pp \rightarrow hhh$ hadronic cross sections and corresponding scale uncertainties in the SM at different collider center-of-mass energies.	68

4.2	SM contributions of pentagon, box, and triangle diagrams to the total cross section at different collider center-of-mass energies, displaying a destructive interference effect.	69
4.3	A comparison of different perturbative orders in QCD coupling contributing to $pp \rightarrow hhZ$ hadronic cross section at $\sqrt{s} = 8, 13, 33$, and 100 TeV. We also calculate ratios R_1 , R_2 , and R_3 which quantify the gg fusion channel contribution with respect to the LO and NLO $q\bar{q}$ initiated channel contributions.	74
4.4	SM contribution of pentagon, box, and triangle diagrams to the total cross section in $gg \rightarrow hhZ$ at different collider center-of-mass energies, displaying a destructive interference effect.	75
5.1	A comparison of different perturbative orders in QCD coupling contributing to $pp \rightarrow ZZh$ cross section at $\sqrt{s} = 14, 27$, and 100 TeV. The ratio R_3 quantifies the gg fusion channel contribution with respect to the NLO correction in $q\bar{q}$ initiated process.	100
5.2	Effect of various anomalous couplings on ZZh production at the 100 TeV collider. The production cross section of $q\bar{q}$ initiated channel shows strong dependence on κ_V coupling. The gg fusion channel shows strong dependence on κ_t and κ_V anomalous couplings. The numbers in the square brackets show the percentage change in the cross section from the SM value in the corresponding channel because of anomalous coupling.	104

5.3	A comparison of different perturbative orders in QCD coupling contributing to $pp \rightarrow WW h$ hadronic cross section at $\sqrt{s} = 14, 27$, and 100 TeV. The ratio R_3 quantifies the gg fusion channel contribution with respect to the $q\bar{q}$ (LO) and $q\bar{q}$ (NLO) contributions. $q\bar{q}$ initiated channel results do not include bottom quark contribution.	108
5.4	Effect of various anomalous couplings on $WW h$ production for the 100 TeV collider. The production cross section via $q\bar{q}$ initiated channel shows strong dependence on κ_V only. The gg fusion channel shows strong dependence on κ_t and κ_V . The numbers in the square brackets show percentage change in the cross section in BSM scenario with respect to the SM value. $q\bar{q}$ initiated channel results do not include bottom quark contribution.	113
5.5	A comparison of different perturbative orders in QCD coupling contributing to $pp \rightarrow \gamma Zh$ hadronic cross section at $\sqrt{s} = 14, 27$, and 100 TeV for two cuts on p_T^γ and $ \eta^\gamma < 2.5$. We calculate ratio R_3 which quantify the gg fusion channel contribution with respect to the NLO correction in $q\bar{q}$ initiated process. Contribution of $b\bar{b}$ channel has also been taken into account. .	115
5.6	Cross sections for $pp \rightarrow \gamma Zh$ production at the 100 TeV collider (FCC-hh). A pseudo-rapidity cut of $ \eta^\gamma < 2.5$ has been imposed. b quark contribution has also been considered in these results.	115

5.7	Effect of various anomalous couplings on γZh production for the 100 TeV collider. The effect of anomalous κ_t on gg fusion channel cross section is smaller than that of anomalous κ_V . The $q\bar{q}$ initiated channel does not depend on κ_t , as no diagram has this $t\bar{t}h$ vertex. The numbers in the square brackets show percentage change in the cross section in BSM scenario with respect to the SM value.	119
5.8	A comparison of different perturbative orders in QCD coupling contributing to $pp \rightarrow \gamma\gamma h$ hadronic cross section at $\sqrt{s} = 14, 27$, and 100 TeV for two cuts on p_T^γ , $ \eta^\gamma < 2.5$, and $\Delta R_{\gamma\gamma} > 0.4$. Unlike the previous processes, here we don't show the ratio (R_3) of gg fusion channel contribution to NLO QCD correction in $q\bar{q}$ initiated channel, since the tree level contribution of the latter channel is too small in comparison to the former one.	120
5.9	Cross sections for $pp \rightarrow \gamma\gamma h$ production at the 100 TeV collider (FCC-hh). A pseudo-rapidity cut of $ \eta^\gamma < 2.5$ and $\Delta R_{\gamma\gamma} > 0.4$ have been imposed. Only bottom quark can contribute to the $q\bar{q}$ initiated process. The cross section in this channel is too small, owing to the tiny bottom Yukawa coupling.	120
5.10	Effect of various anomalous couplings on $\gamma\gamma h$ production for the 100 TeV collider. $p_T^\gamma > 50$ GeV and $\Delta R_{\gamma\gamma} > 0.4$ have been imposed.	122
6.1	Higgs boson couplings, defined in Eqs. (6.1) and (6.2), for the SM and different BSM scenarios. Here $\xi = \frac{v}{f}$, where f is the scale of the new physics.132	

6.2	Form factors as defined in Eq. (6.3) at the 14 TeV, 27 TeV, and 100 TeV proton-proton colliders.	135
6.3	Numerical values of various terms of Eq. 6.4 at the 100 TeV hadron col- lider.	148

Chapter 1

Introduction

After a long search for the last missing particle of the Standard Model (SM), i.e., the Higgs boson, in many previous colliders, finally in 2012, a particle of mass 125 GeV was discovered at the Large Hadron Collider (LHC) [3, 4]. Although the initial discovery gave significant hints, further verification was needed for it to be called the SM Higgs boson. The subsequent measurements of its various properties such as spin, CP state, couplings with other Standard model particles, especially top quark and vector bosons, probed through various production and decays channels are also so far consistent with the SM predictions within experimental uncertainties [5]. The discovery of this particle is a great triumph for particle physics community, since it can theoretically explain the generation of masses of weak gauge bosons via spontaneous breaking of gauge symmetry without sacrificing renormalizability. From a theoretical point of view, this is remarkable as while in a renormalizable theory where UV divergences can be absorbed in a finite number of parameters, is strongly predictive, a non-renormalizable one does not have the same predictive power since it needs an infinite number of parameters to tackle the divergences.

Historically, in 1957, Schwinger attempted to unify weak and electromagnetic interactions by putting two vector boson fields of weak interaction and neutral field of electromagnetic interaction in the triplet of $SU(2)$ [6]. At that time, there was no hint of neutral current interaction. After that, in around 1960, the experimental data for non-leptonic de-

cays of strange particles indicated the presence of at least another neutral massive vector boson [7]. In 1961, Glashow formulated a model with $SU(2) \times U(1)$ symmetry for four vector bosons comprising three vector bosons of weak interaction, and photon [8]. However, in this work, masses of weak gauge bosons had to be put in by hand. This breaks the gauge symmetry, making the model non-renormalizable (as it is a non-abelian theory). Subsequently, Weinberg (1967) and Salam (1968) showed that the masses of massive gauge bosons can be accounted by using Higgs mechanism [9–13]. One can introduce a complex scalar doublet. The gauge symmetry is spontaneously broken by giving a non-zero vacuum expectation value to one of the components of this doublet [14, 15]. Weinberg speculated in his work that as the masses are generated by spontaneous symmetry breaking rather than by explicit breaking, his theory might be renormalizable. Later t’Hooft in 1971 proved that Glashow, Weinberg, and Salam (GWS) model of electroweak interaction is indeed renormalizable [16, 17]. While the presence of charged weak current was known from the mid 1930s, the first experimental evidence of weak neutral current came in 1973 from electron–anti-neutrino scattering [18]. This gave a boom to GWS model. Later, in 1983, massive electroweak bosons, W^\pm and Z , were directly discovered by UA1 and UA2 collaborations [19–22].

Like the electroweak interaction, several decades of research culminated in the present form of quantum chromodynamics (QCD), based on $SU(3)$ color gauge symmetry. Historically, many new particles such as Kaons, Lambda were discovered around 1950s, which decay much more slowly than their production. To explain this property of various such particles a new¹ quantum number S , Strangeness, was introduced independently by Gell-

¹Back then only isospin quantum number was used in the context of strong interaction.

Mann [23], and Nakano and Nishijima [24] around 1953. This number is conserved during the production of these strong particles, but not in their decay. In 1961, Gell-Mann [25, 26] and Ne'eman [27] independently found a way to organize these various strongly interacting particles in a specific pattern (the eight fold way). The principle of eightfold way was also used to organize the spin-3/2 baryons in a decuplet which led to the prediction of Omega (Ω^-) particle and its subsequent discovery in 1965. The eightfold way, in 1964, led to the introduction of quark model independently by Gell-Mann [28] and Zweig [29, 30]. However, here the underlying symmetry was $SU(3)$ flavor symmetry, not the $SU(3)$ color symmetry. In the quark sector, the need for a new quantum number other than flavor was first hinted in 1965 for the consistency of Δ^{++} and Ω^- particle wave-functions [31–33]. Finally, in 1973, Gell-Mann, Fritzsch, and Leutwyler formulated quantum chromodynamics based on $SU_C(3)$, in which three color states of a quark and eight color states of the gluons were considered [34]. The direct evidence of gluon was found later in 1979 in the observation of three jets [35, 36]. In 1968, in a deep inelastic scattering experiment at SLAC, the phenomena of scaling was discovered. It could be understood using current algebra tools, as shown by Bjorken [37], or using parton model which was later introduced by Feynman [38, 39]. Subsequent identification of partons with quarks, and discovery of scaling violation gave strong support to QCD. The quantum chromodynamics (QCD) shows two important features: color confinement which explains non-observation of free color particles and the asymptotic freedom [40, 41], i.e., the QCD coupling constant decreases asymptotically with increase in energy scale. At high energy, this asymptotic freedom allows us to use perturbation theory for QCD calculations. To compute, proton-proton collision cross section to some final states, we must know parton distribution functions, i.e., probability distribution

of quarks, antiquarks, and gluon with some fraction of proton's momentum. Because of lack of our proper understanding of low energy QCD, the parton distribution functions are obtained by using experimental data. However, lattice QCD calculation has been partially successful in calculating parton distribution functions. The evolution of parton distribution functions with energy scale is governed by Dokshitzer-Gribov-Lipatov-Altarelli-Parisi (DGLAP) equation [42–44].

Although, the quark model in 1964 was based on three light quarks (u,d,s), later in 1970, Glashow, Iliopoulos, and Maiani used a fourth quark, charm, to explain vanishingly small *flavor changing neutral current* [45]. Subsequently, in 1974, charm quark was discovered in the bound state J/ψ ($c\bar{c}$) [46,47]. The third generation quarks were also discovered [48–50] in 1977 (b-quark) and in 1995 (t-quark). The existence of this generation was important to incorporate CP violation in the quark sector as only two generations cannot give CP violation [51]. Meanwhile, the third generation charged lepton (tau) was also anticipated in 1971 [52] and was later discovered in 1975 [53]. Finally with the discovery of the Higgs boson in 2012, all the particles of the SM are now discovered. In the SM, there are nineteen² free parameters which need to be fixed by experiments. These are six quarks and three charged leptons masses, four Cabibbo-Kobayashi-Maskawa (CKM) parameters, three electroweak parameters, mass of the Higgs boson, one strong coupling, and one strong CP phase. Except the Higgs boson's mass, all other parameters were known before 2012. In 2012, with the discovery of the Higgs boson with 125 GeV mass, all the nineteen free parameters of the SM are now fixed. All the couplings in the SM depend on these parameters only. The measurements of various couplings for various particle interactions at

²With the discovery of the neutrino masses, at least seven more parameters are needed.

experiments are so far consistent with the SM theoretical predictions within experimental uncertainty. Except some couplings involving Higgs boson, all other couplings are very tightly constrained from various experiments at the LEP [54], the Tevatron [55], various previous colliders, and more recently at the LHC.

As we have just seen, the SM of particle physics has been spectacularly successful in explaining various phenomena. Various experiments and theoretical propositions moulded the current form of the SM. Despite its rich history and successes, there are still many questions on which the standard model is completely silent. Some of these unresolved questions include hierarchy problem, why three generations, strong CP problem, unification, matter-antimatter asymmetry, dark matter, nature of neutrino mass and so on [56]. Various beyond the standard model scenarios, such as Supersymmetry, Technicolor, 2HDM, Little Higgs model, pseudo Goldstone models, Dilaton model, and a host of other models with larger symmetry and field contents have been proposed to tackle these various questions [57]. The predictions of these models still have to be tested experimentally in order to validate them as theory. Models with Supersymmetry are one class of models which have shown potential to answer many of the unresolved questions. But so far no experimental evidence has been found for these models, neither in terms of discovery of a new resonance nor by observation of any new phenomena. The data collected so far at the LHC has only elevated the lower bounds on the masses of supersymmetric particles [58]. Models like Technicolor are seriously constrained after the discovery of the Higgs boson. Parameters of pseudo-Goldstone model, little Higgs model, and others are also getting constrained. Getting some signature to validate string theory at the LHC seems next to impossible.

In the absence of the discovery of any new resonance, model independent study of

new physics are becoming important. The dimension-six ($D=6$) operators, even though non-renormalizable, are being used to parametrize the effect of UV-complete arbitrary new physics lying at a high energy scale at comparatively much lower scale³. In 1986, Buchmuller and Wyler listed $D=6$ operators [59] which obey $SU_C(3) \times SU_L(2) \times U_Y(1)$. Some of the redundant operators in this list have been reported from time to time. Now, in the literature, there is Warsaw basis [60], in which after using equations of motions and other properties, it has been shown that there are only 59 $D=6$ operators if baryon number conservation is assumed. If this baryon number conservation is relaxed, there are 4 extra operators. There are other bases, such as SILH basis [61], Higgs basis [62] etc. It is possible to go from one basis to others using equation of motion and some identities. Depending on the processes under consideration, one decides which basis to work on. The coefficients of these operators, called Wilson coefficients, are getting constrained with the accumulation of more and more data at the LHC. There is another EFT, called Higgs EFT, where electroweak symmetry is non-linearly realized, and Higgs boson there appears as a singlet of custodial symmetry. This EFT is more general and, thereby, less predictive than SMEFT.

In the absence of any new signal, precision study is another way to search for any new physics effect. Only experimental precision is not enough, theoretical precision is needed as well so that if some mismatch is found between experiment and theory, one can claim that as an evidence for beyond the SM physics. Here comes the importance of radiative corrections. Techniques for one-loop calculation are quite straightforward and follow some standard steps. For one loop calculation, every scalar integral or tensor integral

³Fermi theory of beta decay is one such example of effective field theory parametrizing the effect of UV-complete SM at energies much lower than the electroweak scale.

of any rank, with any number of denominators, can be written in terms of only four basic types of scalar integrals — box, triangle, bubble, and tadpole [63] — which are known as master integrals of one-loop calculation. There are several ways in which one can perform the reduction of tensor integrals to master scalar integrals — Passarino-Veltman technique, Oldenburg-Vermaseren technique, OPP method etc. [64]. During the reduction of integrals to the master scalar integrals, sometimes rational terms appear, which are an artifact of dimensional regularization. There are several publicly available packages to perform the reduction of tensor integrals, most of which are based on Passarino-Veltman Technique. In our calculation, however, we have used an in-house package, OVRReduce [65], which is based on Oldenburg-Vermaseren technique [66]. For the computation of master scalar integrals, we have used publicly available OneL0op package [67].

As already discussed, parameters of several beyond-the-standard-model (BSM) scenarios are getting severely constrained with the accumulation of more and more data. In such a scenario, rare processes and radiative corrections may provide hint for new physics when experiments will reach certain level of accuracy. This thesis considers various production channels of a few multi-boson final states including the Higgs boson. In particular, we focus on gluon-gluon (gg) fusion channels, which occurs at one loop. At a pp collider with the increase in the center-of-mass energy gluon-gluon flux also increases. For this reason, at the future high energy colliders, gg fusion channel processes will play an important role. In one of the chapters, we consider the production of hhh , hhZ , and $hh\gamma$. Our main focus is the gg fusion channel contribution to the production of these final states. We also study new physics effects in these processes. The effect of various anomalous couplings, inspired partly by dimension-six operators, have been discussed. In particular, we consider

the modification of $t\bar{t}h$, hhh , $hhhh$, hZZ , and $hhZZ$ couplings. Out of these, the $t\bar{t}h$ and hZZ couplings have already been constrained up to 10-20% at 1σ confidence level, [68]. But the rest are practically unconstrained. Although the effect of scaling of some of these couplings on these processes have already been considered in the literature, we study the effect of derivative couplings as well which have not been considered before.

The hhh production process is particularly important as it depends on quartic Higgs boson coupling. The gluon-gluon fusion channel is the dominant production channel for this process. The $gg \rightarrow hhh$ process is specially sensitive to anomalous trilinear Higgs boson coupling. The $pp \rightarrow hhZ$ production has quark-antiquark ($q\bar{q}$) initiated tree level contribution. The gg fusion channel for this process is next-to-next-leading order (NNLO) in α_s . This gg fusion channel is important also because it is one of the processes which contains $hhZZ$ coupling. For the triangle diagrams in this channel, the presence of axial vector current introduces anomaly if only one flavor of a generation is considered in the loop. However, with all the flavors in a generation, the anomaly cancels. The NNLO contribution can be similar to next-to-leading order (NLO) contribution at the LHC, and significantly more at higher center-of-mass energy machines. For the $gg \rightarrow hhZ$ process, there is some modest dependence on anomalous hZZ couplings. The $gg \rightarrow hh\gamma$ process doesn't occur at the LO, owing to Furry's theorem [69].

In another chapter, we consider the production of $\gamma\gamma h$, γZh , ZZh , and W^+W^-h at the LHC, HE-LHC (27 TeV), and FCC-hh (100 TeV) colliders. In the SM scenario, some of them have already been considered before [70, 71]. However, we use different tensor reduction technique, different package for scalar integrals, and above all different philosophy for the calculation. In addition, we examine various other aspects for these processes. Our

main focus is to estimate the gg fusion channel contributions to their production and compare them with corresponding contributions from the $q\bar{q}$ initiated channel. We compare the contribution of gg fusion channel with NLO QCD correction to $q\bar{q}$ initiated process at FCC-hh collider. In $gg \rightarrow WWh$ process, Furry's theorem does not work for diagrams where both top and bottom quarks are present in the loop. In this channel, $t\bar{t}$ threshold effect can be seen at 350 GeV in the center-of-mass energy distribution. Here we have adopted kappa framework to study the effect of anomalous couplings on these processes. We consider the effect on both gg fusion and $q\bar{q}$ initiated channels.

This thesis also discusses possibility of distinguishing various Higgs potential scenarios at the hadron colliders and the effect of these scenarios on hh and hhh productions through gg fusion channel [72]. After the discovery of the Higgs boson, next quests are to explore its exact nature, electroweak symmetry breaking mechanisms, shape of the Higgs potential and so on. Besides Landau-Ginzburg potential of the SM, there are various other existing scenarios for the Higgs potential. Some of such new physics scenarios are — Elementary Higgs in which scaling of the SM Higgs boson coupling and SMEFT are considered, Nambu-Goldstone model [73] which arises from strong dynamics at high scales, Coleman-Weinberg Higgs [74], Tadpole-induced Higgs [75]. The Higgs potentials in these models have very different trilinear and quartic Higgs boson couplings than the ones in the SM. Despite having different couplings from the SM ones, these models are still allowed by the data collected at the LHC. So far, the trilinear Higgs boson coupling is very weakly constrained [76] and there is no constraint on quartic Higgs boson coupling. In order to distinguish these various Higgs potential scenarios, we consider hh production via the gg fusion channel at various colliders. Out of box and triangle diagrams in this channel, the

trilinear Higgs boson vertex is present only in the triangle diagrams. As different Higgs potential scenarios predict different trilinear Higgs boson couplings, hh production, being dependent on it, is capable of distinguishing these scenarios. We have studied interference between the box and triangle diagrams and discuss its effect on total and differential cross sections. The triangle diagram, being an s-channel one, contributes significantly near the threshold of hh production. Because of this, with some p_T^h cut, the triangle contribution decreases faster than other contributions to the cross section. In addition, we consider the possibility of constraining trilinear Higgs boson coupling if cross section can be measured with some benchmark accuracies.

The trilinear and quartic Higgs boson couplings decrease in pseudo-Goldstone models, increase in Coleman-Higgs model, and become nearly zero in the tadpole-induced model. Pseudo-Goldstone model, besides changing $t\bar{t}h$ coupling, introduces $t\bar{t}hh$ and $t\bar{t}hhh$ vertices, and cross section for this model is found to be more than that in the SM for both hh and hhh productions. The contribution of the new pure square and interference terms arising because of these new vertices have been computed. Unlike pseudo-Goldstone models, in the tadpole-induced and Coleman-Higgs models neither $t\bar{t}h$ coupling changes from the SM value nor new vertices are introduced. The tadpole-induced model has larger cross section than that of SM. The Coleman-Higgs model on the other hand has smaller cross section. All these different cross sections allow us to discriminate these models at 27 TeV collider and even more at 100 TeV collider. However, as is also well-known, the $gg \rightarrow hhh$ process detection is very difficult — the cross section for this process in the SM is around 30 ab and 3000 ab at 14 TeV (LHC) and 100 TeV (FCC-hh) colliders, respectively. There are a total fifty diagrams — twenty-four penta, eighteen box, and eight triangle diagrams (if

only top quark is considered in the loop). Out of these fifty diagrams, the quartic Higgs boson coupling is present only in two (triangle) diagrams. Constraining quartic Higgs boson coupling with some reasonable degree will be extremely challenging as the cross section depends very mildly on it. Interference of various classes of diagrams has been discussed in detail in order to discern dependence of various parts of the cross section on the quartic Higgs boson coupling. In addition, we have shown how the quartic Higgs boson coupling measurement will depend on some benchmark values of trilinear Higgs boson coupling.

The thesis is organized as follows. In Chapter 2, we discuss the SM and EFT scenarios. In Chapter 3, we describe the techniques of one-loop calculation. The production of hhh and hhV , where $V = \gamma, Z$ via gluon fusion channel and the effect of different D=6 operators have been discussed in chapter 4. Next, in chapter 5, we discuss production of di-vector boson in association with a Higgs boson at various hadron colliders. In Chapter 6, we describe various Higgs potential scenarios and possibility of distinguishing them at hadron colliders. We also examine the possibility of measuring the self couplings of the Higgs boson. Finally, in Chapter 7, we conclude this thesis.

Chapter 2

Standard Model and Effective field theories

Contents

2.1	SM	14
2.2	SMEFT	22
2.2.1	Warsaw basis	24
2.2.2	SILH basis	27
2.2.3	Effective Lagrangian of mass eigenstates	29
2.2.4	Higgs basis	30
2.2.5	Other frameworks	30
2.3	HEFT	31

In the absence of any new signal at the LHC after the discovery of the Higgs boson, model independent studies of new physics in the effective field theory (EFT) framework are gaining importance for constraining parameters of the BSM scenarios. Our main goal in this chapter is to give a brief overview of various EFT frameworks. An EFT framework can be used to describe the effect of new physics lying at some high energy scale at comparatively low energy where the experiment is performed. One drawback of EFTs is that these are non-renormalizable. The heavy degrees of freedom of the new physics can be integrated out when the physics at relatively low energy scale is being studied, and, this way matching of parameters of BSM scenarios with parameters of EFT can be done. In this way, the parameters of an EFT framework, known as Wilson coefficients, are constrained. This can be translated to obtain bounds on parameters of a host of BSM models. In the SM, $SU(2)_L \times U(1)_Y$ symmetry is realized linearly. There are two types of EFTs for electroweak sector — one, where $SU(2)_L \times U(1)_Y$ is linearly realized and other where the symmetry is non-linearly realized. These two types of EFT frameworks are known as SMEFT and HEFT¹, respectively. Before discussing various EFT scenarios, we will briefly summarize the SM.

2.1 SM

Our current understanding of strong and electroweak interactions is encapsulated in the SM, which is based on the gauge group $SU_C(3) \times SU_L(2) \times U_Y(1)$. There are six flavors of quarks, three charged leptons and three neutrinos as matter fields in the SM. Moreover, each

¹In the literature, the same word HEFT is also used in completely different context: to describe effective Lagrangian for the Higgs processes with infinitely heavy top quark limit.

of the six quarks has three color states. All the matter particles in the SM except neutrino have both right and left chiral states, while a neutrino has only left chiral state². Each of the matter particle has antiparticle counterpart with opposite chirality. Thus anti-neutrino has right chiral state only. The strong, weak, and electromagnetic interaction in the SM are mediated by gauge bosons. There are 8 colored gluons (g) which mediate strong interaction, two heavy charged bosons (W^\pm) and one neutral boson (Z) which mediate weak interaction, and one photon (γ) which mediates electromagnetic interaction. The strong interaction is governed by $SU_C(3)$ gauge symmetry, where each color of a quark transforms under fundamental representation and each colored gluon transforms in the adjoint representation of the group. As the group is non-abelian, the gluons also interact with themselves. This is unlike electrodynamics where a photon does not interact with itself, being governed by abelian group. While the weak charged bosons interact only with left-chiral fermions³ in a doublet, the neutral weak boson, Z , interact with both left and right handed fermions. The electromagnetic interactions between two charged particles is mediated by photon, γ . In the SM, weak and electromagnetic interaction is unified in the gauge group $SU_L(2) \times U_Y(1)$ ⁴. The gauge bosons for these groups are W^1, W^2, W^3 , and B . The first two unphysical fields mix to give physical W^\pm . The last two unphysical fields mix by Weinberg angle to give Z and γ . This clarifies how W^\pm interact with left handed fermions only, while Z and γ can interact with both. Because of non-abelian nature, like gluons, electroweak gauge bosons also interact among themselves. In the SM, $SU_L(2) \times U_Y(1)$ gauge symme-

²Now neutrinos are known to have masses. Neutrinos can be either Dirac or Majorana type. Models accommodating masses for Dirac type neutrinos include both chiral states.

³We will not separately talk about anti-fermions. It is implicit that whatever is true for fermions with specific chirality is also true for anti-fermions with opposite chirality unless stated otherwise. The exception occurs in the case of CP violation.

⁴The “ L ” in $SU_L(2)$ tells that only left-handed fermions form doublet.

try is spontaneously broken to $U_Q(1)$ by introducing a Higgs doublet and giving one of its component a non-zero vacuum expectation value. In the unbroken phase, the full standard model Lagrangian can be written as

$$\begin{aligned}
\mathcal{L}_{SM} = & \sum_{f \in q,l} i \bar{f}_L \gamma^\mu D_\mu f_L + \sum_{f \in u,d,e} i \bar{f}_R \gamma^\mu D_\mu f_R \\
& - \frac{1}{4} G_{\mu\nu}^a G^{a\ \mu\nu} - \frac{1}{4} W_{\mu\nu}^i W^{i\ \mu\nu} - \frac{1}{4} B_{\mu\nu} B^{\mu\nu} \\
& + (D_\mu H)^\dagger (D^\mu H) - \mu_H^2 H^\dagger H - \lambda (H^\dagger H)^2 \\
& + [y_d \bar{q}_L H d_R + y_u \bar{q}_L \tilde{H} u_R + y_e \bar{l}_L H e_R + h.c.], \tag{2.1}
\end{aligned}$$

where the covariant derivative is defined as $D_\mu = \partial_\mu - ig S^I W^I - ig' Y B - ig_s T^a G^a$, $S^I = \sigma^I/2$ and $T^a = \lambda^a/2$. σ^I and λ^a are Pauli and Gell-Mann matrices, respectively. The field strength tensors are defined⁵ as $G_{\mu\nu}^a = \partial_\mu G_\nu^a - \partial_\nu G_\mu^a + g_s f^{abc} G_\mu^b G_\nu^c$, $W_{\mu\nu}^I = \partial_\mu W_\nu^I - \partial_\nu W_\mu^I + g \epsilon^{IJK} W_\mu^J W_\nu^K$ and $B_{\mu\nu} = \partial_\mu B_\nu - \partial_\nu B_\mu$. The \tilde{H}_i is defined as $\tilde{H}_i = \epsilon_{ij} H_j^*$. In the doublet form, this can be written as $\tilde{H} = i\sigma_2 H^*$. While the left handed quarks and leptons form doublet of $SU_L(2)$, that is, $q_L = \begin{pmatrix} u_L \\ d_L \end{pmatrix}$, $l_L = \begin{pmatrix} \nu_L \\ e_L \end{pmatrix}$, the right handed fermions, u_R, d_R , and e_R are singlet, i.e., they remain invariant under $SU_L(2)$ group transformation. Leptons and Higgs fields are singlet under $SU(3)_C$.

Various comments and physics emerging from the above Lagrangian are as follows:

- We have suppressed here the Dirac indices, color indices, and generation indices for brevity.
- The operators in the first line of Eq. 2.1 express fermions' kinetic term and their interaction terms with gauge bosons.

⁵The sign in front of coupling constants in covariant derivative and field strength tensor are correlated.

- The operators in the second line of Eq. 2.1, express gauge bosons kinetic term and self interaction of non-abelian gauge fields, G_μ^a , W_μ^I .
- The operators in the last two lines are related to Higgs sector in the standard model. The first term in the third line describes kinetic term of Higgs boson and interactions of Gauge boson with Higgs boson. It also generates mass of the weak gauge boson, when one of the component of the Higgs doublet gets a non zero vacuum expectation value.
- The last two terms in the third line is the Landau Ginzberg potential in the standard model, minimization of which generates Higgs boson's mass. μ^2 is negative. After symmetry breaking, the physical Higgs boson gets positive mass. Although the Higgs boson is discovered in 2012, the trilinear Higgs boson coupling is experimentally so far poorly constrained and there is practically no constraint on quartic Higgs boson coupling.
- The operators in the last line generates mass for quarks and charged leptons after one of the component of Higgs doublet gets vacuum expectation value (vev). In the SM, masses of fermions and vev can be taken as free parameters. As these parameters are fixed by experiments, one has prediction for the Yukawa couplings of fermions with the Higgs boson. Currently, measured Yukawa coupling of top quark with the Higgs boson is consistent with prediction of Standard model within 10-20% 1σ experimental uncertainty.
- We have not added the gauge fixing terms and Faddeev-Popov ghost, required for

proper quantization of gauge fields. The Faddeev-Popov ghost is especially required in non-abelian gauge theory.

- $S^I W^I = \frac{1}{\sqrt{2}} S^+ W^+ + \frac{1}{\sqrt{2}} S^- W^- + S^3 W^3$, where $S^+ = S^1 + iS^2 = \frac{\sigma^1 + i\sigma^2}{2} = \begin{pmatrix} 0 & 1 \\ 0 & 0 \end{pmatrix}$ and $S^- = S^1 - iS^2 = \frac{\sigma^1 - i\sigma^2}{2} = \begin{pmatrix} 0 & 0 \\ 1 & 0 \end{pmatrix}$, and $W^\pm = \frac{1}{\sqrt{2}}(W^1 \mp iW^2)$, where W^\pm are the physical weak charged boson fields.
- The CKM matrix did not appear in Eq. 2.1 since the Yukawa matrices have not been diagonalized. By field rotations of up and down type quarks, Yukawa matrices can be diagonalized. To diagonalize up and down type Yukawa matrices, up and down type quark fields of both helicities need to be rotated by four different unitary matrices⁶. These rotation matrices will disappear from the neutral current interaction. But in the charge current interaction, the associated unitary matrices for left-chiral up and down type quark fields will remain and give rise to CKM matrix.
- W^3 and B fields mix together to give the physical weak neutral field, Z , and photon field A . They follow $\begin{pmatrix} W^3 \\ B \end{pmatrix} = \begin{pmatrix} \cos \theta_w & \sin \theta_w \\ -\sin \theta_w & \cos \theta_w \end{pmatrix} \begin{pmatrix} Z \\ A \end{pmatrix}$. Using these equations, $gS^3 W^3 + g'YB$ can be written in the following form: $(g \cos \theta_w S^3 - g' \sin \theta_w Y)Z + (g \sin \theta_w S^3 + g' \cos \theta_w Y)A$. We would like to identify $(g \sin \theta_w S^3 + g' \cos \theta_w Y)A$ as eQA , where e is the magnitude of electric charge. We can assign values to weak Hypercharge Y depending on fermionic fields. But once Hypercharge for one particle is arbitrarily assigned, because of the assumed universality of electroweak couplings other hypercharges are also fixed. In the following we will see how this happens. The left-handed fermions are put in doublet, and right handed ones remain as singlet.

⁶See Chapter. 20 of Peskin and Schroeder.

The doublets are denoted by $q_L = \begin{pmatrix} u_L \\ d_L \end{pmatrix}$ and $l_L = \begin{pmatrix} \nu_L \\ e_L \end{pmatrix}$. The corresponding Q for them are $\begin{pmatrix} +\frac{2}{3} & 0 \\ 0 & -\frac{1}{3} \end{pmatrix}$ and $\begin{pmatrix} 0 & 0 \\ 0 & -1 \end{pmatrix}$, respectively. Now using leptonic doublet, we get the following two equations:

$$\begin{aligned} 0 &= \frac{g}{2} \sin \theta_w + g' \cos \theta_w y^l \\ -e &= -\frac{g}{2} \sin \theta_w + g' \cos \theta_w y^l, \end{aligned} \quad (2.2)$$

solving which we get $e = g \sin \theta_w$ and $e = -2g' \cos \theta_w y^l$. Here we can assign any value to y^l , and if we wish, accordingly we can redefine g' . But for convenience, let us take $y^l = -\frac{1}{2}$. This sets $e = g' \cos \theta_w$. Now, the hypercharge of all the doublets and singlets can be calculated assuming weak universality. Let's find hypercharge of quark doublet:

$$\begin{aligned} +\frac{2}{3}e &= \frac{g}{2} \sin \theta_w + g' \cos \theta_w y^q \\ \Rightarrow +\frac{2}{3}e &= \frac{e}{2} + e y^q \\ \Rightarrow +\frac{2}{3} &= \frac{1}{2} + 1 y^q \\ \Rightarrow y^q &= \frac{1}{6} \end{aligned}$$

As the S^3 acting on right-chiral field gives zero, it is easy to see for right-chiral fields, hypercharge is equal to their electric charge quantum number, i.e., $y^{e_R} = -1, y^{\mu_R} = +\frac{2}{3}$, and $y^{d_R} = -\frac{1}{3}$. Similarly, it can be shown that $y^H = +\frac{1}{2}$ and $y^{\tilde{H}} = -\frac{1}{2}$.

- In the Eq. 2.2, there are five unknowns, namely e, θ, g, g' , and y^l . We have fixed

y' to be $-\frac{1}{2}$. So there are four unknowns. We can choose two to be independent and express other two in terms of them. We will choose e and θ to be independent, and express g and g' in terms of them. So $g = \frac{e}{\sin \theta_w}$ and $g' = \frac{e}{\cos \theta_w}$. So, we can use this to write $(g \cos \theta_w S^3 - g' \sin \theta_w Y)Z = \frac{e}{\cos \theta_w \sin \theta_w} (\cos^2 \theta_w S^3 - \sin^2 \theta_w Y)Z = \frac{e}{\cos \theta_w \sin \theta_w} (\cos^2 \theta_w S^3 - \sin^2 \theta_w (Q - S^3))Z = \frac{e}{\cos \theta_w \sin \theta_w} (S^3 - \sin^2 \theta_w Q)Z$.

- When Higgs doublet gets a vev, i.e., $\langle H \rangle_0 = \frac{1}{\sqrt{2}} \begin{pmatrix} 0 \\ v \end{pmatrix}$, W^\pm and Z get masses, while photon remains massless. This happens as $S^+ \langle H \rangle_0 \neq 0$, $S^3 \langle H \rangle_0 \neq 0$, and $Q \langle H \rangle_0 = 0$. We say the symmetry is only partially broken by the vacuum, and it still possess the $U_Q(1)$ symmetry. The full symmetry in the Lagrangian is still there, but hidden. Using $\langle H \rangle_0 = \frac{1}{\sqrt{2}} \begin{pmatrix} 0 \\ v \end{pmatrix}$ in $(D_\mu H)^\dagger (D^\mu H)$, we get masses for W^\pm and Z as $M_W = \frac{gv}{2}$ and $M_Z = \frac{ev}{2 \cos \theta_w \sin \theta_w} = \frac{gv}{2 \cos \theta_w} = \frac{M_W}{\cos \theta_w}$. As the vacuum possesses $U_Q(1)$ symmetry, i.e., $Q \langle H \rangle_0 = 0$, the photon remains massless.
- After the spontaneous breaking of electroweak symmetry by the non-zero vacuum expectation value of the Higgs doublet, some parts of standard model Higgs sector still possess a symmetry, known as custodial symmetry. This can be seen in the Higgs potential where after one of the components of the Higgs doublet gets vev, the associated $SO(4)$ symmetry of the Higgs potential breaks to $SO(3)$ symmetry, which is locally isomorphic to $SU_V(2)$. However this symmetry is not obeyed by all the operators in Higgs sector, as the fermion masses of the third generation are not same and also because of weak Hypercharge couplings which does not allow masses of the three weak vector bosons to be same. At the tree level, the $\rho = \frac{M_W}{M_Z \cos \theta}$ parameter is equal to 1. At the loop level, however, it gets correction from fermionic sector where

the custodial symmetry is broken because of unequal masses of the quarks in the third generation. But because of the loop suppression, the correction is still small.

- There are nineteen free parameters in the SM — nine masses (six quark masses and three lepton masses), three Euler angles, one CP phase, one strong coupling g_s , two electroweak coupling g and g' , vev v , mass of the Higgs boson m_H (or quartic Higgs boson couplings λ), and strong CP phase δ_{CP} . Instead of g , g' , and v , some electroweak precision observables can be used as input variables for prediction of other observables. Two popular choices are (i) $\alpha_e = \frac{e^2}{4\pi} = \frac{g^2 g'^2}{4\pi(g^2 + g'^2)}$, $M_Z = \sqrt{g^2 + g'^2} \frac{v}{2}$, and $G_F = \frac{1}{\sqrt{2}v^2}$ — known as α scheme and (ii) $M_W = g \frac{v}{2}$, $M_Z = \sqrt{g^2 + g'^2} \frac{v}{2}$, and $G_F = \frac{1}{\sqrt{2}v^2}$ — known as M_W scheme. The α scheme is widely used in the literature. One of the electroweak observable it predicts is M_W and is given by $M_W = \frac{gv}{2} = \sqrt{\frac{e^2 v^2}{4 \sin^2 \theta_w}} = \sqrt{\frac{\pi \alpha_e}{\sqrt{2} G_F \sin^2 \theta_w}} = \frac{M_Z}{\sqrt{2}} \sqrt{1 + \sqrt{1 - \frac{2\sqrt{2}\pi\alpha_e}{G_F M_Z^2}}}$, where we have used $\sin \theta_w = \sqrt{1 - \frac{M_W^2}{M_Z^2}}$ to solve for M_W . Using experimental values for α_e , M_Z , and G_F , gives tree level M_W mass as 80.94 GeV [77], while the experimental results point to a mass of 80.363 ± 0.020 GeV [5]. Higher order correction reduce the theoretical M_W mass significantly and now the theoretical prediction is within experimental uncertainty. There are many other electroweak observables which have been used to validate the SM electroweak sector [5, 77] and constrain parameters of new physics models.
- In the SM, neutrinos are massless and there is no right handed neutrino. If we consider neutrino masses and mixing angles, at least seven more free parameters appear, increasing the total number of free parameters from nineteen to twenty six. It is to be

noted that inclusion of right handed neutrino in the SM does not give rise to any fundamental problem. The charged weak boson still interact with left-handed doublets and does not interact with right handed neutrino as it is singlet under $SU_L(2)$. Since neutrino were considered to be massless, in the original SM, one Yukawa coupling was set to be zero. There are many ways to give masses to neutrino. One popular choice for generating neutrino mass is seesaw mechanism.

In this brief summary, we could not provide many other details of SM. For an elaborate pedagogical review of the SM, readers are referred to [78].

2.2 SMEFT

An effective field theory describing physics at energies much below the mass scale Λ of new resonances can be parametrized as

$$\mathcal{L}_{eff} = \mathcal{L}_{SM} + \sum_i \frac{c_i^{(5)}}{\Lambda} \mathcal{Q}_i^{(5)} + \sum_i \frac{c_i^{(6)}}{\Lambda^2} \mathcal{Q}_i^{(6)} + \sum_i \frac{c_i^{(7)}}{\Lambda^3} \mathcal{Q}_i^{(7)} + \sum_i \frac{c_i^{(8)}}{\Lambda^4} \mathcal{Q}_i^{(8)} + \dots \quad (2.3)$$

where each \mathcal{Q}_i^D is an operator of canonical dimension D satisfying $SU_C(3) \times SU_L(2) \times U_Y(1)$ symmetry and the parameters c_i are known as Wilson coefficients. The coefficients are dimensionless. All the operators are formed using the SM fields only. This EFT is known as SMEFT where the electroweak symmetry is linearly realized. As already mentioned in the introduction of this chapter, the main goal of studying new physics in EFT framework is to constrain parameters of EFT scenario, which later can be translated to obtain bounds on the couplings and masses of a host of BSM scenarios whose resonances

lie in much higher energy regime than where the EFT is being applied. As far as the low-energy phenomenology with respect to the new physics energy scale, Λ , is concerned, generally operators with larger dimension are more suppressed, unless because of some symmetry, lower dimensional operators' effect is smaller. The effect of a D-dimensional operator at the energy scale ν is suppressed by the factor $(\frac{\nu}{\Lambda})^{D-4}$ in comparison to SM effects. There is only one operator in D=5, known as Weinberg operator, which gives Majorana mass to neutrinos. All the odd-dimensional operators violate B-L symmetry. Experiments searching for the B-L symmetry violating processes have put stringent constraints on the corresponding Wilson coefficients. So the leading new physics effects come from D=6 operators, which is suppressed by $(\frac{\nu}{\Lambda})^2$ with respect to SM effects. We don't discuss further suppressed next even dimension (D=8) operators here. The D=5 operator, and D=6 operators in various bases will be discussed in this section. The list of D=7 and D=8 operators can be found in [79–81].

We start our discussion with D=5 dimensional operators. In D=5 canonical dimension, there is actually only one operator which satisfies $SU_C(3) \times SU_L(2) \times U_Y(1)$ symmetry. This generates Majorana mass for neutrino, as well as mixing. This is also known as Weinberg operator and is given by

$$Q^{(5)} = (\tilde{H}^\dagger l)^T C (\tilde{H}^\dagger l) \quad (2.4)$$

where C is the Charge conjugation operator, given by $C = i\gamma^2\gamma^0$.

There are many bases in which one can study the effects of D=6 operators. In 2010, in Ref. [60], it was shown for the first time that for one generation there are only 59 non-

redundant set of operators if baryon number conservation is assumed. This basis is now popularly known as Warsaw basis. Although there are 59 B-conserving operators, there are 76 real parameters — 53 CP-even and 23 CP-odd parameters. If one consider full-flavor structure this number balloons to 2499 [82]. One can choose any basis and the predictions for new physics effects should not depend on the choice of basis. By the use of equation of motion, Bianchi identity, field redefinitions, integration by parts, Fierz transformation, one can move from one basis to other. Warsaw basis [60], SILH basis [61, 83], and Higgs basis [62] are the widely used bases. One meticulously chooses one basis over other depending on the observables under study. In the following, we will discuss these bases. We will write down all the operators in Warsaw basis in the following subsection. Next, we will write the SILH basis operators and show the translations from Warsaw basis to SILH basis. After that we will discuss the effective Lagrangian in mass eigenstate and Higgs basis. At the end of the section, we will briefly discuss various other frameworks people use for EFT studies.

2.2.1 Warsaw basis

In 1986, Buchmuller and Wyler listed 80 B-conserving $D=6$ operators [59] which obey $SU_C(3) \times SU_L(2) \times U_Y(1)$ symmetry. There were 16 bosonic, 35 two-fermionic and 29 four-fermionic Baryon number conserving operators. In 2010, in Ref. [60], it was shown that there are actually 59 ($=15+19+25$) non-redundant operators. The numbers 15, 19, and 25 correspond to number of bosonic, two-fermionic (bosonic-fermionic mixed), and four-fermionic (only fermionic) operators, respectively. In what follows, we briefly discuss

these 15+19+25 non-redundant B-conserving operators. In Ref. [59], one operator was redundant in the bosonic sector, and this reduces down the number of bosonic operators in it from 16 to 15. Out of 35 two-fermionic operators in [59], 16 have been shown to be redundant using equation of motions, integration by parts, and Bianchi identity. In the four-fermionic sector, it missed one operator. However, using Fierz transformation it has been shown that 5 four-fermionic operators are redundant. This makes total number of non-redundant B-conserving four-fermionic operator as 25. However, all this discussion is for B-conserving operators. If the baryon number conservation is relaxed, the number 25 in the four-fermionic sector increases to 29.

Q	CP-even	\tilde{Q}	CP-odd
$Q_{H\Box}$	$\partial_\mu(H^\dagger H)\partial^\mu(H^\dagger H)$		
Q_{HD}	$(H^\dagger D_\mu H)^*(H^\dagger D^\mu H)$		
Q_6	$(H^\dagger H)^3$		
Q_{HG}	$(H^\dagger H)G_{\mu\nu}^a G^{a\mu\nu}$	$\tilde{Q}_{H\tilde{G}}$	$(H^\dagger H)\tilde{G}_{\mu\nu}^a G^{a\mu\nu}$
Q_{HB}	$(H^\dagger H)B_{\mu\nu} B^{\mu\nu}$	$\tilde{Q}_{H\tilde{B}}$	$(H^\dagger H)\tilde{B}_{\mu\nu} B^{\mu\nu}$
Q_{HW}	$(H^\dagger H)W_{\mu\nu}^I W^{I\mu\nu}$	$\tilde{Q}_{H\tilde{W}}$	$(H^\dagger H)\tilde{W}_{\mu\nu}^I W^{I\mu\nu}$
Q_{HWB}	$(H^\dagger \tau^I H)W_{\mu\nu}^I B^{\mu\nu}$	$\tilde{Q}_{H\tilde{W}B}$	$(H^\dagger \tau^I H)\tilde{W}_{\mu\nu}^I B^{\mu\nu}$
Q_{3G}	$f^{abc}G_{\mu\nu}^a G^{b\nu\rho} G_{\rho\mu}^c$	\tilde{Q}_{3G}	$\epsilon^{abc}\tilde{G}_{\mu\nu}^a G^{b\nu\rho} G_{\rho\mu}^c$
Q_{3W}	$\epsilon^{IJK}W_{\mu\nu}^I W^{J\nu\rho} W_{\rho}^{K\mu}$	\tilde{Q}_{3W}	$\epsilon^{IJK}\tilde{W}_{\mu\nu}^I W^{J\nu\rho} W_{\rho}^{K\mu}$

Table 2.1: Bosonic CP-even and CP-odd D=6 operators in Warsaw basis. There are 9 bosonic CP-even and 6 CP-odd operators. So, in the Warsaw basis there are 15 bosonic operators. The dual tensor $\tilde{F}_{\mu\nu}$ is defined as $\frac{1}{2}\epsilon_{\mu\nu\rho\sigma}F^{\rho\sigma}$.

In Tab. 2.1, we list all the fifteen bosonic operators in Warsaw basis. Out of fifteen operators, nine are CP-even and six are CP-odd. The operator Q_6 gives correction to Higgs boson mass and to SM trilinear and quartic Higgs boson self couplings. Moreover, it introduces penta and hexa Higgs boson couplings. It is to be noted that both Q_{HD} and $Q_{H\Box}$ contribute to the kinetic term. If we wish to have canonical kinetic term, we need to redefine

fields. Additionally, these operators contribute to the Higgs-Gauge boson couplings. Other operators which can contribute to Higgs-Gauge boson couplings are Q_{HG} , Q_{HB} , Q_{HW} , Q_{HWB} . The operators Q_{3G} and Q_{3W} introduce many penta and hexa gauge bosons self couplings. The Wilson coefficients for many of these operators are constrained using Electroweak precision data from the LEP, Tevatron, and the LHC, and the Higgs data from the LHC [84]. The effects of six CP-odd operators are also found to be interesting [85, 86].

In Tab. 2.2, there are 19 operators. Out of which, 8 contribute to vertex corrections, 3 contribute to the Yukawa correction and the rest 8 contribute to the dipole correction. Many of these Wilson coefficients are well constrained [84, 87, 88]. 12 of these 19 operators are not Hermitian and for them Hermitian conjugate terms need to be added. In Tab. 2.3, we tabulate all the B-conserving four-fermionic operators. For only one generation, there are 25 of them. However for general flavor structure, the number of four fermionic operators becomes very large. Many of the Wilson coefficients are well constrained [89, 90] and will be further constrained with the accumulation of more data in the current experiments or at future colliders. Five of 25 four-fermionic operators are not Hermitian and for them Hermitian conjugate terms need to be added. This makes the total number of CP-odd parameters to be 23, that is, 6 from bosonic operators, 12 from two-fermionic operators and 5 from four-fermionic operators.

Q	Vertex	\tilde{Q}	Yukawa	\tilde{Q}	Dipole
Q_{Hl}	$(\bar{l}_i \gamma_\mu l_j)(H^\dagger \overleftrightarrow{D}_\mu H)$	Q_{eH}	$(\bar{l}_i H e_j)(H^\dagger H)$	Q_{eB}	$(\bar{l}_i \sigma^{\mu\nu} H e_j) B_{\mu\nu}$
Q'_{Hl}	$(\bar{l}_i \sigma^k \gamma_\mu l_j)(H^\dagger \sigma^k \overleftrightarrow{D}_\mu H)$	Q_{dH}	$(\bar{q}_i H d_j)(H^\dagger H)$	Q_{dB}	$(\bar{q}_i \sigma^{\mu\nu} H d_j) B_{\mu\nu}$
Q_{Hq}	$(\bar{q}_i \gamma_\mu q_j)(H^\dagger \overleftrightarrow{D}_\mu H)$	Q_{uH}	$(\bar{q}_i \tilde{H} u_j)(H^\dagger H)$	Q_{uB}	$(\bar{q}_i \sigma^{\mu\nu} \tilde{H} u_j) B_{\mu\nu}$
Q'_{Hq}	$(\bar{q}_i \sigma^k \gamma_\mu q_j)(H^\dagger \sigma^k \overleftrightarrow{D}_\mu H)$			Q_{eW}	$(\bar{l}_i \sigma^{\mu\nu} \tau^I H e_j) W_{\mu\nu}^I$
Q_{He}	$(\bar{e}_i \gamma_\mu e_j)(H^\dagger \overleftrightarrow{D}_\mu H)$			Q_{dW}	$(\bar{q}_i \sigma^{\mu\nu} \tau^I H d_j) W_{\mu\nu}^I$
Q_{Hu}	$(\bar{u}_i \gamma_\mu u_j)(H^\dagger \overleftrightarrow{D}_\mu H)$			Q_{uW}	$(\bar{q}_i \sigma^{\mu\nu} \tau^I \tilde{H} u_j) W_{\mu\nu}^I$
Q_{Hd}	$(\bar{d}_i \gamma_\mu d_j)(H^\dagger \overleftrightarrow{D}_\mu H)$			Q_{dG}	$(\bar{q}_i \sigma^{\mu\nu} T^a H d_j) G_{\mu\nu}^a$
Q_{Hud}	$(\bar{u}_i \gamma_\mu d_j)(\tilde{H}^\dagger \overleftrightarrow{D}_\mu H)$			Q_{uG}	$(\bar{q}_i \sigma^{\mu\nu} T^a \tilde{H} u_j) G_{\mu\nu}^a$

Table 2.2: Two-fermionic operators. Here l, q are left-handed doublet and e, u, d are right handed singlet of SU(2), respectively. There are 19 two-fermionic operators — 8 vertex, 3 Yukawa and 8 dipole operators. Moreover, Hermitian conjugates of Q_{Hud} , all the Yukawa operators, and all the Dipole operators need to be added.

Q	$(\bar{L}L)(\bar{L}L)$	Q	$(\bar{R}R)(\bar{R}R)$	Q	$(\bar{L}L)(\bar{R}R)$	Q	$(\bar{L}R)(\bar{L}R)$ and $(\bar{L}R)(\bar{R}L)$
Q_{ll}	$(\bar{l}_i \gamma_\mu l)(\bar{l}_j \gamma_\mu l)$	Q_{ee}	$(\bar{e}_i \gamma_\mu e)(\bar{e}_j \gamma_\mu e)$	Q_{le}	$(\bar{l}_i \gamma_\mu l)(\bar{e}_j \gamma_\mu e)$	Q_{lequ}	$(\bar{l}^j e) \epsilon_{jk} (\bar{q}^k u)$
Q_{lq}	$(\bar{l}_i \gamma_\mu l)(\bar{q}_j \gamma_\mu q)$	Q_{eu}	$(\bar{e}_i \gamma_\mu e)(\bar{u}_j \gamma_\mu u)$	Q_{lu}	$(\bar{l}_i \gamma_\mu l)(\bar{u}_j \gamma_\mu u)$	Q'_{lequ}	$(\bar{l}^j \sigma^{\mu\nu} e) \epsilon_{jk} (\bar{q}^k \sigma_{\mu\nu} u)$
Q_{qq}	$(\bar{q}_i \gamma_\mu q)(\bar{q}_j \gamma_\mu q)$	Q_{ed}	$(\bar{e}_i \gamma_\mu e)(\bar{d}_j \gamma_\mu d)$	Q_{ld}	$(\bar{l}_i \gamma_\mu l)(\bar{d}_j \gamma_\mu d)$	Q_{qdqu}	$(\bar{q}^j d) \epsilon_{jk} (\bar{q}^k u)$
Q'_{lq}	$(\bar{l}_i \gamma_\mu \sigma^I l)(\bar{q}_j \gamma_\mu \sigma^I q)$	Q_{uu}	$(\bar{u}_i \gamma_\mu u)(\bar{u}_j \gamma_\mu u)$	Q_{qe}	$(\bar{q}_i \gamma_\mu q)(\bar{e}_j \gamma_\mu e)$	Q'_{qdqu}	$(\bar{q}^j \sigma^{\mu\nu} d) \epsilon_{jk} (\bar{q}^k \sigma_{\mu\nu} u)$
Q'_{qq}	$(\bar{q}_i \gamma_\mu \sigma^I q)(\bar{q}_j \gamma_\mu \sigma^I q)$	Q_{ud}	$(\bar{u}_i \gamma_\mu u)(\bar{d}_j \gamma_\mu d)$	Q_{qu}	$(\bar{q}_i \gamma_\mu q)(\bar{u}_j \gamma_\mu u)$	Q_{ledq}	$(\bar{l}^j e)(\bar{d} q^j)$
		Q_{dd}	$(\bar{d}_i \gamma_\mu d)(\bar{d}_j \gamma_\mu d)$	Q_{qd}	$(\bar{q}_i \gamma_\mu q)(\bar{d}_j \gamma_\mu d)$		
		Q'_{ud}	$(\bar{u}_i \gamma_\mu T^a u)(\bar{d}_j \gamma_\mu T^a d)$	Q'_{qu}	$(\bar{q}_i \gamma_\mu T^a q)(\bar{u}_j \gamma_\mu T^a u)$		
				Q'_{qd}	$(\bar{q}_i \gamma_\mu T^a q)(\bar{d}_j \gamma_\mu T^a d)$		

Table 2.3: Four-fermionic operators. There are 25 B-conserving four-fermionic operators. Hermitian conjugates of 5 operators in $(\bar{L}R)(\bar{L}R)$ and $(\bar{L}R)(\bar{R}L)$, i.e., the operators in the last column need to be added.

In the next subsection, we will discuss the SILH basis.

2.2.2 SILH basis

Even though physical studies can be done in any complete basis, some studies are more transparent in one basis than others. One can go from one basis to other using equation of motion, integration by parts, field redefinition etc. For some studies of new physics effects, the SILH basis [61, 83] may be more suitable than the other bases. For example, when new

physics sector has direct coupling with the Higgs boson but not with the SM fermions, it is better to parametrize new physics effects in terms of purely bosonic operators containing Higgs boson rather than in terms of two-fermionic operators. For studying Higgs physics, the SILH basis can be sometimes more suitable than the Warsaw basis. In the following, we tabulate the bosonic operators in the SILH basis. Many operators here are same as that in the Warsaw basis.

O	CP-even	\tilde{O}	CP-odd
O_H	$\partial_\mu(H^\dagger H)\partial^\mu(H^\dagger H)$		
O_T	$(H^\dagger \overleftrightarrow{D}_\mu H)(H^\dagger \overleftrightarrow{D}^\mu H)$		
O_6	$(H^\dagger H)^3$		
O_g	$(H^\dagger H)G_{\mu\nu}^a G^{a\mu\nu}$	\tilde{O}_g	$(H^\dagger H)\tilde{G}_{\mu\nu}^a G^{a\mu\nu}$
O_γ	$(H^\dagger H)B_{\mu\nu}B^{\mu\nu}$	\tilde{O}_γ	$(H^\dagger H)\tilde{B}_{\mu\nu}B^{\mu\nu}$
O_B	$(H^\dagger \overleftrightarrow{D}_\mu H)D_\nu B^{\mu\nu}$		
O_{HB}	$(D_\mu H^\dagger D_\nu H)B^{\mu\nu}$	\tilde{O}_{HB}	$(D_\mu H^\dagger D_\nu H)\tilde{B}^{\mu\nu}$
O_W	$(H^\dagger \sigma^i \overleftrightarrow{D}_\mu H)D_\nu W^{i\mu\nu}$		
O_{HW}	$(D_\mu H^\dagger \sigma^i D_\nu H)W^{i\mu\nu}$	\tilde{O}_{HW}	$(D_\mu H^\dagger \sigma^i D_\nu H)\tilde{W}^{i\mu\nu}$
O_{2G}	$D_\mu G^{a\mu\nu} D^\rho G_{\rho\nu}^a$		
O_{2B}	$D_\mu B^{\mu\nu} D^\rho B_{\rho\nu}$		
O_{2W}	$D_\mu W^{i\mu\nu} D^\rho W_{\rho\nu}^i$		
O_{3G}	$f^{abc} G_{\mu\nu}^a G^{b\ \nu\rho} G_{\rho\mu}^c$	\tilde{O}_{3G}	$\varepsilon^{abc} \tilde{G}_{\mu\nu}^a G^{b\ \nu\rho} G_{\rho\mu}^c$
O_{3W}	$\varepsilon^{ijk} W_{\mu\nu}^i W^{j\ \nu\rho} W_{\rho\mu}^k$	\tilde{O}_{3W}	$\varepsilon^{ijk} \tilde{W}_{\mu\nu}^i W^{j\ \nu\rho} W_{\rho\mu}^k$

Table 2.4: Bosonic CP-even and CP-odd D=6 operators. There are 14 bosonic CP-even and 6 CP odd operators. In the Warsaw basis, however, there are 15 bosonic operators. Extra 5 bosonic operators here in SILH basis are traded off for 2 two-fermionic operator and 3 four-fermionic operators in the Warsaw basis. It is to be noted that first 7 operators and last four operators are also present in the Warsaw basis. Only 4 bosonic operators in Warsaw basis are replaced by 9 bosonic operators in SILH basis.

We do not tabulate the two-fermionic and four-fermionic operators in the SILH basis, as they are same as that in the Warsaw basis with the exception that $[Q_{HI}]_{11}, [Q'_{HI}]_{11}, [Q_{ll}]_{1122}, [Q_{ll}]_{1221}, [Q_{uu}]_{3333}$ are absent by definition, in order to account for the fact that the number of bosonic operators in SILH is more than that in Warsaw basis by number five. It is often

convenient to express result from one basis to another. The translation between Warsaw basis and SILH basis can be obtained using Rosetta package [91].

2.2.3 Effective Lagrangian of mass eigenstates

In all the bases discussed above, we have considered dimension six operators where $SU_C(3) \times SU_L(2) \times U_Y(1)$ symmetry is manifest. In order to connect these new operators to phenomenology, we need to work with Lagrangian in terms of mass eigenstates after electroweak symmetry breaking by the vacuum. The $SU_L(2) \times U_Y(1)$ symmetry is still present in a non-manifest way in the effective Lagrangian of the mass eigenstates. As redefining fields and couplings do not change physics, one can use this to bring the Lagrangian in more organized form which will, in turn, allow us to interpret the effect of new physics on physical observables conveniently. The parameters in the mass eigenstate can be written as the linear combination of Wilson coefficients in SILH basis, or Warsaw basis or any other suitable basis, and these relations can be found in [62, 92].

This framework is also known as **Beyond-the-Standard Model Characterization (BSM C)** [91]. Here we do not impose any relation between the parameters and this is why the number of parameters here is more than that of SMEFT D=6 operator bases. Therefore, it can be used to constrain some more general theory that do not reduce to SM EFT at low energies. As we do not impose any relation between the parameters in this framework, this cannot be called a basis for D=6 operators. In the following subsection, we are going to discuss a framework where parameters are related so that it can be called a basis.

2.2.4 Higgs basis

Although Wilson coefficients in Warsaw and SILH basis can be connected to the parameters in the Lagrangian in the mass eigenstate basis, the relations are often complicated. That is why sometimes another basis is used where observables can be directly connected to Higgs physics. This basis is called Higgs basis [62] which is defined using a subset of couplings in the mass eigenstate and the rest of the couplings in the mass-eigenstate are considered dependent couplings, so that it can be called a basis. There are in total 2499 real couplings in any D=6 operator basis. However, a much smaller subset is relevant for the Higgs physics. The four fermionic operators and three field tensor operators do not enter in the Higgs physics. In addition, one can impose minimum flavor violation (where CP-violation comes only from SM operators), CP-conservation, custodial symmetry etc. However, one should not set any parameter to zero without an underlying symmetry. After all these symmetries (without minimal flavor violation) and constraints from EWPT, the total 2499 number of parameters get reduced to eleven bosonic and fifty-four fermionic parameters [92]. The fifty-four fermionic parameters get reduced to six parameters with minimal flavor violation. Out of these seventeen parameters, ten parameters are CP-even and seven are CP-odd. If we assume CP-conservation in the Higgs sector, there are only ten CP-even parameters relevant for Higgs physics.

2.2.5 Other frameworks

Besides Warsaw, SILH, Higgs basis, there are other bases in the literature, such as HISZ basis [93]. These bases are completely equivalent. The Rosetta package [91] can translate

one basis to another. The Higgs basis can be considered as an extension of κ -framework. In this framework, one just scales existing Higgs boson couplings to fermions, bosons and itself without changing or introducing any new Lorentz structure. Thus κ -framework is less general than the Higgs basis even when a lot of symmetry restrictions are imposed in the latter. So, while the results obtained in the Higgs basis may be translated to κ -framework parameters, reverse is not generally true.

Instead of SMEFT, sometimes a more general framework, **pseudo-observable** [92, 94] are used where they are defined as the form-factors parametrizing the amplitude of physical processes subject to Lorentz invariance. These are more general than SMEFT as this does not impose any relation between the Form factors, and therefore constraints on the pseudo-observable can always be projected into the constraint of D=6 operator basis parameters but the reverse is not true.

Another widely used framework is **Higgs characterization** [95], where Higgs boson couplings to gauge boson and fermions are more general than the Higgs basis, or any other D=6 basis, as this does not impose various relations between them as present in the Higgs basis. But it is not completely general than the D=6 basis since it does not include many other corrections to standard model Lagrangian predicted in the SMEFT.

2.3 HEFT

In the previous two sections, we have discussed SM and SMEFT where the Higgs boson, along with three goldstone bosons, is part of $SU(2)_L$ doublet. However current experiments still allow the scenarios where the Higgs boson is not necessarily part of a doublet.

There are models, such as dilaton model, for which SMEFT is not an appropriate framework for the description of low energy behaviour. To describe IR behaviour for these models, another EFT framework, known as Higgs EFT framework (HEFT) [73, 96–108], is used. Here the symmetry is realized non-linearly. Custodial symmetry should be preserved while constructing such effective Lagrangian. This symmetry further gets broken down by the fermion mass splitting and hypercharge $U(1)_Y$ group. The Lagrangian for the HEFT framework is parametrized as

$$\begin{aligned}
\mathcal{L} = & \sum_{f \in q,l} i \bar{f}_L \gamma^\mu D_\mu f_L + \sum_{f \in u,d,e} i \bar{f}_R \gamma^\mu D_\mu f_R \\
& - \frac{1}{4} G_{\mu\nu}^a G^{a\ \mu\nu} - \frac{1}{4} W_{\mu\nu}^i W^{i\ \mu\nu} - \frac{1}{4} B_{\mu\nu} B^{\mu\nu} \\
& + (\partial_\mu h)^\dagger (\partial^\mu h) - V(h) \\
& + \frac{v^2}{4} \text{Tr}[(D_\mu U)^\dagger (D^\mu U)] (1 + 2a \frac{h}{v} + b \frac{h^2}{v^2} + \dots) \\
& - [\sum_f m_f \bar{f}_L U (1 + c_1 \frac{h}{v} + c_2 \frac{h^2}{v^2} + c_3 \frac{h^3}{v^3} + \dots) f_R + h.c.], \tag{2.5}
\end{aligned}$$

where $V(h)$, the Higgs potential, is given by

$$V(h) = \frac{1}{2} m_h^2 h^2 + d_3 \left(\frac{1}{6} \frac{3m_h^2}{v} h^3 \right) + d_4 \left(\frac{1}{24} \frac{3m_h^2}{v^2} h^4 \right) + \dots \tag{2.6}$$

U is given by

$$U = \exp(i\phi^a \sigma^a / v) \tag{2.7}$$

and $D_\mu U$ is given by

$$D_\mu U = \partial_\mu U + i \frac{g}{s} W_\mu^I \sigma^I U - i \frac{g'}{2} B_\mu U \sigma_3 \quad (2.8)$$

In the SM, $a = 1$, $b = 1$, $c_1 = 1, c_{2,3,\dots} = 0$, $d_3 = 1$, $d_4 = 1$. In Eq. 2.5, the first two lines give rise to same couplings as that in SM, cf. Eq. 2.1. The term non-linear in this EFT comes from the fact that the Goldstone bosons, ϕ_a , transform non-linearly under the $SU(2)_L \times U(1)_Y$. However, the Higgs field h , being a singlet of custodial symmetry, remains invariant. This is in sharp contrast with the SM (or SMEFT), where Higgs doublet, H , containing both the Goldstone bosons ϕ_a and Higgs field h , is a doublet of $SU(2)_L$ and transform linearly under $SU(2)_L \times U(1)_Y$. In HEFT, various Higgs couplings are not related as the Higgs field h is a singlet here. On the other hand, in the SMEFT at fixed order, the various Higgs couplings are related as it is determined by the associated doublet structure.

In this section, the EFT we have considered is known as electroweak chiral Lagrangian including a light Higgs boson. In the literature, there have been studies without Higgs also. The QCD chiral Lagrangian is analogous to Higgs less electroweak chiral Lagrangian. Pions in the former Lagrangian are like Goldstone bosons in the latter. Recently, the bounds on the parameters of HEFT in the current and future experiments have been obtained in [109]. Higher order terms in HEFT is determined by loop expansion rather than dimensional counting. Details about the organization of higher order terms in HEFT can be found in [98, 99, 110]. For more details about the HEFT framework, one is referred to [73, 96–108].

Chapter 3

One loop calculation

Contents

3.1	Scalar Integrals	37
3.2	Tensor Reduction	43
3.2.1	Passarino Veltman Technique	44
3.2.2	Oldenborg Vermaseren Technique	46
3.2.3	OPP Technique	48
3.3	Rational terms	51
3.4	Tools for one loop calculation	52

Precision calculations have been crucial for testing various features of the SM, constraining parameters of BSM models and others for past several decades. The tree level results suffer from large scale uncertainty, and higher order calculations help reduce this scale dependence. In this chapter, our goal is to give a brief introduction to techniques of one loop calculation. In loop processes, the amplitude contains integrals with respect to undetermined loop momentum. Some of these are tensor integrals and others are scalar integrals. However, any tensor integral can be reduced to a set of scalar integrals, called master integrals. The tensor integral reduction to master integrals can be done following any of the several techniques: Passarino-Veltman technique, Oldenborg-Vermaseren technique, OPP method and others. These master scalar integrals can be found in Ref [63, 111]. As the loop momentum can take arbitrarily large or small value, many of these scalar integrals contain divergences. Another issue that loop calculation often suffers from is numerical instability for certain phase space points both in scalar integral and tensor reduction formulae. This chapter will discuss these reduction techniques, possible sources of divergences, numerical instability, rational terms etc.

One loop amplitude can be reduced to *four types of master scalar integrals* as follows:

$$\mathcal{M}^{oneloop} = \sum_i \left(a_i A_0^i \right) + \sum_{i,j} \left(b_{i,j} B_0^{i,j} \right) + \sum_{i,j,k} \left(c_{i,j,k} C_0^{i,j,k} \right) + \sum_{i,j,k,l} \left(d_{i,j,k,l} D_0^{i,j,k,l} \right) + \mathcal{R},$$

where

$$\begin{aligned} A_0^i &= \int \frac{d^D Q}{(2\pi)^D} \frac{1}{d_i}, \quad B_0^{i,j} = \int \frac{d^D Q}{(2\pi)^D} \frac{1}{d_i d_j}, \\ C_0^{i,j,k} &= \int \frac{d^D Q}{(2\pi)^D} \frac{1}{d_i d_j d_k}, \quad D_0^{i,j,k,l} = \int \frac{d^D Q}{(2\pi)^D} \frac{1}{d_i d_j d_k d_l}, \end{aligned} \quad (3.1)$$

where, d_i s, the denominator factors, are given by $d_i = (Q + q_{i-1})^2 - m_i^2$ with $q_i = \sum_{j=1}^i p_j$ and $q_0 = 0$. \mathcal{R} is the rational term which is an artifact of tensor reduction in dimensional regularization.

This chapter is organized as follows. In the first section, we discuss the scalar integrals and possible sources of divergences. Next we discuss various tensor reduction techniques used for one loop calculations. After that, there will be some discussion on the rational parts. At the end, we discuss various available tools for one loop calculation.

3.1 Scalar Integrals

The four types of master scalar integrals are tadpole, bubble, triangle, and box integrals. Tadpole and bubble scalar integrals contain UV divergences if they are not scaleless (if they are scaleless, in the dimensional regularization they can be shown to be zero). On the other hand, triangle and box scalar integrals can only have infrared divergences if certain conditions are satisfied. However, tensor triangle integral of rank more than two and tensor box integral of rank more than four will also have UV divergence, which can easily be seen from naive power counting. Infrared divergences are of two types — soft and collinear. Both of these give single pole in dimensional regularization. However, if both soft and

collinear divergences are present in the same diagram, double pole can also appear. These scalar integrals can be solved using Feynman parameters trick. All the scalar integrals have been solved in terms of Spence functions and logarithms by t'Hooft and Veltman [63]. Nowadays, there are many packages to calculate scalar loop integrals — FF [66], OneLOop [67], QCDloop [111], Collier [112] etc.

We define scalar integrals in D dimension in the following way:

$$\begin{aligned}
I_1^D(m_1^2) &= \frac{\mu^{4-D}}{i\pi^{D/2}r_\Gamma} \int d^D Q \frac{1}{Q^2 - m_1^2 + i\epsilon}, \\
I_2^D(p_1^2; m_1^2, m_2^2) &= \frac{\mu^{4-D}}{i\pi^{D/2}r_\Gamma} \int d^D Q \frac{1}{(Q^2 - m_1^2 + i\epsilon)((Q + q_1)^2 - m_2^2 + i\epsilon)}, \\
I_3^D(p_1^2, p_2^2, p_3^2; m_1^2, m_2^2, m_3^2) &= \frac{\mu^{4-D}}{i\pi^{D/2}r_\Gamma} \times \\
&\quad \int d^D Q \frac{1}{(Q^2 - m_1^2 + i\epsilon)((Q + q_1)^2 - m_2^2 + i\epsilon)((Q + q_2)^2 - m_3^2 + i\epsilon)}, \\
I_4^D(p_1^2, p_2^2, p_3^2, p_4^2, (p_1 + p_2)^2, (p_2 + p_3)^2; m_1^2, m_2^2, m_3^2, m_4^2) &= \frac{\mu^{4-D}}{i\pi^{D/2}r_\Gamma} \times \\
&\quad \int d^D Q \frac{1}{(Q^2 - m_1^2 + i\epsilon)((Q + q_1)^2 - m_2^2 + i\epsilon)((Q + q_2)^2 - m_3^2 + i\epsilon)((Q + q_3)^2 - m_4^2 + i\epsilon)},
\end{aligned} \tag{3.2}$$

where $q_n \equiv \sum_{i=1}^n p_i$ and we do the integration using dimensional regularization. We use $D = 4 - 2\epsilon$. μ is a scale with mass dimension one, which is introduced to maintain the dimension of the integrals same as that in D=4 dimension. It is to be borne in mind that ϵ in $D = 4 - 2\epsilon$ and ϵ in $i\epsilon$'s of Eq. 3.2 are different. The constant r_Γ is given by

$$r_\Gamma = \frac{\Gamma^2(1-\epsilon)\Gamma(1+\epsilon)}{\Gamma(1-2\epsilon)} = 1 - \gamma\epsilon + \frac{1}{12}(6\gamma^2 - \pi^2)\epsilon^2 + O(\epsilon^3), \tag{3.3}$$

where $\gamma = 0.5772\dots$, Euler-Mascheroni constant. Notice that Eq. 3.1 and Eq. 3.2 differ by some overall factor. To obtain Eq. 3.1, which appears in the calculation of amplitude of one-loop diagram, from Eq. 3.2, we need to multiply the latter equation by a factor $\frac{ir_\Gamma}{(4\pi)^{\frac{D}{2}}} = \frac{i}{(4\pi)^2} \frac{r_\Gamma}{(4\pi)^{-\varepsilon}} = \frac{i}{(4\pi)^2} (1 - \gamma\varepsilon + O(\varepsilon^2))(1 + \varepsilon \log 4\pi + O(\varepsilon^2)) = \frac{i}{(4\pi)^2} \left(1 + \varepsilon(-\gamma + \log 4\pi) + O(\varepsilon^2)\right)$.

Next, we will discuss divergence structure of the integrals in Eq. 3.2. Naive power counting reveals that, under certain conditions, tadpole and bubble scalar integrals can give only UV divergence, whereas triangle and box scalar integrals can give only IR divergence¹. Below we will first investigate sources of divergence in triangle and box integrals. Then we will discuss UV divergence in tadpole and bubble integrals.

IR divergence

IR divergence can be collinear, or soft, or both. In first two cases, divergences appear as $\frac{1}{\varepsilon}$ in dimensional regularization or as logarithm divergence in mass-regularization). However, in the last case, i.e., in the overlapping region, divergence appear as $\frac{1}{\varepsilon^2}$ in dimensional regularization or as double log in mass regularization. Below we will discuss circumstances when collinear or soft divergences [111, 113] can appear in a loop integration.

Collinear Divergence: *When two massless internal lines meet with an external line with zero virtuality, collinear divergence occurs.*

¹Bubble integral could give IR divergence when both the masses are zero. But in that case the integral is scaleless and, thereby, can be shown to be identically zero in dimensional regularization. In this regularization, the scaleless bubble integral becomes zero by the cancellation of UV and IR divergences.

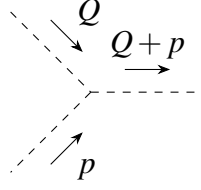


Figure 3.1: Collinear divergence. The lines with Q are parts of loop. The line with only p is external line. A dashed line signifies masslessness for lines in the loop and zero virtuality ($p^2 = 0$) for external lines.

Let's investigate the loop integration for the Fig. 3.1

$$\int \frac{d^D Q}{(Q^2 - m_1^2)((Q+p)^2 - m_2^2)} \quad (3.4)$$

In the region of loop momentum where $Q = x p + \delta_\perp$, where δ_\perp is a small number and perpendicular to p , Eq. 3.4 becomes

$$\int \frac{d^D \delta_\perp}{(x^2 p^2 + 2xp \cdot \delta_\perp + \delta_\perp^2 - m_1^2)((1+x)^2 p^2 + 2(1+x)p \cdot \delta_\perp + \delta_\perp^2 - m_2^2)} \quad (3.5)$$

So, from the Eq. 3.5, we see that only collinear loop momentum with the external line is not sufficient to give IR divergence. It is clear from the above expression if any of p^2 , m_1 , and m_2 is non-zero², the integral is finite. When $p^2 = 0$, $m_1 = 0$, and $m_2 = 0$, the denominator becomes δ_\perp^4 and loop integration gives logarithmic divergence (or $\frac{1}{\epsilon}$ in dimensional regularization) in the region $Q = x p + \delta_\perp$. As in addition to the above mentioned conditions, this divergence can occur only when the loop momenta Q is parallel to external momenta p , this infrared divergence is called *collinear divergence*. Notice for $D > 4$ di-

² $x=0$ with $p^2 = m_2^2 \neq 0$ and $m_1 = 0$ or $x=-1$ with $p^2 = m_1^2 \neq 0$ and $m_2 = 0$ can also give IR divergence. But we will consider $x = 0, -1$ cases, where momentum of some of the massless internal line becomes zero, separately.

mension, IR divergence is not present in Eq. 3.5. Also not all Q s which are around x p give divergence, only those Q s which make $p \cdot \delta$ zero give divergence (see Eq. 3.5). This shows why if two massless internal lines meet with an external line of zero virtuality, there will be collinear IR divergence at some region of loop integration.

Soft Divergence: When a massless particle is exchanged between two onshell particles, soft divergence occurs.

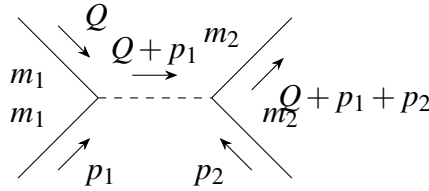


Figure 3.2: Soft divergence. The lines with Q are parts of loop. The lines with only p 's are external lines. A dashed line signifies masslessness.

Let's investigate the loop integration for the Fig. 3.2

$$\int \frac{d^D Q}{(Q^2 - m_1^2)((Q + p_1)^2 - m_3^2)((Q + p_1 + p_2)^2 - m_2^2)} \quad (3.6)$$

In the region of loop momentum where $Q + p_1 = \delta$, where δ is a four vector with vanishing magnitude, Eq. 3.6 becomes

$$\int \frac{d^D \delta}{(p_1^2 - 2p_1 \cdot \delta + \delta^2 - m_1^2)(\delta^2 - m_3^2)(p_2^2 + 2p_2 \cdot \delta + \delta^2 - m_2^2)} \quad (3.7)$$

So, from the Eq. 3.7, it is evident that only zero-momentum transfer is not sufficient to give IR divergence. If any of $m_3 = 0$, $p_1^2 = m_1^2$, and $p_2^2 = m_2^2$ is not satisfied, the integral is

finite. When $m_3 = 0$, $p_1^2 = m_1^2$, and $p_2^2 = m_2^2$, the denominator becomes $p_1 \cdot \delta \times \delta^2 \times p_2 \cdot \delta$. As in addition to the above mentioned conditions, this divergence occurs only when the momentum transfer between the two on-shell lines is $Q + p_1 = \delta \approx 0$, this divergence is called *soft divergence*. This shows why when *a massless particle is exchanged between two on-shell particles, soft divergence occurs*. Here as well, like the collinear divergence, for $D > 4$, IR divergence does not occur.

Collinear-Soft Overlap: When both collinear and soft divergences are present in an integral, most of the time divergence appears as $\frac{1}{\epsilon^2}$ in dimensional regularization or as double log in mass regularization.

In the above, we have investigated the cases where IR divergences can occur. There are six types of basic IR divergent triangle scalar integrals from which others can be obtained. And for box integrals the number of IR divergent integrals is sixteen [111]. However, it has been shown that infrared structure of box integrals can also be written in terms of triangle integrals, which can be used as a powerful check for the correctness of the IR structure of the scalar integrals [113].

UV divergence

Having discussed the IR divergence of triangle and box integrals in the previous subsection, here we will discuss the UV divergences which, as already stated before, can come among all the scalar integrals from tadpole and bubble integrals only. We will show below the di-

vergence structure of these UV-divergent scalar integrals in the dimensional regularization.

The expressions [111] for tadpole and bubble integrals are given by, respectively,

$$I_1^{D=4-2\epsilon}(m_1^2) = m^2 \left(\frac{\mu^2}{m^2 - i\epsilon} \right)^\epsilon \left\{ \frac{1}{\epsilon} + 1 \right\} + \mathcal{O}(\epsilon) \quad (3.8)$$

$$I_2^{D=4-2\epsilon}(s; m_1^2, m_2^2) = \mu^{2\epsilon} \left\{ \frac{1}{\epsilon} + 2 - \ln(s - i\epsilon) + \sum_{i=1}^2 \left[\gamma_i \ln\left(\frac{\gamma_i - 1}{\gamma_i}\right) - \ln(\gamma_i - 1) \right] \right\} + \mathcal{O}(\epsilon), \quad (3.9)$$

where $\gamma_{1,2}$ are given by

$$\gamma_{1,2} = \frac{s - m_2^2 + m_1^2 \pm \sqrt{(s - m_2^2 + m_1^2)^2 - 4s(m_1^2 - i\epsilon)}}{2s} \quad (3.10)$$

From Eq. 3.10, one can understand a source of threshold effects. For illustration, let us consider $m_1 = m_2 = m$. Then $\gamma_{1,2}$ can be written as

$$\gamma_{1,2} = \frac{s \pm s \sqrt{1 - \frac{4(m^2 - i\epsilon)}{s}}}{2s} \quad (3.11)$$

So from Eq. 3.11, we see that there is a discontinuity in $\gamma_{1,2}$ when center-of-mass energy, s , crosses $2m$. This is the reason of $t\bar{t}$ threshold effect, the effect of which will be discussed in the distribution of some processes in one of the subsequent chapters.

3.2 Tensor Reduction

For reduction of tensor integral to scalar integrals, there are many techniques available.

Passarino-Veltman (PV) [64, 114] and Oldenborgh-Vermaseren (OV) [66] techniques are

two traditional analytic techniques for tensor reduction, with the former being more popular. Another method, based on numerical technique, known as OPP method is widely used nowadays for reduction of amplitude to scalar integrals [115–117]. In this method, instead of reducing individual tensor integrals, as done in PV and OV method, reduction is done at the integrand level using kinematical equations for integration momenta. Loop reduction can also be done using unitarity cut method [118–123], but here one cannot reconstruct full rational parts of the amplitude. In the following subsections, we are going to discuss Passarino-Veltman technique, Oldenborg-Vermaseren technique, and OPP method. However, we will not discuss unitary cut method, for which readers are referred to [64] and references therein.

3.2.1 Passarino Veltman Technique

In this reduction method, we basically write all possible tensor structures of an integral with coefficients in front of them, known as form factors. Contracting both sides of the integral with external momenta (or some combination of them) or metric tensor gives a system of linear algebraic equations, solving which gives expressions for form factors. The next job is to write numerators in terms of denominators so that the integrals can be reduced to a set of scalar integrals. For illustration, we will show how tensor rank-one bubble integral can be written in terms of scalar integrals.

$$B_\mu = \int \frac{d^D Q}{(2\pi)^D} \frac{Q_\mu}{(Q^2 - m^2)((Q + p)^2 - m^2)} \quad (3.12)$$

Lorentz covariance tells us that we can write Eq. 3.12 as follows

$$B_\mu = p_\mu B_1 \quad (3.13)$$

where B_1 is the form factor, the expression for which we wish to find. Contracting Eq. 3.13 with p^μ , and using Eq. 3.12 for expression of B_μ , we have

$$B_1 = \frac{1}{p^2} \int \frac{d^D Q}{(2\pi)^D} \frac{Q \cdot p}{(Q^2 - m^2)((Q + p)^2 - m^2)} \quad (3.14)$$

$$= \frac{1}{p^2} \int \frac{d^D Q}{(2\pi)^D} \frac{\frac{1}{2}\{(Q + p)^2 - Q^2 - p^2\}}{(Q^2 - m^2)((Q + p)^2 - m^2)} \quad (3.15)$$

$$= \frac{1}{2p^2} \int \frac{d^D Q}{(2\pi)^D} \left[\frac{1}{(Q^2 - m^2)} - \frac{1}{((Q + p)^2 - m^2)} - \frac{p^2}{(Q^2 - m^2)((Q + p)^2 - m^2)} \right] \quad (3.16)$$

$$= -\frac{1}{2} \int \frac{d^D Q}{(2\pi)^D} \frac{1}{(Q^2 - m^2)((Q + p)^2 - m^2)} = -\frac{1}{2} B_0$$

This is how a tensor integral can be reduced to a scalar integral(s). Notice how the first two terms in Eq. 3.16 get cancelled after shifting the integration variable in the latter. One can reduce other tensor integrals of higher rank to master scalar integrals by solving a system of linear equations found using the same trick of contraction with external momenta or metric tensor. These can be found in Appendix. A.1. One can refer to the articles [114] and [64] for further details.

3.2.2 Oldenborg Vermaseren Technique

For the processes considered in this thesis, we have used Oldenborg-Vermaseren technique [66]. To discuss this tensor reduction technique, we need to first discuss van Neerven-Vermaseren basis. Here we will give a brief introduction to this basis and reduction technique. For further details about this basis, one is referred to Appendix. A.

The generalized Kronecker delta for $\mu_1 \mu_2$ and $v_1 v_2$ is defined as:

$$\delta_{v_1 v_2}^{\mu_1 \mu_2} = \begin{vmatrix} \delta_{v_1}^{\mu_1} & \delta_{v_2}^{\mu_1} \\ \delta_{v_1}^{\mu_2} & \delta_{v_2}^{\mu_2} \end{vmatrix} = \delta_{v_1}^{\mu_1} \delta_{v_2}^{\mu_2} - \delta_{v_2}^{\mu_1} \delta_{v_1}^{\mu_2} ; \quad (3.17)$$

$$\begin{aligned} \delta_{q_1 q_2}^{p_1 p_2} &= \delta_{v_1 v_2}^{\mu_1 \mu_2} p_{1\mu_1} p_{2\mu_2} q_1^{v_1} q_2^{v_2} . \\ &= (p_1 \cdot q_1)(p_2 \cdot q_2) - (p_1 \cdot q_2)(p_2 \cdot q_1) . \end{aligned} \quad (3.18)$$

For any two linearly independent vectors q_1 and q_2 , we can define two dual vectors u_1 and u_2 such that $u_i \cdot q_j = \delta_{ij}$. Now if we write $u_1 = a_1 q_1 + a_2 q_2$, then using this in $q_i \cdot u_1 = \delta_{i1}$, we will get a matrix equation for a_1 and a_2 :

$$\begin{bmatrix} q_1 \cdot q_1 & q_1 \cdot q_2 \\ q_2 \cdot q_1 & q_2 \cdot q_2 \end{bmatrix} \begin{bmatrix} a_1 \\ a_2 \end{bmatrix} = \begin{bmatrix} 1 \\ 0 \end{bmatrix} .$$

The above 2×2 matrix is known as Gram matrix of q_1 and q_2 , and its determinant is known as Gram determinant. Solving the matrix equation for a_1 and a_2 , we will get $u_1^\mu = \frac{\delta_{q_1 q_2}^{\mu q_2}}{\delta_{q_1 q_2}^{q_1 q_2}}$. Similarly, $u_2^\mu = \frac{\delta_{q_1 q_2}^{q_1 \mu}}{\delta_{q_1 q_2}^{q_1 q_2}}$. u_1 and u_2 are known as van Neerven-Vermaseren basis vectors.

Using above expressions of u_1 and u_2 , it can be shown that

$$\begin{bmatrix} u_1 \cdot u_1 & u_1 \cdot u_2 \\ u_1 \cdot u_2 & u_2 \cdot u_2 \end{bmatrix} = \begin{bmatrix} q_1 \cdot q_1 & q_1 \cdot q_2 \\ q_1 \cdot q_2 & q_2 \cdot q_2 \end{bmatrix}^{-1}.$$

For m linearly independent vectors $q_1, q_2, q_3, \dots, q_m$, we will similarly get $u_1^\mu = \frac{\delta_{q_1 q_2 q_3 \dots q_m}^\mu}{\delta_{q_1 q_2 q_3 \dots q_m}^\mu}$, and so on.

The projective tensor is defined as

$$\omega_v^\mu = \frac{\delta_{q_1 q_2 \dots q_m}^\mu}{\delta_{q_1 q_2 \dots q_m}^\mu} = \left(\delta_v^\mu - \sum_{i=1}^m u_{iv} q_i^\mu \right) = \left(\delta_v^\mu - \sum_{i=1}^m u_i^\mu q_{iv} \right) \quad (3.19)$$

where ω_v^μ can be shown to hold the following properties:

$$\omega_v^\mu q_{i\mu} = \omega_v^\mu q_i^\nu = \omega_v^\mu u_{i\mu} = \omega_v^\mu u_i^\nu = 0, \quad \omega_v^\mu \omega_\rho^\nu = \omega_\rho^\mu, \text{ and } \omega_\mu^\mu = n - m \quad (3.20)$$

Using the definition of ω_v^μ (Eq. 3.19), we have $\delta_v^\mu = \left(\sum_{i=1}^m u_i^\mu q_{iv} + \omega_v^\mu \right)$. Contracting this with Q^ν on both sides, we have

$$\boxed{Q^\mu = \left(\sum_{i=1}^m u_i^\mu Q \cdot q_i + \omega_Q^\mu \right)}, \quad (3.21)$$

which is known as van Neerven-Vermaseren decomposition.

Now after having defined all the required definitions, let us see how one does use these formulae to reduce tensor integrals to scalar. Let's take example of tensor rank-one triangle

integral:

$$C^\mu = \int \frac{d^D Q}{(2\pi)^D} \frac{Q^\mu}{(Q^2 - m^2)((Q + q_1)^2 - m^2)((Q + q_2)^2 - m^2)} \quad (3.22)$$

$$\begin{aligned} C^\mu &= \int \frac{d^D Q}{(2\pi)^D} \frac{\left(\sum_{i=1}^2 u_i^\mu Q \cdot q_i + \omega_Q^\mu\right)}{(Q^2 - m^2)((Q + q_1)^2 - m^2)((Q + q_2)^2 - m^2)} \quad [\text{using Eq. 3.21}] \\ &= \int \frac{d^D Q}{(2\pi)^D} \frac{\left(\sum_{i=1}^2 (u_i^\mu)(Q \cdot q_i)\right)}{(Q^2 - m^2)((Q + q_1)^2 - m^2)((Q + q_2)^2 - m^2)} \end{aligned} \quad (3.23)$$

In the above, the part with ω_Q^μ gives zero (see Eq. 3.20) as the integration can depend only on q_1^μ and q_2^μ . u_i^μ is one of the sources of numerical instability. Other source of numerical instability in one loop calculation is the master scalar integrals. In the above $Q \cdot q_i$ can be written as the denominator factors (see Eq. A.5 and Eq. A.16), which will facilitate the reduction of tensor to scalar integrals. More detailed description of this technique can be found in Appendix. A.

3.2.3 OPP Technique

Unlike the previous two methods where reduction is done for each individual one loop tensor integral of any rank and any point^{3,4}, in the OPP method [115], reduction is done at the integrand level. In the following, we will outline the basic steps of the OPP method.

³An N-point integral has N number of denominators.

⁴Scalar integrals of more than four points can also be reduced to master scalar integrals (see Appendix. A.4).

The integrand of any m-point one-loop amplitude can be written as

$$A(Q) = \frac{N(Q)}{D_1 D_2 \cdots D_m}, \quad (3.24)$$

where $D_i = (Q + q_{i-1})^2 - m_i^2$, and $q_0 = 0$, $q_1 = p_1$, and $q_i = \sum_{j=1}^i p_j$. The numerator $N(Q)$

of the above equation can be written in the following form [124]

$$\begin{aligned} N(Q) = & \sum_{i_0 < i_1 < i_2 < i_3}^m [d(i_0 i_1 i_2 i_3) + \tilde{d}(Q; i_0 i_1 i_2 i_3)] \prod_{i \neq i_0, i_1, i_2, i_3}^m D_i \\ & + \sum_{i_0 < i_1 < i_2}^m [c(i_0 i_1 i_2) + \tilde{c}(Q; i_0 i_1 i_2)] \prod_{i \neq i_0, i_1, i_2}^m D_i \\ & + \sum_{i_0 < i_1}^m [b(i_0 i_1) + \tilde{b}(Q; i_0 i_1)] \prod_{i \neq i_0, i_1}^m D_i \\ & + \sum_{i_0}^m [a(i_0) + \tilde{a}(Q; i_0)] \prod_{i \neq i_0}^m D_i \\ & + [\tilde{P}(Q)] \prod_i^m D_i \end{aligned} \quad (3.25)$$

From the above expression, it is clear that (d, \tilde{d}) , (c, \tilde{c}) , (b, \tilde{b}) , (a, \tilde{a}) are the coefficients of box, triangle, bubble, and tadpole scalar integrals, respectively. The coefficients with tilde, which depend on the loop momentum, are known as “spurious terms”. The spurious terms have been defined in such a way that they vanish upon integration over $d^D Q$. Although Q dependence of these terms are known [115, 124], there are still some Q-independent coefficients in these which need to be obtained numerically. Although these spurious terms vanish upon integration over $d^D Q$, knowing them is essential to find d , c , b , a . For m-point functions, the numbers of d, c, b, a coefficients (without spurious terms) are ${}^m C_4$, ${}^m C_3$, ${}^m C_2$, and ${}^m C_1$, respectively. Therefore, for six-point one-loop ampli-

tude, total number of these coefficients is equal to ${}^6C_4 + {}^6C_3 + {}^6C_2 + {}^6C_1 = 15 + 20 + 15 + 6 = 56$. For five-point and four-point one-loop amplitude, the number of coefficients are $5 + 10 + 10 + 5 = 30$ and $1 + 4 + 6 + 4 = 15$, respectively. In principle, for example, for five-point one-loop amplitude, one could sample $N(Q)$ at 30 different Q values which would give 30 linear equations. By inverting the resultant 30×30 matrix, one should be able to find all the coefficients for a particular phase-space point and helicity configuration. However, instead of inverting this huge matrix, one could find solutions for these coefficients d, c, b, a sequentially by choosing particular Q values. For example, for five-point one loop amplitude, first line of Eq. 3.25 is given by $d(1234)D_5 + d(1235)D_4 + d(1245)D_3 + d(1345)D_2 + d(2345)D_1$ (we have not written spurious terms explicitly). By solving for Q s which satisfy $D_1 = D_2 = D_3 = D_4 = 0$, we will have only $d(1234)D_5 + \tilde{d}(Q; 1234)D_5$ on the right hand side of Eq. 3.25 (as each term in second line to last line of Eq. 3.25 has at least one of the denominator factors which is zero). Because of the quadratic nature of the equations $D_1 = D_2 = D_3 = D_4 = 0$, solving them gives two distinct values of Q . As the Q dependence of the spurious terms are known, one can find $d(1234)$ and $\tilde{d}(1234)$ by solving two equations found by putting two values of Q satisfying $D_1 = D_2 = D_3 = D_4 = 0$ in Eq. 3.25, where $\tilde{d}(1234)$ is the unknown Q -independent coefficient in $\tilde{d}(Q; 1234)$. Other box coefficients can be found in exactly similar manner. After all the box coefficients (b, \tilde{b}) are known, triangle coefficients can be found by making three denominators zero. For example, by making $D_1 = D_2 = D_3 = 0$, we can find $c(123)$ and $\tilde{c}(123)$ using the box coefficients (as now box coefficients appear in the equations for $c(123)$ and $\tilde{c}(123)$), which are just obtained in the previous step. This way, once the coefficients of higher point scalar integrals are known, the coefficients of lower-point integrals can be found in exactly similar

manner. We will not discuss how to find rational terms using OPP method, for which one can refer to the original paper [115].

3.3 Rational terms

Rational terms, \mathcal{R} , are artifacts of tensor reduction in dimensional regularization. During tensor reduction, some form factors may have terms containing the dimension $D (= 4 - 2\varepsilon)$ in the coefficients of master scalar integral. The ε present in D multiplying with poles ($\frac{1}{\varepsilon}$ or $\frac{1}{\varepsilon^2}$) of master scalar integral generates these rational terms.

To illustrate this, let's take the example of B_{00} in $B^{\mu\nu} = B_{00}g^{\mu\nu} + B_{11}q^\mu q^\nu$. The formula for the form factor B_{00} is given by (Eq. A.9)

$$B_{00} = \frac{1}{2(D-1)} \left(A_0(2) + 2m_1^2 B_0(1,2) - f_1 B_1(1,2) \right) \quad (3.26)$$

Both A_0 and B_0 , being ultraviolet divergent integral, contain a $\frac{1}{\varepsilon}$ pole (see appendix. B.1). On the other hand, $\frac{1}{D-1}$ can be approximated as $\frac{1}{3}(1 + \frac{2\varepsilon}{3}) + O(\varepsilon^2)$. When this ε multiplies $\frac{1}{\varepsilon}$ pole of the scalar integrals, it generates a finite term which is known as rational term. It is noted that the constant term, $\log(4\pi e^{-\gamma})$, in master scalar integrals and rational terms are not same. The former constant term originates from the loop integration in dimensional regularization while the rational terms are the artifacts of reduction of tensor integrals in dimensional regularization. Anomaly such as non-conservation of axial vector current for the quantum theory can be shown to have connection with rational terms.

3.4 Tools for one loop calculation

The one loop calculation is standardized to a high degree. Nowadays, many packages are publicly available to calculate scalar and tensor integrals. Few such packages which use Passarino-Veltman reduction technique are LoopTools [125], FeynCalc [126], Package-X [127], HEPMath [128], and Collier [112] etc. The OPP method has been implemented in the package CutTools [117]. To calculate the master scalar integral, packages like FF [66], OneLOop [67], QCDloop [111], and Collier [112] etc are mainly used. However, in our calculation, for tensor reduction we have used an in-house package, OVReduce [65], based on Oldenburg-Vermaseren Technique, and for scalar integral computation we use OneLOop package [67]. We have used FORM [129], a symbolic manipulator software, for finding traces of γ matrices and for simplifying amplitude.

Chapter 4

Production of hhh and hhV ($V = \gamma, Z$) at the hadron colliders

In this chapter, we consider the production of two Higgs bosons in association with a gauge boson or another Higgs boson at the hadron colliders. We compute the cross sections and distributions for the $pp \rightarrow hhh$ and hhZ processes within the standard model (cross section for $pp \rightarrow hh\gamma$ is zero by Furry's theorem). In particular, we compute the contributions from gluon-gluon (gg) fusion channel mediated via heavy quarks in the loop. It is the leading order contribution to the $pp \rightarrow hhh$ process. To the $pp \rightarrow hhZ$ process, it is next-to-next-to-leading-order (NNLO) contribution in the QCD coupling, α_s . We also compare this contribution to the next-to-leading-order (NLO) QCD contribution to this process. The NNLO contribution (coming from gg fusion channel) can be comparable to the NLO contribution (coming from quark-antiquark ($q\bar{q}$) initiated channel) at the Large Hadron Collider (LHC), and significantly more at higher center-of-mass energy machines. We also study the effects of anomalous $t\bar{t}h, hhh, hhhh, hZZ$, and $hhZZ$ interactions in these processes. The anomalous couplings can enhance the cross sections significantly. The $gg \rightarrow hhh$ process is specially sensitive to anomalous trilinear Higgs boson coupling. For the $gg \rightarrow hhZ$ process, there is some modest dependence on anomalous hZZ couplings.

Contents

4.1	Processes	57
4.2	Anomalous couplings	60
4.2.1	Anomalous $t\bar{t}h$ coupling	60
4.2.2	Anomalous hhh and $hhhh$ couplings	61
4.2.3	Anomalous hZZ and $hhZZ$ couplings	62
4.3	Techniques and Checks	64
4.4	Numerical Results	67
4.4.1	The process $pp \rightarrow hhh$	67
4.4.2	The process $pp \rightarrow hhZ$	73
4.5	Conclusion	82

In the absence of discovery of any new resonance after the Higgs boson in 2012, another way of exploring any possible new physics is to study rare processes and radiative corrections to various leading order processes. At a hadron collider, as the center-of-mass energy increases, so does gluon-gluon luminosity. Therefore, at the LHC and at future probable hadron colliders, the gg fusion processes would play important role. In this and the following chapters, we will consider a few $2 \rightarrow 3$ processes that occur at one-loop level. Many gg fusion $2 \rightarrow 3$ one-loop processes have been considered in the literature before. Many authors have computed the contribution of the gg fusion processes on ‘multi-bosons +jets’ [71, 130–141]. These different calculations use different tensor reduction techniques, different packages for computing scalar integrals, and overall different philosophy for the computation. We use our own tensor-reduction code, and have developed a comprehensive package for such calculations.

In this chapter, we have considered hhh , hhZ , and $hh\gamma$ production at the LHC and various future colliders. Our main focus is at the contributions of gg fusion channel. To the process $pp \rightarrow hhh$, the contribution of the $q\bar{q}$ initiated channel is negligible because of extremely small Yukawa couplings of light quarks with Higgs boson, and the most of the contribution comes from the gg fusion channel. To the process $pp \rightarrow hhZ$, the leading order tree level $q\bar{q}$ initiated production channel contributes at the zeroth order and gg fusion channel contributes at next-to-next-to-leading-order (NNLO) in QCD coupling, α_s . One can also compute next-to-leading-order (NLO) QCD corrections to the tree-level process [142]. We compare this gg fusion channel contribution which occurs at NNLO in α_s with the LO and NLO contributions from $q\bar{q}$ initiated channel. The gg fusion channel cross section can be similar to the NLO QCD correction to the tree level process at the LHC

and can be significantly more at the 100 TeV collider (FCC-hh). We also study various interference effects in gg fusion channel.

The study of the production of hhh is important, as it is one of the very few processes where quartic Higgs boson coupling is involved. This process may allow the *direct* measurement of this coupling at future colliders. With the measurement of self couplings of the Higgs boson, one can confirm the form of the Higgs potential. In addition to revealing the exact form of the Higgs potential, this process might also help us know the dynamics of electroweak symmetry breaking. As already mentioned, unlike the hhh production, the process $pp \rightarrow hhZ$ gets contribution from the tree-level processes. But here our focus is on gg fusion channel. The production of $gg \rightarrow hhZ$ is important, as it involves poorly determined hhh and $hhZZ$ couplings. It is also a background to hhh production.

We also consider possible modification of standard model interactions, mainly inspired by D=6 operators in effective field theory. The $gg \rightarrow hhh$ is specially sensitive to anomalous trilinear Higgs boson coupling. The $gg \rightarrow hhZ$ is sensitive to anomalous hZZ coupling. The cross section for these processes in the SM have been reported before in [140] and references therein. Although our work on the $gg \rightarrow hhh$ process has some overlap with [2, 143–147], our detailed study of $gg \rightarrow hhZ$ process in the SM and beyond is new and is presented for the first time in our paper [148], on which this chapter is based. In the literature, hhh production is studied with only SM-like deviation of trilinear and quartic Higgs boson couplings, whereas we have also studied the effect of derivative couplings for these interactions. Moreover, earlier only CP-even $t\bar{t}h$ coupling was considered for hhh production, whereas we have considered both CP-even and CP-odd couplings. Besides, our approach towards new physics is more phenomenological. Similar approach is taken to

study new physics effect in the $gg \rightarrow hhZ$ process.

This chapter is organized as follows. In Sec. 4.1, we will discuss the Feynman diagrams for the processes we have considered. In Sec. 4.2, the anomalous couplings and their possible sources will be discussed. In Sec. 4.3, the calculation techniques and various checks to verify the correctness of the code have been discussed. The numerical results are discussed in Sec. 4.4. Finally, we summarize in Sec. 4.5.

4.1 Processes

The prototype Feynman diagrams for the gg fusion channels have been shown in Fig. 4.1 and Fig. 4.2. We do not need to numerically compute all the diagrams as some diagrams give exactly same value as the others because of charge conjugation symmetry. This is also known as (generalized) Furry's theorem [69]. This (generalized) Furry's theorem also helps us remove some parts of amplitude if under charge conjugation it is exactly equal in magnitude but opposite in sign. This way Furry's theorem helps us reduce the computational load. In the loop we consider only quarks from the third generation only, as the contributions from first two generations are extremely small owing to tiny Yukawa couplings of light quarks with the Higgs boson. We do not need to write routines for all the diagrams as we have divided the diagrams into various classes for which we write routines. The amplitudes for all the diagrams can be obtained by using crossing, i.e., by exchanging external legs in these routines.

For the $gg \rightarrow hhh$ process, there are 24 pentagon, 18 box, and 8 triangle diagrams for each quark in the loop. Out of these 24 pentagon diagrams, we need to numerically compute

only 12 diagrams as each of these is exactly same in magnitude with one or another from the other 12 diagrams. Amplitudes for these 12 diagrams can be obtained by permuting three external Higgs bosons in two classes PENTA1 and PENTA2 (see Fig. 4.1), for which we have written Fortran routines. Similarly, out of 18 box diagrams, we need to numerically compute only 9 diagrams. Out of this 9 diagrams, six can be obtained from BOX1 class and 3 diagrams can be obtained from BOX2 class. Similarly, out of 8 triangle diagrams, only 4 diagrams need to be numerically computed; one comes from TRIANGLE1 class and rest 3 come from TRIANGLE2 class. Note that there are some other diagrams at this order which are identically zero because of color conservation. Mathematically, that comes from $\text{Tr}(\lambda^a) = 0$, where λ^a is SU(3) generator.

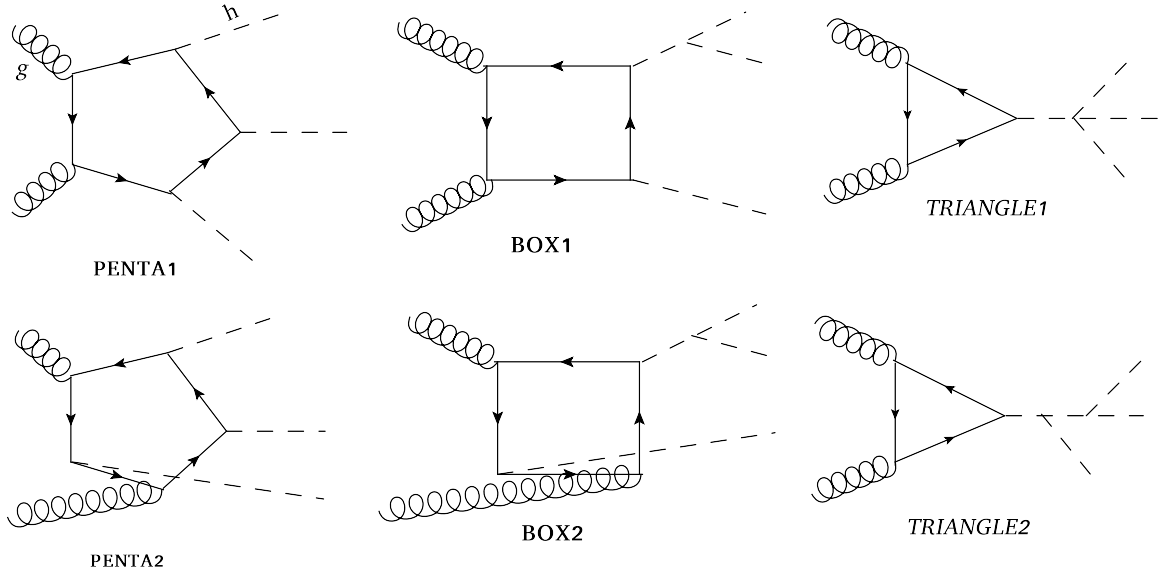


Figure 4.1: Prototype Feynman diagram for $gg \rightarrow hhh$ production.

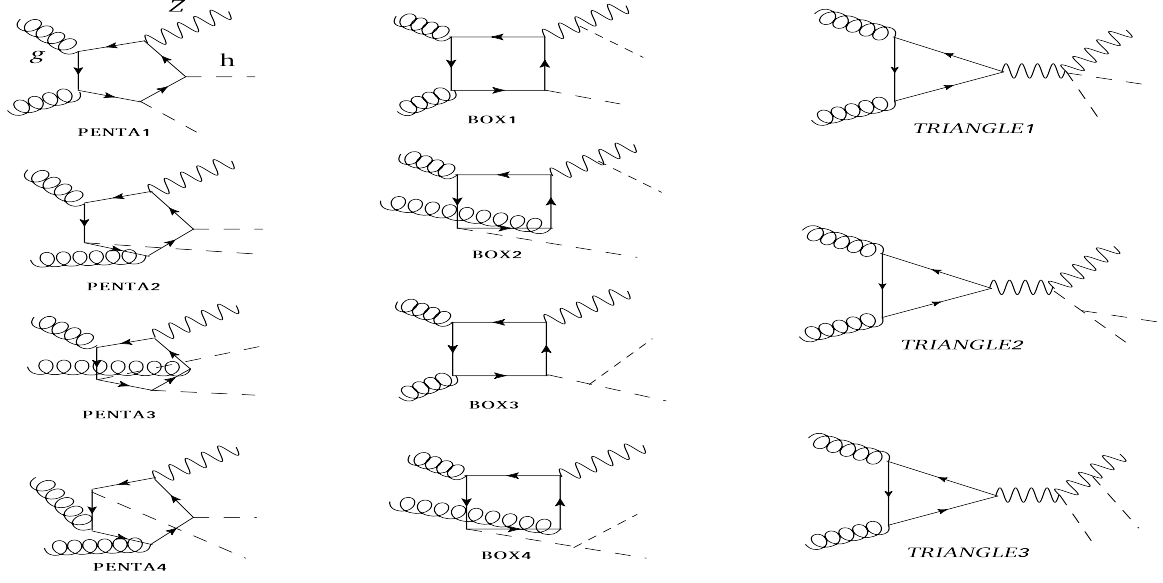


Figure 4.2: Prototype Feynman diagram for $gg \rightarrow hhZ$ production.

Like the case of $pp \rightarrow hhh$, in the case of $pp \rightarrow hhZ$, there are 24 pentagon, 18 box, and 8 triangle diagrams, but we need to numerically compute only 12 pentagon, 9 box, and 4 triangle diagrams. Here the vector part of $t\bar{t}Z$ coupling does not contribute because of Furry's theorem. As mentioned for $gg \rightarrow hhh$, here also crossings have been used to reduce number of routines. Various subclasses in each pentagon, box, and triangle category have been shown in Fig. 4.2. Out of the 12 pentagon diagrams, each of PENTA1 and PENTA2 give four diagrams, and each of PENTA3 and PENTA4 give two diagrams. In the case of box diagrams, BOX1, BOX2, BOX3, and BOX4 prototype diagrams give 4, 2, 2, and 1 diagrams, respectively. In the class of triangle diagrams, each of TRIANGLE1 and TRIANGLE2 give one diagram, while TRIANGLE3 gives two diagrams. Feynman diagrams in Fig. 4.1 and Fig. 4.2 have been made using JaxoDraw [149].

We have not shown $gg \rightarrow hh\gamma$ channel diagrams which can be easily visualized by replacing Z by γ in Fig. 4.2 wherever it is allowed, keeping in mind that γ does not couple

with Higgs boson. The cross section for this channel is zero as for every diagram for this process, there is another diagram the amplitude of which is equal in magnitude but opposite in sign, owing to Furry's theorem. Also at the tree level, the production cross section for $hh\gamma$ is too small because of the extremely small Yukawa couplings of light quarks with Higgs boson.

4.2 Anomalous couplings

As we discussed in the introduction of this chapter, in the absence of discovery of any new resonance at the LHC, searching anomalous coupling is one of the ways to explore new physics. We are mainly interested in the anomalous couplings of the Higgs boson which would affect the processes under consideration, i.e., we consider the anomalous coupling for $t\bar{t}h$, hZZ , $hhZZ$, hhh , and $hhhh$ interactions. The first two, i.e., $t\bar{t}h$ and hZZ are already well constrained by the existing LHC data [5]. On the other hand, even though the trilinear Higgs boson coupling is very weakly constrained [150, 151], there is practically no experimental bounds on the other Higgs boson couplings. In the following, we consider most general interaction Lagrangians for various Higgs related couplings.

4.2.1 Anomalous $t\bar{t}h$ coupling

So far the $t\bar{t}h$ coupling is constrained with an accuracy of 10-20% at 1σ level [5] and will be further constrained after the analysis of run 2 data of LHC. The Lagrangian for $t\bar{t}h$ vertex incorporating BSM physics can be parametrized as¹

¹We are only interested in modification of SM vertices and we are not concerned about the source of new physics. The source may be dimension six operator or others. For example, some dimension six operators

$$\mathcal{L}_{\bar{t}th} = -\frac{m_t}{v} \bar{t} \left[(1 + \kappa_t) + i \tilde{\kappa}_t \gamma_5 \right] t h. \quad (4.1)$$

In the standard model, $\kappa_t = \tilde{\kappa}_t = 0$. We have used the following bounds for κ_t and $\tilde{\kappa}_t$:

$$\begin{aligned} -0.2 &\leq \kappa_t \leq 0.2 \\ -0.1 &\leq \tilde{\kappa}_t \leq 0.1 \end{aligned} \quad (4.2)$$

These anomalous couplings contribute significantly to both hhh and hhZ production via gluon channel. However, it is to be noted that even in the presence of anomalous pseudo-scalar coupling, $\tilde{\kappa}_t$, the cross section for $gg \rightarrow hh\gamma$ remains zero.

4.2.2 Anomalous hhh and $hhhh$ couplings

Measuring trilinear and quartic Higgs boson couplings is one of the important tasks as they will reveal actual shape of the Higgs potential. This may reveal information about dynamics of electroweak symmetry breaking, strength of EW phase transition etc. Any possible deviation from the SM Higgs boson couplings will give evidence of new physics.

However measuring these couplings are extremely difficult. We are going to discuss about this in detail in one of the subsequent chapters which is based on the preprint [72]. The

Higgs boson self-interaction including anomalous couplings motivated from D=6 operators allow $t\bar{t}hh$ coupling, which also modify $t\bar{t}h$ coupling. So, here our parametrization does not follow from D=6 operator. We are only interested to see some scaling effect and CP properties.

can be expressed as:

$$\mathcal{L}_{hhh} = -\frac{3m_h^2}{v} \left(\frac{1}{6}(1 + g_{3h}^{(0)}) h^3 + \frac{1}{6m_h^2} g_{3h}^{(1)} h \partial_\mu h \partial^\mu h \right), \quad (4.3)$$

$$\mathcal{L}_{hhhh} = -\frac{3m_h^2}{v^2} \left(\frac{1}{24}(1 + g_{4h}^{(0)}) h^4 + \frac{1}{24m_h^2} g_{4h}^{(1)} h^2 \partial_\mu h \partial^\mu h \right). \quad (4.4)$$

In the SM, $g_{3h}^{(0)} = g_{4h}^{(0)} = g_{3h}^{(1)} = g_{4h}^{(1)} = 0$. Among the processes we have considered here, the quartic Higgs boson coupling appear only in $gg \rightarrow hhh$, while the trilinear Higgs boson coupling appear in both $gg \rightarrow hhh, hhZ$ processes. So far trilinear Higgs boson coupling is poorly constrained by studying hh production channel, whereas there is practically no constraint on the quartic Higgs boson coupling as it appear only in processes with small cross section. For the trilinear Higgs boson coupling, it may take a decade or more to put any serious bound and for quartic Higgs boson coupling, it will take even further time as it will require building higher energy future colliders with significant luminosity. In this chapter, we vary these anomalous parameters in the range between -1.0 to 1.0 for the sake of illustration.

4.2.3 Anomalous hZZ and $hhZZ$ couplings

Like the Lagrangian for Higgs boson self couplings, here also the Lagrangian for hZZ and $hhZZ$ is motivated from D=6 operators in the SMEFT framework. Measuring these couplings will be one of the goals of the LHC. The Lagrangian that we use to parametrize these anomalous couplings, after the Higgs doublet gets a vev, is expressed as

$$\mathcal{L}_{hZZ} = \frac{gM_Z}{c_W} \left\{ \frac{1}{2}(1+g_{hZZ}^{(0)})hZ_\mu Z^\mu - \frac{1}{4M_Z^2}g_{hZZ}^{(1)}hZ_\mu \nu Z^{\mu\nu} - \frac{1}{M_Z^2}g_{hZZ}^{(2)}hZ_\nu \partial_\mu Z^{\mu\nu} \right\}. \quad (4.5)$$

$$\mathcal{L}_{hhZZ} = \frac{gM_Z}{c_W \nu} \left\{ \frac{1}{4}(1+g_{hhZZ}^{(0)})hhZ_\mu Z^\mu \right\}. \quad (4.6)$$

In the SM, $g_{hZZ}^{(0)} = g_{hZZ}^{(1)} = g_{hZZ}^{(2)} = 0$. The hZZ coupling is already present in other the processes like $pp \rightarrow hZ$ using which it is already well constrained. We use the following bounds on the anomalous hZZ couplings parameters [152]

$$\begin{aligned} -0.10 &\leq g_{hZZ}^{(0)} \leq 0.10 \\ -0.09 &\leq g_{hZZ}^{(1)} \leq 0.04 \\ -0.07 &\leq g_{hZZ}^{(2)} \leq 0.03 \end{aligned} \quad (4.7)$$

However, $hhZZ$ coupling is poorly constrained as it appears mainly in processes involving double Higgs boson production, which have relatively smaller cross section. In the absence of any available bound for this coupling, we vary this parameter from -0.1 to 0.1.

All these anomalous interactions that we have considered are mainly motivated within the framework of effective field theory where the new physics are parametrized by higher dimensional operators. These operators are constructed out of the SM fields and respect symmetries of the SM. A complete list of independent D=6 operators can be found here [59–61] as discussed in Chapter 2. The anomalous couplings introduced above are related to Wilson coefficients of these operators [93, 153–156].

The Feynman rules for the anomalous Higgs vertices are listed in appendix C.1. As we shall see, in the allowed range of parameters values, the contribution of anomalous vertices

can be significant in our processes.

4.3 Techniques and Checks

To find the cross section of a process, one needs to find the Feynman diagrams contributing to the process. Sometime we find diagrams by hand and sometime we use FeynArts [157]. As the focus here is gg fusion channel processes which contain fermionic loop, we need to calculate trace of γ matrices. This has been done using symbolic manipulator software FORM [129]. After finding traces, there will be many integrals on undetermined loop momenta — some of which will be tensor integrals and some will be scalar integrals. Some steps of tensor integral reduction are done using FORM. After that amplitude is dumped in Fortran format. We have used OneLoop package [67] to calculate the scalar integrals. To reduce the tensor integrals to scalar integrals, we have used an in-house package, OVRReduce, which is based on Oldenborgh-Vermaseren technique [66].

After this much is done, we use crossing and Furry's theorem to get the amplitude of all the diagrams. Once the overall amplitude is obtained, utilizing Monte-Carlo integration, we find the total and differential cross sections. To do phase-space integration, we have used Advanced Monte Carlo Integration (AMCI) package, which is based on Parallel Virtual Machine (PVM) Software.

Before proceeding further and producing results, it is crucial to check the correctness of the code. We have checked gauge invariance (GI), IR cancellation, UV cancellation, anomaly cancellation in order to be sure about the correctness of the code. Let's discuss the pentagon diagrams first. Numerically each pentagon diagram is found to be UV finite

as is also expected from the naive power counting. GI test has been done by replacing the polarization of any of the gluons by its momenta. The individual pentagon diagrams is not gauge invariant. However, sum of all of them is found to be gauge invariant. There is no infrared divergence as there are only top and bottom quark loops, and contribution from the other quark loops is too small to be considered. As the process occurs via gg fusion channel and leptons do not take part in QCD, leptons cannot be present in the loop. Here individual box diagrams are also UV finite, since at most rank-two or rank-three tensor box integrals can be there for $gg \rightarrow hhh$ or $gg \rightarrow hhZ$, respectively. Here also like the pentagon case only the sum of the box diagrams is found to be gauge invariant, not the individual ones. Each triangle diagram is UV finite, despite the fact that there can be rank-two tensor integral. As the one loop diagrams of $gg \rightarrow hhh$ channel contributes at the leading order for the channel, the overall amplitude at one loop for this channel cannot be UV divergent. Each triangle diagram is also found to be gauge invariant. It is interesting to note that pentagon, box, and triangle classes are separately gauge invariant. So it may be tempting to use only one class of diagrams to calculate cross section. However as we will see this will lead to serious errors as there is strong destructive interference between various classes of diagrams. So calculating cross section for this process in the Higgs EFT² will also produce wrong results as that will be equivalent to considering triangle diagrams only.

For the $gg \rightarrow hhZ$, we have studied the diagrams considering γ_5 in 4 dimension and also using Larin's prescription [158]. Both gave same results. All the things that we have discussed for $gg \rightarrow hhh$ hold true for this production process as well. Each triangle diagram

²Here Higgs EFT means effective interaction in the limit of heavy top mass, which is not to be confused with the same name used in a different context where electroweak symmetry is non-linearly realized, as discussed in Chapter. 2.

is gauge invariant with respect to only one gluon in 4-D if we consider only one quark. If clockwise diagram is gauge invariant with respect one gluon, the corresponding anticlockwise will be gauge invariant with respect to the other gluon only. As a matter of fact, all triangle diagrams taken together in a class are not gauge invariant wrt either gluons. This is because of quantum anomaly ³. But as we know if we take all the fermions in a generation the anomaly should go away, which we have also tested using our code, providing further support for the correctness of our code. In D-dimension, however, diagrams with the same overall coupling taken together are gauge invariant with respect to either gluons for any particular quark in the loop. However, these are vector current conservations, the axial vector current will still remain un-conserved if only one quark is considered.

While doing one loop calculation, code often suffers from numerical instability because of vanishingly small gram determinants. As the number of such numerically unstable points is too small, their contribution is not expected to be large. We therefore remove these points by setting some suitable upper bound on the amplitude-squared. This upper bound is chosen after finding out the possible values that amplitude-squared can have by running the code. This upper bound is increased until we hit some unstable phase space points. The cross section should remain stable and does not change even when this upper bound is increased by several order of magnitudes. We have cross checked our results using a more robust way of removing unstable points by employing gauge invariance check as the unstable phase space points fail to satisfy this check.

³See Chapter. 19 of Peskin and Schroeder

4.4 Numerical Results

We have used the following basic cuts for the computation of cross section and distribution:

$$p_T^{h,Z} > 1 \text{ GeV},$$

$$|y^{h,Z}| < 5.$$

The 1 GeV cut on the p_T of Higgs boson and Z-boson is just to reduce the number of numerically unstable points. The results for gluon fusion processes are obtained here using CTEQ611 parton distribution functions [159]. We have used partonic center-of-mass energy, \sqrt{s} , as the renormalization and factorization scale. Uncertainties in the results for the variation of renormalization and factorization scale by a factor of 2 have also been included.

4.4.1 The process $pp \rightarrow hhh$

We present cross sections for this process at 8 TeV, 13 TeV, 33 TeV, and 100 TeV colliders in Table. 4.1. The cross section at the 13 TeV collider is 32 autobarn. So even at the end of HL-LHC phase with 3 ab^{-1} data, there will be around 100 events. However, this is the events number for hhh production. Branching of the final state Higgs boson in the decay products will reduce the numbers further. So it is next to impossible to detect hhh at LHC. At 100 TeV, the cross section is around 100 times larger. So with a benchmark 30 ab^{-1} data, there will be around 1 lakh events. It is to be noted that this cross section suffer from large scale uncertainty (-22% to 32% at 13 TeV) because of the significant dependence of

the strong coupling constant, α_s , on the renormalization scale.

\sqrt{s} [TeV]	8	13	33	100
$\sigma_{gg}^{hhh, LO}$ [ab]	$7.0^{+34.6\%}_{-24.0\%}$	$32.0^{+30.6\%}_{-22.2\%}$	$330.8^{+23.8\%}_{-18.4\%}$	$3121.1^{+17.4\%}_{-14.1\%}$

Table 4.1: $pp \rightarrow hhh$ hadronic cross sections and corresponding scale uncertainties in the SM at different collider center-of-mass energies.

In the Table. 4.2, we have shown the cross sections when either pentagon, or box, or triangle type diagrams are considered. As discussed in the previous section, these categories of diagrams are separately gauge invariant. However, all the diagrams in any particular order must be considered. This is because there is large destructive interference between the diagrams. For example if you would consider only triangle diagrams we would underestimate the cross section by an order, while inclusion of box or pentagon diagrams would overestimate the cross section. For 13 TeV collider, we see that the total cross section is about 32 ab, whereas penta, box, and triangle contribute 94, 53, and 3.5 ab, respectively. Therefore, as already discussed in the previous section, if one computes the process using Higgs effective field theory, which will give results same as the one for considering triangle diagrams only, one would make an order of magnitude error.

\sqrt{s} [TeV]	8	13	33	100
$\sigma_{\text{penta}}^{\text{hhh}}$ [ab]	22.1	94.4	916.4	8067.8
$\sigma_{\text{box}}^{\text{hhh}}$ [ab]	12.9	53.6	502.5	4287.4
$\sigma_{\text{triangle}}^{\text{hhh}}$ [ab]	0.8	3.5	32.1	270.8
$\sigma_{\text{total}}^{\text{hhh}}$ [ab]	7.0	32.0	330.3	3121.3

Table 4.2: SM contributions of pentagon, box, and triangle diagrams to the total cross section at different collider center-of-mass energies, displaying a destructive interference effect.

In Fig. 4.3, we have plotted the contributions of various categories of diagrams with respect to the p_T of the leading Higgs boson at $\sqrt{s} = 13$ TeV and 100 TeV. We see that the pentagon diagrams give harder Higgs bosons than the other categories of diagrams. However, interference kills such events. The p_T of the leading Higgs, considering all diagrams, peaks between 130 GeV and 160 GeV.

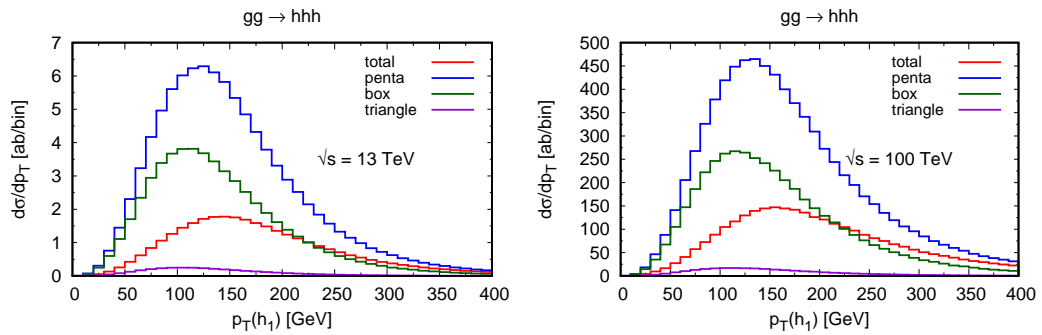


Figure 4.3: SM contribution of pentagon (blue), box (green), and triangle (violet) diagrams to leading $p_T(h)$ distribution in $gg \rightarrow hhh$ at 13 TeV (left) and 100 TeV (right) colliders.

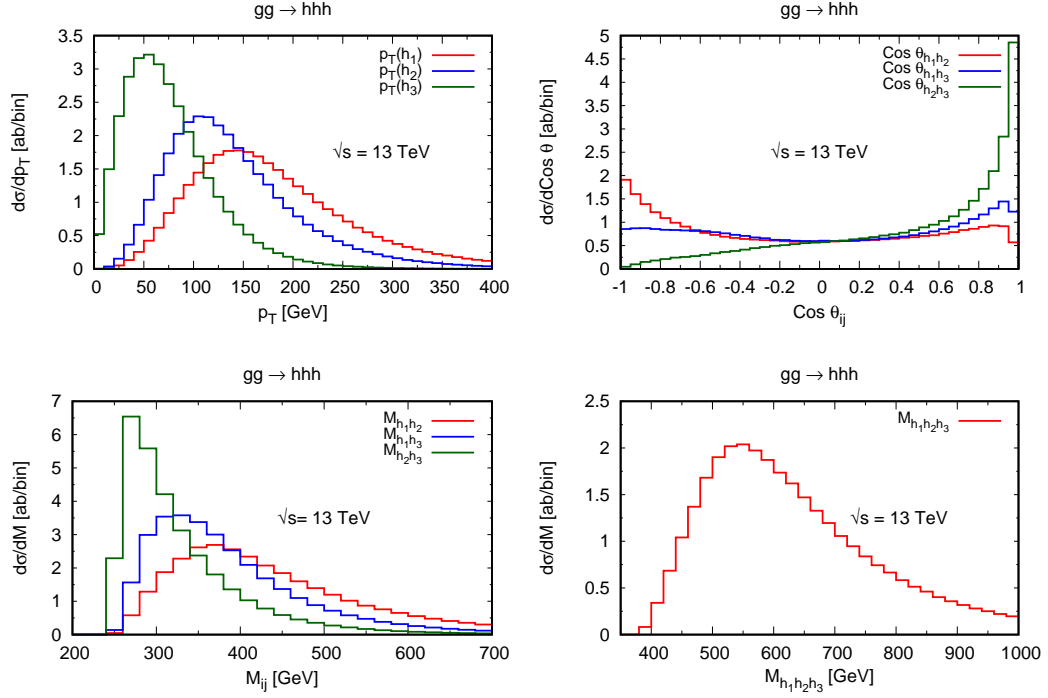


Figure 4.4: Kinematic distributions for $gg \rightarrow hhh$ in the SM at 13 TeV collider. These plots are obtained after p_T ordering the Higgs bosons. h_1, h_2 , and h_3 refer to the hardest, second hardest, and third hardest Higgs bosons in p_T , respectively.

In Fig. 4.4, we have plotted differential distributions with a number of kinematic variables involving the final state Higgs bosons. The final state Higgs bosons are distinguished according to their p_T . As would be expected leading p_T Higgs boson is the hardest and it peaks around 140-160 GeV. Softest p_T Higgs boson peaks around 50 GeV. All the three Higgs boson are produced centrally. While the leading and next-to-leading Higgs boson are produced more back-to-back, the mass of the two of softer Higgs boson are produced closer to each other. The masses of the two harder p_T Higgs bosons peaks around 375 GeV, while the peak for the two softer Higgs bosons is near the twice of Higgs boson mass. The invariant mass of the three Higgs bosons peaks around 550 GeV. At higher center of mass energy machines, the behavior of the distribution is largely same, so we have not provided

separate plots for them.

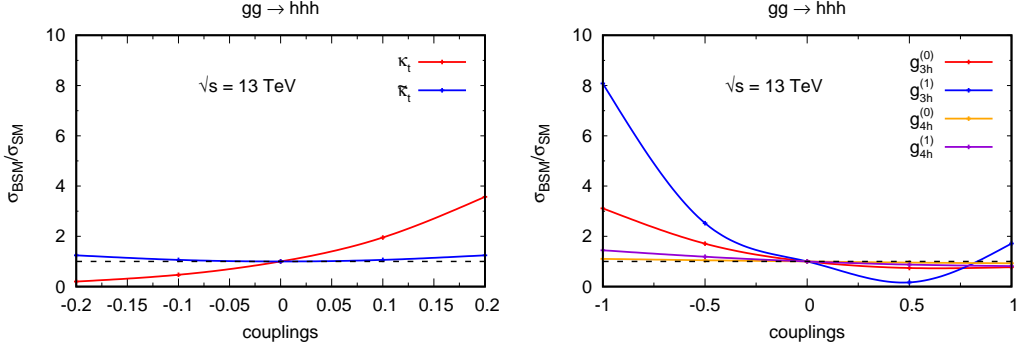


Figure 4.5: $\frac{\sigma_{\text{BSM}}}{\sigma_{\text{SM}}}$ as function of various Higgs anomalous couplings affecting $gg \rightarrow hhh$ at 13 TeV.

In Fig. 4.5, we have displayed the ratio of cross section with anomalous coupling and the cross section for the SM. We have plotted for the range of parameters mentioned in Sec. 4.2, except for $\tilde{\kappa}_t$ for which we doubled the range. As can be seen, the cross section is not sensitive to pseudo-scalar $t\bar{t}h$ couplings, $\tilde{\kappa}_t$, and quartic Higgs boson coupling. The cross section is symmetric for $\tilde{\kappa}_t$. The fact that it is not sensitive to anomalous quartic Higgs boson coupling is obvious as three final state Higgs bosons coming out of fourth Higgs boson makes the latter far off-shell, thereby making the contribution of the diagram too small. We will discuss the effect of anomalous quartic Higgs boson coupling in one of the subsequent chapter in more detail. The process is sensitive to the scaling of scalar $t\bar{t}h$ coupling, κ_t , and cross section can change by a factor of 3-4. The cross section is also sensitive to the sign of the anomalous coupling. It is also sensitive to the trilinear Higgs boson coupling. While the cross section can change by a factor of 3 by change in the scaling coupling, $g_{3h}^{(0)}$, it can change by an order of magnitude by the change of derivative coupling, $g_{3h}^{(1)}$. From Fig. 4.6, we see that while the scaling of couplings changes low p_T

events more, the derivative coupling changes high p_T events. Therefore, one can probe both couplings by focusing on low p_T region in one case and high p_T region in another case. We don't show p_T distribution for other Higgs bosons and mass distribution of two and three Higgs bosons as they show more or less similar sensitivity.

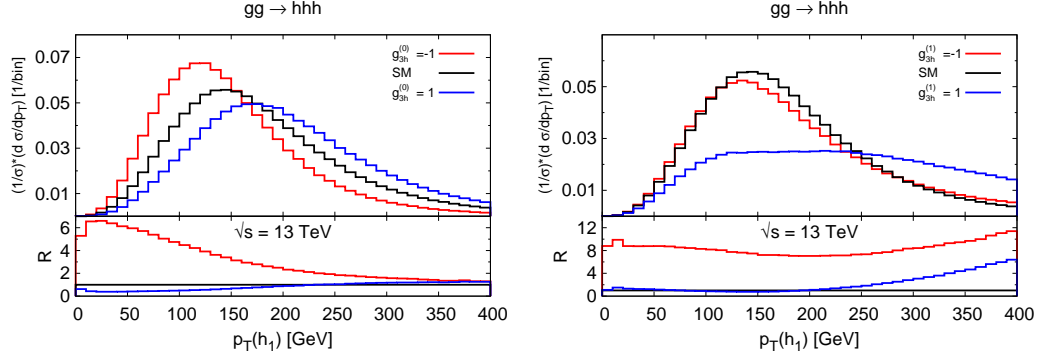


Figure 4.6: Normalized leading $p_T(h)$ distribution in $gg \rightarrow hhh$ at 13 TeV for some benchmark values of anomalous trilinear Higgs boson coupling. In the lower panels R is defined as the ratio of the distributions $(d\sigma/dp_T)$ in BSM and in the SM.

We will now consider the possibility of observing the production of triple Higgs bosons, hhh . As already mentioned, even at the end of HL-LHC phase, accumulating 3 ab^{-1} of data, there will be only around 100 odd events for the SM. Obviously, the anomalous trilinear Higgs boson coupling, if present in nature, can enhance this number by a factor of 3 to 8. Even with this enhancement, once we include branching fractions, kinematic cuts, tagging, and other efficiencies, there will be too few events to be observable. However, at 100 TeV collider (FCC), the cross section increases by a factor of around 100. So with an integrated luminosity of 30 ab^{-1} , there will be a factor of 1000 enhancement in the events number, which might be observable. The process $pp \rightarrow hhh$ gives rise to various signatures. There will be an irreducible background from ZZZ production and an array of reducible background. The ZZZ production is around 136 fb which can be controlled if we

consider branching fractions and construct Higgs boson masses. In the case of reducible backgrounds, there will be top pair production with jets or vector boson, or multi vector boson production with jets, or multi-jets. To tame these backgrounds, one may require tagging of bottom and tau jets. The authors in [145] have studied the $hhh \rightarrow bbbb\gamma\gamma$ channel and have shown that it will be difficult to detect the hhh signal. The studies of the channels ‘ $bbbb\tau\tau$ ’ and ‘ $bbl^+l^- + 4 \text{ jets}$ ’ in [146] and [147], respectively, have also shown that it will be extremely difficult to detect the signal using these channels. Therefore a modification of the interactions that will enhance the signal significantly and improved search strategies may be needed to detect hhh signal and thereafter put reasonable constraints on quartic Higgs boson coupling. More on this can be found in one of subsequent chapters.

4.4.2 The process $pp \rightarrow hhZ$

Unlike $pp \rightarrow hhh$ process, this process can occur at tree level. However, here our main focus will be on $gg \rightarrow hhh$ process, which gives NNLO contribution in α_s to $pp \rightarrow hhh$. In addition, we have estimated tree level and NLO QCD correction to it using MadGraph5_aMC@NLO [159]. Interestingly, we will see that the NNLO QCD contribution is comparable to NLO QCD correction at LHC. At 100 TeV collider, because of large gluon flux it becomes comparable to even tree level results.

\sqrt{s} (TeV)	8	13	33	100
$\sigma_{gg}^{hhZ, LO}$ [ab]	$10.0^{+34.0\%}_{-24.0\%}$	$42.3^{+30.9\%}_{-21.4\%}$	$406.7^{+23.9\%}_{-17.9\%}$	$3562.4^{+16.8\%}_{-13.9\%}$
$\sigma_{q\bar{q}}^{hhZ, LO}$ [ab]	$97.2^{+3.9\%}_{-3.8\%}$	$236.7^{+1.3\%}_{-1.5\%}$	$988.8^{+2.6\%}_{-3.3\%}$	$4393.0^{+7.1\%}_{-7.8\%}$
$\sigma_{q\bar{q}}^{hhZ, NLO}$ [ab]	$122.0^{+1.7\%}_{-1.6\%}$	$294.5^{+1.5\%}_{-1.0\%}$	$1197.0^{+1.7\%}_{-1.9\%}$	$4971.0^{+1.8\%}_{-3.2\%}$
$R_1 = \frac{\sigma_{gg}^{hhZ, LO}}{\sigma_{q\bar{q}}^{hhZ, LO}}$	0.10	0.18	0.41	0.81
$R_2 = \frac{\sigma_{gg}^{hhZ, LO}}{\sigma_{q\bar{q}}^{hhZ, NLO}}$	0.08	0.14	0.34	0.72
$R_3 = \frac{\sigma_{gg}^{hhZ, LO}}{(\sigma_{q\bar{q}}^{hhZ, NLO} - \sigma_{q\bar{q}}^{hhZ, LO})}$	0.40	0.73	1.95	6.16

Table 4.3: A comparison of different perturbative orders in QCD coupling contributing to $pp \rightarrow hhZ$ hadronic cross section at $\sqrt{s} = 8, 13, 33$, and 100 TeV. We also calculate ratios R_1 , R_2 , and R_3 which quantify the gg fusion channel contribution with respect to the LO and NLO $q\bar{q}$ initiated channel contributions.

In Table. 4.3, we have shown the LO, NLO QCD, and NNLO QCD contributions to these processes at various hadron colliders. We have used here CTEQ611 parton distribution for LO and NNLO and CTEQ6m for the NLO calculation [159]. For renormalization and factorization scale, we have used \sqrt{s} for $gg \rightarrow hhZ$ process, which occurs at NNLO in α_s , and sum of transverse mass for LO and NLO $q\bar{q}$ initiated channel calculation (in Madgraph5_aMC@NLO). Uncertainties are computed using other CTEQ6 parton distribution and varying the scale by a factor of 2. At the 13 TeV and 100 TeV colliders, the LO cross sections are 237 ab and 4393 ab, respectively. NLO corrections add nearly 24% and 13%, respectively. However, NNLO corrections add nearly 18% and 81%. We see that NNLO contribution approaches towards LO value. This is however not alarming as the NNLO con-

tribution comes from gg fusion channel and there is large gluon flux at 100 TeV collider, while leading order contribution comes from $q\bar{q}$ initiated channel. The scale uncertainty for the gg fusion channel is between -21% to 31%. As discussed before, the large uncertainty is because of the strong dependence of α_s on the scale. On the other hand, uncertainties in the LO process is small, as these are electroweak processes. The total cross sections including LO, NLO, and NNLO contribution are about 336 ab and 8533 ab for 13 TeV and 100 TeV colliders, respectively. These numbers lead to about 1k and 2.5 lakh events with 3 ab^{-1} and 30 ab^{-1} of data for the respective colliders.

\sqrt{s} (TeV)	8	13	33	100
$\sigma_{\text{penta}}^{\text{hhZ}}$ [ab]	30.8	148.1	1718.4	17694.0
$\sigma_{\text{box}}^{\text{hhZ}}$ [ab]	73.1	434.7	7468.2	115747.2
$\sigma_{\text{triangle}}^{\text{hhZ}}$ [ab]	78.4	475.6	8157.2	124273.1
$\sigma_{\text{total}}^{\text{hhZ}}$ [ab]	10.0	42.3	406.4	3557.5

Table 4.4: SM contribution of pentagon, box, and triangle diagrams to the total cross section in $gg \rightarrow hhZ$ at different collider center-of-mass energies, displaying a destructive interference effect.

In Table. 4.4, we show the interference effect in $gg \rightarrow hhZ$ process. Here, unlike $gg \rightarrow hhh$, contribution of pentagon diagram is least, while triangle and box contribute more or less at the same order. However, there is strong destructive interference which leads to much smaller total cross section. We see that at the 100 TeV collider, the total cross section is 3560 ab, whereas penta, box, and triangle class contribute 17694 ab, 115747 ab, and

124273 ab, respectively. In Fig. 4.7, we display the contributions of various categories of diagrams with respect to p_T of the leading Higgs boson. Here both box and triangle diagrams contribute to high p_T events, however interference kills these high p_T events. The p_T distribution of the leading (in p_T) Higgs boson, after the interference, shifts to lower values and peaks around 120 GeV.

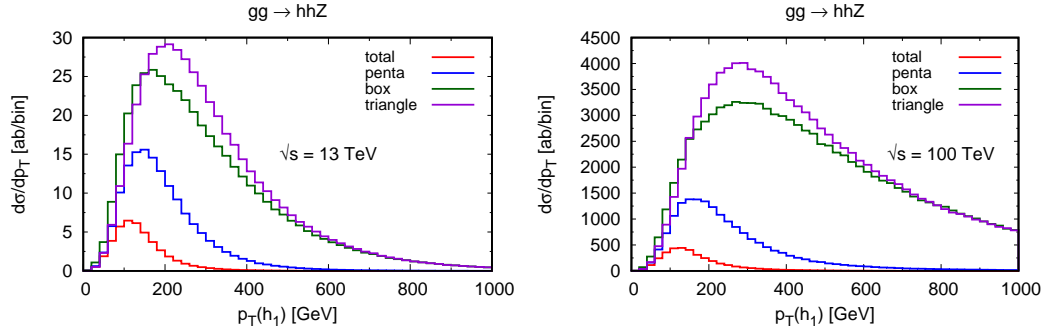


Figure 4.7: SM contribution of pentagon (blue), box (green) and triangle (violet) diagrams to leading $p_T(h)$ distribution in $gg \rightarrow hhZ$ at 13 TeV (left) and 100 TeV (right).

In Fig. 4.8, we have plotted a number of kinematic variables involving final state particles. The p_T distribution of leading Higgs boson and Z boson is similar. As is expected, p_T of leading Higgs boson is more harder than next-to-leading Higgs boson. All the three final state particles are produced centrally. While the leading (in p_T) Higgs boson and Z boson are produced more back-to-back, the next-to-leading Higgs boson is produced more along the leading Higgs boson than along Z boson. The invariant mass distribution of h_1 and Z, M_{h_1Z} , has harder tail than $M_{h_1h_2}$ and M_{h_2Z} . The distribution of partonic center of mass energy peaks around 500 GeV. At the higher center of mass energy colliders, these distributions behave similarly.

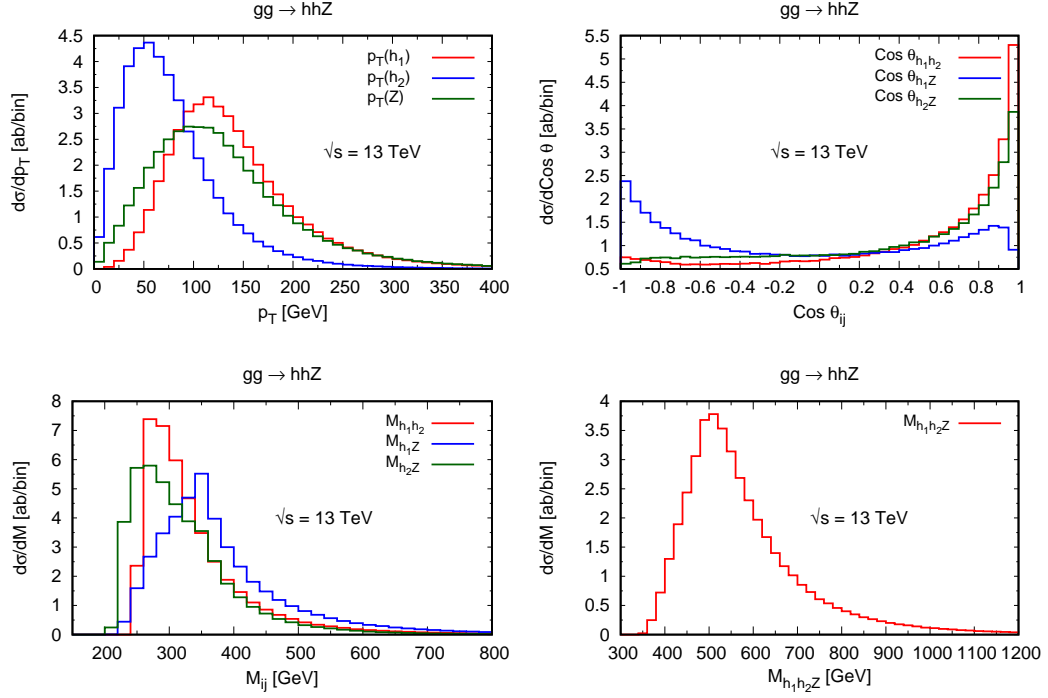


Figure 4.8: Kinematic distributions for $gg \rightarrow hhZ$ in the SM at 13 TeV. These plots are obtained after p_T ordering the Higgs bosons. h_1 and h_2 refer to the hardest and second hardest Higgs bosons in p_T respectively.

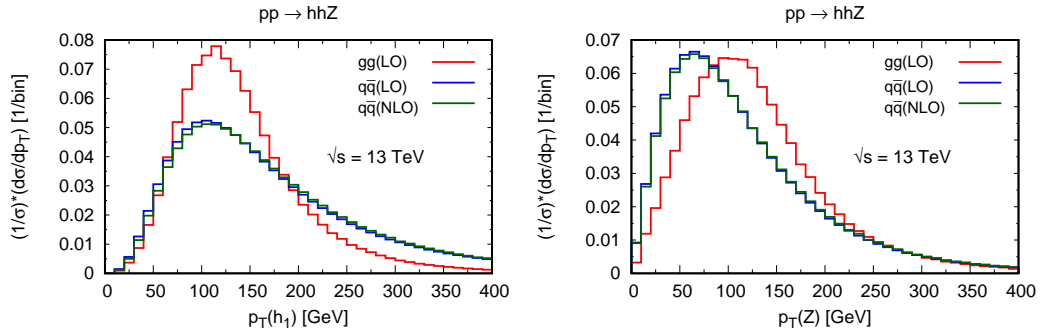


Figure 4.9: A comparison of normalized distributions for $p_T(h_1)$ and $p_T(Z)$ due to $gg \rightarrow hhZ$ and $q\bar{q} \rightarrow hhZ$ in the SM at 13 TeV.

In Fig. 4.9, we compare the gg (LO) and $q\bar{q}$ (LO and NLO) contributions in kinematic distributions for $p_T(h_1)$ and $p_T(Z)$. We see the gg fusion channel distribution is character-

istically different from $q\bar{q}$ initiated channel distribution. The gg fusion channel gives softer events in $p_T(h_1)$, whereas harder events for $p_T(Z)$. At 100 TeV machine, the behavior of the distributions are similar. In Fig. 4.10, we show $p_T(h_1)$ and $p_T(Z)$ distributions combining $q\bar{q}$ (NLO) and gg (LO) channels at 13 TeV and 100 TeV colliders. At 13 TeV, although the gg fusion channel contributes total 14% with respect to the $q\bar{q}$ (NLO) channel contribution to cross section, in the distributions in some of the bins it contributes more than 20%. Similarly, at 100 TeV collider, although the contribution of the gg fusion channel is 72% with respect to $q\bar{q}$ (NLO) channel, in some of the bins it can be more than 100%.

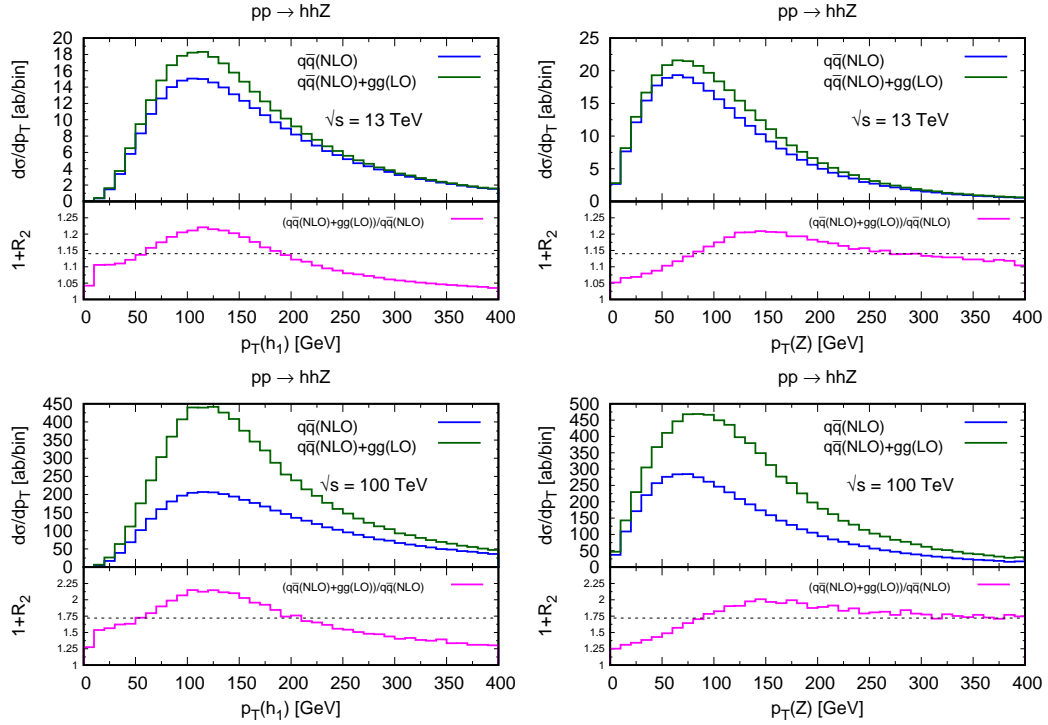


Figure 4.10: Combined $gg \rightarrow hhZ(\text{LO}) + q\bar{q} \rightarrow hhZ(\text{NLO})$ contribution to $p_T(h_1)$ and $p_T(Z)$ distributions in the SM at 13 TeV and 100 TeV. Lower panels show the ratio of $q\bar{q}(\text{NLO}) + gg(\text{LO})$ and $q\bar{q}(\text{NLO})$ for each of these distributions. The dashed straight line in the lower panel of each plot refers to the same quantity at inclusive or total cross section level (see R_2 in Table 4.3).

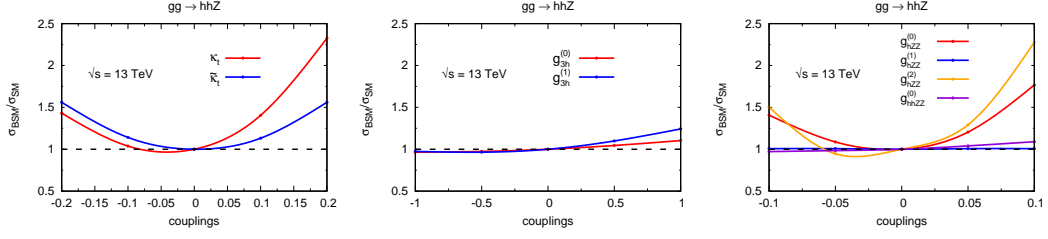


Figure 4.11: $\frac{\sigma_{\text{BSM}}}{\sigma_{\text{SM}}}$ as a function of anomalous couplings of the Higgs boson in $gg \rightarrow hhZ$ at 13 TeV.

The process $gg \rightarrow hhZ$ has four types of vertices involving Higgs boson— $t\bar{t}h$, hhh , hZZ , and $hhZZ$. In Fig. 4.11, we examine the sensitivity of production of hhZ through gluon-gluon channel on anomalous couplings for these vertices. The cross section is mainly sensitive to $t\bar{t}h$ and hZZ couplings. The cross section can double with allowed range of some of these parameters. The cross section is symmetric for $\tilde{\kappa}_t$ and like $gg \rightarrow hhh$ process, this process is also not sensitive to it in the allowed range. We see that the hhh and $hhZZ$ couplings also do not play any significant role for the parameter range we have considered. One of the derivative hZZ coupling, $g_{hZZ}^{(1)}$, also does not play any significant role.

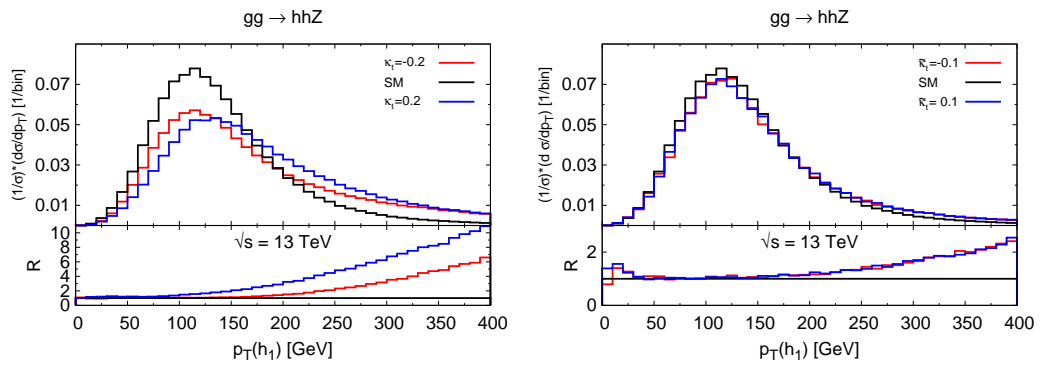


Figure 4.12: Normalized leading $p_T(h)$ distribution in $gg \rightarrow hhZ$ at 13 TeV for some benchmark values of anomalous top Yukawa couplings.

In Fig. 4.12, 4.13, and 4.14, we show the effects of various anomalous coupling in the

distribution of leading (in p_T) Higgs boson in this process. We find that both κ_t and $\tilde{\kappa}_t$ lead to harder tail in comparison to SM prediction. The contribution to the cross section at higher p_T is significantly large for higher k_t . Distribution for anomalous $g_{3h}^{(0)}$ does not show any special feature. For $g_{3h}^{(1)}$, there seems to be harder tail, especially for positive values. As far as hZZ coupling is concerned, $g_{hZZ}^{(0)}$ and $g_{hZZ}^{(2)}$ couplings show similar features as for anomalous κ_t . However, the effect of $g_{hZZ}^{(1)}$ is negligible. The distribution for $g_{hhZZ}^{(0)}$ shows interesting feature. At higher p_T , positive anomalous $g_{hhZZ}^{(0)}$ coupling leads to harder tail, while negative anomalous coupling leads to softer tail in comparison to the standard model prediction. As the distributions for anomalous coupling show similar behavior at 100 TeV collider, we do not provide separate plots for this collider.

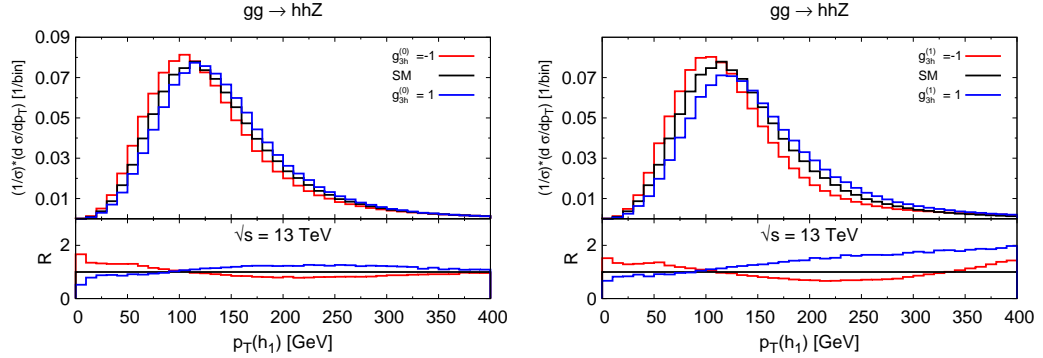


Figure 4.13: Normalized leading $p_T(h)$ distribution in $gg \rightarrow hhZ$ at 13 TeV for some benchmark values of hhh anomalous couplings.

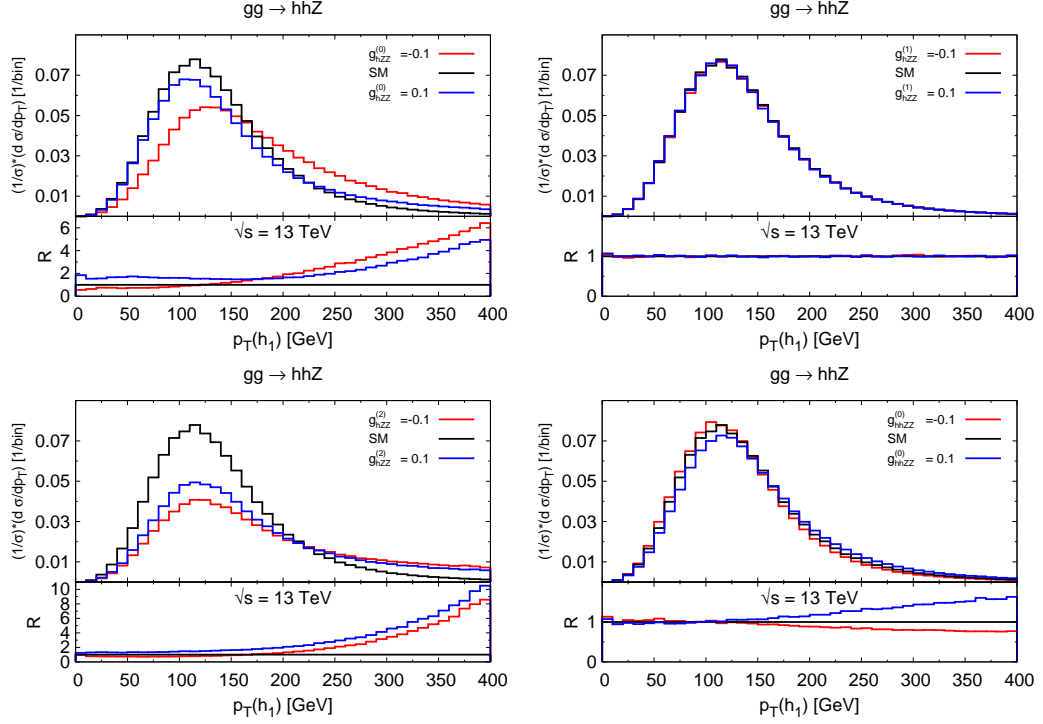


Figure 4.14: Normalized leading $p_T(h)$ distribution in $gg \rightarrow hhZ$ at 13 TeV for some benchmark values of hZZ and $hhZZ$ anomalous couplings.

In this chapter, our focus has been $gg \rightarrow hhZ$ process. That is why we have presented detailed results for this channel. One might be interested to know how sensitive is the LO process to anomalous coupling. We have explored this using Madgraph_aMC@NLO. By including anomalous vertices, we find that LO $q\bar{q}$ initiated channel contribution is quite sensitive to the anomalous derivative hZZ coupling. The cross section can increase by an order of magnitude. The increase is more at higher center-of-mass energy. This is unlike NNLO $gg \rightarrow hhZ$ process.

The process $pp \rightarrow hhZ$ is likely to be observed at the LHC. Considering up to NNLO correction, the cross section is 336 ab at 13 TeV collider, which will lead to around 1000 events at the end of the high luminosity phase of the LHC. This process should be visible in

various multilepton + jets signature. The main irreducible background ZZZ has the cross section around 9.2 fb. But the $Z \rightarrow b\bar{b}, \tau\tau$ branching ratios are smaller by a factor of 2-3 as compared to Higgs boson decay. So by restricting number of jets in the signature, one may be able to detect this process. To look for the evidence of any new physics one may look at the tail of the p_T distribution of the leading Higgs boson. Reducible backgrounds can be tamed by flavor tagging of jets. Higher energy machines with high luminosity will be suitable for the observation of this process.

4.5 Conclusion

In this chapter, we have considered the processes – $pp \rightarrow hhh, hh\gamma$, and hhZ . Our focus was on the gg fusion channel contribution to them. The one-loop amplitude for the process $gg \rightarrow hh\gamma$ vanishes exactly due to Furry's theorem. The process $pp \rightarrow hhh$ is important as it involves trilinear and quartic Higgs boson couplings, which are important to know the exact form of the Higgs potential. A measurement of this process along with di-Higgs boson production can help in achieving this. However, this process may be observed at the LHC only if there exists large anomalous interactions. This process is specially sensitive to trilinear Higgs boson couplings. It can be observed at large center-of-mass energy machines with high luminosity. It will be challenging though. The process $pp \rightarrow hhZ$ may be observable at the LHC after accumulation of 3 ab^{-1} integrated luminosity. The $gg(\text{LO})$ contribution to this process is actually an NNLO contribution in α_s , and due to a large gluon flux it is 14% of the $q\bar{q}(\text{NLO})$ contribution to the $pp \rightarrow hhZ$ process at 13 TeV LHC. In certain kinematic windows, $gg(\text{LO})$ contribution can be more than 20%. At a 100 TeV

machine, the $gg \rightarrow hhZ$ process can be as important as the $q\bar{q} \rightarrow hhZ$ process. This process is important, as it involves hhh and $hhZZ$ couplings and is a background to triple Higgs bosons production. The effect of $t\bar{t}h$ and hZZ anomalous couplings are more significant in the distributions than in the total cross section. This process can definitely be observed at higher center-of-mass energy colliders, such as a 100 TeV machine, with enough integrated luminosity.

Chapter 5

Production of VVh ($V = \gamma, Z, W$) at the hadron colliders

In this chapter, we consider the production of a Higgs boson in association with two electroweak vector bosons at hadron colliders. In particular, we examine $\gamma\gamma h$, γZh , ZZh , and W^+W^-h production at the LHC (14 TeV), HE-LHC (27 TeV), and FCC-hh (100 TeV) colliders. Our main focus is to estimate the gluon-gluon (gg) fusion channel contributions to $pp \rightarrow VVh$ ($V = \gamma, Z, W$) processes and compare them with corresponding contributions arising from the quark-antiquark ($q\bar{q}$) initiated channels. Technically, the leading order gg fusion contribution to $pp \rightarrow VVh$ cross section is an NNLO correction in strong coupling parameter, α_s . We find that in the gg fusion channel, W^+W^-h has the largest cross section. However, relative contribution of gg fusion channel is more important for the $pp \rightarrow ZZh$ production. At the FCC-hh, $gg \rightarrow ZZh$ contribution is comparable with the NLO QCD correction to $q\bar{q} \rightarrow ZZh$. We have also studied beyond the standard model effects in these processes using the κ -framework parameters κ_t , κ_V , and κ_λ . We find that the gg fusion channel processes ZZh and WWh have very mild dependence on κ_λ , but strong dependence on κ_t and κ_V . The $q\bar{q}$ initiated channel processes mainly depend on κ_V .

Contents

5.1	Gluon fusion diagrams for VVh	89
5.2	BSM Parametrization	93
5.3	Calculation and Checks	95
5.4	Numerical Results	97
5.4.1	The process $pp \rightarrow ZZh$	98
5.4.2	The process $pp \rightarrow WW h$	107
5.4.3	The process $pp \rightarrow \gamma Zh$	114
5.4.4	The process $pp \rightarrow \gamma\gamma h$	119
5.5	Conclusion	123

As discussed in the previous chapter, many of the couplings involving Higgs boson are so far poorly constrained by experiments. One of the major goals of the LHC and other proposed high energy colliders is to explore the Higgs sector of the SM and put constraints on the couplings of the Higgs boson. Any possible deviations from the SM predictions will be an evidence for the presence of new physics. Vector boson fusion and associated production of Higgs boson can be used to put constraints on VVh coupling, while gluon-gluon (gg) fusion channel production of a Higgs boson constraints $t\bar{t}h$ coupling [5]. Moreover, the production of a Higgs boson in association with a top-quark pair provides direct constraints on the $t\bar{t}h$ coupling [160, 161]. So far Higgs self-couplings are not constrained significantly. The trilinear Higgs coupling is being constrained using hh production at the LHC [162–167]. However, serious bound may be put only at future HE-LHC (27 TeV). The bound on the quartic Higgs coupling may only be possible at FCC-hh through hhh production process. The $hhVV$ coupling is also poorly constrained at the colliders [168]. In this chapter, we consider the production of ZZh , W^+W^-h , γZh , and $\gamma\gamma h$. As these processes involve one or other poorly constrained or completely unconstrained Higgs boson couplings, discovering these processes at the LHC may help us put some bounds on these couplings. Moreover, these processes are also background to $pp \rightarrow hh$ when one of the Higgs bosons decays into $\gamma\gamma/\gamma Z/ZZ^*/WW^*$ final states. The process $pp \rightarrow ZZh$ is also a background to $pp \rightarrow hhh$ when two of the three Higgs bosons decay into $b\bar{b}$ final states.

Although the dominant contributions to ZZh , W^+W^-h , γZh production come from tree level quark-antiquark ($q\bar{q}$) initiated diagrams and its NLO QCD correction, the LO gg fusion channels, which is NNLO in α_s , become important at a higher center-of-mass energy collider. The production of ZZh and WWh have been studied in the past. Ref. [71] did the

first study on W^+W^-h production via gg fusion channel. Subsequently, many works have been done on ZZh and W^+W^-h production via gg fusion [70, 169]. NLO QCD correction to the production of γZh has been computed in Ref. [170]. To the best of our knowledge, the gg fusion channel contribution to this process has not been studied before. We are also presenting for the first time the production of $\gamma\gamma h$ via gg fusion channel. Although quite small, this is the leading order process in $pp \rightarrow \gamma\gamma h$. In the literature, it has been shown that $b\bar{b}$ initiated process are important when precision is one of the main goals [70]. For all the processes, barring $pp \rightarrow W^+W^-h$ process, our results include $b\bar{b}$ initiated channel contribution in five-flavor scheme at the LO and NLO order. For the NLO correction in the bottom initiated channel for W^+W^-h production, technical problem relating to pole cancellation arises as some of the real diagrams have top resonance, which can decay to b and W . This problem arises both in five flavor and four flavor schemes. In such cases, the top propagator should be handled using special method [171–174]. Because of this technical complication, we have presented only tree level bottom quark initiated channel contribution to W^+W^-h production separately and skipped the corresponding NLO contribution, which we are planning to compute in future. The effect of anomalous coupling on the LO W^+W^-h production and its detection in several channels have been studied in Ref. [175]. We study the effect of new physics on all the processes using a common BSM framework — the κ framework [176, 177].

This chapter is organized as follows. In Sec. 5.1, we are going to discuss different prototype diagrams for the processes under consideration. Sec. 5.2 discusses the model independent framework to study new physics. In Sec. 5.3, we describe calculation techniques and various checks we have performed in order to verify the correctness of our code. In

Sec. 5.4, we present numerical results for the production of ZZh , WWh , γZh , and $\gamma\gamma h$ in the SM and BSM scenarios. Finally, we summarize all the results in Sec. 5.5.

5.1 Gluon fusion diagrams for VVh

In this section, we discuss various diagrams for the production of VVh in the gg fusion channel. The gg fusion contribution to $pp \rightarrow VVh$ occurs at one loop with quark circulating in the loop. The classes of diagrams contributing to $gg \rightarrow VVh$ processes are shown in Fig. 5.1. For convenience, the diagrams contributing to $gg \rightarrow WWh$ process are shown separately in Fig. 5.2. The Feynman diagrams have been made using Jaxodraw [149]. Unlike the previous chapter where we showed all the classes of diagrams for which we had to write routines, here we show only classes which have different couplings. So here number of routines needed will be more than the classes shown in Fig. 5.1 and Fig. 5.2. The $\gamma\gamma h$ process receives contribution only from the pentagon diagrams, while, γZh receives contribution from both pentagon and box class of diagrams. In case of $gg \rightarrow ZZh$, WWh processes, triangle class of diagrams also contribute. We have taken all quarks but the top-quark as massless due to which only top-quark contribution is relevant in diagrams where Higgs boson is directly attached to the quark loop. In the diagrams where Higgs boson does not directly couple to quark loop, light quarks can also contribute.

The complete set of diagrams for each process can be obtained by permuting external legs. In the Fig. 5.1, these permutations imply that for each quark, there are 24 diagrams in pentagon topology, 6 diagrams in each box topology and 2 diagrams in each triangle topology. In Fig. 5.2, the number of diagrams obtained from permutation are same as

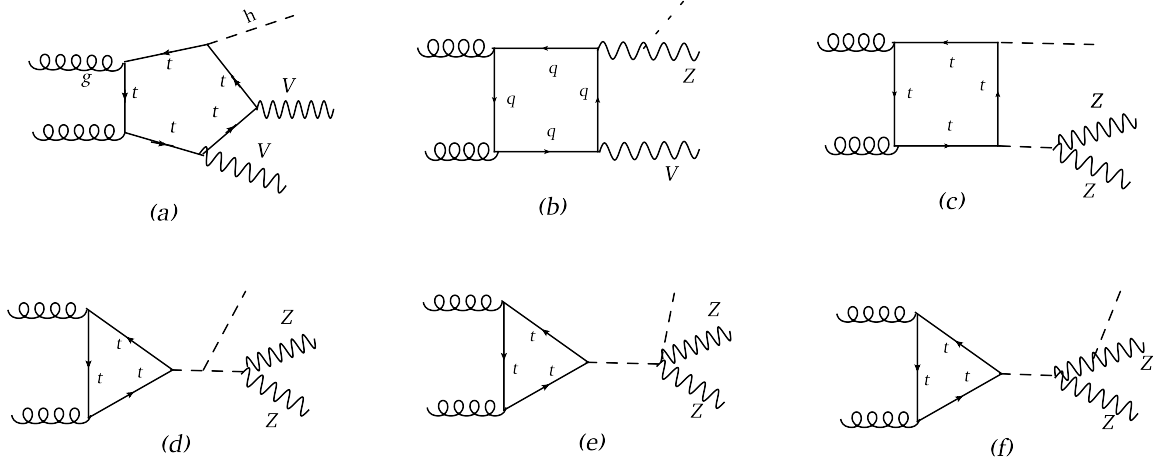


Figure 5.1: Different classes of diagrams for $gg \rightarrow VVh$, $V = \gamma, Z$. In diagram (b), q represents all quark flavors. Process $gg \rightarrow \gamma\gamma h$ receives contribution only from (a) type diagrams, while $gg \rightarrow \gamma Zh$ gets contribution from both (a) and (b) type diagrams. In the case of ZZh , all the diagrams contribute; the diagrams (b) and (f) cover the situation in which h is attached to the other Z boson.

above with the exception that for Fig. 5.2 (a) and Fig. 5.2 (b) those are now the numbers for each generation rather than each quark because of the presence of both quarks in the same loop. When there is only one type of quark flavor in the loop, calculating only half of the diagrams numerically is enough as other half are related to former via Furry's theorem [69]. As numerical evaluation of these loop diagrams are computationally expensive and time consuming, this observation leads to a significant simplification in the overall calculation. This simplification, however, is not applicable to the WWh case, where flavor changing interaction is involved in the quark loop. For example, see (a) and (b) in Fig. 5.2.

Thus, out of 24 pentagon diagrams (Fig. 5.1(a)) due to top-quark loop contributing to $\gamma\gamma H$ production, we need to numerically compute only 12 diagrams. Similarly, for the process γZh , we numerically calculate only 12 pentagon diagrams (Fig. 5.1(a)) due to top-quark loop and 3 box diagrams (Fig. 5.1(b)) for each quark flavor. In principle, 5 light

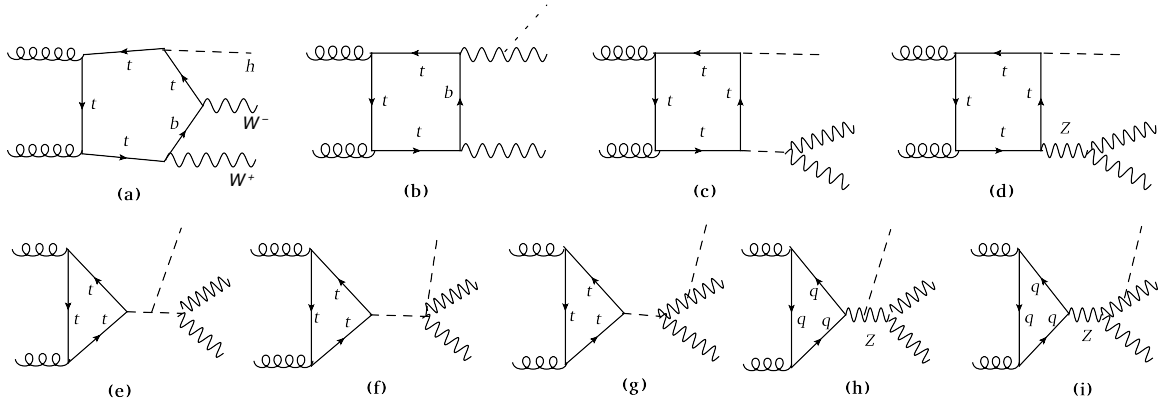


Figure 5.2: Different classes of diagrams contributing to $gg \rightarrow WW h$ process. With respect to ZZh , new classes of box and triangle diagrams appear due to ZWW coupling. In (a) and (b), due to the flavor changing interaction of W with quarks, both the quark flavors of a given generation enter in the loop. The diagrams (b), (g) and (i) cover the case when h is attached to the other W boson.

quarks (u, d, c, s, b) and 1 heavy quark (t) contribute. The box class of diagram arises due to ZZh coupling and has effective box topology of $gg \rightarrow \gamma Z^*$ amplitude. Furry's theorem, in this case, implies that the axial vector coupling of Z boson with quark does not contribute to $gg \rightarrow \gamma Zh$ amplitude.

Like the process $gg \rightarrow \gamma Zh$, for $gg \rightarrow ZZh$ amplitude, we numerically evaluate only 12 pentagon diagrams with top-quark in the loop (Fig. 5.1(a)). We numerically compute 6 box diagrams with effective box topology of $gg \rightarrow ZZ^*$ amplitude for each quark flavor which covers the possibilities of h coupling with any of the two external Z bosons (Fig. 5.1(b)). Further, a new box type contribution arises which has effective box topology of $gg \rightarrow hh^*$ amplitude (Fig. 5.1(c)). Once again there are 3 such diagrams with only top-quark in the loop, which are numerically evaluated. In addition to that, we numerically compute only 4 triangle diagrams with top-quark in the loop and having effective triangle topology of $gg \rightarrow h^*$ amplitude (Fig. 5.1 (d), (e), (f)). In $gg \rightarrow ZZh$ amplitude, the Furry's theorem

implies that the vector and axial vector coupling of Z boson with quarks can contribute at the quadratic level only.

Among all VVh amplitudes, the structure of $gg \rightarrow WW h$ amplitude is the most complex. Due to the involvement of flavor changing interactions in Fig. 5.2 (a) and (b), the Furry's theorem is not applicable to these diagrams. Therefore, 24 independent pentagon diagrams contribute to $WW h$ process for each generation of quarks. However, since we neglect Higgs boson coupling with light quarks including the b quark, there are only 12 non-zero pentagon diagrams. In Fig. 5.2 (b), all the three quark generations contribute. Taking into account the possibility of Higgs boson coupling with any of the two external W bosons, there are total 12 independent box diagrams of type (b) for each generation. In diagrams (a) and (b), the axial vector coupling of W with quarks contributes at quadratic as well as at linear level. Like in the ZZh process, we numerically compute 3 box diagrams of type (c). Due to ZWW coupling a new box contribution of type (d) having effective box topology of $gg \rightarrow hZ^*$ amplitude appears. Furry's theorem for diagram (d) implies that the vector coupling of Z with quarks does not contribute to the amplitude. The same explains the absence of similar box diagram due to γWW coupling. As in case of the ZZh process, we need to numerically evaluate 4 triangle diagrams with top-quark loop (Fig. 5.2 (e), (f), (g)). Further, we need to numerically compute 3 triangle diagrams of new type for each quark flavor with effective triangle topology of $gg \rightarrow Z^*$, once again due to ZWW coupling (Fig. 5.2 (h), (i)). These triangle diagrams are anomalous and they can receive contribution only from the third generation quarks as the bottom and top-quarks have very different masses. This is indeed the case for (h) type diagrams. However, we find that (i) type diagrams do not contribute. This is explained in the appendix of the paper [178] on which

this chapter is based.

5.2 BSM Parametrization

Measuring the couplings of the Higgs boson with fermions, gauge bosons and with itself is an important aspect of finding the signatures of new physics at colliders. With the help of the data collected so far at the LHC, we now know couplings of the Higgs boson with top quark with an accuracy of 10-20% and with vector bosons with an accuracy of 10% at 1σ [5]. The Higgs boson self couplings, on the other hand, are practically unconstrained [76].

In this chapter, to study new physics effects in VVh processes, we work in kappa framework [176, 177]. In this framework, only SM-like couplings get modified and no new Lorentz structures or no new interaction vertices appear. The LHC experiments have interpreted the data using this framework so far. The couplings of our interest are $t\bar{t}h$, VVh , hhh and $VVhh$. Out of these couplings, $gg \rightarrow \gamma\gamma h$ is sensitive to only $t\bar{t}h$ coupling. The VVh coupling affects all other processes. The couplings hhh and $VVhh$ affect only $gg \rightarrow VVh$, $V = Z, W$ processes.

The modification in these couplings due to new physics is implemented through scale factor κ_i for various couplings of the Higgs boson in the SM. In kappa framework, there are three such scale factors namely κ_t for Higgs boson coupling with top-quark, κ_V for Higgs boson coupling with vector bosons ($\kappa_{ZZh} = \kappa_{WWh} = \kappa_V$)¹ and κ_λ for Higgs boson coupling with itself. Since in the SM both VVh and $VVhh$ couplings are related, the scaling of $VVhh$ is also parametrized by κ_V .

¹Note that in the SM, the tree level interaction vertices $h\gamma\gamma$ and $h\gamma Z$ do not exist.

The amplitudes for the gg fusion processes in terms of kappa framework parameters κ_t , κ_V , and κ_λ are expressed as:

$$\mathcal{M}^{\text{BSM}}(gg \rightarrow \gamma\gamma h) = \kappa_t \mathcal{M}_{\text{PEN}}^{\text{SM}} \quad (5.1)$$

$$\mathcal{M}^{\text{BSM}}(gg \rightarrow \gamma Zh) = \kappa_t \mathcal{M}_{\text{PEN}}^{\text{SM}} + \kappa_V \mathcal{M}_{\text{BX}_1}^{\text{SM}} \quad (5.2)$$

$$\begin{aligned} \mathcal{M}^{\text{BSM}}(gg \rightarrow ZZh) = & \kappa_t \mathcal{M}_{\text{PEN}}^{\text{SM}} + \kappa_V \mathcal{M}_{\text{BX}_1}^{\text{SM}} + \kappa_t^2 \kappa_V \mathcal{M}_{\text{BX}_2}^{\text{SM}} + \\ & \kappa_t \kappa_V \kappa_\lambda \mathcal{M}_{\text{TR}_1}^{\text{SM}} + \kappa_t \kappa_V \mathcal{M}_{\text{TR}_2}^{\text{SM}} + \kappa_t \kappa_V^2 \mathcal{M}_{\text{TR}_3}^{\text{SM}} \end{aligned} \quad (5.3)$$

$$\begin{aligned} \mathcal{M}^{\text{BSM}}(gg \rightarrow WW h) = & \kappa_t \mathcal{M}_{\text{PEN}}^{\text{SM}} + \kappa_V \mathcal{M}_{\text{BX}_1}^{\text{SM}} + \kappa_t^2 \kappa_V \mathcal{M}_{\text{BX}_2}^{\text{SM}} + \\ & \kappa_t \mathcal{M}_{\text{BX}_3}^{\text{SM}} + \kappa_t \kappa_V \kappa_\lambda \mathcal{M}_{\text{TR}_1}^{\text{SM}} + \kappa_t \kappa_V \mathcal{M}_{\text{TR}_2}^{\text{SM}} + \\ & \kappa_t \kappa_V^2 \mathcal{M}_{\text{TR}_3}^{\text{SM}} + \kappa_V \mathcal{M}_{\text{TR}_4}^{\text{SM}} \end{aligned} \quad (5.4)$$

In the above, parts of the amplitudes $\mathcal{M}_i^{\text{SM}}$ are related to diagram classes displayed in Fig. 5.1 (Fig. 5.2 for $WW h$). Which amplitude corresponds to which diagram can be easily identified by looking at κ -factors in front of the amplitude. Note that in $WW h$ amplitude, $\mathcal{M}_{\text{TR}_4}^{\text{SM}}$ includes both (h) and (i) type diagrams of Fig. 5.2. This parametrization does not affect the gauge invariance of the amplitudes with respect to the gluons as it will become clear in the next section. The standard model prediction can be obtained by setting $\kappa_t = \kappa_V = \kappa_\lambda = 1$. For non-SM values of BSM parameters, we can expect nontrivial interference effects on inclusive and differential cross sections for ZZh and $WW h$ processes.

5.3 Calculation and Checks

Like in the previous chapter, here also the tensor reduction is done using semi-automated in-house package `OVReduce` [65], based on Oldenborgh-Vermaseren Technique [66]. Trace calculation and simplification of the amplitude is done using symbolic manipulation software `FORM` [129]. Further, the one-loop master integrals here also are calculated numerically using the `OneLoop` package [67]. To regulate ultraviolet (UV) and infrared (IR) singularities of one-loop master integrals, we perform the calculation in $4 - 2\varepsilon$ space-time dimensions. Since the couplings of Z and W bosons with quarks involve γ_5 , the trace calculation needs special care. We have used 4-dimensional properties of γ_5 in the calculation. This works because the SM is anomaly free. We have adopted Unitary gauge for the calculation of the amplitudes.

As explained in the Section 5.1, the amplitude calculation for each process can be efficiently organized using prototype amplitudes for each class of diagrams. The full amplitude for each process is a function of external momenta and polarization vectors/helicities. Due to huge expressions of the amplitudes, we calculate helicity amplitudes and the squaring of the amplitude for each process is done numerically. The number of helicity amplitudes for $gg \rightarrow \gamma\gamma h$, γZh , ZZh , $WW h$ processes are 16, 24, 36, and 36, respectively.

There are a number of checks that we have performed to ascertain the correctness of the amplitudes. We have checked that the amplitudes are separately UV and IR finite. In $4 - 2\varepsilon$ dimensions, these divergences appear as poles in $1/\varepsilon$ (for UV and IR) and $1/\varepsilon^2$ (for IR only). Each pentagon diagram is UV finite, which is expected from the naive power

counting. The individual box diagram is not UV finite, however, the full box amplitude, in each class, is UV finite. The UV finiteness of triangle amplitudes holds for each diagram. One-loop diagrams with all massive internal lines are IR finite, as expected. Thus, IR finiteness check is relevant to the diagrams with massless quarks in the loop. This includes box class of diagrams of Fig. 5.1(b) in γZh and ZZh . In $WW h$ case, potentially IR divergent diagrams include Fig. 5.2(a), (b), (h) and (i). Unlike UV, the IR finiteness holds for each diagram [136].

We have also checked the gauge invariance of the amplitudes with respect to the external gluons. For that, we numerically replace the gluon polarization vector $\varepsilon^\mu(p)$ by its four momentum p^μ and expect a gauge invariant amplitude to vanish. We find that the gauge invariance check holds for each class of diagrams. This is expected because different box and triangle topologies for each process arise due to the existence of various electroweak couplings. This is a very strong check on the organization of our calculation for each process using only a few prototype amplitudes. However, this check cannot verify relative signs between different classes of diagrams. To verify relative signs, one needs to perform gauge invariance check in electroweak theory which is a non-trivial task. We rather rely on cross checking the calculation using different methods and tools. We have compared our matrix element for each process with those calculated using MadLoop [159] and have found an excellent agreement.

Numerical predictions for cross section and kinematic distributions are obtained using Monte Carlo techniques for phase space integration. We use AMCI [179] package for Monte Carlo phase space integration which is based on VEGAS [180] algorithm and allows parallelization of phase space point generation and matrix-element computation using PVM

software [181].

5.4 Numerical Results

The cross section and kinematic distributions for $pp \rightarrow VVh$ processes in the SM and in BSM constitute the main results of this section. The numerical results are produced using following basic selection cuts unless stated otherwise,

$$|\eta^\gamma| < 2.5, \Delta R_{\gamma\gamma} > 0.4, |y^{H,Z,W}| < 5. \quad (5.5)$$

The results for gg fusion processes are calculated using CT14L0 parton distribution function (PDF) and partonic center-of-mass energy ($\sqrt{\hat{s}}$) is chosen as common scale for renormalization (μ_R) and factorization (μ_F). The results are calculated for three different choices of collider energies: $\sqrt{s} = 14, 27$, and 100 TeV.

We compare the gg fusion channel contribution to $pp \rightarrow VVh$ with contribution from $q\bar{q}$ initiated channels. The $q\bar{q}$ initiated channel contribution is calculated at LO and NLO in α_s using MadGraph5_aMC@NLO [159]. The LO $q\bar{q}$ initiated channel contributions are pure electroweak processes and they do not depend on α_s . For LO and NLO results, we use CTEQ14L0 and CT14NLO PDFs, respectively [182]. The scale choice is same as in gg calculation. In both gg and $q\bar{q}$ calculations, the scale uncertainties are estimated by varying μ_R and μ_F independently by a factor of two. We quote only minimum and maximum uncertainties thus obtained. In the literature, it has been shown that $b\bar{b}$ initiated process are important when precision is one of the main goals [70]. For all the processes, barring

$pp \rightarrow WW h$ process, the results include $b\bar{b}$ initiated channel contribution in five flavor scheme at LO and NLO. For $pp \rightarrow WW h$ process, in five flavor scheme, we separately present the contribution due to LO $b\bar{b}$ initiated channel only, as in calculating the NLO correction we encounter some technical issue regarding pole cancellation because of top quark resonance. Coupling of b quark with Higgs boson is not ignored in the $b\bar{b}$ initiated channel.

Next, we study the BSM effect in these processes which as mentioned above is parametrized in terms of κ_t , κ_V and κ_λ . To compare the relative importance of these couplings we vary them independently by 10% about their SM values. We have organized results process by process.

5.4.1 The process $pp \rightarrow ZZ h$

Standard Model Predictions

The cross sections for $ZZ h$ production via various channels have been tabulated in Table 5.1 with the corresponding scale uncertainties. We compute the quantity R_3 which represents the ratio of gg fusion contribution to QCD NLO correction in the $q\bar{q}$ channel². The gg fusion contribution becomes important at higher center-of-mass energy collider, as in this case smaller partonic momentum fraction (x) are accessible, where gluon flux is significantly large. The gg fusion contributions to $ZZ h$ at 14, 27, and 100 TeV colliders are 124 ab, 579 ab, and 7408 ab, respectively. The corresponding values of the LO $q\bar{q}$ initiated channel contributions are 2184, 5997, and 36830 ab, respectively³. The ratio, R_3 , is found

²Unlike the previous chapter, in this chapter we do not tabulate R_1 and R_2 .

³ $b\bar{b}$ initiated channel contributions are included in here, which are 46 ab, 234 ab, and 4210 ab, respectively. This has been done in five flavor scheme using Madgraph.

to be 0.25, 0.4, and 1.05, respectively. As has been discussed above, this increase in ratio R_3 with collider energy is due to the large gluon flux.

In the gg fusion channel, the scale uncertainties of the total cross sections are in the range of 20-30%. The uncertainty due to renormalization scale variation is more than that due to factorization scale variation. The uncertainty for the renormalization scale variation are nearly same for all the colliders. For all the colliders, contribution to total cross section come from nearly same region of partonic center of mass energy of the process. In every bin of this region, α_s decreases by nearly same factor for the change in renormalization scale. Therefore, uncertainty due to renormalization scale variation is nearly same for all the colliders. However uncertainty for factorization scale variation is different for different colliders. Change in factorization scale mainly causes change in parton distribution functions. For different collider energies, different x regions, where x is partonic momentum fraction, contribute to the process. As for different x regions change in parton distribution function with factorization scale is different, uncertainty due to factorization scale variation is different for different colliders. One interesting fact that we have noticed is that at 100 TeV collider with increase in factorization scale, the cross section increases, while at 14 TeV and 27 TeV colliders it decreases.

\sqrt{s} (TeV)	$\sigma_{gg}^{ZZh, LO}$ [ab]	$\sigma_{q\bar{q}}^{ZZh, LO}$ [ab]	$\sigma_{q\bar{q}}^{ZZh, NLO}$ [ab]	$R_3 = \frac{\sigma_{gg}^{ZZh, LO}}{(\sigma_{q\bar{q}}^{ZZh, NLO} - \sigma_{q\bar{q}}^{ZZh, LO})}$
14	$124^{+28.2\%}_{-21.0\%}$	$2184^{+0.2\%}_{-0.6\%}$	$2710^{+1.4\%}_{-1.0\%}$	0.24
27	$579^{+23.3\%}_{-18.5\%}$	$5997^{+2.4\%}_{-3.0\%}$	$7396^{+1.3\%}_{-1.6\%}$	0.41
100	$7408^{+22\%}_{-18\%}$	$36830^{+8.0\%}_{-8.7\%}$	$43940^{+1.2\%}_{-2.6\%}$	1.04

Table 5.1: A comparison of different perturbative orders in QCD coupling contributing to $pp \rightarrow ZZh$ cross section at $\sqrt{s} = 14, 27$, and 100 TeV. The ratio R_3 quantifies the gg fusion channel contribution with respect to the NLO correction in $q\bar{q}$ initiated process.

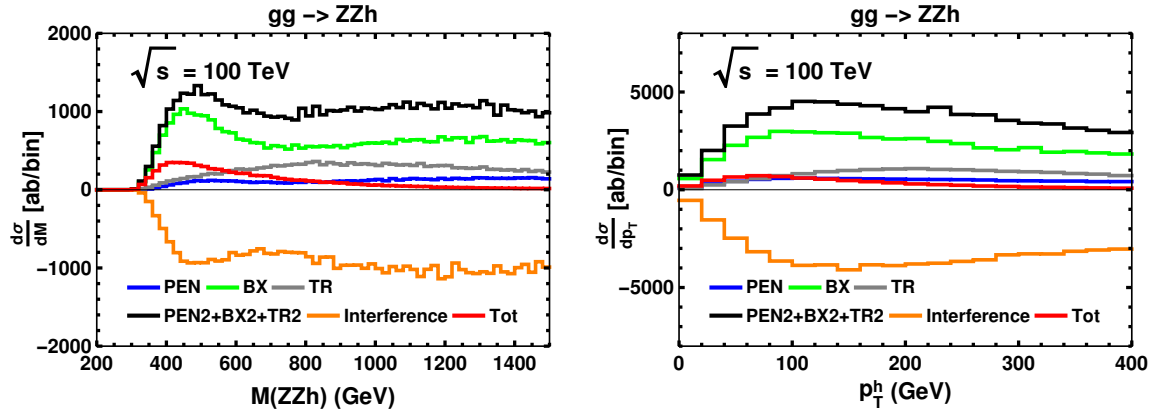


Figure 5.3: SM contribution of pentagon (blue), box (green), triangle (gray) diagrams, as well as their squared sum (black), interference (orange) and total (red) contribution to partonic center-of-mass energy and $p_T(h)$ distributions in $gg \rightarrow ZZh$ at 100 TeV collider (FCC-hh). As can be seen, there is a strong destructive interference between the penta, box, and triangle diagrams.

In the tree level $q\bar{q}$ initiated channel, there is no QCD vertex. So here change in renormalization scale does not affect the cross section (as change in the electroweak coupling is too small). But, the change in factorization scale can affect the cross section, and uncertainty increases with collider energy. However, when NLO QCD correction is considered, change in either of renormalization and factorization scales changes the cross section. Nevertheless, the uncertainty in the cross section due to renormalization scale variation is small

as NLO QCD correction is much smaller than the tree level results. The overall uncertainty in this case is smaller than the LO case, which is as expected for higher order calculation. The gg fusion channel uncertainties are more ($\sim 20\text{-}30\%$) as there α_s^2 appears as an overall factor, whereas in $q\bar{q}$ initiated channel only α_s appears, that is even only in NLO correction part which is smaller than the tree level result.

Interference of various diagrams plays a major role in $gg \rightarrow ZZh$ production. In Fig. 5.3, we have shown the $M(ZZh)$ and $p_T(h)$ distributions for penta, box, triangle, sum of their individual contributions, interference, and total at the 100 TeV collider (FCC-hh). As can be seen, the box diagrams give the largest contribution, then comes the triangle contribution and penta contributes the least. However because of the large *destructive* interference, the total contribution is smaller by about a factor of five than the box contribution.

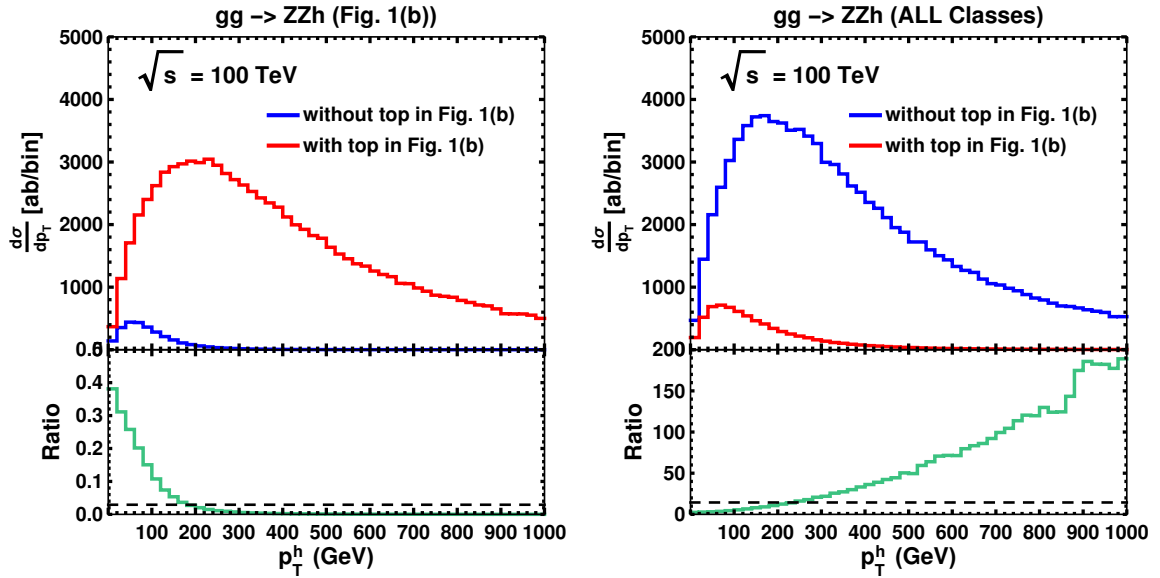


Figure 5.4: Left: The top-quark contribution to box diagram of Fig. 1(b). Right: The effect of excluding top-quark contribution from Fig. 1(b) to full amplitude. In the lower panel, we have taken ratio of contributions without top and with top quark in Fig 1(b). While the green histogram shows ratio for differential distributions, the black dashed line shows the ratio for the cross sections.

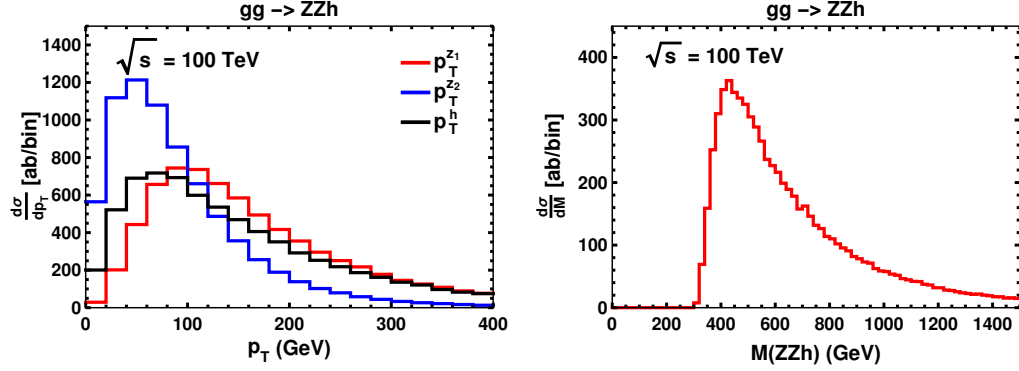


Figure 5.5: Kinematic distributions for $gg \rightarrow ZZh$ in the SM at the 100 TeV collider. These plots are made with the histogram data obtained after p_T ordering of the Z bosons. Z_1 and Z_2 refer to the hardest, and second hardest in p_T , respectively.

We have found that the top-quark contribution in $ggZZ^*$ -type box diagram is quite significant despite the propagators suppression. This is due to the coupling of off-shell longitudinal Z boson (effectively the Goldstone boson) with top-quark and it is proportional to m_t . We show the effect of excluding the top-quark contribution in $ggZZ^*$ -type box diagram (Fig.1(b)) on $p_T(h)$ distribution in Fig. 5.4. As we expect, excluding top-quark contribution in $ggZZ^*$ -type box diagram leads to non-unitary behavior in the full amplitude.

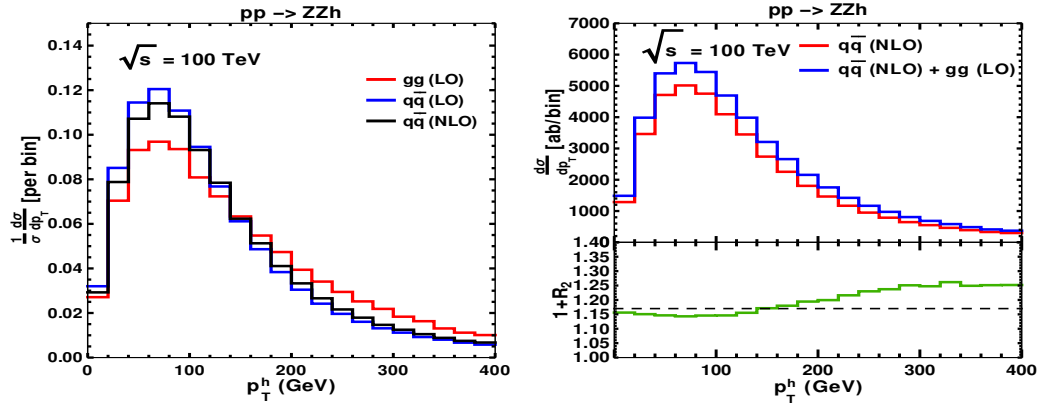


Figure 5.6: The left figure shows the normalized distribution for $p_T(h)$ in gg and $q\bar{q}$ initiated process. In the top panel of the right figure, we show the distribution of $q\bar{q}$ (NLO) + gg (LO) and $q\bar{q}$ (NLO) production with $p_T(h)$. The lower panel shows the ratio of them.

In Fig. 5.5, we have plotted p_T distribution for leading $p_T(Z_1)$, next-to-leading $p_T(Z_2)$,

and $p_T(h)$ in the left figure, and partonic center-of-mass energy distribution in the right figure for the 100 TeV collider. The p_T distributions for them peak around 100 GeV, 50 GeV, and 80 GeV, respectively. $\sqrt{\hat{s}}$ distribution peaks around 400 GeV with the threshold production energy around 300 GeV.

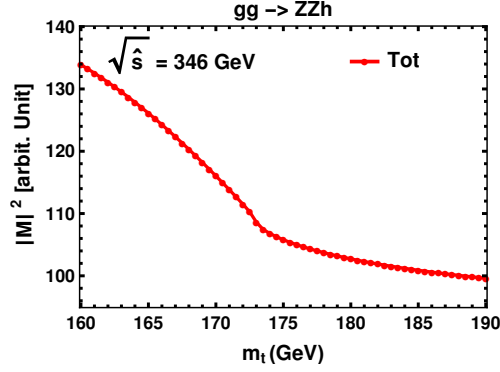


Figure 5.7: $t\bar{t}$ threshold effect for ZZh production via gg fusion channel. We have chosen an arbitrary phase space point with $\sqrt{\hat{s}} = 346$ GeV and then vary m_t from 160 GeV to 190 GeV. We see a sudden change in the slope of $|M|^2$ plot around $m_t = 173$ GeV.

In the left figure of Fig. 5.6, we see that the shape of p_T distribution for Higgs boson in gg fusion and $q\bar{q}$ initiated process is nearly same at 100 TeV collider (FCC-hh). In the right figure, in the top panel, distribution of NLO $q\bar{q}$ + LO gg and NLO $q\bar{q}$, and in the bottom panel ratio of them have been displayed. In the bottom panel, R_2 signifies the ratio of differential cross section for LO gg fusion channel contribution to that of NLO $q\bar{q}$ initiated process. The dashed line shows the ratio of corresponding cross sections at inclusive level, which is 0.17. At the tail of the distribution, we see the gg fusion channel contribution becomes further important, but there differential cross section itself is quite small.

For $gg \rightarrow ZZh$ production, unlike $gg \rightarrow WW h$ production which is going to be discussed in the next section, we do not see any significant $t\bar{t}$ threshold effect in $M(ZZh)$ distribution,

Fig. 5.5. However, for $gg \rightarrow ZZh$ production, this effect can be seen at the amplitude level if we choose a phase space point and vary m_t . For this, we have chosen a phase space point with center-of-mass energy, \sqrt{s} equaling 346 GeV, and then vary m_t from 160 GeV to 190 GeV. When $2m_t$ is less than \sqrt{s} , the amplitude is real, but as soon as it crosses \sqrt{s} , it develops some imaginary parts which leads to some sudden change in the slope of the matrix element square, $|M|^2$, plot with m_t , as can be seen in Fig. 5.7.

\sqrt{s} (TeV)	κ_i	$\sigma_{gg}^{ZZh,LO}$ [ab]	$\sigma_{q\bar{q}}^{ZZh,LO}$ [ab]	$\sigma_{q\bar{q}}^{ZZh,NLO}$ [ab]	$R_3 = \frac{\sigma_{gg}^{ZZh,LO}}{(\sigma_{q\bar{q}}^{ZZh,NLO} - \sigma_{q\bar{q}}^{ZZh,LO})}$
100	SM	7408	36830	43940	1.04
	κ_t	1.1 12426 [68%]	36830	43940	1.75
		0.9 6061 [-18%]			0.85
	κ_λ	1.1 7313 [-1%]	36840	43980	1.02
		0.9 7686 [4%]			1.09
	κ_V	1.1 10728 [45%]	44730 [21%]	53240 [21%]	1.26
		0.9 5333 [-28%]			0.92

Table 5.2: Effect of various anomalous couplings on ZZh production at the 100 TeV collider. The production cross section of $q\bar{q}$ initiated channel shows strong dependence on κ_V coupling. The gg fusion channel shows strong dependence on κ_t and κ_V anomalous couplings. The numbers in the square brackets show the percentage change in the cross section from the SM value in the corresponding channel because of anomalous coupling.

Effect of Anomalous Couplings

After discussing the SM predictions, we now consider BSM effect for this process both in gg fusion and $q\bar{q}$ initiated channel. The $q\bar{q}$ initiated channel depends mainly on κ_V . For the $b\bar{b}$ initiated channel, we have taken κ_b to be non-zero in order to see the effect of anomalous values of κ_λ on the $q\bar{q}$ initiated channel contribution⁴. As can be seen from the

⁴For the gg fusion channel, we have taken κ_b to be zero, as the dependence on κ_λ will come mainly due to the top-loop diagrams.

Fig. 5.1, the gg channel depends on κ_t , κ_λ , and κ_V . We vary these κ 's by 10% from their SM values. The results for these anomalous couplings have been tabulated in Tab. 5.2. The gg fusion channel strongly depends on both κ_t and κ_V . In the gg fusion channel, $\pm 10\%$ change in κ_t causes 68% and -18% change in the cross section, respectively. And $\pm 10\%$ change in κ_V causes 45% and -28% change in the cross section, respectively. In the $q\bar{q}$ channel, κ_V comes as an overall factor both for LO and NLO amplitude, and so the effect of 10% change in κ_V causes around 20% change in the cross section. In the table, it can be seen that the dependence of $q\bar{q}$ initiated channel contribution on κ_λ is milder than that of gg fusion channel contribution.

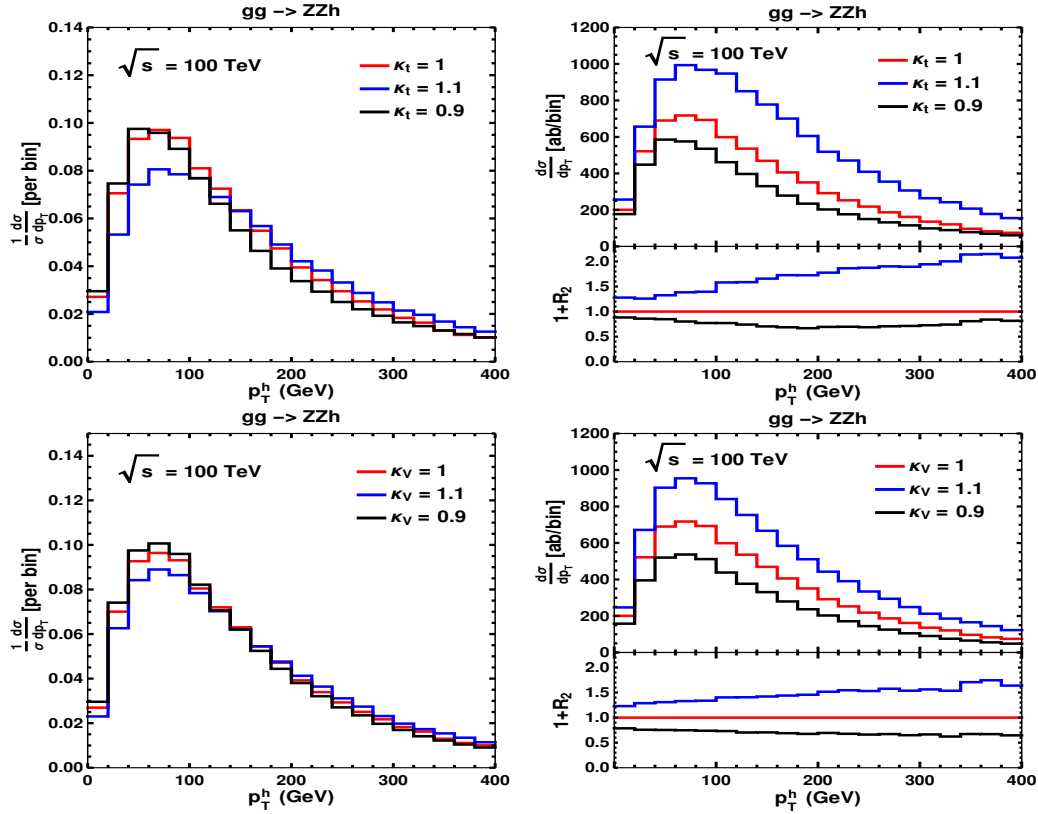


Figure 5.8: Effect of anomalous values of κ_t and κ_V on ZZh production via gg fusion channel. The left column shows normalized distribution, and right column shows distributions and their ratio with the SM value.

In Fig. 5.8, we display the distributions which show the effect of κ_t and κ_V in gg fusion channel. We present distributions only for these two anomalous couplings since the cross section shows strong dependence on them. In the top left figure, the shape remains more or less same. The proportion of higher and lower p_T Higgs boson increase slightly for increase and decrease in κ_t , respectively. In the top right figure, we show the absolute distribution in the top panel, while in the bottom panel we show the ratio of distribution with anomalous coupling with that of the SM coupling. We see that in the bins around 400 GeV, this ratio is around 2 for $\kappa_t = 1.1$. In the lower row, we show the corresponding plots for κ_V . In this case also, shape remains more or less same. In the bottom panel of the right plot, at some of the bins, the ratio of distribution with $\kappa_V = 1.1$ with that of SM is around 1.5.

In Fig. 5.9, we show the effect of κ_V on the NLO $q\bar{q}$ initiated channel. In the left figure, we see that all the lines overlap, which is obvious since κ_V appears as an overall factor in the amplitude for this channel because it is present in all the diagrams linearly. This behavior is in sharp contrast with the case for the gg fusion channel where the distributions do not overlap, since κ_V is present only in some specific diagrams. In the right figure, in the top panel we show the distributions and in the bottom panel we show the ratio of the distribution with the anomalous coupling to the distribution for the SM. It can be seen, in all the bins the ratio is nearly same, 1.2 and 0.8 for $\kappa_V = 1.1$ and 0.9, respectively, which is obvious since the differential cross section depends on k_V^2 as an overall factor.

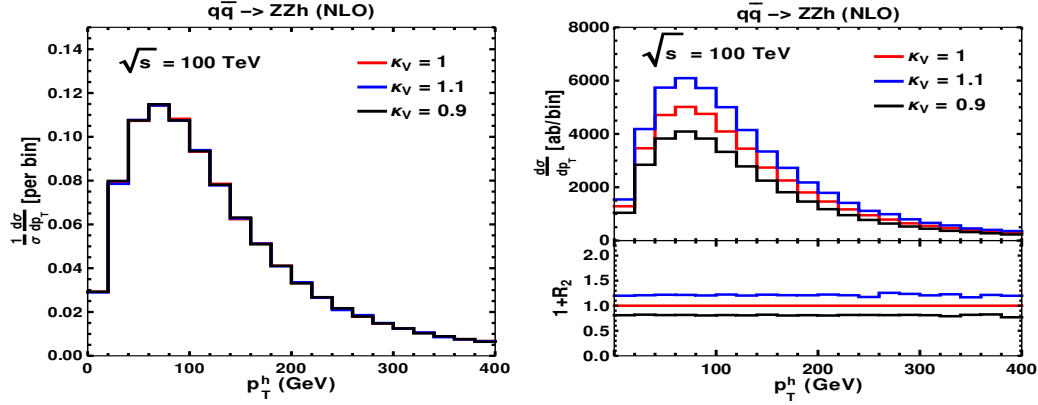


Figure 5.9: Effect of anomalous value of κ_V on NLO QCD ZZh production via $q\bar{q}$ initiated channel. We have not shown the effect of scaling of other couplings as their effect on the total cross section is negligible.

5.4.2 The process $pp \rightarrow WW h$

Standard Model Predictions

The cross sections for $WW h$ production via different channels have been tabulated in Tab. 5.3 with their scale uncertainties. The gg fusion channel contributions to $WW h$ production at 14, 27, and 100 TeV colliders are 290 ab, 1344 ab, and 17403 ab, respectively (These numbers are roughly 2.3 times higher than ZZh cross sections). The corresponding values of the LO $q\bar{q}$ contribution are 8658, 23040, and 128000 ab, respectively⁵. The ratio, R_3 , is found to be 0.15, 0.19, and 0.43, respectively. Unlike ZZh production, the contribution of the gg fusion channel is relatively smaller.

⁵ $b\bar{b}$ initiated channel contributions are not included in here as we faced some technical issues for NLO correction, which arises because of top resonance in the real diagrams, which needs to be handled carefully. As the LO $b\bar{b}$ initiated process can be computed easily in Madgraph, we report cross section for LO $b\bar{b}$ initiated channel separately in here. In five flavor scheme, they are 287 ab, 1557 ab, and 25800 ab, respectively.

\sqrt{s} (TeV)	$\sigma_{gg}^{WWh, LO}$ [ab]	$\sigma_{q\bar{q}}^{WWh, LO}$ [ab]	$\sigma_{q\bar{q}}^{WWh, NLO}$ [ab]	$R_3 = \frac{\sigma_{gg}^{WWh, LO}}{(\sigma_{q\bar{q}}^{WWh, NLO} - \sigma_{q\bar{q}}^{WWh, LO})}$
14	$290^{+27.6\%}_{-21.0\%}$	$8658^{+0.3\%}_{-0.7\%}$	$11220^{+1.5\%}_{-1.1\%}$	0.11
27	$1344^{+22.5\%}_{-18.8\%}$	$23040^{+2.1\%}_{-2.7\%}$	$30090^{+1.7\%}_{-1.8\%}$	0.19
100	$17403^{+20.6\%}_{-17.8\%}$	$128000^{+7.5\%}_{-8.1\%}$	$167300^{+2.0\%}_{-3.3\%}$	0.44

Table 5.3: A comparison of different perturbative orders in QCD coupling contributing to $pp \rightarrow WWh$ hadronic cross section at $\sqrt{s} = 14, 27$, and 100 TeV. The ratio R_3 quantifies the gg fusion channel contribution with respect to the $q\bar{q}$ (LO) and $q\bar{q}$ (NLO) contributions. $q\bar{q}$ initiated channel results do not include bottom quark contribution.

As regards scale uncertainties, the $gg \rightarrow WWh$ channel cross section follow same pattern as discussed in $gg \rightarrow ZZh$. For the $q\bar{q}$ initiated channel also, our conclusions are same as that for ZZh case.

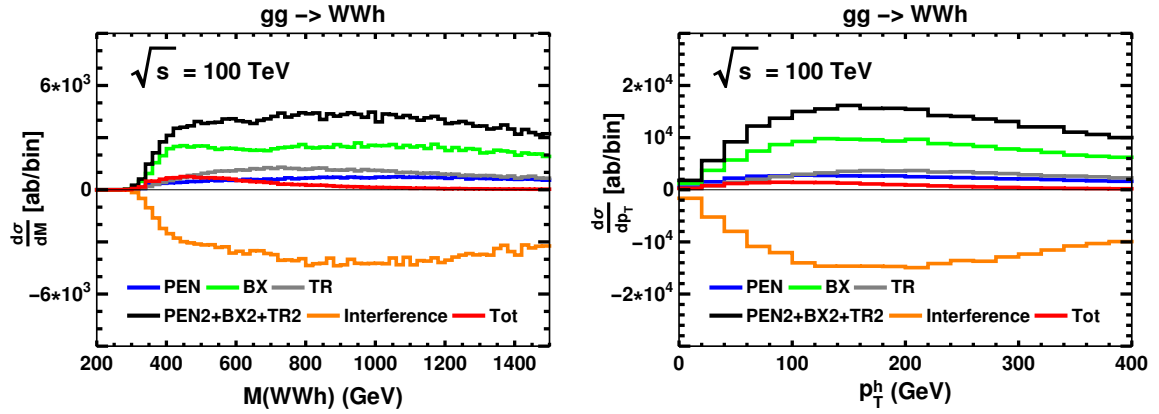


Figure 5.10: SM contribution of pentagon (blue), box (green), triangle (gray) diagrams, as well as their square sum, interference and total contribution to partonic center-of-mass energy and $p_T(h)$ distributions in $gg \rightarrow WWh$ at 100 TeV FCC-hh collider. As can be seen, there is strong destructive interference between the penta, box, and triangle diagrams.

Like $gg \rightarrow ZZh$ production case, interference of various diagrams plays a major role in $gg \rightarrow WWh$ production as well. In Fig. 5.10, we have shown the $M(WWh)$ and $p_T(h)$ distributions for penta, box, triangle, sum of their individual contributions, interference,

and total at the 100 TeV collider (FCC-hh). As can be seen, the individual box, triangle and penta contribute from highest to lowest. The total contribution is much smaller than the box contribution because of strong destructive interference effect which is shown by orange line in the figure. Another important observation is that while box contributes significantly at higher partonic center-of-mass energy, the contribution of total amplitude is very small there.

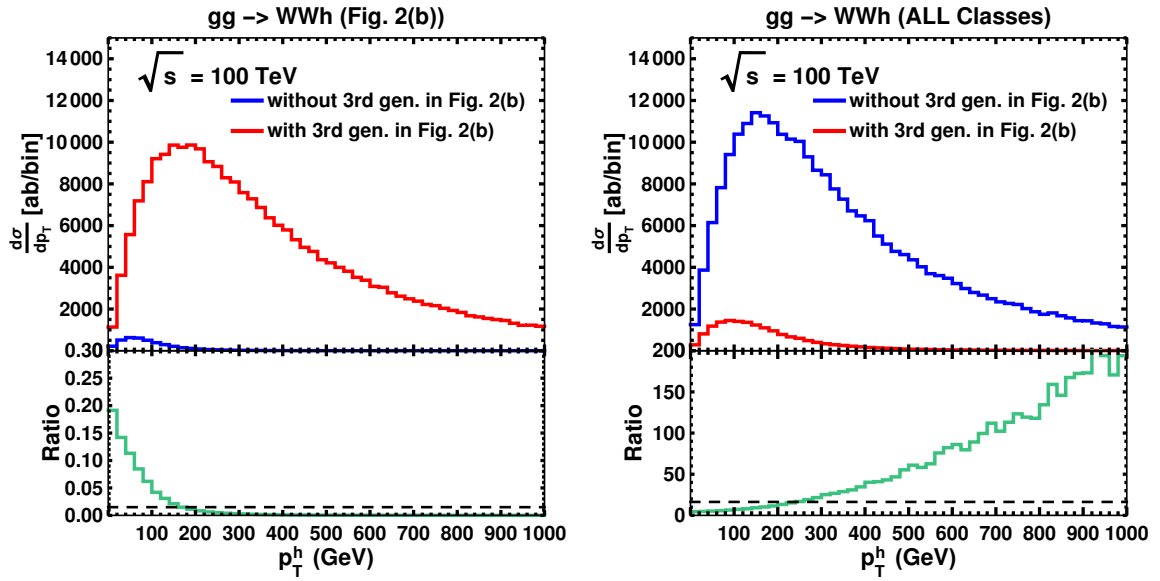


Figure 5.11: Left: The third generation quark contribution to box diagram of Fig. 2(b). Right: The effect of excluding third generation quark contribution from Fig. 2(b) to full amplitude.

The $gg \rightarrow WW h$ amplitude also receives significant contribution from third generation quarks via $ggWW^*$ type box diagram. In Fig. 5.11, we show the effect of excluding the third generation quark contribution from the $ggWW^*$ type box diagram, on the $p_T(h)$ distribution. We can once again see that the third generation quark contribution in $ggWW^*$ type box diagram is necessary for the unitarization of full amplitude.

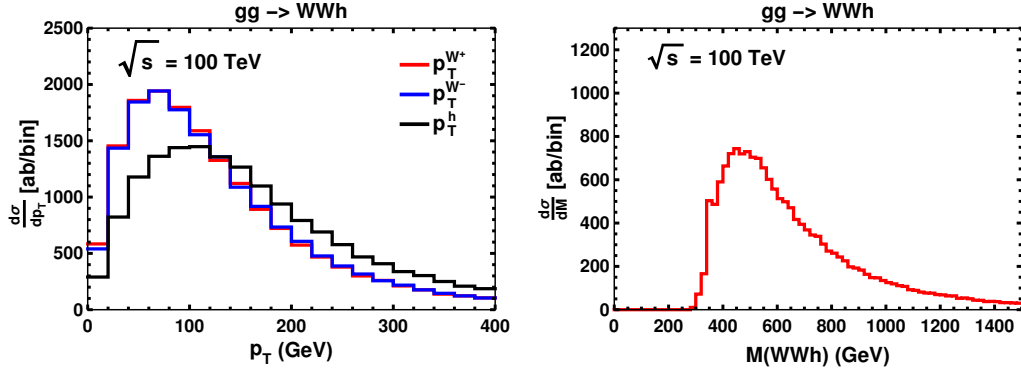


Figure 5.12: p_T and $M(WWh)$ distributions for $gg \rightarrow WW h$ in the SM at the 100 TeV collider (FCC-hh). As expected, the p_T distributions for W^+ and W^- fall on each other as the process is a gg fusion one. A small peak can be seen at 350 GeV in the $M(WWh)$ distribution, which occurs due to $t\bar{t}$ threshold effect.

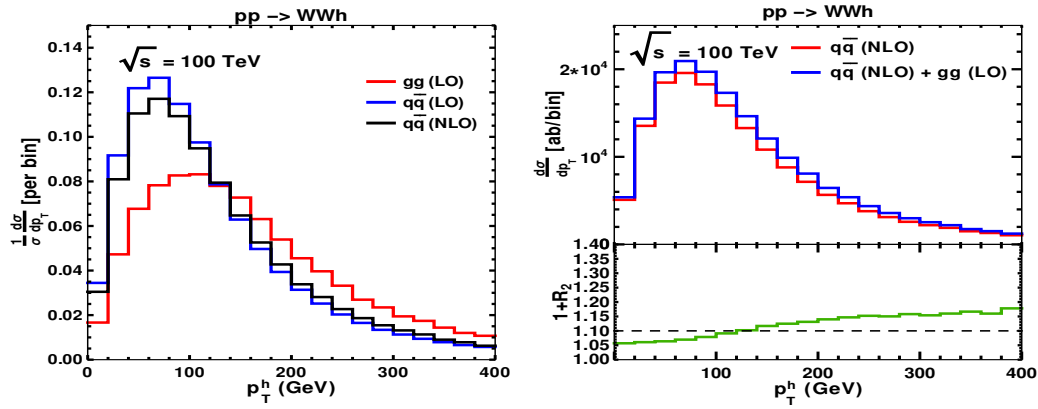


Figure 5.13: The left figure shows the normalized distribution for $p_T(h)$ in gg and $q\bar{q}$ initiated process. In the top panel of the right figure, we show the distribution of $q\bar{q}$ (NLO)+ gg (LO) and $q\bar{q}$ (NLO) production with $p_T(h)$. The lower panel shows their ratio. Results do not include contribution of $b\bar{b}$ initiated process .

In the left figure of Fig. 5.12, we can see that the p_T distribution of W^+ and W^- overlap with each other, which is as expected in the case of gg fusion channel. The p_T -distribution peaks around 100 GeV, and we see the production cross section for very large p_T Higgs boson is more than that of W^+ or W^- . In the right figure of Fig. 5.12, the distribution for center-of-mass energy has been shown, which peaks around 450 GeV. A smaller peak around 350 GeV can be seen in this. This happens because of the $t\bar{t}$ threshold effect.

In the left figure of Fig. 5.13, the normalized p_T distribution for Higgs boson in gg fusion and $q\bar{q}$ initiated processes have been shown for 100 TeV collider (FCC-hh). In the right figure, in the top panel, distribution of $q\bar{q}$ (NLO) + gg (LO) and $q\bar{q}$ (NLO), and in the bottom panel their ratio is displayed. The dashed straight line shows the ratio of corresponding inclusive cross sections, which is 0.1. Once again, we find that gg fusion channel contribution is more relevant in higher p_T bins.

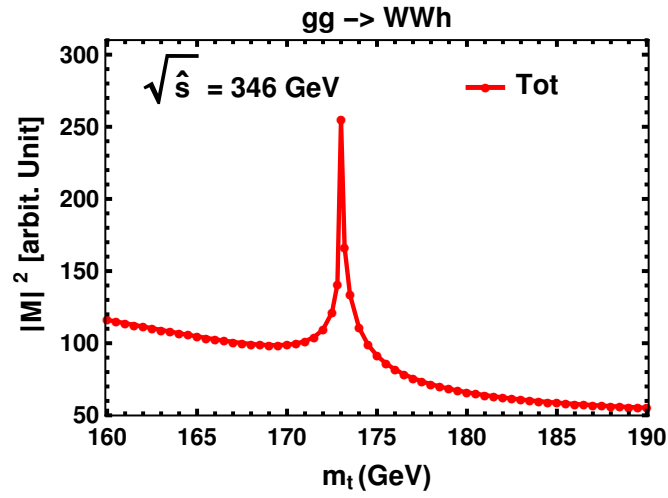


Figure 5.14: $t\bar{t}$ threshold effect for WW_h via gg fusion channel. To show this effect, after arbitrarily choosing a phase space point with $\sqrt{\hat{s}} = 346$ GeV, we vary m_t from 160 GeV to 190 GeV. We see a peak around $m_t = 173$ GeV, which happens to be half of $\sqrt{\hat{s}}$ for the chosen phase space point.

In the Fig. 5.14, as in the case of ZZh process, we show the threshold effects for WW_h production via gg fusion channel at the amplitude level. These effects are more prominent in this process than $gg \rightarrow ZZh$. This could be due to tbW vertex in the diagrams. Here top-quark can go on-shell, leading to significant increase in the cross section. In the ZZh case we had a slight change in the slope, while here we have a prominent peak. To show this effect, we arbitrarily choose a phase space point with $\sqrt{\hat{s}} = 346$ GeV and then vary m_t

from 160 GeV to 190 GeV. In the total amplitude square, we see a peak around $m_t = 173$ GeV, which happens to be half of $\sqrt{\hat{s}}$ for the chosen phase space point.⁶

Effect of Anomalous Couplings

Next we focus on the effect of anomalous coupling on the total and differential cross sections. The $q\bar{q}$ initiated channel depends on κ_V only. The gg fusion channel depends on κ_t , κ_λ , and κ_V (see Fig. 5.2). We vary these κ 's by 10% from their SM values. The results for these anomalous couplings have been shown in Tab. 5.4. While the gg fusion channel shows mild dependence on anomalous κ_λ , it shows strong dependence on anomalous κ_t and κ_V . In the gg fusion channel, $\pm 10\%$ change in κ_t causes 54% and -3% change in the cross section, respectively, while $\pm 10\%$ change in κ_V causes 38% and -26% change in the cross section, respectively. Like the case in $q\bar{q} \rightarrow ZZh$, as in $q\bar{q}$ initiated channel κ_V^2 comes as an overall factor in the cross section, a 10% change in κ_V gives around 20% change in the cross section of this channel.

⁶Here we have chosen a phase space point where effect is prominent. At some other phase space point, effect may be milder or show up in a different way.

\sqrt{s} (TeV)	κ_i	$\sigma_{gg}^{\text{WWh, LO}}$ [ab]	$\sigma_{q\bar{q}}^{\text{WWh, LO}}$ [ab]	$\sigma_{q\bar{q}}^{\text{WWh, NLO}}$ [ab]	$R_3 = \frac{\sigma_{gg}^{\text{WWh, LO}}}{(\sigma_{q\bar{q}}^{\text{WWh, NLO}} - \sigma_{q\bar{q}}^{\text{WWh, LO}})}$	
100	SM	17403	128000	167300	0.44	
	κ_t	1.1	26572 [54%]	128000	167300	0.68
		0.9	16868 [-3%]			0.43
	κ_λ	1.1	16696 [-4%]	128000	167300	0.42
		0.9	17708 [2%]			0.45
	κ_V	1.1	23970 [38%]	154900 [21%]	202500 [21%]	0.50
		0.9	12837 [-26%]	103700 [-19%]	135500 [-19%]	0.40

Table 5.4: Effect of various anomalous couplings on WWh production for the 100 TeV collider. The production cross section via $q\bar{q}$ initiated channel shows strong dependence on κ_V only. The gg fusion channel shows strong dependence on κ_t and κ_V . The numbers in the square brackets show percentage change in the cross section in BSM scenario with respect to the SM value. $q\bar{q}$ initiated channel results do not include bottom quark contribution.

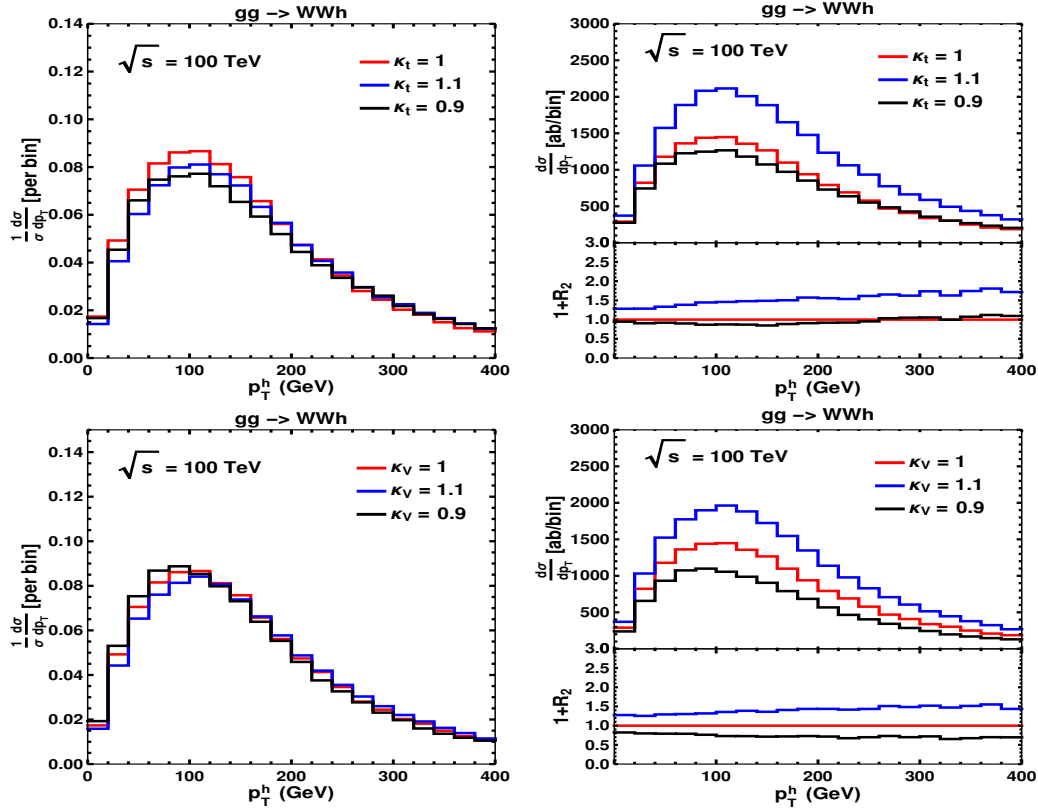


Figure 5.15: Effect of anomalous values of κ_t and κ_V on WWh production via gg fusion channel. The left panel shows normalized distribution, and the right panel shows distributions and the ratio of the distributions to the SM distribution.

In Fig. 5.15, we show the distributions which show the effect of κ_t and κ_V in gg fusion channel. We do not show the distribution for anomalous κ_λ as its effect on cross section is very small. In the left panel, we see the shape remains more or less same. In the top parts of the plots in the right panel, we show the absolute distribution. In the bottom part of the plots, we show the ratio of distribution for BSM scenario to that of the SM one. We see that in the bins around 400 GeV, this ratio is around 1.5 for $\kappa_t = 1.1$ and $\kappa_V = 1.1$. For $\kappa_t = 0.9$, the ratio remains close to 1 throughout all the bins and for $\kappa_V = 0.9$, it is in the range 0.7–0.8. The effect of anomalous κ_V coupling on the distribution for $q\bar{q}$ initiated channel is similar to what has been discussed in $q\bar{q} \rightarrow ZZh$ channel.

5.4.3 The process $pp \rightarrow \gamma Zh$

Standard Model Predictions

The gg fusion contribution is very small for this process. As mentioned in Sec. 5.1, only vector part of Z coupling to quarks contributes to the total cross section because of Furry's theorem. From Tab. 5.5, it can be seen that R_3 , which shows the ratio of gg fusion channel contribution to NLO correction to $q\bar{q}$ initiated channel, is at most 0.06 for 100 TeV collider, and even smaller for HE-LHC (27 TeV) and LHC (14 TeV). We present results for two cuts on p_T of γ : 50 GeV and 100 GeV. It can be seen that with larger p_T^γ , reduction in $q\bar{q}$ initiated channel is more than that in gg fusion channel. With $p_T^\gamma > 50$ GeV, the gg fusion contribution to γZh at 14, 27, and 100 TeV colliders are 4 ab, 16 ab, and 168 ab, respectively. The corresponding values for the LO $q\bar{q}$ initiated channel contribution are

689, 1733, and 7498 ab, respectively⁷.

\sqrt{s} (TeV)	$\sigma_{gg}^{\gamma Zh, LO}$ [ab]		$\sigma_{q\bar{q}}^{\gamma Zh, LO}$ [ab]		$\sigma_{q\bar{q}}^{\gamma Zh, NLO}$ [ab]		$R_3 = \frac{\sigma_{gg}^{\gamma Zh, LO}}{(\sigma_{q\bar{q}}^{\gamma Zh, NLO} - \sigma_{q\bar{q}}^{\gamma Zh, LO})}$	
	$p_T^\gamma > 50$ GeV	$p_T^\gamma > 100$ GeV	$p_T^\gamma > 50$ GeV	$p_T^\gamma > 100$ GeV	$p_T^\gamma > 50$ GeV	$p_T^\gamma > 100$ GeV	$p_T^\gamma > 50$ GeV	$p_T^\gamma > 100$ GeV
14	$4.0^{+26\%}_{-20\%}$	$1.8^{+27\%}_{-21\%}$	$689^{+0\%}_{-0.2\%}$	$225^{+1.2\%}_{-1.4\%}$	$909^{+1.7\%}_{-1.3\%}$	$295^{+1.8\%}_{-1.5\%}$	0.018	0.026
27	$16^{+22\%}_{-17\%}$	$8.1^{+22\%}_{-17\%}$	$1773^{+3.0\%}_{-3.6\%}$	$613^{+1.7\%}_{-2.2\%}$	$2349^{+1.7\%}_{-2.1\%}$	$853^{+1.8\%}_{-1.8\%}$	0.028	0.034
100	$168^{+21\%}_{-19\%}$	$93^{+23\%}_{-15\%}$	$7498^{+8.8\%}_{-9.4\%}$	$2749^{+7.2\%}_{-7.8\%}$	$10430^{+2.2\%}_{-3.8\%}$	$4106^{+2.7\%}_{-3.8\%}$	0.057	0.069

Table 5.5: A comparison of different perturbative orders in QCD coupling contributing to $pp \rightarrow \gamma Zh$ hadronic cross section at $\sqrt{s} = 14, 27$, and 100 TeV for two cuts on p_T^γ and $|\eta^\gamma| < 2.5$. We calculate ratio R_3 which quantify the gg fusion channel contribution with respect to the NLO correction in $q\bar{q}$ initiated process. Contribution of $b\bar{b}$ channel has also been taken into account.

In Tab. 5.6, the effect of various p_T^γ cuts in the gg fusion and $q\bar{q}$ initiated channel has been shown. As the cut on p_T^γ increases, $q\bar{q}$ initiated channel cross section decreases faster than the gg fusion channel one. In going from 20 GeV to 100 GeV cut, the cross section of gg fusion channel decreases by a factor of around 2.4, while in LO $q\bar{q}$ channel, it decreases by a factor of around 7.

cuts	$gg \rightarrow \gamma Zh$ [ab]	$q\bar{q} \rightarrow \gamma Zh(LO)$ [ab]	$q\bar{q} \rightarrow \gamma Zh(NLO)$ [ab]
$p_T^\gamma > 20$ GeV	229	19870	25750
$p_T^\gamma > 30$ GeV	204	13440	18000
$p_T^\gamma > 50$ GeV	167	7589	10340
$p_T^\gamma > 100$ GeV	95	2812	4072
$p_T^\gamma > 100$ GeV, $p_T^{Z, H} > 50$ GeV	68	2245	3255

Table 5.6: Cross sections for $pp \rightarrow \gamma Zh$ production at the 100 TeV collider (FCC-hh). A pseudo-rapidity cut of $|\eta^\gamma| < 2.5$ has been imposed. b quark contribution has also been considered in these results.

In Fig. 5.16, we show the $M(\gamma Zh)$ and $p_T(h)$ distributions for penta, box, sum of their

⁷ $b\bar{b}$ initiated channel contributions are included in here, which are 4.8 ab, 24.0 ab, and 251 ab, respectively. This has been done in five-flavor scheme using Madgraph.

individual contributions, their interference, and total at the 100 TeV collider. The interference effect is particularly interesting here. In some range of center-of-mass energy it is constructive, at some other range it is destructive. The contribution of box diagrams is more than that of the pentagon diagrams. Later, we will see because of this, dependence of cross section on anomalous k_V is more than anomalous k_t . Since the $gg\gamma Z^*$ type box amplitude does not depend on the axial-vector coupling of the off-shell longitudinal Z-boson with the quarks, the top-quark contribution is not very significant. This is shown in Fig. 5.17.

In Fig. 5.18, we have plotted p_T distribution for final state particles in the left figure, and partonic center-of-mass energy distribution in the right figure for the 100 TeV collider. The p_T distributions for them peak around 50–100 GeV. $\sqrt{\hat{s}}$ distribution peaks around 400 GeV. Like the $gg \rightarrow ZZh$ production case, we do not see any visible $t\bar{t}$ threshold effect in the partonic center-of-mass energy distribution.

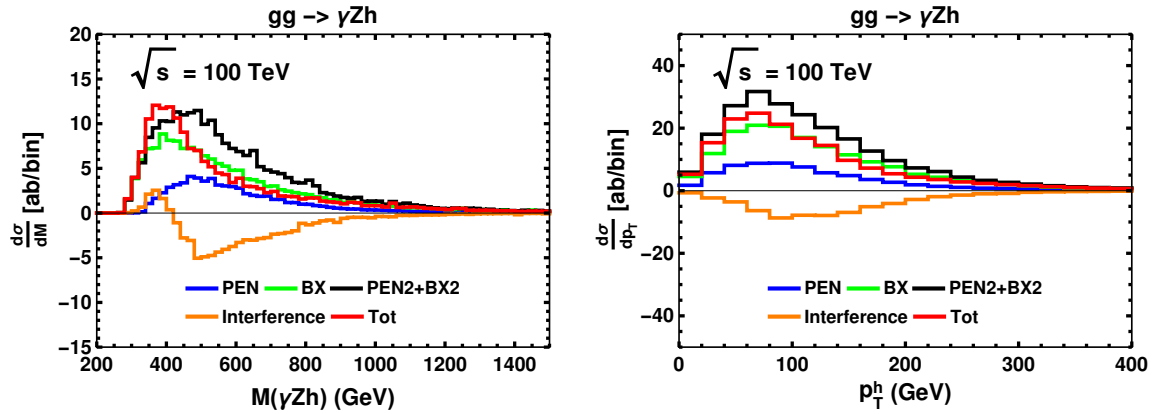


Figure 5.16: SM contribution of pentagon (blue) and box (green) diagrams, as well as their square sum, interference, and total contribution to partonic center-of-mass energy and $p_T(h)$ distributions in $gg \rightarrow \gamma Zh$ at 100 TeV FCC-hh collider. The interference shows an interesting effect. In 300 – 400 GeV range of partonic center-of-mass energy, it is constructive, while it is destructive at energies higher than that. $p_T^\gamma > 50$ GeV has been imposed.

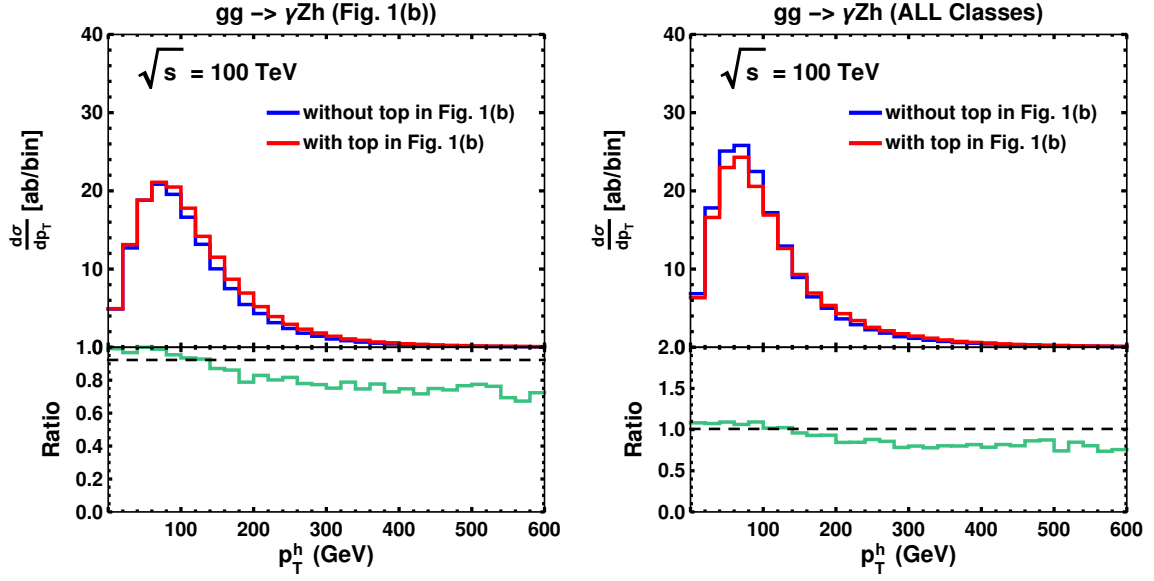


Figure 5.17: Left: The top-quark contribution to box diagram of Fig. 1(b). Right: The effect of excluding top-quark contribution from Fig. 1(b) to full amplitude.

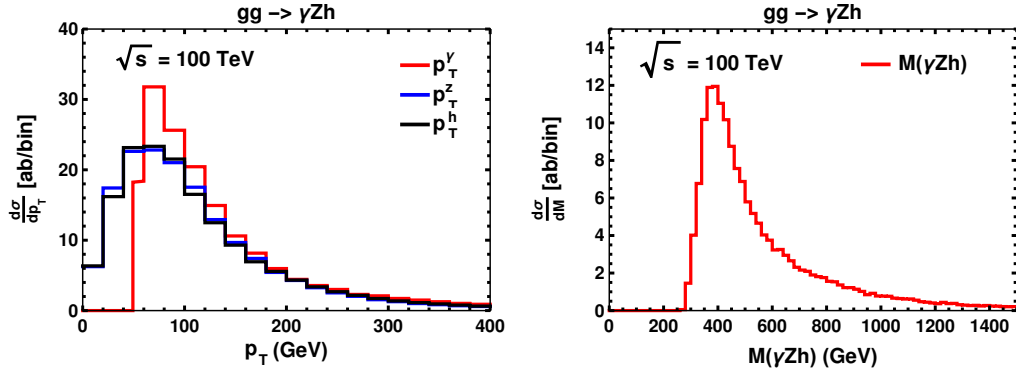


Figure 5.18: Kinematic distributions for $gg \rightarrow \gamma Zh$ in the SM at 100 TeV. $p_T^\gamma > 50$ GeV has been imposed.

In Fig. 5.19, we show the $t\bar{t}$ threshold effect for γZh production via gg fusion channel at the amplitude level. However, like ZZh production case, the effect is too small to be visible in the $M(\gamma Zh)$ distribution, Fig. 5.18.

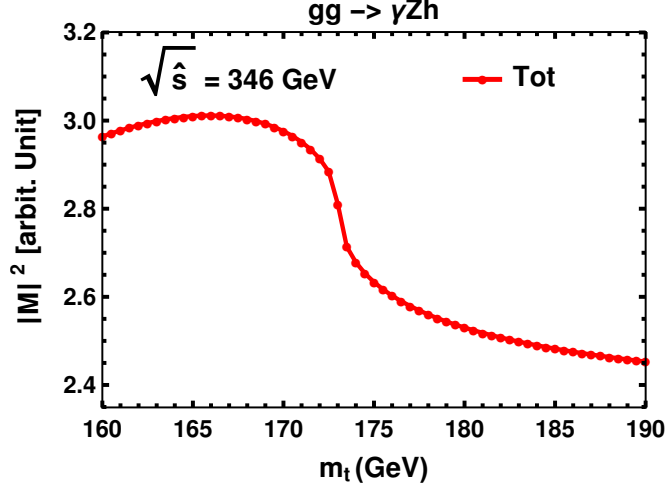


Figure 5.19: $t\bar{t}$ threshold effect for γZh production via gg fusion channel at the amplitude level.

Effect of Anomalous Couplings

In this section, we discuss the effect of anomalous κ_t and κ_V . The gg fusion channel shows very small dependence on anomalous κ_t , as it is present only in pentagon diagram whose contribution is small (see Fig. 5.16). However, it strongly depends on κ_V , as the box contribution is much more than the penta contribution. The results are tabulated in Tab. 5.7. We do not show the effect of anomalous coupling on the distribution. However, it can be understood qualitatively from the effect in the gg fusion channel using Eq. 5.2 and Fig. 5.16. For the $q\bar{q}$ initiated channel, like the previous processes here also only κ_V is relevant⁸. We do not show the effect of anomalous κ_V on the distribution of $q\bar{q}$ initiated channel as those are similar to what has been discussed for the previous two processes.

⁸As the $b\bar{b}h$ coupling is too small, its contribution will be tiny. Most of the $b\bar{b}$ initiated channel contribution comes from the diagrams where Higgs boson is radiated off Z boson.

\sqrt{s} (TeV)	κ_i	$\sigma_{gg}^{\gamma Z h, \text{LO}}$ [ab]	$\sigma_{q\bar{q}}^{\gamma Z h, \text{LO}}$ [ab]	$\sigma_{q\bar{q}}^{\gamma Z h, \text{NLO}}$ [ab]	$R_3 = \frac{\sigma_{gg}^{\gamma Z h, \text{LO}}}{(\sigma_{q\bar{q}}^{\gamma Z h, \text{NLO}} - \sigma_{q\bar{q}}^{\gamma Z h, \text{LO}})}$
100	SM	166	7498	10430	0.06
	κ_t 1.1	175 [5.4%]	7498	10430	0.06
	0.9	164 [-1.2%]			0.06
	κ_V 1.1	196 [18%]	9049 [21%]	12650 [21%]	0.05
	0.9	141 [-15%]	6138 [-18%]	8448 [-19%]	0.06

Table 5.7: Effect of various anomalous couplings on $\gamma Z h$ production for the 100 TeV collider. The effect of anomalous κ_t on gg fusion channel cross section is smaller than that of anomalous κ_V . The $q\bar{q}$ initiated channel does not depend on κ_t , as no diagram has this $t\bar{t}h$ vertex. The numbers in the square brackets show percentage change in the cross section in BSM scenario with respect to the SM value.

5.4.4 The process $pp \rightarrow \gamma\gamma h$

This process is important as it is a background to $pp \rightarrow hh$ process when one Higgs boson decays into a photon pair. To manage the background one usually looks at ‘ $\gamma\gamma b\bar{b}$ ’ final state, instead of ‘ $b\bar{b}b\bar{b}$ ’, as the signature of the double Higgs boson production.

Like $\gamma Z h$ production, the cross sections for this process are small. But unlike $\gamma Z h$, gg fusion process gives the dominant contribution to $pp \rightarrow \gamma\gamma h$ process. We present results for two cuts on p_T of γ s: 50 GeV and 100 GeV. With $p_T^\gamma > 50$ GeV, the gg fusion contribution to $\gamma\gamma H$ at 14, 27, and 100 TeV colliders are 5.4 ab, 22 ab, and 220 ab, respectively. As far as $q\bar{q}$ initiated production is concerned, only $b\bar{b}$ channel can produce $\gamma\gamma h$. However, this cross section is quite small, owing to small bottom Yukawa coupling. The LO cross sections for this $b\bar{b}$ channel in five flavor scheme are 0.033 ab, 0.153 ab, and 1.4ab, respectively. The results are tabulated in Tab. 5.8.

Standard Model Predictions

\sqrt{s} (TeV)	$\sigma_{gg}^{\gamma\gamma h, LO}$ [ab]		$\sigma_{q\bar{q}}^{\gamma\gamma h, LO}$ [ab]		$\sigma_{q\bar{q}}^{\gamma\gamma h, NLO}$ [ab]	
	$p_T^\gamma > 50$ GeV	$p_T^\gamma > 100$ GeV	$p_T^\gamma > 50$ GeV	$p_T^\gamma > 100$ GeV	$p_T^\gamma > 50$ GeV	$p_T^\gamma > 100$ GeV
14	$5.36^{+28\%}_{-20\%}$	$2.98^{+28\%}_{-20\%}$	$0.033^{+13\%}_{-14\%}$	$0.0031^{+9\%}_{-10\%}$	$0.046^{+5\%}_{-6\%}$	$0.0039^{+4\%}_{-5\%}$
27	$22.0^{+22\%}_{-19\%}$	$13.0^{+22\%}_{-18\%}$	$0.153^{+15\%}_{-17\%}$	$0.0181^{+12\%}_{-13\%}$	$0.234^{+5\%}_{-7\%}$	$0.025^{+4\%}_{-6\%}$
100	$220.1^{+27\%}_{-21\%}$	$137.8^{+32\%}_{-19\%}$	$1.4^{+20\%}_{-20\%}$	$0.21^{+16\%}_{-16\%}$	$2.25^{+5\%}_{-8\%}$	$0.34^{+5\%}_{-7\%}$

Table 5.8: A comparison of different perturbative orders in QCD coupling contributing to $pp \rightarrow \gamma\gamma h$ hadronic cross section at $\sqrt{s} = 14, 27$, and 100 TeV for two cuts on p_T^γ , $|\eta^\gamma| < 2.5$, and $\Delta R_{\gamma\gamma} > 0.4$. Unlike the previous processes, here we don't show the ratio (R_3) of gg fusion channel contribution to NLO QCD correction in $q\bar{q}$ initiated channel, since the tree level contribution of the latter channel is too small in comparison to the former one.

In Tab. 5.9, the effect of various p_T^γ cuts in the gg fusion and $q\bar{q}$ initiated channels has been shown. As the cut on p_T^γ increases, $q\bar{q}$ initiated channel cross section decreases faster than the gg fusion channel one. In going from 20 GeV to 100 GeV cut, the cross section of gg fusion channel decreases by a factor of around 2.2, while in LO $q\bar{q}$ initiated channel decreases by a factor of around 57.

cuts	$gg \rightarrow \gamma\gamma h$ [ab]	$q\bar{q} \rightarrow \gamma\gamma h(LO)$ [ab]	$q\bar{q} \rightarrow \gamma\gamma h(NLO)$ [ab]
$p_T^\gamma > 20$ GeV	245	10.8	16.9
$p_T^\gamma > 30$ GeV	243	4.6	7.5
$p_T^\gamma > 50$ GeV	222	1.4	2.2
$p_T^\gamma > 100$ GeV	139	0.21	0.34
$p_T^\gamma > 100$ GeV, $p_T^{Z,H} > 50$ GeV	113	0.19	0.31

Table 5.9: Cross sections for $pp \rightarrow \gamma\gamma h$ production at the 100 TeV collider (FCC-hh). A pseudo-rapidity cut of $|\eta^\gamma| < 2.5$ and $\Delta R_{\gamma\gamma} > 0.4$ have been imposed. Only bottom quark can contribute to the $q\bar{q}$ initiated process. The cross section in this channel is too small, owing to the tiny bottom Yukawa coupling.

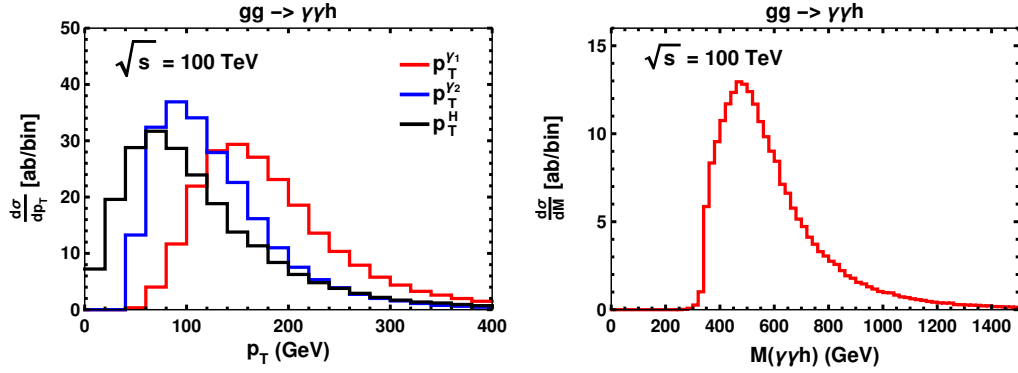


Figure 5.20: Kinematic distributions for $gg \rightarrow \gamma\gamma h$ process in the SM at 100 TeV. These plots have been made using histogram data obtained after p_T ordering of two γ s — γ_1 and γ_2 refer to the hardest and second hardest in p_T , respectively. $p_T^\gamma > 50$ GeV and $\Delta R_{\gamma\gamma} > 0.4$ have been imposed.

Unlike the previous processes, there is no box or triangle diagrams in the gg fusion channel. There are pentagon diagrams only. So here we do not have any interference effect between various classes of diagrams, see Eq. 5.1. In Fig. 5.20, we have plotted p_T distribution for hardest γ , next-to-hardest γ , and h in the left figure, and partonic center-of-mass energy distribution in the right figure for the 100 TeV collider (FCC-hh). The p_T distributions for them peak around 150 GeV, 90 GeV, and 70 GeV, respectively. $\sqrt{\hat{s}}$ distribution peaks around 475 GeV. Like the $gg \rightarrow ZZh$ and $gg \rightarrow \gamma Zh$ production cases, we do not see any visible $t\bar{t}$ threshold effect in the partonic center-of-mass energy distribution. However, for illustration, in Fig. 5.21 we show the threshold effect for $\gamma\gamma h$ production at the amplitude level.

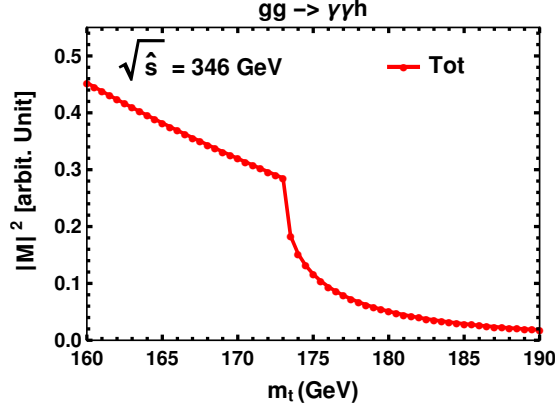


Figure 5.21: $t\bar{t}$ threshold effect for $\gamma\gamma h$ production via gg fusion channel.

Effect of Anomalous Couplings

Let us consider first gg fusion channel. As there are only pentagon diagrams, in the cross section expression, κ_t^2 is present as an overall factor. So a 10% change in κ_t will render an obvious change of around 20% in the cross section, which we see in the Tab. 5.10. We do not show the effect of this anomalous coupling on the distribution, as the cross section in every bin will simply be scaled by same factor, κ_t^2 . For the $q\bar{q}$ initiated process, the cross section is too small. It depends on κ_b , which we do not change from the standard model value.

\sqrt{s} (TeV)	κ_i	$\sigma_{gg}^{\gamma\gamma h, \text{LO}}$ [ab]	$\sigma_{q\bar{q}}^{\gamma\gamma h, \text{LO}}$ [ab]	$\sigma_{q\bar{q}}^{\gamma\gamma h, \text{NLO}}$ [ab]
100	SM	222.4	1.4	2.2
	1.1	269.6 [21%]	1.4	2.2
	0.9	180.1 [-19%]		

Table 5.10: Effect of various anomalous couplings on $\gamma\gamma h$ production for the 100 TeV collider. $p_T^\gamma > 50$ GeV and $\Delta R_{\gamma\gamma} > 0.4$ have been imposed.

5.5 Conclusion

In this chapter, we have considered production of VVh ($\gamma\gamma h$, γZh , ZZh , and WWh) at proton-proton collider. Our main focus had been the gg fusion channel contribution, which occurs at NNLO in α_s . At 100 TeV, the cross sections for these processes via gg fusion channel range from 0.2 fb to 17 fb, $gg \rightarrow WWh$ being the dominant one among all. As the gg fusion channel contributes at NNLO in α_s , its contribution is found to be smaller than $q\bar{q}$ initiated channel contribution. We have compared the gg fusion channel contribution with the fixed order NLO QCD correction to $pp \rightarrow VVh$ in order to emphasize their relative importance. We find, at 100 TeV collider, the contribution of gg fusion channel to ZZh and WWh production is comparable to the fixed order QCD NLO correction to $q\bar{q}$ initiated channel. We have also studied production of γZh and $\gamma\gamma h$. The γZh production shows one interesting feature: with p_T cut on photon, $q\bar{q}$ initiated channel contribution decreases faster than the gg fusion channel contribution. For $\gamma\gamma h$ production, the gg fusion channel can be said to be only production channel, as the $b\bar{b}$ initiated channel contribution is negligibly small.

In addition to the SM results, effect of anomalous couplings for $t\bar{t}h$, VVh , $VVhh$, and hhh vertices have been studied in the kappa framework. A strong dependence on anomalous κ_t and κ_V could be seen in the gg fusion channel, if the Feynman diagrams of the process under consideration have the corresponding vertices. A 10% change in κ_t on the higher side can enhance the ZZh and WWh cross sections by 68% and 54% respectively. Similar change in κ_V enhances these cross sections by about 40%. The $q\bar{q}$ initiated channel, on

the other hand, depends mainly on κ_V and its 10% variation changes the cross section by 20%. Another distinction is that in the gg fusion channel anomalous κ_t and κ_V changes the shape of the distribution. But in the $q\bar{q}$ initiated channel where κ_V is present in every diagram linearly, the shape of the normalized distribution does not change as the differential cross section in every bin gets scaled by same factor, κ_V^2 . We did not see any large effect of anomalous trilinear Higgs boson coupling as it is present only in very small number of diagrams whose contribution is small for $gg \rightarrow ZZh$ and $gg \rightarrow WWh$ processes. The dependence of the $q\bar{q}$ initiated channel on this coupling is further smaller, owing to very small Yukawa coupling of light quarks with the Higgs boson.

Chapter 6

Phenomenology of Higgs Potential at Future Colliders

After the discovery of the Higgs boson, one of the next goals of the colliders is to measure self couplings of the Higgs boson. While the trilinear Higgs boson coupling is poorly constrained from analysis of data collected so far at LHC, no experimental study has yet been carried out for the more difficult quartic Higgs boson coupling. The absence of practically no reasonable experimental constraints on the Higgs boson self couplings, therefore, leave the shape of the Higgs potential undetermined. There are various new physics scenarios, such as elementary Higgs in SMEFT, Nambu-Goldstone Higgs, Coleman-Weinberg Higgs, Tadpole-induced Higgs, which give rise to Higgs potentials different from the SM one. We use double Higgs boson production to study these various models. We find the constraint that can be put in trilinear Higgs boson couplings in the various models, assuming certain accuracies in the cross section measurement. Next we use triple Higgs bosons production at the 100 TeV collider to put constraint on quartic Higgs boson coupling in these models, again assuming certain accuracies in the cross section measurement.

Contents

6.1	Various scenarios and relevant couplings	130
6.2	Double Higgs production	132
6.2.1	Cross Section and Distributions	133
6.2.2	Interference Effects	138
6.2.3	constraints on d_3 in various models	143
6.3	Triple Higgs production	145
6.3.1	Cross Section and Distributions	146
6.3.2	Interference Effects	152
6.3.3	Constraints on d_4 in various models	155
6.4	Conclusion	158

After the discovery of the Higgs boson, one of the major goals is to determine the shape of the Higgs potential. The SM Landau-Ginzburg potential is not the only Higgs potential proposed so far. There are various models which predict quite different Higgs potential, and till today these are valid models as although experimentally the parameters of those models have been constrained, the models themselves are still feasible. In this chapter, we consider various Higgs potential scenarios — namely, elementary Higgs boson in SMEFT, Nambu Goldstone boson, Coleman-Weinberg Higgs boson, and Tadpole induced Higgs boson.

At the colliders, trilinear and quartic Higgs boson couplings can be directly measured using hh and hhh production, respectively. So far the ATLAS and CMS collaborations have been able to put only very loose bound on the trilinear Higgs boson coupling. It will be quite challenging to tightly constraint the trilinear Higgs boson coupling even at the end of the High-Luminosity LHC (HL-LHC). To constraint it properly, one will need high energy colliders. To put direct constraint on the quartic Higgs boson coupling, we study hhh production. The production cross section for hhh is very small. As hhh production has not been investigated using data available at LHC, there is so far no experimental constraint available for the quartic Higgs boson coupling. Observing hhh production and, thereafter, constraining the quartic Higgs boson coupling to some reasonable degree will be difficult even at the 100 TeV collider.

The various Higgs potentials, $V(H)$, that we are going to consider have the following analytic structure¹:

¹ H denotes Higgs doublet, while h denotes physical Higgs boson.

Elementary Higgs :	$-m^2 H^\dagger H + \lambda (H^\dagger H)^2 + \frac{c_6 \lambda}{\Lambda^2} (H^\dagger H)^3,$
Nambu – Goldstone Higgs :	$-a \sin^2 \left(\frac{\sqrt{H^\dagger H}}{f} \right) + b \sin^4 \left(\frac{\sqrt{H^\dagger H}}{f} \right),$
Coleman – Weinberg Higgs :	$\lambda (H^\dagger H)^2 + \varepsilon (H^\dagger H)^2 \log \left(\frac{H^\dagger H}{\mu^2} \right),$
Tadpole – induced Higgs :	$-\kappa^3 \sqrt{H^\dagger H} + m^2 H^\dagger H,$

where f denotes the decay constant of the Nambu-Goldstone Higgs boson and μ denotes the renormalization scale in case EWSB is triggered by radiative corrections. m^2 , λ , c_6 , Λ , a , b , ε , κ are dimensionful or dimensionless parameters in one or other new physics scenarios.

We study these various scenarios using $gg \rightarrow hh$ and $gg \rightarrow hhh$ processes at the high luminosity LHC (HL-LHC), high energy LHC (HE-LHC), and 100 TeV hadron collider (FCC-hh). The $gg \rightarrow hh$ has been extensively studied in the literature for measuring trilinear Higgs boson coupling [183–202], for probing $t\bar{t}hh$ coupling in the EFT framework [203–205] and for studying many new physics scenarios [206–217]. In particular, the composite Higgs models using this channel have been studied in [215–217]. However, we take a more unified approach and consider a number of Higgs potential scenarios together. We examine interference between various diagrams which give us better understanding of behavior of cross sections and distributions with various parameters of these models. We find that different scenarios of Higgs potential can be distinguished via measuring cross section of hh production. We further consider the possibility of constraining the trilinear Higgs boson coupling in these scenarios, assuming certain accuracies for the measured cross section.

We also compute cross sections and distributions for the $gg \rightarrow hhh$ process in different Higgs potential scenarios. The process $gg \rightarrow hhh$ was studied in [143] including the scaling of SM Higgs boson couplings. It would not be easy to observe this process even at the FCC-hh. The role of triple Higgs bosons production is to determine the shape of the Higgs potential by measuring quartic Higgs boson coupling. We study various interference effects between the diagrams for $gg \rightarrow hhh$ process which helps us understand the dependence of these terms on various couplings, including quartic Higgs boson coupling. As the dependence of the cross section on the quartic Higgs boson coupling is too weak, it will be quite difficult to extract it. In the composite Higgs model, the presence of $t\bar{t}hhh$ coupling further complicates the extraction of it. Assuming that the triple Higgs bosons production cross section can be measured to a certain accuracy at the FCC-hh, we also obtain the possible bounds on quartic Higgs coupling and $t\bar{t}hhh$ coupling.

This chapter is organized as follows. In Sec. 6.1, we briefly discuss various scenarios for Higgs potentials. In Sec. 6.2, we use double Higgs production to study different Higgs potential scenarios and find the constraints on the trilinear Higgs boson coupling, assuming certain uncertainty in the cross section measurement. In Sec. 6.3, we investigate triple Higgs bosons production to probe quartic Higgs boson coupling and find the constraints on this coupling in the various models, again assuming certain uncertainty in the cross section measurement. Finally, in Sec. 6.4 we summarize our results.

6.1 Various scenarios and relevant couplings

As discussed in the introduction of this chapter, we consider four new physics scenarios — namely, the elementary Higgs in SMEFT, pseudo Nambu-Goldstone Higgs model, Coleman-Weinberg Higgs model and Tadpole Higgs model. The operators in SMEFT are constructed from SM field contents and respect the symmetries of the SM. The pseudo Nambu-Goldstone Higgs arises from strong dynamics at some high energy scale. In the Coleman-Weinberg Higgs model, electro-weak symmetry breaking is triggered by renormalization group running effects. In the tadpole induced Higgs, symmetry breaking is triggered by tadpole Higgs. We study the various scenarios in the general effective field theory framework, i.e., in HEFT, discussed in Sec. 2.3.

The most general Lagrangian, with the non-linearly realized symmetry can be written as

$$\begin{aligned} \mathcal{L} = & \frac{1}{2}(\partial_\mu h)^2 - V(h) + \frac{v^2}{4}\text{Tr}[(\partial_\mu U)^\dagger \partial^\mu U] \left(1 + 2a\frac{h}{v} + b\frac{h^2}{v^2} + \dots \right) \\ & - \frac{v}{\sqrt{2}}(\bar{t}_L, \bar{b}_L)U \left(1 + c_1\frac{h}{v} + c_2\frac{h^2}{v^2} + c_3\frac{h^3}{v^3} + \dots \right) \begin{pmatrix} y_t t_R \\ y_b b_R \end{pmatrix} + \text{h.c.} , \end{aligned} \quad (6.1)$$

where $V(h)$ is given by

$$V(h) = \frac{1}{2}m_h^2 h^2 + d_3 \left(\frac{m_h^2}{2v} \right) h^3 + d_4 \left(\frac{m_h^2}{8v^2} \right) h^4 + \dots \quad (6.2)$$

In this section, we collect all the relevant couplings for hh and hhh production for various BSM scenarios in Table. 6.1. For details about the Higgs potentials arising from

the various new physics scenarios, one is referred to the preprint [72], on which this chapter is based. Below we just describe some specific assumptions that we have used to derive these couplings in each of these scenarios:

- For the Elementary Higgs boson, we only include the O_6 operator of SMEFT, i.e., $(H^\dagger H)^3$, since all the other operators are (and will be further) constrained by precision Higgs boson coupling measurements. Here d_3 and d_4 are correlated as they both arise from the same operator, O_6 .
- For the Nambu-Goldstone Higgs scenarios, we consider only two specific benchmark models, MCH_{5+5} and CTH_{8+1} . The 5+5 denotes both right handed and left handed fermions transform under fundamental representation **5** of global $SO(5)$ symmetry, while 8+1 means left handed fermions transform under **8** and right handed ones are singlet of global $SO(8)$ symmetry. Values of non-linearity parameter, ξ , in these models has been constrained to less than 0.1 by the precision hVV couplings. For consistency, deviations of the other Higgs boson couplings caused by Higgs non-linearity effects have also been considered. But we neglect the contribution of composite states to Higgs boson couplings assuming all the composite particles are heavy enough. For more about these models one is referred to [73, 218–222].
- For the Coleman-Weinberg Higgs scenario [74, 223–226], except the Higgs boson self couplings d_3 and d_4 , we take all other Higgs boson couplings to be same as SM couplings, which can be achieved if extra scalar particles do not mix with the Higgs boson after EWSB. At one loop order, the Higgs boson self couplings are found to be $d_3 = \frac{5}{3}$ and $d_4 = \frac{11}{3}$.

- For the Tadpole-induced Higgs scenarios [75, 227], we approximate $d_3 = d_4 \approx 0$, as they can be highly suppressed, though their exact value would depend on the self couplings of the auxiliary scalar field.

	c_1	c_2	c_3	d_3	d_4
relevant couplings	$h\bar{t}t$	$hh\bar{t}t$	$hhh\bar{t}t$	hhh	$hhhh$
SM	1	0	0	1	1
SMEFT (with O_6)	1	0	0	$1 + c_6 \frac{v^2}{\Lambda^2}$	$1 + c_6 \frac{6v^2}{\Lambda^2}$
MCH ₅₊₅	$1 - \frac{3}{2}\xi$	-2ξ	$-\frac{2}{3}\xi$	$1 - \frac{3}{2}\xi$	$1 - \frac{25}{3}\xi$
CTH ₈₊₁	$1 - \frac{1}{2}\xi$	$-\frac{1}{2}\xi$	$-\frac{1}{6}\xi$	$1 - \frac{3}{2}\xi$	$1 - \frac{25}{3}\xi$
CW Higgs (doublet)	1	0	0	$\frac{5}{3}$	$\frac{11}{3}$
Tadpole-induced Higgs	$\simeq 1$	0	0	$\simeq 0$	$\simeq 0$

Table 6.1: Higgs boson couplings, defined in Eqs. (6.1) and (6.2), for the SM and different BSM scenarios. Here $\xi = \frac{v}{f}$, where f is the scale of the new physics.

6.2 Double Higgs production

In this section, we use the double-Higgs production to study different Higgs scenarios. At a high energy hadron collider, the gg fusion channel is the dominant production mechanism for double Higgs boson production. As different Higgs potential scenarios predict different trilinear couplings, hh production, being dependent on it, is capable of distinguishing these scenarios. This process has been widely considered in the literature for validating the SM cross section, measuring the Higgs trilinear coupling [183–199, 202] and the $t\bar{t}hh$ coupling [205], to discriminate various NP scenarios [183–199, 202] etc. However, it will not be seen at 5σ level even at the end of high luminosity phase of LHC if there is no new physics.

The ATLAS and CMS Collaborations have been looking for the hh signal in the data

collected so far at the LHC and have accordingly set upper limits on its production cross section [162–167]. Both collaborations have also examined the prospects of detecting hh signal at the high-luminosity LHC (HL-LHC) and the high-energy LHC (HE-LHC), respectively [228, 229]. At the HL-LHC, without (with) systemic uncertainty, the signal can be measured at 31% (40%) accuracy relative to the standard model prediction with the significance 3.5σ (3σ), and the trilinear Higgs boson coupling can be constrained in the range $-0.1 < \frac{\lambda}{\lambda_{SM}} < 2.7$ and $5.5 < \frac{\lambda}{\lambda_{SM}} < 6.9$ ($-0.4 < \frac{\lambda}{\lambda_{SM}} < 7.3$). At the HE-LHC (27 TeV with 15 ab^{-1} data), the signal can be measured at significance of 7.1σ and 11σ , without systematic uncertainty, in the $b\bar{b}\gamma\gamma$ and $b\bar{b}\tau\tau$ channels, respectively [229]. A number of the above studies have performed detailed background analysis with optimized cut-based efficiency or with multivariate techniques. However in this chapter, we do not intent to perform detailed signal-to-background analysis. Instead, we find new physics cross sections after primary cuts and find the constraints the can be put on the trilinear Higgs boson coupling in the different Higgs scenarios, assuming some benchmark uncertainties in the cross section measurement.

6.2.1 Cross Section and Distributions

In terms of parameters of HEFT as described in Eqs. (6.1) and (6.2), the total cross section for $gg \rightarrow hh$ can be written as

$$\sigma = c_1^4 \sigma_b^{\text{SM}} + c_1^2 d_3^2 \sigma_t^{\text{SM}} + c_1^3 d_3 \sigma_{bt}^{\text{SM}} + c_2^2 \sigma_{t\bar{t}hh} + c_1^2 c_2 \sigma_{b,\bar{t}hh} + c_1 d_3 c_2 \sigma_{t,\bar{t}hh}, \quad (6.3)$$

where we have six pieces of form factors: the first three pieces are from the box contribution (σ_b^{SM}), the triangle contribution (σ_t^{SM}), and the interference of them (σ_{bt}^{SM}) for the SM-like diagrams, respectively, and the rest come from the new triangle contribution ($\sigma_{t\bar{t}hh}$), the interference of new triangle with the SM-like box ($\sigma_{b,t\bar{t}hh}$), the interference of new triangle with the SM-like triangle ($\sigma_{t,t\bar{t}hh}$). A representative set of diagrams for $gg \rightarrow hh$ production are given in the Fig. 6.1.

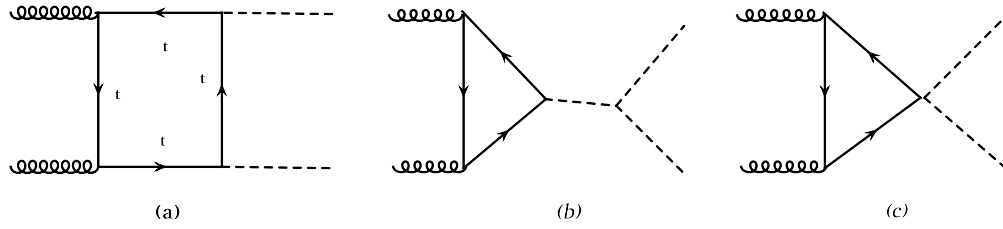


Figure 6.1: Different classes of diagrams for the hh production via gg fusion channel. The third diagram occurs in models having $t\bar{t}hh$ vertex.

Methodology of the computation is same as discussed in the previous two chapters. We use leading order CTEQ parton distribution functions, CT14llo [182], and renormalization/factorization scale as $\sqrt{\hat{s}}$. Numerical value for each form factor is listed in Table 6.2 for the 14, 27, and 100 TeV proton-proton colliders. To suppress the large QCD background, one needs to apply a large cut on the transverse momentum (p_T) of the Higgs boson. Therefore, the table also includes the cross sections with cut $p_T^h > 70$ GeV. No further kinematic cuts are considered here, as we are not doing detailed signal-to-background study. As we see from Table 6.2, there is some interesting interference pattern between different classes of diagrams. This pattern can help us to understand the dependence of cross sections and distributions on various couplings. This will be discussed in more detail in the next section. All these results are from leading order diagrams. The NLO QCD corrections are large and can increase the cross section by about a factor of 1.7 [1]. However,

our numerical results in this section do not include this factor.

Collider	p_T^h	σ_b^{SM}	σ_t^{SM}	σ_{bt}^{SM}	$\sigma_{b,\bar{t}hh}$	$\sigma_{t,\bar{t}hh}$	$\sigma_{\bar{t}hh}$
14 TeV	no cut	36.1	4.9	-23.8	-147.0	48.9	175.8
	$p_T^h > 70 \text{ GeV}$	29.6	2.9	-17.1	-122.4	36.3	151.9
27 TeV	no cut	149.2	18.9	-94.5	-618.9	197.92	777.0
	$p_T^h > 70 \text{ GeV}$	124.1	11.6	-69.6	-524.5	151.1	684.5
100 TeV	no cut	1607.6	184.3	-961.8	-6872	2077.3	9356
	$p_T^h > 70 \text{ GeV}$	1370	118.8	-732	-5970	1645	8464

Table 6.2: Form factors as defined in Eq. (6.3) at the 14 TeV, 27 TeV, and 100 TeV proton-proton colliders.

The cross sections for 14 TeV, 27 TeV, and 100 TeV colliders can be easily obtained for all the models we are considering using Table. 6.1, Eq. 6.3, and Table 6.2. For the 14 TeV collider, the SM cross section for no cut and $p_T^h > 70 \text{ GeV}$ are 17.2 fb and 15.4 fb, respectively. The corresponding values for the 27 TeV collider are 73.6 fb and 66.2 fb, respectively, which are about 4-5 times 14 TeV value. The cross sections at 100 TeV collider are 830.1 fb and 756.8 fb, respectively, which are about 50 times the corresponding quantity at 14 TeV collider. For the new physics scenarios, in what follows we will write the cross section at 27 TeV collider only. At this collider, for no cut the cross sections for Tadpole-induced Higgs model and Coleman-Weinberg model are 149.2 fb and 124.1 fb, respectively, while with $p_T^h > 70 \text{ GeV}$ they are 44.2 fb and 40.3 fb, respectively. For the $\xi = 0.05$ benchmark value, for no cut the cross section for the MCH and CTH models are 97.7 fb and 79.9 fb, respectively, while with $p_T^h > 70 \text{ GeV}$ they are 87.2 fb and 71.5 fb, respectively. For the cross sections for these models at the 14 TeV and 100 TeV colliders, one can use Table. 6.1, Eq. 6.3, and Table 6.2.

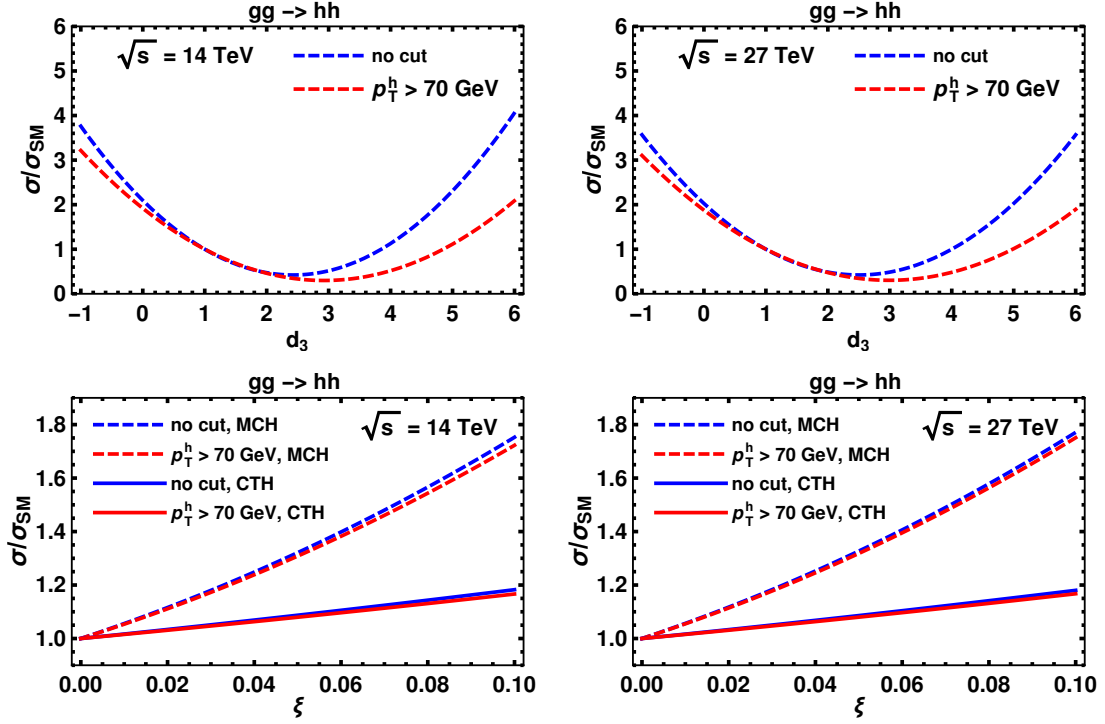


Figure 6.2: Variation of the ratio of the new-physics cross section to that of the SM for hh production with respect to the trilinear Higgs boson coupling d_3 as in the fundamental Higgs, Coleman-Weinberg Higgs and Tadpole-induced Higgs scenarios (upper row), and with respect to the parameter ξ in Nambu-Goldstone Higgs scenario (lower row).

In Fig. 6.2, we display the ratio of the new physics cross section to the SM value in various Higgs potential scenarios at the 14 TeV LHC and the 27 TeV HE-LHC, respectively. In the top row of Fig. 6.2, we see that the ratio of the cross sections increases for negative values and large positive values of d_3 . The reason for this feature of this plot will be explained in the next subsection. The bottom row of the figure displays the ratio as a function of the parameter ξ of Nambu-Goldstone Higgs scenario. While in the case of the MCH model, the cross section ratio increases rapidly with increasing ξ , for CTH model the increase is rather slow. These behaviors remain almost same for $p_T^h > 70$ GeV cut as well. The behavior of the cross section ratio in these models can be understood on the basis of

interference pattern, as to be explained in the next section. In Fig. 6.3, this ratio is plotted in a 2-d plot as a function of c_2 and d_3 couplings. In this figure, the ratios for the SM Higgs, Coleman-Weinberg Higgs, and Tadpole-induced Higgs scenarios are marked.

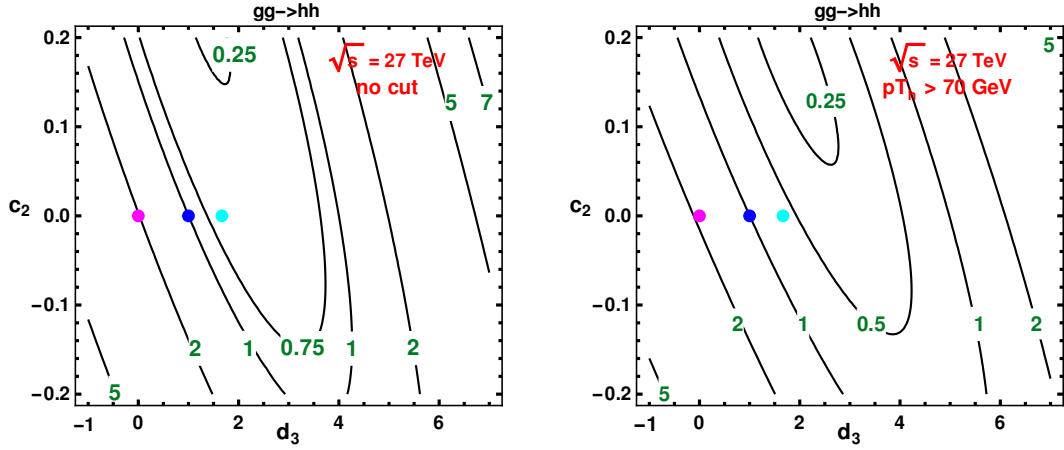


Figure 6.3: Cross section ratio σ/σ_{SM} as a function of c_2 and d_3 ; (a) without any cut, and (b) with the only kinematic cut $p_T^h > 70$ GeV. The standard model cross sections, at the 27 TeV HE-LHC collider, for the above mentioned two cuts are 73.6 fb and 66.2 fb, respectively. For no cut the cross sections for Tadpole-induced Higgs model and Coleman-Weinberg model are 149.2 fb and 124.1 fb, respectively, while with $p_T^h > 70$ GeV they are 44.2 fb and 40.3 fb, respectively. The magenta, blue, and cyan dots denote the ratios for Tadpole-induced Higgs model, the SM, and Coleman-Weinberg model, respectively.

In Fig. 6.4, we display the normalized distribution for invariant mass $M(hh)$ and p_T^h at the 14 TeV LHC and the 27 TeV HE-LHC. These distributions play role in determining suitable kinematic cuts to reduce the backgrounds. The upper row of Fig. 6.4 shows the normalized $M(hh)$ distribution with a range of values of d_3 . The case of $d_3 = 3$ shows an interesting two-peak structure in the normalized $M(hh)$ distribution, arising from the competition between the contributions of triangle and box diagrams. We will come back to this discussion in the next subsection, around Fig. 6.5.

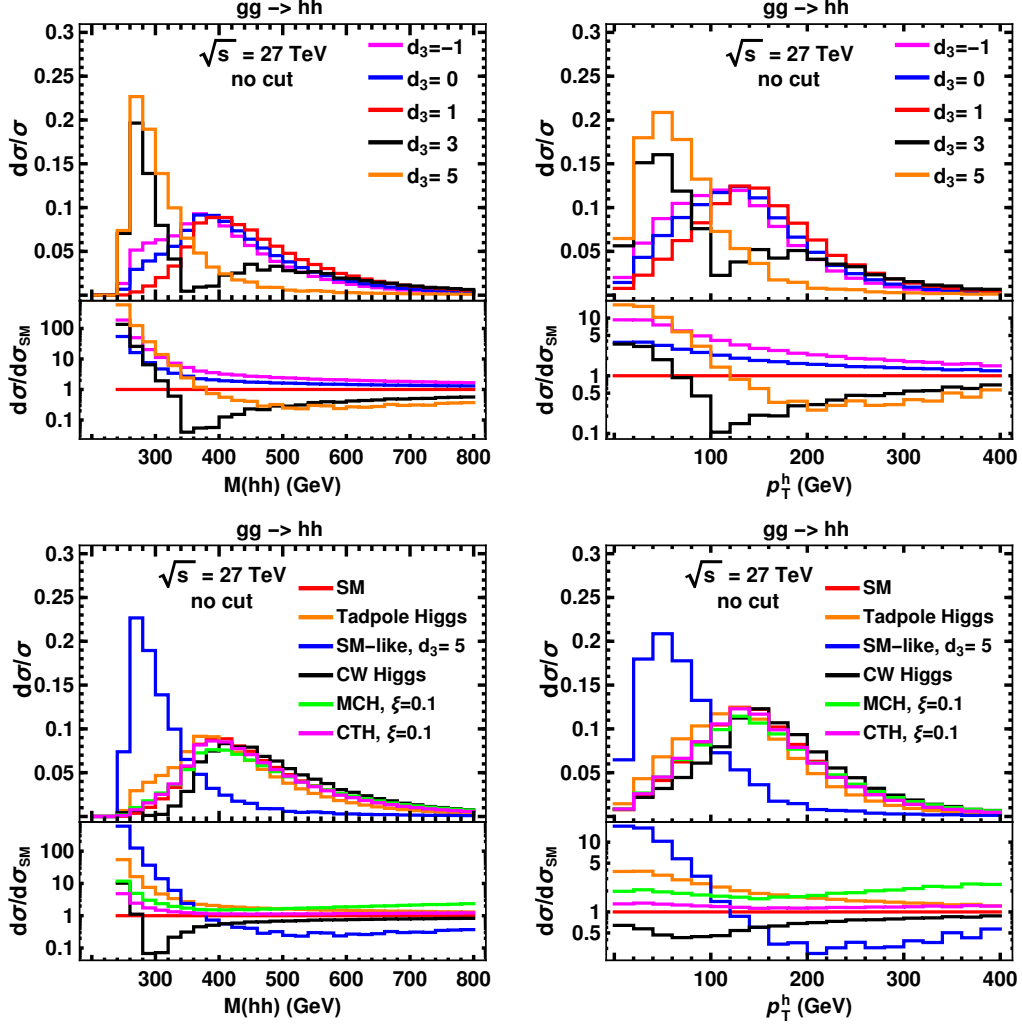


Figure 6.4: Normalized distributions for hh production via gg fusion channel against par-tonic center of mass energy and p_T of either Higgs. The case of $d_3 = 3$ shows an interesting feature, caused by the competition between the triangle and box diagram contributions, as explained in the text, around Fig. 6.5.

6.2.2 Interference Effects

As shown in Fig. 6.1, the trilinear Higgs boson coupling is present only in triangle diagrams. But as the box and triangle diagrams interfere, the trilinear Higgs boson coupling's contribution to the cross section depends also on the box amplitude, and the interference is destructive. In the Table 6.2, we observe that for the SM couplings, $d_3 = 1$, the pure box

contribution is large, the pure triangle contribution is small, and the interference contribution is large and negative, i.e. destructive. This leads to the small total cross section of $pp \rightarrow hh$. Some of the new Higgs potential scenarios would allow large deviations of the Higgs boson couplings, and the cross section and distributions will change significantly. Moreover², the Nambu-Goldstone Higgs scenario also predicts non-zero $t\bar{t}hh$ coupling due to Higgs non-linearity, and there is correlation between the $t\bar{t}hh$ and $t\bar{t}h$ couplings [230]. Because of this new $t\bar{t}hh$ interaction, two new triangle diagrams appear. These diagrams interfere with the triangle diagram containing trilinear Higgs boson coupling destructively, and with box diagram constructively. This happens as in this scenario the $t\bar{t}hh$ coupling has a negative sign relative to $t\bar{t}h$ coupling (see Table. 6.1).

Interference effects without $t\bar{t}hh$

Let us first consider scenarios without the $t\bar{t}hh$ vertex. As can be seen from Eq. (6.3), the pure triangle contribution depends quadratically and the interference term depends linearly on d_3 . However, the pure box contribution does not depend on d_3 . For the negative d_3 , the cross section keeps on increasing with increasing magnitude of d_3 , cf. Fig. 6.2, as both σ_t^{SM} and σ_{bt}^{SM} contributions increase. For positive d_3 , however, the cross section first decreases and then keeps on increasing after reaching some threshold value of d_3 , as first σ_{bt}^{SM} dominates which decreases the cross section, then σ_t^{SM} dominates which increases the cross section. This explains the feature found in the upper row of Fig. 6.2.

²In elementary Higgs scenario, $t\bar{t}hh$ can also be induced via integrating out heavy particles. Here for simplicity, we take the $t\bar{t}h$ coupling and the hVV to be same as the SM ones, which eliminates the $t\bar{t}hh$ coupling.

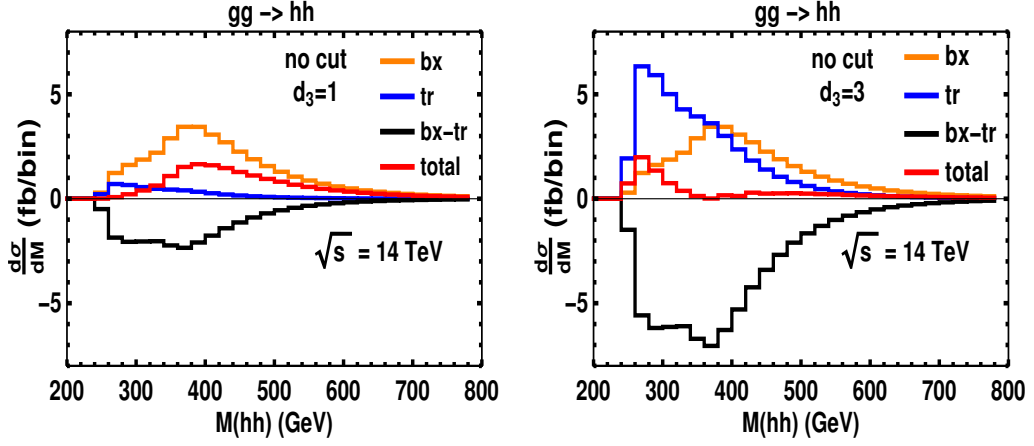


Figure 6.5: Contribution of various classes of diagrams and their interference to the $M(hh)$ distribution of hh production for $d_3 = 1$ and $d_3 = 3$. The triangle diagrams contribution and interference (negative) term get scaled by 9 and 3, respectively, when we go to $d_3 = 3$ from $d_3 = 1$. However, as “bx” does not depend on d_3 , it remains the same. The peak of the total distribution gets shifted to left with increase in d_3 as the triangle diagram, being a s-channel one, contributes significantly near the threshold of hh production.

To understand the feature found in Fig. 6.4, let us examine the contribution from each class of Feynman diagrams and their interference to the $M(hh)$ distribution. As shown in Fig. 6.5, the triangle diagram mostly contributes near the Higgs pair threshold, while the box diagram mainly contributes to the threshold of the top pair system. As d_3 increases, the contribution of the triangle diagram to the $M(hh)$ and P_T^h distributions increases and eventually exceeds the box diagram when d_3 becomes very large. For $d_3 = 3$, both the triangle and box diagrams are sizeable, which, together with their interference effect, result in the two peaks in the $M(hh)$ and P_T^h distributions. Moreover, as we increase the minimum cut of the p_T variable of the Higgs boson, which is to suppress large QCD background further, the relative contribution of the pure triangle diagrams decreases more than the interference and the pure box term, which can be seen in Table 6.2. In particular, with the $p_T^h > 70$ GeV cut on the final state Higgs bosons within the SM, the pure triangle contribution decreases

by a factor of around 1.7, the magnitude of interference term by 1.4, and the pure box term by 1.2. This explains why, in Fig. 6.2, the minimum of the curves, where the pure triangle contribution starts to dominate over interference term, shifts to the right with increase in p_T^h cut. For the SM, since the triangle contribution is small, the reduction in the total cross section is not that significant with the increase in the minimum p_T^h , and the total contribution decreases by a factor of 1.1 only. However, for larger positive d_3 values, because of the cut, the pure triangle contribution cannot dominate over the negative interference as much as it used to do before applying the cut. Thus for a large d_3 value, imposition of some minimum p_T^h reduces the associated cross section by some factor which is more than that for the SM case. For instance, for $d_3 = 10$, the total cross section is 288.9 fb with no p_T cut; it reduces to 150.8 fb when a $p_T > 70$ GeV cut is applied, i.e. a reduction by a factor of 1.9, whereas in the SM this factor is only 1.1. The cross section for any d_3 , before and after cuts, can easily be obtained from Table 6.2.

At the 14 TeV HL-LHC, the number of events for double-Higgs production is not large. Thus, in the case of the most promising final state signature ‘ $b\bar{b}\gamma\gamma$ ’, one can only have few tens of events, which only put very loose constraints on d_3 . Nevertheless, the cross sections at the 27 TeV HE-LHC are about 5 – 6 times larger than that at the LHC. Therefore, even for the rare decay signature of ‘ $b\bar{b}\gamma\gamma$ ’, one could have significant bound, and d_3 value can be determined within around 20% [229]. At this 27 TeV machine, there is a distinct possibility of distinguishing different Higgs potential models.

Interference effects with $t\bar{t}hh$

In the MCH and CTH models of Nambu-Goldstone Higgs scenario, in addition to the appearance of new $t\bar{t}hh$ vertex, the existing vertices involving Higgs boson (in the SM), namely $t\bar{t}h$ and $h hh$, also get modified, as can be seen in Table 6.1. In Ref. [230], a global fit on the MCH and CTH parameters was performed by using the available data from the LHC Run-2 phase. The 95% CL limit on ξ is obtained to be $\xi < 0.1$ for the MCH5 model. In our study, we will vary ξ up to 0.1.

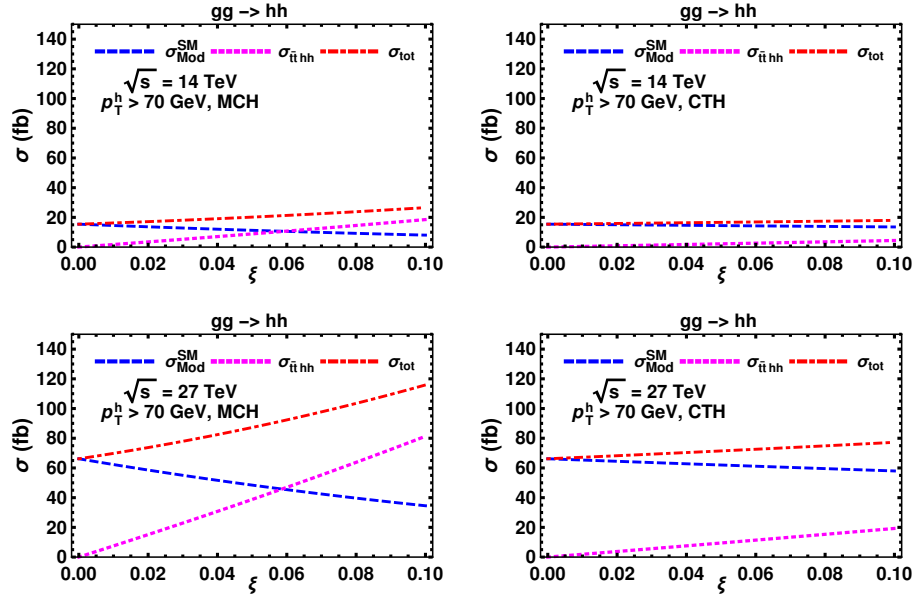


Figure 6.6: Variation of different pieces of Eq. 6.3 with ξ in MCH and CTH models at 14 TeV collider. The Magenta line (which shows the effect of $t\bar{t}hh$) crosses the blue line (which shows the effect of $t\bar{t}h$ and $h hh$ coupling) around $\xi = 0.06$.

Fig. 6.2 shows the variation of the cross section with the parameter ξ . The rate of increase of the cross section in the MCH model is significantly larger than the CTH model. In both models, trilinear Higgs coupling is the same because of the universal form of the Higgs potential, but the $t\bar{t}h$ and $t\bar{t}hh$ couplings are different due to different fermion em-

beddings. From Table 6.2, we see that in the MCH model, the value of $(\sigma_{b,t\bar{t}hh} - \sigma_{t,t\bar{t}hh})$ is larger by a factor of four than that in the CTH model. Also, the value of $\sigma_{t\bar{t}hh}$ in MCH model is larger by a factor of 16 than in the CTH model. This term does not contribute much when ξ is as small as 0.01 because of the ξ^2 scaling. It contributes significantly for $\xi = 0.1$ in the MCH model, while its contribution is still small in the CTH model. This explains the difference in the rate of increase of the cross section in the MCH model and the CTH model. Another feature found in Fig. 6.2 is that the rate of increase of the cross sections of the MCH and CTH models does not change noticeably with the p_T^h cut. Next, in Fig. 6.6, we show the importance of the $t\bar{t}hh$ coupling for increasing the cross section as a function of ξ . As the ξ increases, even though the contribution of the SM-like diagrams decreases, the total cross section increases due to the dominance of the $t\bar{t}hh$ contribution, most noticeably in the MCH model.

6.2.3 constraints on d_3 in various models

In this subsection, we study the possible constraints on the trilinear Higgs boson couplings in different models. We have considered two benchmark values of 1σ uncertainties in the cross section measurement — 10% and 20%. In Fig. 6.7, for these two benchmark uncertainties in the cross section measurement, we show the constraints that can be put on d_3 for $d_3 = 1$, $d_3 = 2$, and $d_3 = \frac{5}{3}$ (CW Higgs model). We find for $d_3 = 1$ and $d_3 = 2$ the range to be $0.86 < \tilde{d}_3/d_3 < 1.15 \cup 4.83 < \tilde{d}_3/d_3 < 5.12$ ($0.73 < \tilde{d}_3/d_3 < 1.31 \cup 4.67 < \tilde{d}_3/d_3 < 5.25$) and $0.94 < \tilde{d}_3/d_3 < 1.07 \cup 1.92 < \tilde{d}_3/d_3 < 2.06$ ($0.88 < \tilde{d}_3/d_3 < 1.16 \cup 1.83 < \tilde{d}_3/d_3 < 2.11$) if the accuracy is 10% (20%), respectively.

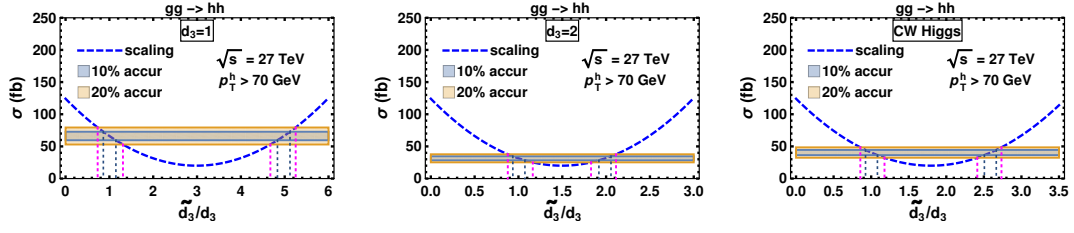


Figure 6.7: Constraints on the scaling \tilde{d}_3/d_3 if the cross section can be measured up to 10% and 20% accuracy, respectively. Here, \tilde{d}_3 denotes the scaled d_3 value.

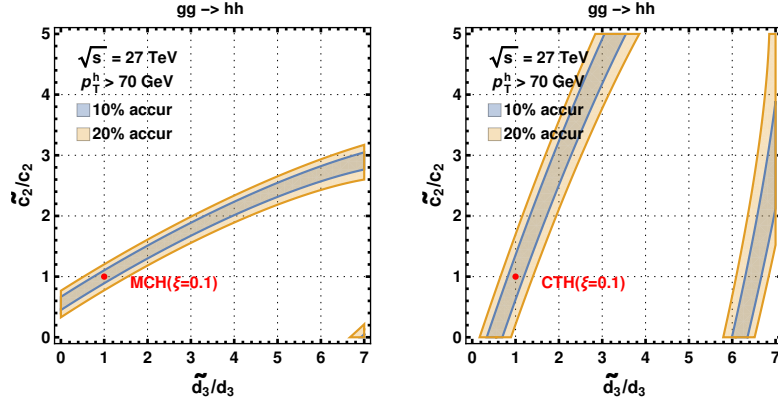


Figure 6.8: Constraints on \tilde{c}_2/c_2 and \tilde{d}_3/d_3 if the cross section can be measured up to 10% and 20% accuracy, respectively, in the MCH and CTH models. Here, \tilde{c}_2 and \tilde{d}_3 denote the scaled c_2 and d_3 values, respectively.

In Fig. 6.8, at the 27 TeV HE-LHC, assuming the 1σ accuracy is 10% and 20% we show the parameter space of general effective couplings c_2 and d_3 (with fixed c_1) that can be constrained by the double-Higgs production. The scaling factors of the trilinear Higgs boson coupling and the contact $t\bar{t}hh$ coupling are denoted as the ratio \tilde{d}_3/d_3 and \tilde{c}_2/c_2 , respectively. Compared to the MCH model, the constrained regions in the CTH model are steeper. This happens as with the scaling of c_2 , the cross section change in CTH model is slower than in MCH model, since c_2 in CTH model is smaller than that in the MCH model, cf. Table. 6.1. Overall, we see that the 27 TeV HE-LHC can already set strict bounds on these Higgs boson couplings.

6.3 Triple Higgs production

In this section, we investigate the possibility to measure the quartic Higgs boson coupling, d_4 , in various scenarios by using $gg \rightarrow hhh$ process. This process can help in a better understanding of the shape of the Higgs potential.

As discussed in the literature [143–148, 231, 232], measuring the quartic Higgs boson coupling in the triple Higgs bosons production channel is not easy even at the 100 TeV hadron collider. This is because the signal of triple Higgs bosons production $pp \rightarrow hhh$ is too small in comparison to its backgrounds. Even worse, the contribution of the quartic Higgs boson coupling is over-shadowed by other couplings. This is because, the quartic Higgs boson coupling appears in a very few diagrams which make very small contribution to the total cross section. The quartic Higgs boson coupling can be constrained only in the ranges of $[-20, 30]$ (at the 2σ CL) by triple Higgs bosons production at the 100 TeV hadron collider with 30 ab^{-1} integrated luminosity [231]. In another approach, there have been attempts to measure trilinear and quartic Higgs boson couplings indirectly using higher order loop corrections [197, 233, 234]. These indirect searches put quite loose bound on the quartic Higgs boson coupling at future colliders, such as the double Higgs production at the future linear collider (ILC). A partial list of other related studies is included as Refs. [235–237].

At the hadron colliders with increase in center-of-mass energy, gluon flux increases. We calculate $gg \rightarrow hhh$ cross sections with general parametrization of new physics effects in different scenarios at 100 TeV collider. We consider five scenarios: Independent scaling

of SM trilinear and quartic Higgs boson couplings, the SMEFT models with correlated trilinear and quartic Higgs boson coupling, the Nambu-Goldstone Higgs, Coleman-Weinberg Higgs and Tadpole-induced Higgs models. We shall first compute and discuss cross sections and distributions in these models, then we estimate how well the quartic Higgs boson coupling can be measured, assuming other couplings are already determined by other experiments. It is expected that one could determine the $t\bar{t}h$ coupling, trilinear Higgs boson coupling, and $t\bar{t}hh$ coupling more precisely before measuring the quartic Higgs boson coupling.

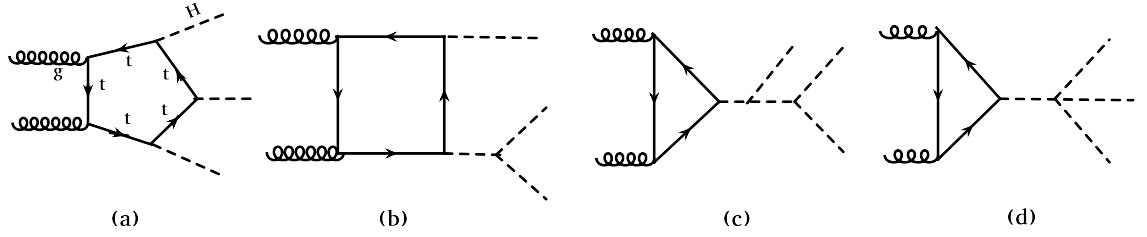


Figure 6.9: Different classes of diagrams for hhh production in the SM.

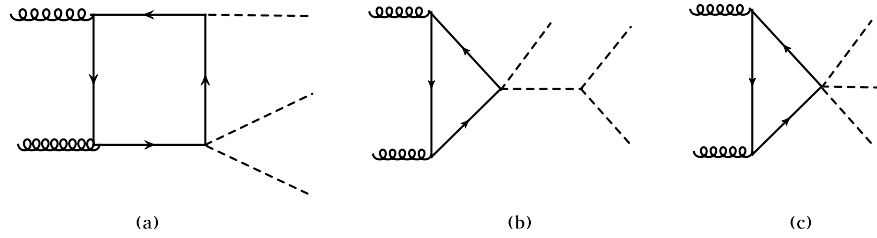


Figure 6.10: New diagrams for hhh production in the presence of $t\bar{t}hh$ and $t\bar{t}hhh$ vertices.

6.3.1 Cross Section and Distributions

As shown in Fig. 6.9, there are several basic classes of Feynman diagrams contributing to the process $gg \rightarrow hhh$, i.e. the pentagon class diagrams, box class diagrams, and triangle

class diagrams. In the pentagon class diagrams, there is no Higgs boson self coupling; the main coupling is $t\bar{t}h$ coupling. In the box class diagrams, trilinear Higgs boson coupling plays the major role. Only the triangle class diagrams have dependence on both the trilinear and quartic Higgs boson couplings. However, only few triangle diagrams depend on the quartic Higgs boson coupling³. Besides, the relative contribution of the triangle class diagrams is comparatively small. Because of this, the process $gg \rightarrow hhh$ is only moderately sensitive to quartic Higgs boson coupling. The cross section could change significantly only with large modification in the quartic Higgs boson coupling. However, for some specific range of trilinear Higgs boson coupling, the cross section can vary substantially with quartic Higgs boson coupling.

Furthermore, as shown in Fig. 6.10, several new diagrams would appear if additional $t\bar{t}hh$ and $t\bar{t}hhh$ couplings are non-zero. This scenario is realized explicitly, e.g. in the Nambu-Goldstone Higgs case, because of the Higgs non-linearity. In these scenarios, there is strong connection between the $t\bar{t}h$ coupling with $t\bar{t}hh$ and $t\bar{t}hhh$ couplings. As we will see, for the nonlinear parameter of $\xi \sim 0.1$, the diagrams with $t\bar{t}hh$ and $t\bar{t}hhh$ couplings make very large contribution, which renders it more complicated to extract out the quartic Higgs boson coupling.

In the process of $pp \rightarrow hhh$, there is strong destructive interference between different classes of diagrams. Interference between pentagon, box, and triangle diagrams plays a crucial role in dictating the cross section and distributions. Before we discuss the interference pattern and the extraction of quartic Higgs boson coupling, we first obtain the contribution

³To be specific, for each quark flavor in the loop, there are 24 pentagon class diagrams, 18 box class diagrams, and 8 triangle class diagrams. Out of these 50 diagrams, only two triangle diagrams have dependence on quartic Higgs boson coupling.

of each class of diagrams and their interferences to the total cross section. To be specific, the total cross section is

$$\begin{aligned}
\sigma = & c_1^6 \sigma_p^{\text{SM}} + c_1^4 d_3^2 \sigma_b^{\text{SM}} + c_1^2 d_3^4 \sigma_{3t}^{\text{SM}} + c_1^2 d_4^2 \sigma_{4t}^{\text{SM}} + c_1^5 d_3 \sigma_{p,b}^{\text{SM}} + c_1^4 d_3^2 \sigma_{p,3t}^{\text{SM}} + c_1^4 d_4 \sigma_{p,4t}^{\text{SM}} + \\
& c_1^3 d_3^3 \sigma_{b,3t}^{\text{SM}} + c_1^3 d_3 d_4 \sigma_{b,4t}^{\text{SM}} + c_1^2 d_3^2 d_4 \sigma_{3t,4t}^{\text{SM}} \\
& + \left(c_1^4 c_2 \sigma_{p,b-2t2h} + c_1^3 d_3 c_2 \sigma_{b,b-2t2h} + c_1^2 d_3^2 c_2 \sigma_{3t,b-2t2h} + c_1^2 d_4 c_2 \sigma_{4t,b-2t2h} + c_1^2 c_2^2 \sigma_{b-2t2h} + \right. \\
& c_1^3 c_2 d_3 \sigma_{p,t-2t2h} + c_1^2 c_2 d_3^2 \sigma_{b,t-2t2h} + c_1 c_2 d_3^3 \sigma_{3t,t-2t2h} + \\
& c_1 c_2 d_3 d_4 \sigma_{4t,t-2t2h} + c_1 c_2^2 d_3 \sigma_{b-2t2h,t-2t2h} + c_2^2 d_3^2 \sigma_{t-2t2h} \left. \right) \\
& + \left(c_1^3 c_3 \sigma_{p,t-2t3h} + c_1^2 d_3 c_3 \sigma_{b,t-2t3h} + c_1 d_3^2 c_3 \sigma_{3t,t-2t3h} + \right. \\
& c_1 d_4 c_3 \sigma_{4t,t-2t3h} + c_1 c_2 c_3 \sigma_{b-2t2h,t-2t3h} + c_2 d_3 c_3 \sigma_{t-2t2h,t-2t3h} + c_3^2 \sigma_{t-2t3h} \left. \right) , \tag{6.4}
\end{aligned}$$

where individual contributions of the diagrams are separated, and one can explicitly read off their dependence on Higgs boson couplings.

Parts	p_T^h		Parts	p_T^h		Parts	p_T^h	
	no_cut	> 70GeV		no_cut	> 70GeV		no_cut	> 70GeV
σ_p^{SM}	7777	3526	$\sigma_{p,b-2t2h}$	-41310	-20509	$\sigma_{p,t-2t3h}$	-9702	-13422
σ_b^{SM}	4113	1542	$\sigma_{b,b-2t2h}$	39685	19693	$\sigma_{b,t-2t3h}$	-35207	-19578
σ_{3t}^{SM}	92.2	26.0	$\sigma_{3t,b-2t2h}$	-3960	-1558	$\sigma_{3t,t-2t3h}$	5829	3034
σ_{4t}^{SM}	46.57	22.52	$\sigma_{4t,b-2t2h}$	-3164	-1628	$\sigma_{4t,t-2t3h}$	6131	4067
$\sigma_{p,b}^{\text{SM}}$	-8026	-2873	σ_{b-2t2h}	130729	85499	$\sigma_{b-2t2h,t-2t3h}$	-228538	-159601
$\sigma_{p,3t}^{\text{SM}}$	381.5	7.5	$\sigma_{p,t-2t2h}$	1363	-1719	$\sigma_{t-2t2h,t-2t3h}$	148590	104409
$\sigma_{p,4t}^{\text{SM}}$	133.5	-49.5	$\sigma_{b,t-2t2h}$	-13626	-5906	σ_{t-2t3h}	443606	377483
$\sigma_{b,3t}^{\text{SM}}$	-985	-298	$\sigma_{3t,t-2t2h}$	2412	976			
$\sigma_{b,4t}^{\text{SM}}$	-673.3	-266	$\sigma_{4t,t-2t2h}$	1943	1011			
$\sigma_{3t,4t}^{\text{SM}}$	121.5	45.0	$\sigma_{b-2t2h,t-2t2h}$	-66447	-36259			
			σ_{t-2t2h}	21774	12329			

Table 6.3: Numerical values of various terms of Eq. 6.4 at the 100 TeV hadron collider.

We carry out the calculation in the same way discussed for the previous processes. Here we do not include the higher order QCD correction, which may lead to a K-factor (the ratio of higher order to LO cross section) of about 2 [2]. Due to the extremely small cross section

of this process ⁴ and the large QCD backgrounds, we only present results at the 100 TeV hadron collider. Basic p_T cuts are also implemented for each Higgs boson in the final state.

At the 100 TeV collider, the SM cross sections for no cut and $p_T > 70$ GeV cut are 2987 ab and 1710 ab, respectively. For easy comparison, we summarize the total cross sections of double and triple Higgs bosons productions for the SM in Fig. 6.11 at the 14 TeV LHC, the 27 TeV HE-LHC and the 100 TeV hadron collider.

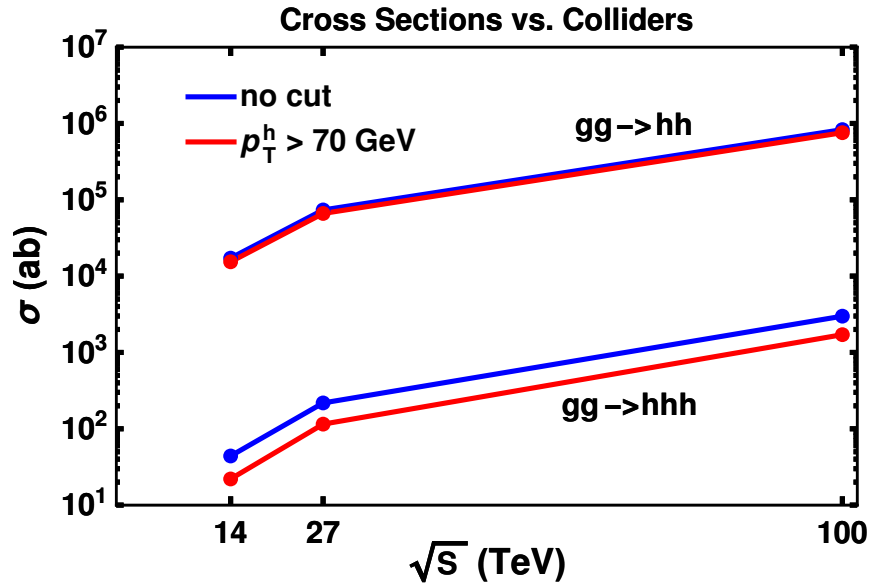


Figure 6.11: We summarize the total cross sections of the $pp \rightarrow hh$ and $pp \rightarrow hhh$ for the SM at the 14 TeV LHC, the 27 TeV HE-LHC and the 100 TeV hadron collider, respectively. The blue lines denote the cross sections without cut, and the red lines denote the ones with rudimentary cuts. Here we do not include the QCD K factors, which are known as around 1.7 [1] for $pp \rightarrow hh$ and around 2 [2] for $pp \rightarrow hhh$, respectively.

At the 100 TeV collider, for no cut the cross sections for Tadpole-induced Higgs model and Coleman-Weinberg model are 7796 ab and 1272 ab, while with $p_T^h > 70$ GeV they are

⁴To be specific, the total cross section is about 44 ab at the 14 TeV LHC, and is only about 218 ab at the 27 TeV HE-LHC, respectively.

3579 ab and 836 ab, respectively. For the $\xi = 0.05$ benchmark value, for no cut the cross section for the MCH and CTH models are 5033 ab and 3479 ab, while with $p_T^h > 70$ GeV they are 3302 ab and 2057 ab, respectively.

Based on these numerical values, we display the cross sections in the (d_3, d_4) parameter plane in Fig. 6.12 and the ξ dependence in Fig. 6.13, for different new physics scenarios, with or without including the contact $t\bar{t}hh$ and $t\bar{t}hhhh$ couplings. Fig. 6.12 shows the total cross section σ as a function of the trilinear and quartic Higgs boson couplings, i.e. d_3 and d_4 . We see there is significant increase in the cross section for zero or negative d_3 . This is because, then the largest negative interference term between box and pentagon diagrams $\sigma_{p,b}^{\text{SM}}$, either vanishes or becomes positive. There is only marginal increase in the cross section for zero or negative value of d_4 . In this figure, we also mark the SM, the Coleman-Weinberg Higgs scenario, the Tadpole-induced Higgs scenario by blue, cyan, and magenta dots, respectively. However, since the Pseudo-Goldstone boson models has additional $t\bar{t}hh$ and $t\bar{t}hhhh$ couplings, and also different $t\bar{t}h$ coupling than the SM one, they cannot be marked in this figure. The orange line denotes the SMEFT, which considers nonzero $O_6 \sim (H^\dagger H)^3$ operator besides the SM operators. The pseudo Nambu-Goldstone Higgs boson scenario is presented in Fig. 6.13, where all the Higgs boson couplings, and so the cross section, depend on the nonlinear parameter ξ . To be concrete, we consider two specific models, i.e. MCH and CTH models, and results are shown in Fig. 6.13. Compared to MCH, the cross section of the CTH remains close to the SM prediction (for the case of $\xi = 0$).

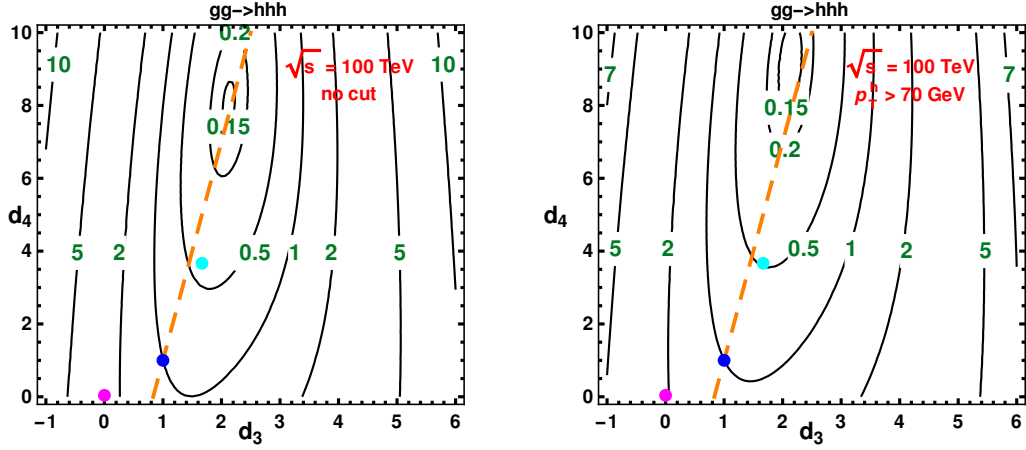


Figure 6.12: Cross section ratio σ/σ_{SM} for the scaling of trilinear and quartic Higgs boson couplings for various cuts. At the 100 TeV collider, the standard model cross section for no-cut and $p_T > 70$ GeV cut are 2987 ab and 1710 ab, respectively. The blue, cyan, and magenta dots denote the SM, CW Higgs and Tadpole-induced Higgs model, respectively. The orange dashed line denotes the SMEFT (with non-vanishing O_6) for d_3 in the range of $[5/6, 2.5]$.

To complete the discussion in this section, we present several basic distributions. In Fig. 6.14, we show the invariant mass, $M(hhh)$, distribution for various d_3 and d_4 values, and the normalized plots to examine the modification of the shape of the distributions. We observe contrasting behavior near the threshold of triple Higgs bosons production. Near threshold, in the case of negative and zero value of d_3 , there is increase in the cross section, while it decreases for positive values of d_3 . The behavior is opposite in the case of d_4 . Most of the increase is for smaller values of the invariant mass of triple Higgs bosons system, up to about 700 GeV, and it is near the threshold where the triangle diagram with quartic Higgs boson coupling is important.

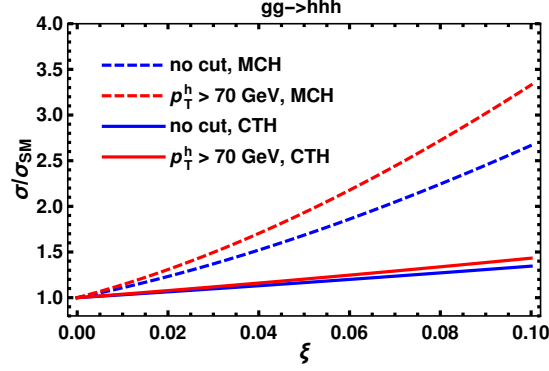


Figure 6.13: Cross section ratio with parameter ξ in the Minimal Composite Higgs (MCH) and Composite Twin Higgs (CTH) Models at the 100 TeV collider (FCC-hh).

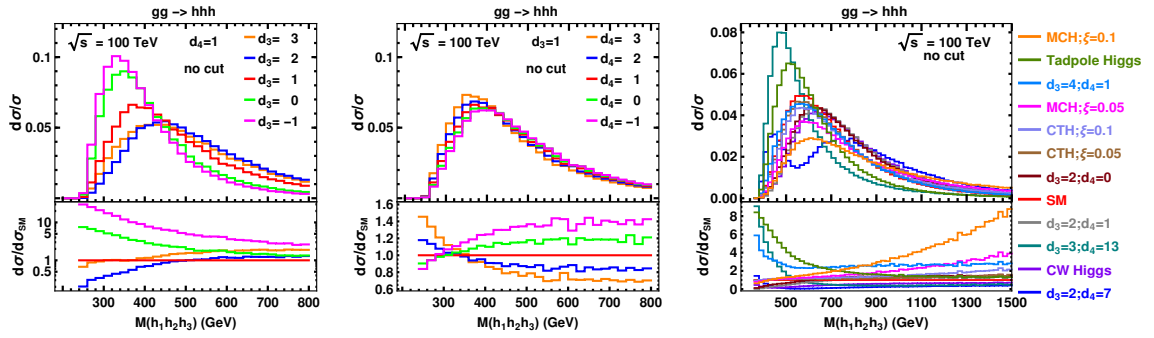


Figure 6.14: Distributions with partonic center-of-mass energy $M(hhh)$ for hhh production via gg fusion channel with different benchmark values of d_3 and d_4 at the 100 TeV collider. No cut on p_T of Higgs bosons has been imposed.

6.3.2 Interference Effects

In this section, we investigate the interference patterns for the process of triple Higgs bosons production $pp \rightarrow hhh$, for better understanding of variation of total cross section in different Higgs scenarios.

Interference without $t\bar{t}hh$ or $t\bar{t}hhh$

Let us first consider the cases without the $t\bar{t}hh$ and $t\bar{t}hhh$ couplings. There are 10 relevant terms for this case, as can be seen in Eq. (6.4). The first four terms are always positive,

and the rest of the six terms are interference terms and can be either positive or negative. It is worth reiterating the fact that the d_4 dependence of the cross section also depends on trilinear Higgs boson coupling d_3 . As shown in the left figure of Fig. 6.15, with d_4 the cross section first decreases and then increases within the shown range $-1 < d_3 < 6$. In addition, we show the variation of cross section, as the green band, with the quartic Higgs boson coupling d_4 varying within $0 < d_4 < 10$. In the right figure of Fig. 6.15, we explicitly see the variation of $\sigma/\sigma_{\text{SM}}$ with d_4 , while d_3 is fixed. Although it is theoretically less plausible for a large d_3 , e.g. $d_3 = 6$, hinted by vacuum stability, we still include this possibility here. In that case, the cross section only moderately varies with change in d_4 . Hence, there will be degeneracy in d_4 determination if d_3 is around 5 to 6.

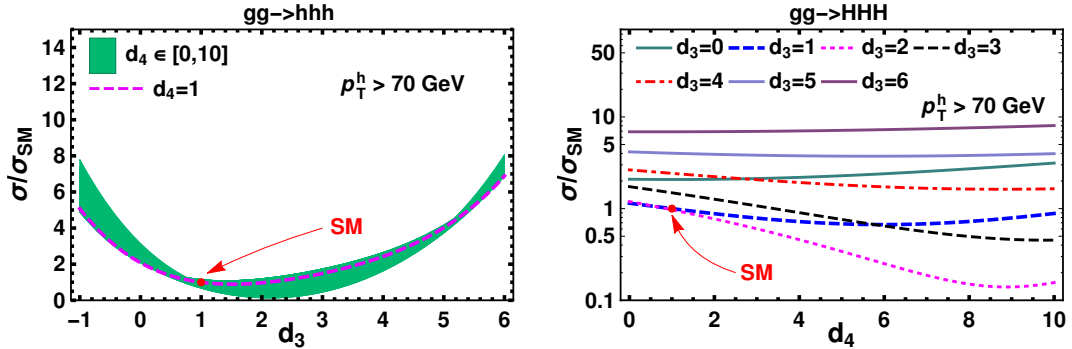


Figure 6.15: Variation of Cross section ratio $\sigma/\sigma_{\text{SM}}$ with d_3 and d_4 at a 100 TeV collider. In the left figure, we see a band for d_4 in the range $[0, 10]$. In the right figure, variation with d_4 for fixed d_3 is shown. The standard model cross section for no cut and $p_T^h > 70$ GeV cut are 2987 ab and 1710 ab, respectively.

Interference with $t\bar{t}hh$ and $t\bar{t}hhh$

In this subsection, we discuss new physics scenarios in which the $t\bar{t}hh$ and $t\bar{t}hhh$ are non-vanishing, e.g. the Nambu-Goldstone Higgs scenario, and investigate the interference terms involving these couplings in detail. In this scenario, all the Higgs boson couplings are correlated to the parameter ξ due to Higgs non-linearity.

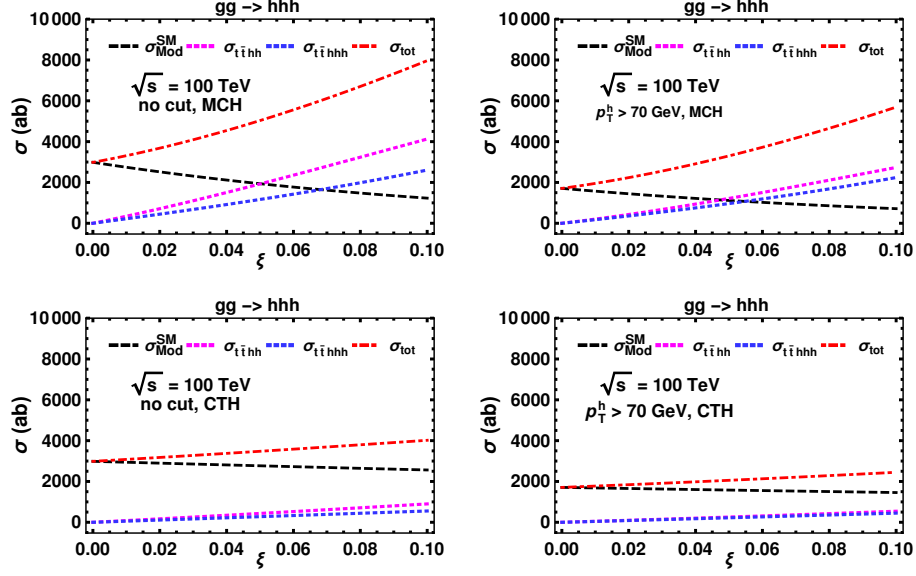


Figure 6.16: Cross section [in ab] with parameter ξ in the Minimum Composite Higgs Model (MCH) and the Composite Twin Higgs Model (CTH). The magenta line shows the effect of $t\bar{t}hh$ coupling. In MCH model, it exceeds the “SM-like” effect (σ_{Mod}^{SM}) around $\xi = 0.05$. The blue line shows the effect of $t\bar{t}hhh$ coupling, which includes interference (which is negative for the shown range of ξ) of $t\bar{t}hhh$ with $t\bar{t}hh$ as well.

In the Fig. 6.16, we show the interference effect of the $t\bar{t}hh$ and $t\bar{t}hhh$ couplings in two specific pseudo Nambu-Goldstone Higgs models, namely the MCH and CTH models. As expected, in the case of CTH model, the contribution of these coupling to the cross section is small, except at large ξ value, where it is also not that significant. However, in the case of MCH model, both the $t\bar{t}hh$ and $t\bar{t}hhh$ couplings play important role. At larger value of ξ , the significant increase in the cross section is induced by these couplings. As ξ increases, the contribution (σ_{Mod}^{SM}) of SM-like diagrams decreases due to smaller $t\bar{t}h$, d_3 , and d_4 couplings, but the contributions of diagrams with $t\bar{t}hh$ and $t\bar{t}hhh$ couplings increase.

In Fig. 6.17, the variation of ratios of the cross sections of MCH and CTH models to the SM value with ξ are depicted. The green band shows variation of the ratios due to scaling of the quartic Higgs boson coupling, denoted by \tilde{d}_4/d_4 . We see the variation due to quartic

Higgs boson coupling scaling decreases with larger values of the parameter ξ ; the dashed line is for $d_4 = 1$.

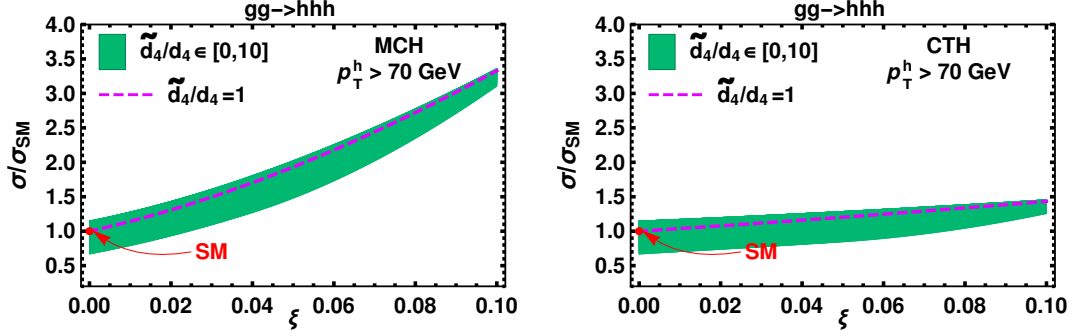


Figure 6.17: Variation of the ratio of cross sections of MCH and CTH models to the SM value with ξ and \tilde{d}_4/d_4 at the 100 TeV proton-proton collider. The bands are obtained by varying \tilde{d}_4/d_4 in the range of $[0, 10]$ for the MCH and CTH models. The standard model cross section for no cut and $p_T^h > 70$ GeV cut are 2987 ab and 1710 ab, respectively.

6.3.3 Constraints on d_4 in various models

As discussed before, double Higgs production channel will be able to distinguish various Higgs potential scenarios. The motivation for studying hhh production is to determine quartic Higgs boson couplings. It is a daunting task even at 100 TeV (FCC-hh) collider. There are several signal-to-background studies to observe the $pp \rightarrow hhh$ process at the 100 TeV collider. In the literature [232], it has been shown that the most promising signature to observe hhh production has one of the Higgs boson decaying into two photons, while the other two Higgs bosons each decay into a pair of bottom jets. The signal-to-background ratio gets worse and worse with lesser number of b-tagged jet events, as then background increases by order of magnitude than the signal. By recasting signal-to-background studies available in the literature [232], we find that to observe hhh signal within 30% accuracy at

1σ in the SM, the required luminosity is around 50 ab^{-1} [72].

We show the constraints which can be put on the quartic Higgs boson coupling if the cross section can be measured with 10% and 20% accuracies. We consider the SM ($d_3 = 1, d_4 = 1$), an arbitrarily chosen example of scaled trilinear Higgs boson coupling ($d_3 = 2, d_4 = 1$), an arbitrarily chosen example of the SMEFT ($d_3 = 2, d_4 = 7$)⁵, and the Coleman-Weinberg Higgs case with ($d_3 = 5/3, d_4 = 11/3$) as the benchmark scenarios. For all these benchmark scenarios, the constraints on the scaling of quartic Higgs coupling have been shown in Fig. 6.18. Furthermore, as for MCH and CTH models c_2 and d_3 are expected to be constrained in hh productions, the allowed parameter space for c_3 and d_4 have been shown in Fig. 6.19.

Here, some comments about the constraints are in order for the SM and New Physics scenarios:

- For the SM, the scaling factor is constrained to be within the range of $0.3 < \tilde{d}_4/d_4 < 1.82 \cup 10.13 < \tilde{d}_4/d_4 < 11.66$ ($0 < \tilde{d}_4/d_4 < 2.85 \cup 9.10 < \tilde{d}_4/d_4 < 12.28$), if the accuracy is 10% (20%).
- For an arbitrary choosen trilinear and quartic Higgs couplings, the bound on the quartic Higgs boson coupling will be generally quite loose, unless cross sections can be measured with better than 10% accuracy. However, as shown in Fig. 6.15, the bounds on the quartic coupling d_4 could be tight when the trilinear coupling $d_3 \simeq 2 - 3$, since in this case the $gg \rightarrow hhh$ production cross section shows sizeable variation with d_4 .

⁵Note in SMEFT, under the assumption that the contributions of all the other operators are negligible, if $d_3 = 2$, d_4 has to be 7 (See Table. 6.1)

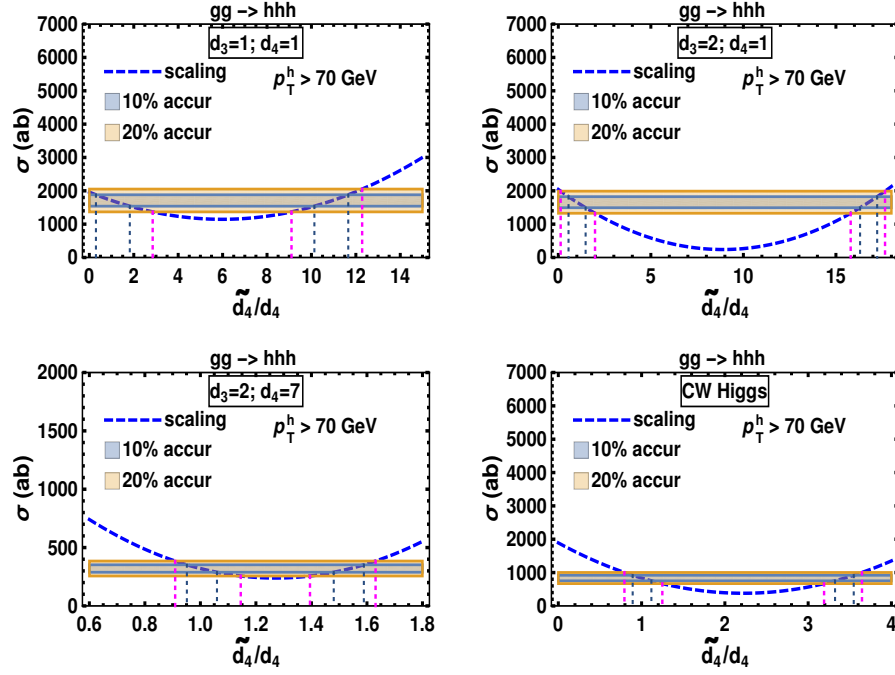


Figure 6.18: Constraints on \tilde{d}_4/d_4 in various new physics models, when the cross section can be measured up to 10% and 20% accuracy, respectively. The parameter \tilde{d}_4/d_4 scales the quartic Higgs boson coupling in a given model.

- For the Coleman-Weinberg Higgs, the bound on the quartic Higgs boson coupling d_4 is relatively tight. This happens as the Higgs trilinear coupling is $5/3$, which is near $d_3 = 2$, for which the cross section shows significant dependence on d_4 .
- For the Nambu-Goldstone Higgs, as can be seen in Fig. 6.19, the scaling factor \tilde{c}_3/c_3 could be constrained within the order of 10, but \tilde{d}_4/d_4 could only be constrained to the order of much larger than 10.
- For the Tadpole-induced Higgs, because the Higgs trilinear coupling d_3 could be highly suppressed, the dependence on the quartic Higgs boson coupling d_4 is very weak (see Fig. 6.12). On top of this, as d_4 is also suppressed in this scenario, only very large scaling factor \tilde{d}_4/d_4 is effective for changing the total cross section. This

makes the precision determination of d_4 very difficult in this scenario.

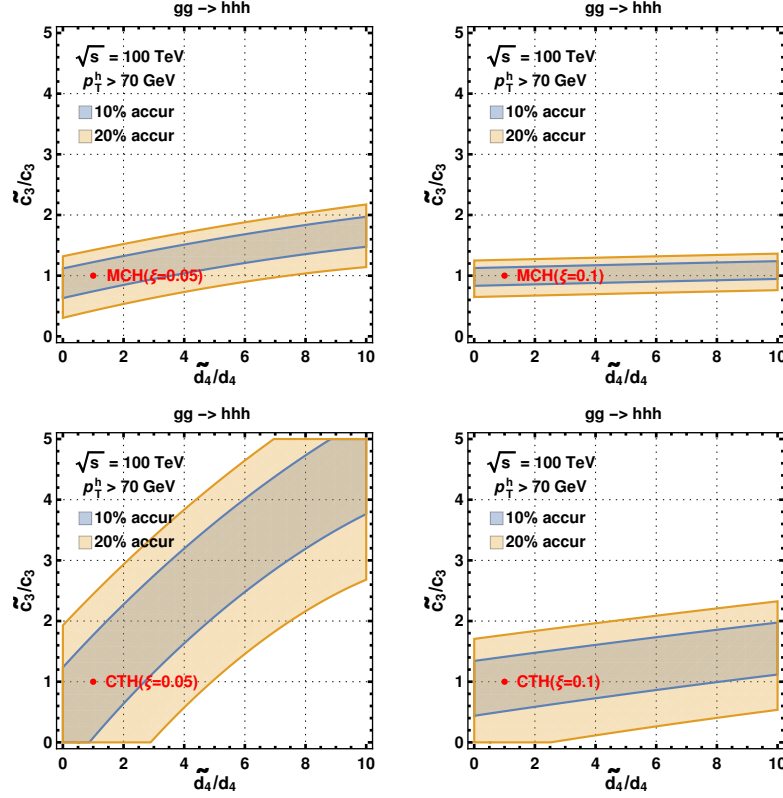


Figure 6.19: Constraints on \tilde{c}_3/c_3 and \tilde{d}_4/d_4 if the cross section can be measured up to 10% and 20% accuracy, respectively, in the MCH and CTH models.

6.4 Conclusion

After the discovery of Higgs boson, although many of its properties have been measured at the colliders, the true shape of the Higgs potential is still unknown. Various beyond the SM scenarios, such as elementary Higgs within SMEFT, pseudo-Goldstone Higgs model, CW Higgs model, Tadpole-induced Higgs, predict Higgs potentials different from the SM. In order to know the exact Higgs potential, we will need to know trilinear and quartic Higgs boson couplings. Even at the end of high luminosity phase of LHC, the trilinear Higgs

boson coupling will not be tightly constrained. However at the 27 TeV HE-LHC collider, this coupling can be well measured. We investigate various Higgs potential models by studying hh production. We compute interference between various class of diagrams to understand various features of cross sections and distributions. Based on the cross section measurement of hh production with some benchmark uncertainties, we calculate the bounds that can be put on the trilinear Higgs boson coupling of these models. The presence of $t\bar{t}hh$ coupling in Pseudo-Goldstone models makes it difficult to extract trilinear Higgs boson coupling in this model.

Detecting the production of hhh is extremely difficult even at a 100 TeV collider. This is one of the processes where quartic Higgs coupling can be measured. However, probing the quartic Higgs boson coupling is not easy as the process depends on this coupling very weakly. The various interference terms have been computed, which help us understand dependence of the cross sections and distributions on the various couplings, including the quartic Higgs boson coupling. Pseudo-Goldstone model introduces $t\bar{t}hhh$ coupling in addition to $t\bar{t}hh$ coupling, which complicates the process of extracting quartic Higgs boson coupling further. Constraints on quartic Higgs boson coupling, assuming certain accuracies for the cross section measurement have been obtained.

Chapter 7

Conclusions

In this thesis, we have explored many aspects of the SM and new physics scenarios at the colliders by considering various processes. In these processes, we had at least one Higgs boson in the final state. After the introduction, in the second chapter, we have reviewed the SM and various EFT scenarios. We have reviewed both EFT scenarios — SMEFT and HEFT where electroweak symmetry are realized linearly and non-linearly, respectively. In the third chapter, we reviewed one-loop calculation, describing various tensor reduction techniques, sources of divergences in the scalar integrals etc. The next three chapters describe the work done. In the fourth chapter, we considered the following processes — $pp \rightarrow hhh, hh\gamma$, and hhZ . Our focus was on the gluon-gluon (gg) fusion channel contribution to these processes. The one-loop amplitude for the $gg \rightarrow hh\gamma$ process vanishes exactly. To $pp \rightarrow hhh$, the dominant production channel is $gg \rightarrow hhh$, the contribution of $q\bar{q} \rightarrow hhh$ is negligible. The $gg \rightarrow hhh$ process is important as it involves both trilinear and quartic Higgs boson couplings. A measurement of this process along with di-Higgs production can help in determining the form of the Higgs potential. The process may be observable only if there exist anomalous interactions. This process is specially sensitive to trilinear Higgs boson coupling. This process can be observed at large center-of-mass energy machines with high luminosity. It will be challenging though. On the other hand, the process $pp \rightarrow hhZ$ may be observable at the LHC after accumulation of 3 ab^{-1} of integrated lu-

minosity. The $gg(\text{LO})$ contribution to this process is actually an NNLO contribution in α_s , and due to a large gluon flux, it is 14% of the $q\bar{q}(\text{NLO})$ contribution to $pp \rightarrow hhZ$ at 13 TeV LHC. At a 100 TeV machine, $gg \rightarrow hhZ$ can be as important as $q\bar{q} \rightarrow hhZ$. This process is important, as it involves hhh and $hhZZ$ couplings and is a background to triple Higgs bosons production. The effect of $t\bar{t}h$ and hZZ anomalous couplings are more significant in the distributions than in the total cross section.

In the fifth chapter, we have considered four processes: production of ZZh , WWh , γZh , and $\gamma\gamma h$ at proton-proton colliders. Here also, we have compared the gg fusion channel contribution with the fixed order (FO) NLO QCD correction to $pp \rightarrow VVh$. We find, at 100 TeV collider, the contribution of $gg \rightarrow ZZh$ production channel to ZZh production is as important as the fixed order QCD NLO correction to $q\bar{q}$ initiated channel. At 100 TeV collider, $gg \rightarrow WWh$ channel cross section is around half the FO NLO QCD correction to $q\bar{q}$ initiated channel. However, $gg \rightarrow \gamma Zh$ channel contribution is around 5% of FO NLO QCD correction in $q\bar{q}$ initiated channel. For $\gamma\gamma h$ production, gg fusion channel can be said to be only production channel, as the $b\bar{b}$ initiated process contribution is negligibly small.

The interference between various classes of diagrams shows many interesting features. We have shown that removing the top quark (or third generation quarks) from box type diagrams of effective topology $gg \rightarrow VV^*$ will lead to erroneous results. Besides, computing cross sections values at LHC, HE-LHC, and FCC-hh, we have obtained kinematic distributions for these processes at the FCC-hh in the gg fusion channel. The $t\bar{t}$ threshold effect can be seen in invariant mass distribution of $gg \rightarrow WWh$ channel. However, for the other processes via gg fusion channel, this effect is not visible in the distribution.

In addition to the SM results, effect of anomalous couplings for $t\bar{t}h$, VVh , $VVhh$, and

hhh vertices have been studied in the kappa framework. A strong dependence on anomalous κ_t and κ_V could be seen in the gg fusion channel, if the Feynman diagrams of the process under consideration have the corresponding vertices. A 10% change in κ_t or κ_V in the positive side can enhance the ZZh and WWh cross sections in the range 40-70%. The $q\bar{q}$ initiated channel, on the other hand, depends mainly on κ_V and its 10% variation changes the cross section by 20%. Also while in gg fusion channel, κ_t and κ_V change the shape of the distribution, in $q\bar{q}$ initiated channel, κ_V cannot change the shape as it is present in every diagram linearly. We did not see any large effect of anomalous trilinear Higgs boson coupling as it is present only in a very small number of diagrams whose contribution is small for $gg \rightarrow ZZh$ and $gg \rightarrow WWh$ processes. The dependence of the $q\bar{q}$ initiated channel on this coupling is also negligibly small owing to very small Yukawa coupling of light quarks with the Higgs boson.

In the sixth chapter, we have studied the possibility of exploring the true shape of the Higgs potential. Various beyond the SM scenarios, such as elementary Higgs within SMEFT, pseudo-Goldstone Higgs model, CW Higgs model, Tadpole-induced Higgs, predict different Higgs potentials. In order to know exact Higgs potential, we will need to know trilinear and quartic Higgs boson couplings. Even at the end of high luminosity phase of the LHC, the trilinear Higgs boson coupling will not be tightly constrained. However at the 27 TeV HE-LHC collider, this coupling can be well constrained. Based on the cross section measurement of hh production with some benchmark uncertainties, we calculate the bounds that can be put on the trilinear Higgs boson coupling of these models. The presence of $t\bar{t}hh$ coupling in pseudo-Goldstone models makes it difficult to extract trilinear Higgs boson coupling in this model. Detecting the hhh signal is extremely difficult even at

a 100 TeV collider. Probing the quartic Higgs boson coupling is even more difficult as the process depends on this coupling very weakly. The various interference terms have been computed, which help us understand dependence of those terms on the various couplings, including the quartic Higgs boson coupling. Pseudo-Goldstone model introduces $t\bar{t}hh$ coupling in addition to $t\bar{t}hh$ coupling, which complicates the process of extracting quartic Higgs boson coupling further. Constraints on quartic Higgs boson coupling, assuming certain accuracies for the cross section measurement, have been obtained.

In summary, in this thesis, we have studied production of some final states which include at least one Higgs boson, where gg fusion at one loop is one of the production channels. We have studied the cross sections, distributions, scale variation effect, interference between diagrams, effect of anomalous couplings on the cross sections and distributions etc. We compare the contribution of gg fusion channel to those of LO $q\bar{q}$ initiated channel and NLO QCD correction to it. We have also explored the possibility of distinguishing various Higgs potential scenarios by studying hh production channel. In addition, we have explored hhh production to study the possibility of measuring quartic Higgs boson coupling. Interference between various classes of diagrams have been studied in detail which help us understand dependence of these interference terms on various couplings. In addition, we have shown how the dependence of cross section on quartic Higgs boson coupling is more for some specific range of trilinear Higgs boson coupling. We have also shown the various constraints that can be put on the trilinear and quartic Higgs boson couplings for some benchmark uncertainties in the cross section measurement at the future colliders.

Appendix A

A.1 Tensor reductions in Passarino-Veltman technique

A.1.1 Bubble integral

We will start by setting up notations for tensor integrals:

$$\begin{aligned}
 B_0(q; i, j) &= \int \frac{d^D Q}{(Q^2 - m_i^2)((Q+q)^2 - m_j^2)} \\
 B^\mu(q; i, j) &= \int \frac{d^D Q Q^\mu}{(Q^2 - m_i^2)((Q+q)^2 - m_j^2)} \\
 B^{\mu\nu}(q; i, j) &= \int \frac{d^D Q Q^\mu Q^\nu}{(Q^2 - m_i^2)((Q+q)^2 - m_j^2)}
 \end{aligned} \tag{A.1}$$

Let us define denominator factor: $N_i = ((Q + q_{i-1})^2 - m_i^2)$ with $q_i = \sum_{j=1}^i p_j$ and $q_0 = 0$.¹

We will exemplify the reduction of tensor bubble integral using the following integral²

¹Here we use a new notation N_i for denominator factor rather than d_i , used in Chapter. 3.

²Sometimes we will use (1,2) instead of $(q_1; 1, 2)$ when compact notation is required. Note we will use (2,3) notation only for $(q_2 - q_1; 2, 3)$, which we will get after shifting the integration variable of associated integral by $-q_1$, that is $Q \rightarrow Q - q_1$.

$$\begin{aligned}
B^\mu(q_1; 1, 2) &= \int \frac{d^D Q Q^\mu}{N_1 N_2} \\
B^{\mu\nu}(q_1; 1, 2) &= \int \frac{d^D Q Q^\mu Q^\nu}{N_1 N_2}
\end{aligned}
\tag{A.2}$$

As after the loop integration the tensor structure should be intact, we can write Eq. A.2 in the following way

$$B^\mu(1, 2) = \int \frac{d^D Q Q^\mu}{N_1 N_2} = B_1 q_1^\mu \tag{A.3}$$

$$B^{\mu\nu}(1, 2) = \int \frac{d^D Q Q^\mu Q^\nu}{N_1 N_2} = B_{00} g^{\mu\nu} + B_{11} q_1^\mu q_1^\nu \tag{A.4}$$

Before proceeding further, let us derive one formula that we will use frequently in the rest of the section

$$\begin{aligned}
Q \cdot q_1 &= \frac{1}{2}((Q + q_1)^2 - Q^2 - q_1^2) \\
&= \frac{1}{2}((Q + q_1)^2 - m_2^2 - (Q^2 - m_1^2) + (m_2^2 - m_1^2 - q_1^2)) \\
&= \frac{1}{2}(N_2 - N_1 + f_1)
\end{aligned}
\tag{A.5}$$

where $f_1 = (m_2^2 - m_1^2 - q_1^2)$.

We are going to denote the scalar integrals as A_0, B_0, C_0, D_0 . The strategy that we are going to adopt to find B_1, B_{00} , and B_{11} in Eq. A.3 and Eq. A.4 is as follows. To find B_1 of Eq. A.3, we will contract $q_{1\mu}$ on both sides of this equation. Then the left hand side can be written in terms of A_0 and B_0 only. Hence B_1 can be written in terms of A_0 and B_0 (see this does not work for $q^2 = 0$). However, in Eq. A.4, there are two unknowns (B_{00} and B_{11})

in the RHS. Therefore, we need two equations, in order to solve them. We will contract Eq. A.4 with $q_{1\mu}$ and $g_{\mu\nu}$, and that will provide two equations. In the LHS, we will have all the scalars after using some identities and Eq. A.3. So, like B_1 , B_{00} , and B_{11} can also be written in terms of A_0 and B_0 .

rank-one bubble integral

Eq. A.3 is given by:

$$\begin{aligned}
B_1 q_1^\mu &= \int \frac{d^D Q Q^\mu}{N_1 N_2} \\
\Rightarrow B_1 q_1 \cdot q_1 &= \int \frac{d^D Q Q \cdot q_1}{N_1 N_2} \quad [\text{contracting with } q_{1\mu} \text{ on both sides}] \\
&= \int \frac{d^D Q \frac{1}{2}(N_2 - N_1 + f_1)}{N_1 N_2} \quad [\text{using Eq. A.5}] \\
&= \frac{1}{2} \int d^D Q \left(\frac{1}{N_1} - \frac{1}{N_2} + \frac{f_1}{N_1 N_2} \right) \\
&= \frac{1}{2} (A_0(1) - A_0(2) + f_1 B_0(1, 2)) \\
\Rightarrow B_1 &= \frac{1}{2q_1^2} (A_0(1) - A_0(2) + f_1 B_0(1, 2)). \tag{A.6}
\end{aligned}$$

Thus, Eq. A.6 gives B_1 of Eq. A.3 in terms of scalar tadpole and scalar bubble integrals. See $A_0(1)$ and $A_0(2)$ will not cancel unless $m_1 = m_2$ even if we shift momentum for $A_0(2)$.

rank-two bubble integral

Our next task is to find B_{00} and B_{11} of Eq. A.4. We will get two equations by contracting A.4 with $q_{1\mu}$ and $g_{\mu\nu}$. Contracting $q_{1\mu}$ with A.4 gives

$$\begin{aligned}
B_{00} q_1^\nu + B_{11} q_1 \cdot q_1 q_1^\nu &= \int \frac{d^D Q Q \cdot q_1 Q^\nu}{N_1 N_2} \\
&= \int \frac{d^D Q \frac{1}{2} (N_2 - N_1 + f_1) Q^\nu}{N_1 N_2} \quad [\text{using Eq. A.5}] \\
&= \frac{1}{2} \int d^D Q \left(\frac{Q^\nu}{N_1} - \frac{Q^\nu}{N_2} + \frac{f_1 Q^\nu}{N_1 N_2} \right) \\
&= \frac{1}{2} \int d^D Q \left(-\frac{Q^\nu}{N_2} + \frac{f_1 Q^\nu}{N_1 N_2} \right) \quad [\text{as } \int d^D Q \frac{Q^\nu}{N_1} = 0] \\
&= \frac{1}{2} \int d^D Q \left(-\frac{(Q + q_1)^\nu - q_1^\nu}{N_2} + \frac{f_1 Q^\nu}{N_1 N_2} \right) \\
&= \frac{1}{2} \int d^D Q \left(\frac{q_1^\nu}{N_2} + \frac{f_1 Q^\nu}{N_1 N_2} \right) \quad [\text{as } \int d^D Q \frac{(Q + q_1)^\nu}{N_2} = 0] \\
&= \frac{1}{2} (q_1^\nu A_0(2) + f_1 B^\nu(1, 2)) \\
&= \frac{1}{2} (q_1^\nu A_0(2) + f_1 B_1(1, 2) q_1^\nu) \quad [\text{using Eq. A.3}] \\
\Rightarrow B_{00} + B_{11} q_1 \cdot q_1 &= \frac{1}{2} (A_0(2) + f_1 B_1(1, 2)) \quad (\text{A.7})
\end{aligned}$$

In the above equation, Eq. A.7, the RHS entirely depends on the scalar integrals as $B_1(1, 2)$ depends on scalar integrals only (see Eq. A.6).

Now we multiply $g_{\mu\nu}$ on both sides of A.4. We get

$$\begin{aligned}
B_{00} D + B_{11} q_1 \cdot q_1 &= \int \frac{d^D Q Q^2}{N_1 N_2} \\
&= \int \frac{d^D Q (N_1 + m_1^2)}{N_1 N_2} \\
&= \int d^D Q \left(\frac{1}{N_2} + \frac{m_1^2}{N_1 N_2} \right) \\
&= (A_0(2) + m_1^2 B_0(1, 2)) \\
\Rightarrow B_{00} D + B_{11} q_1 \cdot q_1 &= (A_0(2) + m_1^2 B_0(1, 2)) \quad (\text{A.8})
\end{aligned}$$

Solving Eq. A.7 and Eq. A.8, we get

$$B_{00}(D-1) = \frac{1}{2} \left(A_0(2) + 2m_1^2 B_0(1,2) - f_1 B_1(1,2) \right)$$

$$\Rightarrow B_{00} = \frac{1}{2(D-1)} \left(A_0(2) + 2m_1^2 B_0(1,2) - f_1 B_1(1,2) \right). \quad (\text{A.9})$$

Using Eq. A.7 and Eq. A.9, we have

$$B_{11} = \frac{1}{2q_1^2} \left(A_0(2) + f_1 B_1(1,2) - 2B_{00} \right) \quad (\text{A.10})$$

A.1.2 Triangle integrals

Here we will describe reduction of tensor triangle integrals using Passarino-Veltman technique

$$C^\mu(1,2,3) = \int \frac{d^D Q Q^\mu}{N_1 N_2 N_3} = C_1 q_1^\mu + C_2 q_2^\mu \quad (\text{A.11})$$

$$C^{\mu\nu}(1,2,3) = \int \frac{d^D Q Q^\mu Q^\nu}{N_1 N_2 N_3} = C_{00} g^{\mu\nu} + C_{11} q_1^\mu q_1^\nu + C_{12} q_1^\mu q_2^\nu + C_{21} q_2^\mu q_1^\nu + C_{22} q_2^\mu q_2^\nu \quad (\text{A.12})$$

$$C^{\mu\nu\sigma}(1,2,3) = \int \frac{d^D Q Q^\mu Q^\nu Q^\sigma}{N_1 N_2 N_3} = C_{001} g^{[\mu\nu} q_1^{\sigma]} + C_{002} g^{[\mu\nu} q_2^{\sigma]} +$$

$$C_{111} q_1^\mu q_1^\nu q_1^\sigma + C_{112} q_1^\mu q_1^\nu q_2^\sigma + C_{121} q_1^\mu q_2^\nu q_1^\sigma + C_{122} q_1^\mu q_2^\nu q_2^\sigma +$$

$$C_{211} q_2^\mu q_1^\nu q_1^\sigma + C_{212} q_2^\mu q_1^\nu q_2^\sigma + C_{221} q_2^\mu q_2^\nu q_1^\sigma + C_{222} q_2^\mu q_2^\nu q_2^\sigma \quad (\text{A.13})$$

where $g^{[\mu\nu} q_1^{\sigma]} = g^{\mu\nu} q_1^\sigma + g^{\mu\sigma} q_1^\nu + g^{\sigma\nu} q_1^\mu$, and as interchange of indices should not change integrals, we have $C_{12} = C_{21}$, $C_{112} = C_{121} = C_{211}$ and $C_{221} = C_{212} = C_{122}$. Note

here we are using the abbreviated form (1,2,3) for $(q_1, q_2; 1, 2, 3)$ ³.

rank-one triangle integral

To find C_1 and C_2 in terms of scalar integral, we take dot products of Eq. A.11 with q_1 and q_2 . This will give following matrix equation

$$\begin{aligned}
 \begin{pmatrix} q_1 \cdot q_1 & q_1 \cdot q_2 \\ q_2 \cdot q_1 & q_2 \cdot q_2 \end{pmatrix} \begin{pmatrix} C_1 \\ C_2 \end{pmatrix} &= \begin{pmatrix} q_{1\mu} C^\mu(1, 2, 3) \\ q_{2\mu} C^\mu(1, 2, 3) \end{pmatrix} \\
 \Rightarrow G_2(q_1, q_2) \begin{pmatrix} C_1 \\ C_2 \end{pmatrix} &= \begin{pmatrix} q_{1\mu} C^\mu(1, 2, 3) \\ q_{2\mu} C^\mu(1, 2, 3) \end{pmatrix} \\
 \Rightarrow \boxed{\begin{pmatrix} C_1 \\ C_2 \end{pmatrix} = G_2^{-1}(q_1, q_2) \begin{pmatrix} q_{1\mu} C^\mu(1, 2, 3) \\ q_{2\mu} C^\mu(1, 2, 3) \end{pmatrix}} & \quad (A.14)
 \end{aligned}$$

Where G_2 is the 2×2 gram matrix. This is the source of numerical instability when its determinant becomes zero.

Let us now calculate $q_{1\mu} C^\mu(1, 2, 3)$ and $q_{2\mu} C^\mu(1, 2, 3)$ one by one

$$\begin{aligned}
 q_{1\mu} C^\mu(1, 2, 3) &= \int \frac{d^D Q \, Q \cdot q_1}{N_1 N_2 N_3} \\
 &= \int \frac{d^D Q \, \frac{1}{2}(N_2 - N_1 + f_1)}{N_1 N_2 N_3} \quad [\text{using Eq. A.5}] \\
 &= \frac{1}{2} \int d^D Q \left(\frac{1}{N_1 N_3} - \frac{1}{N_2 N_3} + \frac{f_1}{N_1 N_2 N_3} \right) \\
 \Rightarrow \boxed{q_{1\mu} C^\mu(1, 2, 3) = \frac{1}{2} (B_0(q_2; 1, 3) - B_0(q_2 - q_1; 2, 3) + f_1 C_0(1, 2, 3))}, & \quad (A.15)
 \end{aligned}$$

³However we will not use (2,3,4) when $N_2 N_3 N_4$ is at the denominator. We will use (2,3,4) only for $(q_2 - q_1, q_3 - q_1; 2, 3, 4)$, that is only after shifting the integration variable by $-q_1$.

where $B_0(q_2; 1, 3) = \int \frac{d^D Q}{(Q^2 - m_1^2)((Q + q_2)^2 - m_3^2)}$ and $B_0(q_2 - q_1; 2, 3) = \int \frac{d^D Q}{(Q^2 - m_2^2)((Q + q_2 - q_1)^2 - m_3^2)}$.

The last integral has been found in this form after the replacement $Q \rightarrow Q - q_1$ in the second integral⁴.

Before calculating $q_{2\mu} C^\mu(1, 2, 3)$, let us calculate $Q \cdot q_2$ in terms of denominators

$$\begin{aligned} Q \cdot q_2 &= \frac{1}{2}((Q + q_2)^2 - Q^2 - q_2^2) \\ &= \frac{1}{2}((Q + q_2)^2 - m_3^2 - (Q^2 - m_1^2) + (m_3^2 - m_1^2 - q_2^2)) \\ &= \frac{1}{2}(N_3 - N_1 + f_2), \end{aligned} \tag{A.16}$$

where $f_2 = (m_3^2 - m_1^2 - q_2^2)$.

Following similar steps as in the derivation of Eq. A.15, we have

$$\boxed{q_{2\mu} C^\mu(1, 2, 3) = \frac{1}{2} (B_0(q_1; 1, 2) - B_0(q_2 - q_1; 2, 3) + f_2 C_0(1, 2, 3))}, \tag{A.17}$$

So using Eq. A.15 and Eq. A.17 in Eq. A.14, we can find C_1 and C_2 of Eq. A.11.

rank-two triangle integral

There are five unknowns in Eq. A.12⁵. We contract Eq. A.12 with $q_{1\mu}$, $q_{2\mu}$, and $g_{\mu\nu}$

which will give five equations⁶

⁴For scalar integral, unlike tensor integral, this shifting is not going to produce more integrals as there is no Q dependence on the numerator. Hence for scalar integral, to use (2,3), basically there is no need to care about shifting.

⁵Actually four as $C_{12} = C_{21}$

⁶Actually four as one of the equation is dependent. However we will solve the unknowns with these five equations and verify whether $C_{12} = C_{21}$ or not, which will provide a way of checking the correctness of calculation.

Contracting $q_{1\mu}$ and $q_{2\mu}$ on both sides of Eq. A.12,

$$(C_{11} q_1 \cdot q_1 + C_{21} q_1 \cdot q_2 + C_{00})q_1^\nu + (C_{12} q_1 \cdot q_1 + C_{22} q_1 \cdot q_2)q_2^\nu = q_{1\mu}C^{\mu\nu}(1,2,3), \quad (\text{A.18})$$

$$(C_{11} q_2 \cdot q_1 + C_{21} q_2 \cdot q_2)q_1^\nu + (C_{12} q_2 \cdot q_1 + C_{22} q_2 \cdot q_2 + C_{00})q_2^\nu = q_{2\mu}C^{\mu\nu}(1,2,3). \quad (\text{A.19})$$

Our next task is to calculate $q_{1\mu}C^{\mu\nu}(1,2,3)$ and $q_{2\mu}C^{\mu\nu}(1,2,3)$:

$$\begin{aligned} q_{1\mu}C^{\mu\nu}(1,2,3) &= \int \frac{d^D Q}{N_1 N_2 N_3} Q \cdot q_1 Q^\nu \\ &= \int \frac{d^D Q}{N_1 N_2 N_3} \frac{1}{2}(N_2 - N_1 + f_1)Q^\nu \quad [\text{using Eq. A.5}] \\ &= \frac{1}{2} \int d^D Q \left(\frac{Q^\nu}{N_1 N_3} - \frac{Q^\nu}{N_2 N_3} + \frac{f_1 Q^\nu}{N_1 N_2 N_3} \right) \\ &= \frac{1}{2} (B^\nu(q_2; 1, 3) - B^\nu(q_2 - q_1; 2, 3) + q_1^\nu B_0(q_2 - q_1; 2, 3) + f_1 C^\nu(1, 2, 3)) \\ &= \frac{1}{2} (B_1(q_2; 1, 3) q_2^\nu - B_1(q_2 - q_1; 2, 3) (q_2 - q_1)^\nu \\ &\quad + q_1^\nu B_0(q_2 - q_1; 2, 3) + f_1 (C_1 q_1^\nu + C_2 q_2^\nu)) \quad [\text{using Eq. A.3}] \\ &= \frac{1}{2} \left((f_1 C_1 + B_0(q_2 - q_1; 2, 3) + B_1(q_2 - q_1; 2, 3)) q_1^\nu \right. \\ &\quad \left. + (f_1 C_2 - B_1(q_2 - q_1; 2, 3) + B_1(q_2; 1, 3)) q_2^\nu \right) \\ \Rightarrow q_{1\mu}C^{\mu\nu}(1,2,3) &= \frac{1}{2} \left((f_1 C_1 + B_0(2, 3) + B_1(2, 3)) q_1^\nu + (f_1 C_2 - B_1(2, 3) + B_1(1, 3)) q_2^\nu \right) \end{aligned} \quad (\text{A.20})$$

Now we calculate $q_{2\mu}C^{\mu\nu}(1,2,3)$;

$$\begin{aligned}
q_{2\mu}C^{\mu\nu}(1,2,3) &= \int \frac{d^D Q}{N_1 N_2 N_3} Q \cdot q_2 Q^\nu \\
&= \int \frac{d^D Q}{N_1 N_2 N_3} \frac{1}{2} (N_3 - N_1 + f_2) Q^\nu \quad [\text{using Eq. A.16}] \\
&= \frac{1}{2} \int d^D Q \left(\frac{Q^\nu}{N_1 N_2} - \frac{Q^\nu}{N_2 N_3} + \frac{f_1 Q^\nu}{N_1 N_2 N_3} \right) \\
&= \frac{1}{2} (B^\nu(q_1; 1, 2) - B^\nu(q_2 - q_1; 2, 3) + q_1^\nu B_0(q_2 - q_1; 2, 3) + f_2 C^\nu(1, 2, 3)) \\
&= \frac{1}{2} (B_1(q_1; 1, 2) q_1^\nu - B_1(q_2 - q_1; 2, 3) (q_2 - q_1)^\nu \\
&\quad + q_1^\nu B_0(q_2 - q_1; 2, 3) + f_2 (C_1 q_1^\nu + C_2 q_2^\nu)) \quad [\text{using Eq. A.3}] \\
&= \frac{1}{2} \left((f_2 C_1 + B_0(q_2 - q_1; 2, 3) + B_1(q_2 - q_1; 2, 3) + B_1(q_1; 1, 2)) q_1^\nu \right. \\
&\quad \left. + (f_2 C_2 - B_1(q_2 - q_1; 2, 3)) q_2^\nu \right) \\
\Rightarrow q_{2\mu}C^{\mu\nu}(1,2,3) &= \frac{1}{2} \left((f_2 C_1 + B_0(2, 3) + B_1(2, 3) + B_1(1, 2)) q_1^\nu + (f_2 C_2 - B_1(2, 3)) q_2^\nu \right)
\end{aligned} \tag{A.21}$$

Using Eq. A.20 and Eq. A.21 in Eq. A.18 and Eq. A.19, respectively, we have following equations

$$\Rightarrow \begin{pmatrix} C_{11} \\ C_{21} \end{pmatrix} = G_2^{-1}(q_1, q_2) \begin{pmatrix} \frac{1}{2} (f_1 C_1 + B_0(2, 3) + B_1(2, 3) - 2C_{00}) \\ \frac{1}{2} (f_2 C_1 + B_0(2, 3) + B_1(2, 3) + B_1(1, 2)) \end{pmatrix} \tag{A.22}$$

$$\Rightarrow \begin{pmatrix} C_{12} \\ C_{22} \end{pmatrix} = G_2^{-1}(q_1, q_2) \begin{pmatrix} \frac{1}{2} (f_1 C_2 - B_1(2, 3) + B_1(1, 3)) \\ \frac{1}{2} (f_2 C_2 - B_1(2, 3) - 2C_{00}) \end{pmatrix} \tag{A.23}$$

Now the only task is to find C_{00} . For that we contract Eq. A.12 with $g_{\mu\nu}$,

$$\begin{aligned}
C_{00} D + C_{11} q_1 \cdot q_1 + C_{12} q_1 \cdot q_2 + C_{21} q_2 \cdot q_1 + C_{22} q_2 \cdot q_2 &= \int \frac{d^D Q Q \cdot Q}{N_1 N_2 N_3} \\
\Rightarrow C_{00} D + C_{11} q_1 \cdot q_1 + C_{21} q_1 \cdot q_2 + C_{12} q_2 \cdot q_1 + C_{22} q_2 \cdot q_2 &= \int \frac{d^D Q (N_1 + m_1^2)}{N_1 N_2 N_3} \\
&= \int d^D Q \left(\frac{1}{N_2 N_3} + \frac{m_1^2}{N_1 N_2 N_3} \right) \\
&= \left(B_0(2, 3) + m_1^2 C_0(1, 2, 3) \right) \\
\Rightarrow C_{00} D + \frac{1}{2} (f_1 C_1 + B_0(2, 3) + B_1(2, 3) - 2C_{00}) + \frac{1}{2} (f_2 C_2 - B_1(2, 3) - 2C_{00}) \\
&= \left(B_0(2, 3) + m_1^2 C_0(1, 2, 3) \right) \quad [\text{using Eq. A.22 and Eq. A.23}] \\
\Rightarrow C_{00} (D - 2) &= \frac{1}{2} \left(B_0(2, 3) + 2m_1^2 C_0(1, 2, 3) - f_1 C_1 - f_2 C_2 \right) \\
\Rightarrow C_{00} &= \frac{1}{2(D-2)} \left(B_0(2, 3) + 2m_1^2 C_0(1, 2, 3) - f_1 C_1 - f_2 C_2 \right) \quad (\text{A.24})
\end{aligned}$$

In the above expression, as discussed before, we have interchangeably used the shorthand $(1, 3)$ for $(q_2; 1, 3)$ and $(2, 3)$ for $(q_2 - q_1; 2, 3)$ whenever further compact notation was required.

rank-three triangle integral

We contract Eq. A.13 with $q_{1\mu}$ and $q_{2\nu}$, and this gives all the 10 equations required to solve for 10 unknowns C_{001} , C_{002} , C_{111} , C_{112} , C_{121} , C_{122} , C_{211} , C_{212} , C_{221} , and C_{222} .⁷

⁷As $C_{112} = C_{121} = C_{211}$ and $C_{221} = C_{212} = C_{122}$, there are actually 6 unknowns. So four of the ten equations must be dependent. But we solve for 10 unknowns anyway as it gives a way of checking correctness

The RHS of Eq. A.13 is

$$\begin{aligned}
& C_{001}(g^{\mu\nu}q_1^\sigma + g^{\mu\sigma}q_1^\nu + g^{\nu\sigma}q_1^\mu) + C_{002}(g^{\mu\nu}q_2^\sigma + g^{\mu\sigma}q_2^\nu + g^{\nu\sigma}q_2^\mu) + \\
& q_1^\mu(C_{111}q_1^\nu q_1^\sigma + C_{112}q_1^\nu q_2^\sigma + C_{121}q_2^\nu q_1^\sigma + C_{122}q_2^\nu q_2^\sigma) + \\
& q_2^\mu(C_{211}q_1^\nu q_1^\sigma + C_{212}q_1^\nu q_2^\sigma + C_{221}q_2^\nu q_1^\sigma + C_{222}q_2^\nu q_2^\sigma)
\end{aligned} \tag{A.25}$$

After contracting with $q_{1\mu}$ it becomes

$$\begin{aligned}
& C_{001}(q_1^\nu q_1^\sigma + q_1^\nu q_1^\sigma + g^{\nu\sigma}q_1 \cdot q_1) + C_{002}(q_1^\nu q_2^\sigma + q_2^\nu q_1^\sigma + g^{\nu\sigma}q_1 \cdot q_2) + \\
& q_1 \cdot q_1(C_{111}q_1^\nu q_1^\sigma + C_{112}q_1^\nu q_2^\sigma + C_{121}q_2^\nu q_1^\sigma + C_{122}q_2^\nu q_2^\sigma) + \\
& q_1 \cdot q_2(C_{211}q_1^\nu q_1^\sigma + C_{212}q_1^\nu q_2^\sigma + C_{221}q_2^\nu q_1^\sigma + C_{222}q_2^\nu q_2^\sigma) \\
& = \\
& (q_1 \cdot q_1 C_{001} + q_1 \cdot q_2 C_{002})g^{\nu\sigma} + \\
& (q_1 \cdot q_1 C_{111} + q_1 \cdot q_2 C_{211} + 2C_{001})q_1^\nu q_1^\sigma + (q_1 \cdot q_1 C_{112} + q_1 \cdot q_2 C_{212} + C_{002})q_1^\nu q_2^\sigma + \\
& (q_1 \cdot q_1 C_{121} + q_1 \cdot q_2 C_{221} + C_{002})q_2^\nu q_1^\sigma + (q_1 \cdot q_1 C_{122} + q_1 \cdot q_2 C_{222} + C_{002})q_2^\nu q_2^\sigma \tag{A.26}
\end{aligned}$$

Similarly, contracting Eq.A.25 with $q_{2\mu}$ gives

of the calculation.

$$\begin{aligned}
& C_{001}(q_2^\vee q_1^\sigma + q_1^\vee q_2^\sigma + g^{\vee\sigma} q_2 \cdot q_1) + C_{002}(q_2^\vee q_2^\sigma + q_2^\vee q_2^\sigma + g^{\vee\sigma} q_2 \cdot q_2) + \\
& q_2 \cdot q_1 (C_{111} q_1^\vee q_1^\sigma + C_{112} q_1^\vee q_2^\sigma + C_{121} q_2^\vee q_1^\sigma + C_{122} q_2^\vee q_2^\sigma) + \\
& q_2 \cdot q_2 (C_{211} q_1^\vee q_1^\sigma + C_{212} q_1^\vee q_2^\sigma + C_{221} q_2^\vee q_1^\sigma + C_{222} q_2^\vee q_2^\sigma) \\
& = \\
& (q_2 \cdot q_1 C_{001} + q_2 \cdot q_2 C_{002}) g^{\vee\sigma} + \\
& (q_2 \cdot q_1 C_{111} + q_2 \cdot q_2 C_{211}) q_1^\vee q_1^\sigma + (q_2 \cdot q_1 C_{112} + q_2 \cdot q_2 C_{212} + C_{001}) q_1^\vee q_2^\sigma + \\
& (q_2 \cdot q_1 C_{121} + q_2 \cdot q_2 C_{221} + C_{001}) q_2^\vee q_1^\sigma + (q_2 \cdot q_1 C_{122} + q_2 \cdot q_2 C_{222} + 2C_{002}) q_2^\vee q_2^\sigma \quad (\text{A.27})
\end{aligned}$$

Here we will contract LHS of Eq. A.13 with $q_{1\mu}$ and $q_{2\mu}$ respectively,

$$\begin{aligned}
& q_{1\mu} C^{\mu\nu\sigma}(1, 2, 3) \\
& = \int \frac{d^D Q}{N_1 N_2 N_3} Q \cdot q_1 Q^\nu Q^\sigma \\
& = \int \frac{d^D Q}{N_1 N_2 N_3} \frac{1}{2} (N_2 - N_1 + f_1) Q^\nu Q^\sigma \quad [\text{using Eq. A.5}] \\
& = \frac{1}{2} \int d^D Q \left(\frac{Q^\nu Q^\sigma}{N_1 N_3} - \frac{Q^\nu Q^\sigma}{N_2 N_3} + \frac{f_1 Q^\nu Q^\sigma}{N_1 N_2 N_3} \right) \\
& = \frac{1}{2} (B^{\vee\sigma}(q_2; 1, 3) - B^{\vee\sigma}(q_2 - q_1; 2, 3) + q_1^\vee B^\sigma(q_2 - q_1; 2, 3) \\
& \quad + q_1^\sigma B^\vee(q_2 - q_1; 2, 3) - q_1^\vee q_1^\sigma B_0(q_2 - q_1; 2, 3) + f_1 C^{\vee\sigma}(1, 3, 3)) \\
& = \frac{1}{2} (g^{\vee\sigma} B_{00}(1, 3) + q_2^\vee q_2^\sigma B_{11}(1, 3) - g^{\vee\sigma} B_{00}(2, 3) - (q_2 - q_1)^\vee (q_2 - q_1)^\sigma B_{11}(2, 3) \\
& \quad + q_1^\vee (q_2 - q_1)^\sigma B_1(2, 3) + q_1^\sigma (q_2 - q_1)^\vee B_1(2, 3) - q_1^\vee q_1^\sigma B_0(2, 3) \\
& \quad + f_1 (C_{00} g^{\vee\sigma} + C_{11} q_1^\vee q_1^\sigma + C_{12} q_1^\vee q_2^\sigma + C_{21} q_2^\vee q_1^\sigma + C_{22} q_2^\vee q_2^\sigma)) \\
& \quad [\text{using Eq. A.3, Eq. A.4, and Eq. A.12}]
\end{aligned}$$

$$\begin{aligned}
&= \frac{1}{2} \left((B_{00}(1,3) - B_{00}(2,3) + f_1 C_{00}) g^{\nu\sigma} \right. \\
&\quad + (-B_{11}(2,3) - 2B_1(2,3) - B_0(2,3) + f_1 C_{11}) q_1^\nu q_1^\sigma \\
&\quad + (B_{11}(2,3) + B_1(2,3) + f_1 C_{12}) q_1^\nu q_2^\sigma \\
&\quad + (B_{11}(2,3) + B_1(2,3) + f_1 C_{21}) q_2^\nu q_1^\sigma \\
&\quad \left. + (B_{11}(1,3) - B_{11}(2,3) + f_1 C_{22}) q_2^\nu q_2^\sigma \right) \tag{A.28}
\end{aligned}$$

$$\begin{aligned}
&q_{2\mu} C^{\mu\nu\sigma}(1,2,3) \\
&= \int \frac{d^D Q \, Q \cdot q_2 Q^\nu Q^\sigma}{N_1 N_2 N_3} \\
&= \int \frac{d^D Q \, \frac{1}{2} (N_3 - N_1 + f_2) Q^\nu Q^\sigma}{N_1 N_2 N_3} \quad [\text{using Eq. A.16}] \\
&= \frac{1}{2} \int d^D Q \left(\frac{Q^\nu Q^\sigma}{N_1 N_2} - \frac{Q^\nu Q^\sigma}{N_2 N_3} + \frac{f_2 Q^\nu Q^\sigma}{N_1 N_2 N_3} \right) \\
&= \frac{1}{2} \left(B^{\nu\sigma}(q_1; 1, 2) - B^{\nu\sigma}(q_2 - q_1; 2, 3) + q_1^\nu B^\sigma(q_2 - q_1; 2, 3) \right. \\
&\quad \left. + q_1^\sigma B^\nu(q_2 - q_1; 2, 3) - q_1^\nu q_1^\sigma B_0(q_2 - q_1; 2, 3) + f_2 C^{\nu\sigma}(1, 2, 3) \right) \\
&= \frac{1}{2} \left(g^{\nu\sigma} B_{00}(1, 2) + q_1^\nu q_1^\sigma B_{11}(1, 2) - g^{\nu\sigma} B_{00}(2, 3) - (q_2 - q_1)^\nu (q_2 - q_1)^\sigma B_{11}(2, 3) \right. \\
&\quad + q_1^\nu (q_2 - q_1)^\sigma B_1(2, 3) + q_1^\sigma (q_2 - q_1)^\nu B_1(2, 3) - q_1^\nu q_1^\sigma B_0(2, 3) \\
&\quad \left. + f_2 (C_{00} g^{\nu\sigma} + C_{11} q_1^\nu q_1^\sigma + C_{12} q_1^\nu q_2^\sigma + C_{21} q_2^\nu q_1^\sigma + C_{22} q_2^\nu q_2^\sigma) \right) \\
&\quad [\text{using Eq. A.3, Eq. A.4, and Eq. A.12}] \\
&= \frac{1}{2} \left((B_{00}(1,2) - B_{00}(2,3) + f_2 C_{00}) g^{\nu\sigma} \right. \\
&\quad + (B_{11}(1,2) - B_{11}(2,3) - 2B_1(2,3) - B_0(2,3) + f_2 C_{11}) q_1^\nu q_1^\sigma \\
&\quad + (B_{11}(2,3) + B_1(2,3) + f_2 C_{12}) q_1^\nu q_2^\sigma \\
&\quad \left. + (B_{11}(2,3) + B_1(2,3) + f_2 C_{21}) q_2^\nu q_1^\sigma \right)
\end{aligned}$$

$$+ (B_{11}(2,3) + f_2 C_{22}) q_2^\nu q_2^\sigma) \quad (\text{A.29})$$

Equating Eq. A.26 with Eq. A.28 and Eq. A.27 with Eq. A.29, we have following five equations:

$$\begin{pmatrix} C_{001} \\ C_{002} \end{pmatrix} = G_2^{-1}(q_1, q_2) \begin{pmatrix} \frac{1}{2} (B_{00}(1,3) - B_{00}(2,3) + f_1 C_{00}) \\ \frac{1}{2} (B_{00}(1,2) - B_{00}(2,3) + f_2 C_{00}) \end{pmatrix} \quad (\text{A.30})$$

$$\begin{pmatrix} C_{111} \\ C_{211} \end{pmatrix} = G_2^{-1}(q_1, q_2) \begin{pmatrix} \frac{1}{2} (-B_{11}(2,3) - 2B_1(2,3) - B_0(2,3) + f_1 C_{11} - 2C_{001}) \\ \frac{1}{2} (B_{11}(1,2) - B_{11}(2,3) - 2B_1(2,3) - B_0(2,3) + f_2 C_{11}) \end{pmatrix} \quad (\text{A.31})$$

$$\begin{pmatrix} C_{112} \\ C_{212} \end{pmatrix} = G_2^{-1}(q_1, q_2) \begin{pmatrix} \frac{1}{2} (B_{11}(2,3) + B_1(2,3) + f_1 C_{12} - C_{002}) \\ \frac{1}{2} (B_{11}(2,3) + B_1(2,3) + f_2 C_{12} - C_{001}) \end{pmatrix} \quad (\text{A.32})$$

$$\begin{pmatrix} C_{121} \\ C_{221} \end{pmatrix} = G_2^{-1}(q_1, q_2) \begin{pmatrix} \frac{1}{2} (B_{11}(2,3) + B_1(2,3) + f_1 C_{21} - C_{002}) \\ \frac{1}{2} (B_{11}(2,3) + B_1(2,3) + f_2 C_{21} - C_{001}) \end{pmatrix} \quad (\text{A.33})$$

$$\begin{pmatrix} C_{122} \\ C_{222} \end{pmatrix} = G_2^{-1}(q_1, q_2) \begin{pmatrix} \frac{1}{2} (B_{11}(1,3) - B_{11}(2,3) + f_1 C_{22}) \\ \frac{1}{2} (B_{11}(2,3) + f_2 C_{22} - 2C_{002}) \end{pmatrix} \quad (\text{A.34})$$

The above five equations Eq. A.30–Eq. A.34 determine all the coefficients of Eq. A.13.

We see that Eq. A.32 and Eq. A.33 are same. $B_1, B_{00}, B_{11}, C_{00}, C_{11}, C_{12}, C_{21}$, and C_{22} can be found from Eq. A.6, Eq. A.9, Eq. A.10, Eq. A.24, Eq. A.22, and Eq. A.23.

A.1.3 Box integrals

Next we will describe reduction for tensor box integrals using the Passarino-Veltman technique.

$$D^\mu(1, 2, 3, 4) = \int \frac{d^D Q Q^\mu}{N_1 N_2 N_3 N_4} = D_1 q_1^\mu + D_2 q_2^\mu + D_3 q_3^\mu \quad (\text{A.35})$$

$$\begin{aligned} D^{\mu\nu}(1, 2, 3, 4) = \int \frac{d^D Q Q^\mu Q^\nu}{N_1 N_2 N_3 N_4} = & D_{00} g^{\mu\nu} + D_{11} q_1^\mu q_1^\nu + D_{12} q_1^\mu q_2^\nu + D_{13} q_1^\mu q_3^\nu \\ & + D_{21} q_2^\mu q_1^\nu + D_{22} q_2^\mu q_2^\nu + D_{23} q_2^\mu q_3^\nu \\ & + D_{31} q_3^\mu q_1^\nu + D_{32} q_3^\mu q_2^\nu + D_{33} q_3^\mu q_3^\nu \end{aligned} \quad (\text{A.36})$$

$$\begin{aligned} D^{\mu\nu\sigma}(1, 2, 3, 4) = \int \frac{d^D Q Q^\mu Q^\nu Q^\sigma}{N_1 N_2 N_3 N_4} = & D_{001} g^{[\mu\nu} q_1^{\sigma]} + D_{002} g^{[\mu\nu} q_2^{\sigma]} + D_{003} g^{[\mu\nu} q_3^{\sigma]} + \\ & q_1^\mu (D_{111} q_1^\nu q_1^\sigma + D_{112} q_1^\nu q_2^\sigma + D_{113} q_1^\nu q_3^\sigma + D_{121} q_2^\nu q_1^\sigma + D_{122} q_2^\nu q_2^\sigma + D_{123} q_2^\nu q_3^\sigma + D_{131} q_3^\nu q_1^\sigma + D_{132} q_3^\nu q_2^\sigma + D_{133} q_3^\nu q_3^\sigma) + \\ & q_2^\mu (D_{211} q_1^\nu q_1^\sigma + D_{212} q_1^\nu q_2^\sigma + D_{213} q_1^\nu q_3^\sigma + D_{221} q_2^\nu q_1^\sigma + D_{222} q_2^\nu q_2^\sigma + D_{223} q_2^\nu q_3^\sigma + D_{231} q_3^\nu q_1^\sigma + D_{232} q_3^\nu q_2^\sigma + D_{233} q_3^\nu q_3^\sigma) + \\ & q_3^\mu (D_{311} q_1^\nu q_1^\sigma + D_{312} q_1^\nu q_2^\sigma + D_{313} q_1^\nu q_3^\sigma + D_{321} q_2^\nu q_1^\sigma + D_{322} q_2^\nu q_2^\sigma + D_{323} q_2^\nu q_3^\sigma + D_{331} q_3^\nu q_1^\sigma + D_{332} q_3^\nu q_2^\sigma + D_{333} q_3^\nu q_3^\sigma) \end{aligned} \quad (\text{A.37})$$

$$\begin{aligned} D^{\mu\nu\sigma\rho}(1, 2, 3, 4) = \int \frac{d^D Q Q^\mu Q^\nu Q^\sigma Q^\rho}{N_1 N_2 N_3 N_4} = & D_{0000} g^{[\mu\nu} g^{\sigma\rho]} + \sum_{i,j=1}^3 D_{00ij} g^{[\mu\nu} q_i^\sigma q_j^{\rho]} + \sum_{i,j,k,l=1}^3 D_{ijkl} q_i^\mu q_j^\nu q_k^\sigma q_l^\rho, \end{aligned} \quad (\text{A.38})$$

where $N_i = (Q + q_{i-1})^2 - m_i^2$ with $q_0 = 0$. Also $q_i = \sum_{j=1}^i p_j$, where p_j are the external momenta. Here we will find only D_1, D_2 , and D_3 and for the rest we will make some remarks.

Besides Eq. A.5 and Eq. A.16, we will need the following identity

$$\begin{aligned}
Q \cdot q_3 &= \frac{1}{2}((Q + q_3)^2 - Q^2 - q_3^2) \\
&= \frac{1}{2}((Q + q_3)^2 - m_4^2 - (Q^2 - m_1^2) + (m_4^2 - m_1^2 - q_3^2)) \\
&= \frac{1}{2}(N_4 - N_1 + f_3),
\end{aligned} \tag{A.39}$$

where $f_2 = (m_4^2 - m_1^2 - q_3^2)$.

rank-one box integral

Contracting Eq. A.35 with q_1, q_2 and q_3 gives

$$\begin{aligned}
&\begin{pmatrix} q_1 \cdot q_1 & q_1 \cdot q_2 & q_1 \cdot q_3 \\ q_2 \cdot q_1 & q_2 \cdot q_2 & q_2 \cdot q_3 \\ q_3 \cdot q_1 & q_3 \cdot q_2 & q_3 \cdot q_3 \end{pmatrix} \begin{pmatrix} D_1 \\ D_2 \\ D_3 \end{pmatrix} = \begin{pmatrix} q_{1\mu} D^\mu(1, 2, 3, 4) \\ q_{2\mu} D^\mu(1, 2, 3, 4) \\ q_{3\mu} D^\mu(1, 2, 3, 4) \end{pmatrix} \\
&\Rightarrow G_3(q_1, q_2, q_3) \begin{pmatrix} D_1 \\ D_2 \\ D_3 \end{pmatrix} = \begin{pmatrix} q_{1\mu} D^\mu(1, 2, 3, 4) \\ q_{2\mu} D^\mu(1, 2, 3, 4) \\ q_{3\mu} D^\mu(1, 2, 3, 4) \end{pmatrix}
\end{aligned}$$

$$\Rightarrow \begin{pmatrix} D_1 \\ D_2 \\ D_3 \end{pmatrix} = G_3^{-1}(q_1, q_2, q_3) \begin{pmatrix} q_{1\mu} D^\mu(1, 2, 3, 4) \\ q_{2\mu} D^\mu(1, 2, 3, 4) \\ q_{3\mu} D^\mu(1, 2, 3, 4) \end{pmatrix} \quad (\text{A.40})$$

where $G_3(q_1, q_2, q_3)$ is the 3×3 gram matrix. Below we will calculate $q_{1\mu} D^\mu(1, 2, 3, 4)$, $q_{2\mu} D^\mu(1, 2, 3, 4)$, and $q_{3\mu} D^\mu(1, 2, 3, 4)$ one by one:

$$\begin{aligned} q_{1\mu} D^\mu(1, 2, 3, 4) &= \int \frac{d^D Q}{N_1 N_2 N_3 N_4} Q \cdot q_1 \\ &= \int \frac{d^D Q}{N_1 N_2 N_3 N_4} \frac{1}{2} (N_2 - N_1 + f_1) \quad [\text{using Eq. A.5}] \\ &= \frac{1}{2} \int d^D Q \left(\frac{1}{N_1 N_3 N_4} - \frac{1}{N_2 N_3 N_4} + \frac{f_1}{N_1 N_2 N_3 N_4} \right) \\ \Rightarrow q_{1\mu} D^\mu(1, 2, 3, 4) &= \frac{1}{2} (C_0(q_2, q_3; 1, 3, 4) - C_0(q_2 - q_1, q_3 - q_1; 2, 3, 4) + f_1 D_0(1, 2, 3, 4)), \end{aligned} \quad (\text{A.41})$$

where $C_0(q_2, q_3; 1, 3, 4) = \int \frac{d^D Q}{(Q^2 - m_1^2)((Q + q_2)^2 - m_3^2)((Q + q_3)^2 - m_4^2)}$ and $C_0(q_2 - q_1, q_3 - q_1; 2, 3, 4) = \int \frac{d^D Q}{(Q^2 - m_2^2)((Q + q_2 - q_1)^2 - m_3^2)((Q + q_3 - q_1)^2 - m_4^2)}$. The second term of Eq. A.41 is found in this form after the replacement $Q \rightarrow Q - q_1$.

$$\begin{aligned}
q_{2\mu}D^\mu(1,2,3,4) &= \int \frac{d^D Q}{N_1 N_2 N_3 N_4} Q \cdot q_2 \\
&= \int \frac{d^D Q}{N_1 N_2 N_3 N_4} \frac{1}{2}(N_3 - N_1 + f_2) \quad [\text{using Eq. A.16}] \\
&= \frac{1}{2} \int d^D Q \left(\frac{1}{N_1 N_2 N_4} - \frac{1}{N_2 N_3 N_4} + \frac{f_1}{N_1 N_2 N_3 N_4} \right) \\
\Rightarrow \boxed{q_{2\mu}D^\mu(1,2,3,4) &= \frac{1}{2} (C_0(q_1, q_3; 1, 2, 4) - C_0(q_2 - q_1, q_3 - q_1; 2, 3, 4) + f_2 D_0(1, 2, 3, 4))},
\end{aligned}
\tag{A.42}$$

$$\begin{aligned}
q_{3\mu}D^\mu(1,2,3,4) &= \int \frac{d^D Q}{N_1 N_2 N_3 N_4} Q \cdot q_3 \\
&= \int \frac{d^D Q}{N_1 N_2 N_3 N_4} \frac{1}{2}(N_4 - N_1 + f_3) \quad [\text{using Eq. A.39}] \\
&= \frac{1}{2} \int d^D Q \left(\frac{1}{N_1 N_2 N_3} - \frac{1}{N_2 N_3 N_4} + \frac{f_1}{N_1 N_2 N_3 N_4} \right) \\
\Rightarrow \boxed{q_{3\mu}D^\mu(1,2,3,4) &= \frac{1}{2} (C_0(q_1, q_2; 1, 2, 3) - C_0(q_2 - q_1, q_3 - q_1; 2, 3, 4) + f_3 D_0(1, 2, 3, 4))},
\end{aligned}
\tag{A.43}$$

rank-two box integral

We will not explicitly show the reduction for rank-two box integral. We will make some general statements and give some information using which the correctness of the calculation can be checked.

There are ten unknowns – $D_{00}, D_{11}, D_{12}, D_{13}, D_{21}, D_{22}, D_{23}, D_{31}, D_{32}, D_{33}$. By contracting Eq. A.36 with $q_{1\mu}$, $q_{2\mu}$, and $q_{3\mu}$, and thereafter comparing coefficient of q_1^ν , q_2^ν and q_3^ν , we will have nine equations. Three equations coming from comparing q_1^ν (or q_2^ν or q_3^ν) co-

efficients can be written as a matrix equation using Gram matrix $G_3(q_1, q_2, q_3)$. So we will have three such matrix equations for $\begin{pmatrix} D_{11} \\ D_{21} \\ D_{31} \end{pmatrix}$, $\begin{pmatrix} D_{12} \\ D_{22} \\ D_{32} \end{pmatrix}$ and $\begin{pmatrix} D_{13} \\ D_{23} \\ D_{33} \end{pmatrix}$. D_{00} can be obtained by contracting Eq. A.36 with $g_{\mu\nu}$ and using three appropriate equations in the nine equations just discussed (it follows similar steps as in the derivation of C_{00}). Out of the ten unknowns only seven are independent because of the following identities: $D_{12} = D_{21}$, $D_{13} = D_{31}$, and $D_{23} = D_{32}$, which follows from the fact that the integral is symmetric under the interchange of the indices μ and ν .

rank-three box integral

There are 30 unknowns in the right hand side of Eq. A.37. Contracting this with any of $q_{1\mu}$, $q_{2\mu}$, and $q_{3\mu}$, will give a tensor structure present in the RHS of Eq. A.36. So comparing these tensor structure on both side will give 10 equations for each of the contraction with $q_{1\mu}$, $q_{2\mu}$, and $q_{3\mu}$. So in total there will be 30 equations. These can be written as 10 matrix equations using Gram matrix $G_3(q_1, q_2, q_3)$. The vectors that need to be solved are — $\begin{pmatrix} D_{001} \\ D_{002} \\ D_{003} \end{pmatrix}$, $\begin{pmatrix} D_{111} \\ D_{211} \\ D_{311} \end{pmatrix}$, $\begin{pmatrix} D_{112} \\ D_{212} \\ D_{312} \end{pmatrix}$, $\begin{pmatrix} D_{113} \\ D_{213} \\ D_{313} \end{pmatrix}$, $\begin{pmatrix} D_{121} \\ D_{221} \\ D_{321} \end{pmatrix}$, $\begin{pmatrix} D_{122} \\ D_{222} \\ D_{322} \end{pmatrix}$, $\begin{pmatrix} D_{123} \\ D_{223} \\ D_{323} \end{pmatrix}$, $\begin{pmatrix} D_{131} \\ D_{231} \\ D_{331} \end{pmatrix}$, $\begin{pmatrix} D_{132} \\ D_{232} \\ D_{332} \end{pmatrix}$, $\begin{pmatrix} D_{133} \\ D_{233} \\ D_{333} \end{pmatrix}$. Out of these 30 unknowns only 13 are independent because of the following relations — $D_{112} = D_{121} = D_{211}$, $D_{113} = D_{131} = D_{311}$, $D_{221} = D_{212} = D_{122}$, $D_{223} = D_{232} = D_{322}$, $D_{331} = D_{313} = D_{133}$, $D_{332} = D_{323} = D_{233}$, $D_{123} = D_{132} = D_{213} = D_{231} = D_{312} = D_{321}$. These relations follow from symmetry of the integrals under the interchange of the indices. We have just seen that out of the 30 equations, only 13 equations are independent. But, as already mentioned for other similar cases, we solve for all the unknowns, and later it can be used to check correctness of the solutions.

rank-four box integral

There are 91 ($=1+9+81$) unknowns in the right hand side of Eq. A.38. Contracting this with any of $q_{1\mu}$, $q_{2\mu}$, and $q_{3\mu}$, will give a tensor structure present in the RHS of Eq. A.37. So each contraction will give 30 equations, totaling 90 equations. To find D_{0000} we can contract with $g_{\mu\nu}$. However there are only 22 ($=1+6+15$) independent coefficients. In the first category, we have D_{0000} (1). In the second category we have: D_{0011} (1), D_{0012} (2), D_{0013} (2), D_{0022} (1), D_{0023} (2), D_{0033} (1). In the last category we have: D_{1111} (1), D_{2222} (1), D_{3333} (1), D_{1112} (4), D_{1113} (4), D_{2221} (4), D_{2223} (4), D_{3331} (4), D_{3332} (4), D_{1123} (12), D_{2213} (12), D_{3312} (12), D_{1122} (6), D_{1133} (6), D_{2233} (6). The numbers in the parentheses signify that there are that many objects with equal value because of symmetry of the integral under the interchange of indices. For example, we have $D_{1112} = D_{1121} = D_{1211} = D_{2111}$, that is why we have written D_{1112} (4). The numbers in the parenthesis if added up in each category will give 1, 9, and 81, respectively. We have not shown the solution explicitly, as it will take too much space to write all of them here. However this can be done using some symbolic manipulator software like Form or Mathematica.

A.2 van Neerven-Vermaseren basis

In the next section, we will present Oldenborg-Vermaseren technique for tensor integral reduction. Before that, here we shall discuss various properties of van Neerven-Vermaseren basis, as that is going to be used in the reduction there. Some of this material has already been discussed in § 3.2.2. There, we defined the generalized Kronecker delta $\delta_{v_1 v_2}^{\mu_1 \mu_2}$. Here we will discuss these in more detail and will provide the explicit proofs. We start from

$\delta_{v_1 v_2 v_3}^{\mu_1 \mu_2 \mu_3}$ and then generalize it for n-dimension.

The Kronecker delta for $\mu_1 \mu_2 \mu_3$ and $v_1 v_2 v_3$ is defined as:

$$\delta_{v_1 v_2 v_3}^{\mu_1 \mu_2 \mu_3} = \begin{vmatrix} \delta_{v_1}^{\mu_1} & \delta_{v_2}^{\mu_1} & \delta_{v_3}^{\mu_1} \\ \delta_{v_1}^{\mu_2} & \delta_{v_2}^{\mu_2} & \delta_{v_3}^{\mu_2} \\ \delta_{v_1}^{\mu_3} & \delta_{v_2}^{\mu_3} & \delta_{v_3}^{\mu_3} \end{vmatrix}$$

$$= \delta_{v_1}^{\mu_1} \delta_{v_2 v_3}^{\mu_2 \mu_3} - \delta_{v_2}^{\mu_1} \delta_{v_1 v_3}^{\mu_2 \mu_3} + \delta_{v_3}^{\mu_1} \delta_{v_1 v_2}^{\mu_2 \mu_3} \quad (\text{A.44})$$

$$= \delta_{v_1}^{\mu_1} \delta_{v_2 v_3}^{\mu_2 \mu_3} - \delta_{v_1}^{\mu_2} \delta_{v_2 v_3}^{\mu_1 \mu_3} + \delta_{v_1}^{\mu_3} \delta_{v_2 v_3}^{\mu_1 \mu_2} \quad (\text{A.45})$$

We can, now, generalize this formula for m upper and lower indices

$$\delta_{v_1 v_2 v_3 \dots v_m}^{\mu_1 \mu_2 \mu_3 \dots \mu_m} = \delta_{v_1}^{\mu_1} \delta_{v_2 v_3 \dots v_m}^{\mu_2 \mu_3 \dots \mu_m} - \delta_{v_2}^{\mu_1} \delta_{v_1 v_3 \dots v_m}^{\mu_2 \mu_3 \dots \mu_m} + \delta_{v_3}^{\mu_1} \delta_{v_1 v_2 \dots v_m}^{\mu_2 \mu_3 \dots \mu_m} - \dots + (-1)^{(1+m)} \delta_{v_m}^{\mu_1} \delta_{v_1 v_2 \dots v_{m-1}}^{\mu_2 \mu_3 \dots \mu_m} \quad (\text{A.46})$$

$$\delta_{v_1 v_2 v_3 \dots v_m}^{\mu_1 \mu_2 \mu_3 \dots \mu_m} = \delta_{v_1}^{\mu_1} \delta_{v_2 v_3 \dots v_m}^{\mu_2 \mu_3 \dots \mu_m} - \delta_{v_1}^{\mu_2} \delta_{v_2 v_3 \dots v_m}^{\mu_1 \mu_3 \dots \mu_m} + \delta_{v_1}^{\mu_3} \delta_{v_2 v_3 \dots v_m}^{\mu_1 \mu_2 \dots \mu_m} - \dots + (-1)^{(m+1)} \delta_{v_1}^{\mu_m} \delta_{v_2 v_3 \dots v_m}^{\mu_1 \mu_2 \dots \mu_{m-1}} \quad (\text{A.47})$$

From the property of determinant, we can see that this generalized Kronecker delta is completely antisymmetric under the interchange of any two upper (or lower) indices. Here we have presented the determinant with the subscripts of indices of μ 's as row numbers and of v 's as column numbers. But it could also be written in the other way around as from the property of determinant we can interchange rows and columns.

For m linearly independent vectors $q_1, q_2, q_3, \dots, q_m$, let us define the following dual vectors $u_1^\mu = \frac{\delta_{q_1 q_2 q_3 \dots q_m}^{\mu q_2 q_3 \dots q_m}}{\delta_{q_1 q_2 q_3 \dots q_m}^{q_1 q_2 q_3 \dots q_m}}$, $u_2^\mu = \frac{\delta_{q_1 q_2 q_3 \dots q_m}^{\mu q_1 q_3 \dots q_m}}{\delta_{q_1 q_2 q_3 \dots q_m}^{q_1 q_2 q_3 \dots q_m}}$, ..., $u_m^\mu = \frac{\delta_{q_1 q_2 q_3 \dots q_m}^{\mu q_1 q_2 q_3 \dots q_{m-1}}}{\delta_{q_1 q_2 q_3 \dots q_m}^{q_1 q_2 q_3 \dots q_m}}$. It follows from the definition of u vectors that $u_i \cdot q_j = \delta_{ij}$.

$$\begin{aligned}
&= \left(\delta_v^\mu - q_1^\mu u_{1v} - q_2^\mu u_{2v} - \dots - q_m^\mu u_{mv} \right) \\
\Rightarrow \omega_v^\mu &= \left(\delta_v^\mu - \sum_{i=1}^m q_i^\mu u_{iv} \right) \tag{A.50}
\end{aligned}$$

Alternatively, ω_v^μ can be written in the following way

$$\begin{aligned}
\omega_v^\mu &= \frac{(-1)^{(2m)} \delta_v^{\mu q_1 q_2 \dots q_m}}{\delta_{q_1 q_2 \dots q_m}^{q_1 q_2 \dots q_m}} \quad [\text{using Eq. A.49}] \\
&= \frac{1}{\delta_{q_1 q_2 \dots q_m}^{q_1 q_2 \dots q_m}} \left(\delta_v^\mu \delta_{q_1 q_2 \dots q_m}^{q_1 q_2 \dots q_m} - \delta_v^{q_1} \delta_{q_1 q_2 \dots q_m}^{\mu q_2 \dots q_m} + \delta_v^{q_2} \delta_{q_1 q_2 \dots q_m}^{\mu q_1 \dots q_m} - \dots + (-1)^{(1+m+1)} \delta_v^{q_m} \delta_{q_1 q_2 \dots q_m}^{\mu q_1 \dots q_{m-1}} \right) \\
&\quad [\text{using Eq. A.47}] \\
&= \frac{1}{\delta_{q_1 q_2 \dots q_m}^{q_1 q_2 \dots q_m}} \left(\delta_v^\mu \delta_{q_1 q_2 \dots q_m}^{q_1 q_2 \dots q_m} - \delta_v^{q_1} \delta_{q_1 q_2 \dots q_m}^{\mu q_2 \dots q_m} - \delta_v^{q_2} \delta_{q_1 q_2 \dots q_m}^{\mu q_1 \dots q_m} - \dots \right. \\
&\quad \left. + (-1)^{(1+m+1)} (-1)^{(m-1)} \delta_v^{q_m} \delta_{q_1 q_2 \dots q_m}^{\mu q_1 \dots q_{m-1}} \right) \\
&= \left(\delta_v^\mu - \delta_v^{q_1} u_1^\mu - \delta_v^{q_2} u_2^\mu - \dots - \delta_v^{q_m} u_m^\mu \right) \\
&= \left(\delta_v^\mu - q_{1v} u_1^\mu - q_{2v} u_2^\mu - \dots - q_{mv} u_m^\mu \right) \\
\Rightarrow \omega_v^\mu &= \left(\delta_v^\mu - \sum_{i=1}^m q_{iv} u_i^\mu \right) \tag{A.51}
\end{aligned}$$

ω_v^μ holds these properties:

$$\boxed{\omega_v^\mu q_j^\nu = \omega_v^\mu u_{j\mu} = 0} \quad [\text{using Eq.A.50 and } q_i \cdot u_j = \delta_{ij}] \tag{A.52}$$

$$\boxed{\omega_v^\mu q_{j\mu} = \omega_v^\mu u_j^\nu = 0} \quad [\text{using Eq.A.51 and } q_i \cdot u_j = \delta_{ij}] \tag{A.53}$$

$$\begin{aligned}
\omega_v^\mu \omega_\rho^\nu &= (\delta_v^\mu - q_{iv} u_i^\mu)(\delta_\rho^\nu - q_{j\rho} u_j^\nu) \quad [\text{using Eq.A.51}] \\
&= (\delta_v^\mu \delta_\rho^\nu - \delta_v^\mu q_{j\rho} u_j^\nu - q_{iv} u_i^\mu \delta_\rho^\nu + q_{iv} u_i^\mu q_{j\rho} u_j^\nu) \\
&= (\delta_\rho^\mu - q_{j\rho} u_j^\mu - q_{i\rho} u_i^\mu + q_{iv} u_j^\nu u_i^\mu q_{j\rho}) \\
&= \left(\delta_\rho^\mu - 2q_{i\rho} u_i^\mu + (q_i \cdot u_j) u_i^\mu q_{j\rho} \right) \\
&= \left(\delta_\rho^\mu - 2q_{i\rho} u_i^\mu + u_i^\mu q_{i\rho} \right) \quad [\text{using } q_i \cdot u_j = \delta_{ij}] \\
&= \left(\delta_\rho^\mu - q_{i\rho} u_i^\mu \right) \\
\Rightarrow \boxed{\omega_v^\mu \omega_\rho^\nu &= \omega_\rho^\mu} \tag{A.54}
\end{aligned}$$

$$\begin{aligned}
\omega_\mu^\mu &= (\delta_\mu^\mu - \sum_{i=1}^m q_{i\mu} u_i^\mu) \\
&= (D - \sum_{i=1}^m \delta_{ii}) \\
\Rightarrow \boxed{\omega_\mu^\mu &= (D - m)} \tag{A.55}
\end{aligned}$$

Using Eq. A.51 for ω_v^μ , we have $\delta_v^\mu = \left(\sum_{i=1}^m u_i^\mu q_{iv} + \omega_v^\mu \right)$. So, contracting both sides of this with Q_v , we have ⁸

$$\boxed{Q^\mu = \left(\sum_{i=1}^m u_i^\mu Q \cdot q_i + \omega_Q^\mu \right)}, \tag{A.56}$$

which is known as *van Neerven Vermaseren decomposition* .

We are now to ready explain the Oldenborg-Vermaseren reduction technique.

⁸If we need Q_v , we will choose Eq. A.50 as that has $\sum_{i=1}^m u_{iv} q_i^\mu$ which would give $Q \cdot q_i$, the most sought after object in tensor reduction, when contracted with Q_μ on both sides.

A.3 Tensor integral reduction using Oldenborg-Vermaseren Technique

We will start from box integrals as has been done in the original paper Ref. [66].

A.3.1 Box integrals

There are three independent vectors q_1 , q_2 , and q_3 for the box integrals. So dimension of the physical space is 3 and transverse space is $D - 3$, which is 1 for $D=4$ dimension. Using Eq. A.56, here Q can be written as

$$Q^\mu = \left(\sum_{i=1}^3 u_i^\mu Q \cdot q_i + \omega_Q^\mu \right), \quad (\text{A.57})$$

where the dual vectors are given by $u_1^\mu = \frac{\delta_{q_1 q_2 q_3}^{\mu q_3}}{\delta_{q_1 q_2 q_3}^{q_3}}$, $u_2^\mu = \frac{\delta_{q_1 q_2 q_3}^{q_1 \mu}}{\delta_{q_1 q_2 q_3}^{q_1}}$, $u_3^\mu = \frac{\delta_{q_1 q_2 q_3}^{q_1 q_2 \mu}}{\delta_{q_1 q_2 q_3}^{q_1 q_2}}$. The projective tensor is given by $\omega_v^\mu = \frac{\delta_{q_1 q_2 q_3}^{q_1 q_2 q_3 \mu}}{\delta_{q_1 q_2 q_3}^{q_1 q_2 q_3}}$.

We will rewrite Eq. A.57 in the following notation in order to shorten the expression

$$Q^\mu = Y_3^\mu + \omega_Q^\mu, \quad (\text{A.58})$$

where $Y_3^\mu = \sum_{i=1}^3 u_i^\mu Q \cdot q_i$. Note that Y here is same as \mathcal{P} in Eq. (100) of Ref. [66]. It can

be also be written in another way

$$\begin{aligned}
Y_3^\mu &= Q \cdot q_1 \frac{\delta_{q_1 q_2 q_3}^{\mu q_2 q_3}}{\delta_{q_1 q_2 q_3}^{q_1 q_2 q_3}} + Q \cdot q_2 \frac{\delta_{q_1 q_2 q_3}^{q_1 \mu q_3}}{\delta_{q_1 q_2 q_3}^{q_1 q_2 q_3}} + Q \cdot q_3 \frac{\delta_{q_1 q_2 q_3}^{q_1 q_2 \mu}}{\delta_{q_1 q_2 q_3}^{q_1 q_2 q_3}} \\
&= \frac{1}{\delta_{q_1 q_2 q_3}^{q_1 q_2 q_3}} \left(Q \cdot q_1 \delta_{q_1 q_2 q_3}^{\mu q_2 q_3} + Q \cdot q_2 \delta_{q_1 q_2 q_3}^{q_1 \mu q_3} + Q \cdot q_3 \delta_{q_1 q_2 q_3}^{q_1 q_2 \mu} \right) \\
&= \frac{1}{\delta_{q_1 q_2 q_3}^{q_1 q_2 q_3}} \left(\delta_Q^{q_1} \delta_{q_1 q_2 q_3}^{\mu q_2 q_3} + \delta_Q^{q_2} \delta_{q_1 q_2 q_3}^{q_1 \mu q_3} + \delta_Q^{q_3} \delta_{q_1 q_2 q_3}^{q_1 q_2 \mu} \right) \\
&= \frac{1}{\delta_{q_1 q_2 q_3}^{q_1 q_2 q_3}} \left(\delta_Q^{q_1} \delta_{q_1 q_2 q_3}^{\mu q_2 q_3} + \delta_Q^{q_2} \delta_{q_1 q_2 q_3}^{q_1 \mu q_3} + \delta_Q^{q_3} \delta_{q_1 q_2 q_3}^{q_1 q_2 \mu} \right) \\
&= \frac{1}{\delta_{q_1 q_2 q_3}^{q_1 q_2 q_3}} \left(\delta_Q^{q_1} \frac{1}{2} (q_{2\alpha} q_{3\beta} - q_{3\alpha} q_{2\beta}) \delta_{q_1 q_2 q_3}^{\mu \alpha \beta} \right. \\
&\quad \left. + \delta_Q^{q_2} \frac{1}{2} (q_{1\alpha} q_{3\beta} - q_{3\alpha} q_{1\beta}) \delta_{q_1 q_2 q_3}^{\alpha \mu \beta} + \delta_Q^{q_3} \frac{1}{2} (q_{1\alpha} q_{2\beta} - q_{2\alpha} q_{1\beta}) \delta_{q_1 q_2 q_3}^{\alpha \beta \mu} \right) \\
&= \frac{1}{2 \delta_{q_1 q_2 q_3}^{q_1 q_2 q_3}} \left(\delta_Q^{q_1} \delta_{\alpha \beta}^{q_2 q_3} - \delta_Q^{q_2} \delta_{\alpha \beta}^{q_1 q_3} + \delta_Q^{q_3} \delta_{\alpha \beta}^{q_1 q_2} \right) \delta_{q_1 q_2 q_3}^{\mu \alpha \beta} \\
\Rightarrow Y_3^\mu &= \frac{1}{2 \delta_{q_1 q_2 q_3}^{q_1 q_2 q_3}} \delta_{Q \alpha \beta}^{q_1 q_2 q_3} \delta_{q_1 q_2 q_3}^{\mu \alpha \beta}. \tag{A.59}
\end{aligned}$$

In Eq. A.57, we will replace $Q \cdot q_i$ in terms of denominator factors and f_i using Eq. A.5, Eq. A.16 and Eq. A.39. Instead of f_i 's, we will sometime use $2s_1 \cdot q_i$ so that we can use Eq. A.59 like shorthand for the expression of Y_3^μ , where s_1 is a vector which obeys these relations $s_1^2 = m_1^2$, $(s_1 + q_1)^2 = m_2^2$, $(s_1 + q_2)^2 = m_3^2$, and $(s_1 + q_3)^2 = m_4^2$.⁹

⁹This s_1 has been used so that compact expression for Y can be written. This is not same as loop momentum Q as that can take any value, while s_1 can take only fixed value so that it obeys these relations.

So Y_3 can be written as

$$\begin{aligned}
Y_3^\mu &= \sum_{i=1}^3 u_i^\mu Q \cdot q_i \\
&= \sum_{i=1}^3 u_i^\mu \frac{1}{2} (N_{i+1} - N_1 + f_i) \quad [\text{using Eq. A.5, Eq. A.16, and Eq. A.39}] \\
&= \sum_{i=1}^3 u_i^\mu \frac{1}{2} (N_{i+1} - N_1 + f_i) \quad [\text{using Eq. A.5, Eq. A.16, and Eq. A.39}] \\
\Rightarrow Y_3^\mu &= \frac{1}{2} \sum_{i=1}^3 u_i^\mu f_i + \frac{1}{2} (N_4 u_3^\mu + N_3 u_2^\mu + N_2 u_1^\mu) - \frac{1}{2} N_1 (u_3^\mu + u_2^\mu + u_1^\mu) \quad (\text{A.60})
\end{aligned}$$

In the above we could write $\frac{1}{2} \sum_{i=1}^3 u_i^\mu f_i = \sum_{i=1}^3 u_i s_1 \cdot q_i = \frac{\frac{1}{2}}{\delta_{q_1 q_2 q_3}^{q_1 q_2 q_3}} \delta_{s_1 \alpha \beta}^{\mu \alpha \beta} \delta_{q_1 q_2 q_3}^{\mu \alpha \beta}$ as well.¹⁰

But Eq. A.60 in its current form is also okay as far as the tensor reduction is concerned.

In the following, we will frequently use Eq. A.58, the structure in RHS of Eq. A.60 and projective tensor w_ν^μ 's properties Eq. A.52, Eq. A.53, Eq. A.54, and Eq. A.55.

rank-one Box integral

$$\begin{aligned}
D^\mu(1, 2, 3, 4) &= \int \frac{d^D Q Q^\mu}{N_1 N_2 N_3 N_4} \\
&= \int \frac{d^D Q (Y_3^\mu + w_Q^\mu)}{N_1 N_2 N_3 N_4} \quad [\text{using Eq. A.58}] \\
&= \int \frac{d^D Q Y_3^\mu}{N_1 N_2 N_3 N_4} + w_\alpha^\mu \int \frac{d^D Q Q^\alpha}{N_1 N_2 N_3 N_4} \\
&= \int \frac{d^D Q Y_3^\mu}{N_1 N_2 N_3 N_4} + \underbrace{w_\alpha^\mu (D_1 q_1^\alpha + D_2 q_2^\alpha + D_3 q_3^\alpha)}_{=0 \quad [\text{see Eq. A.52}]} \quad [\text{see Eq. A.35}] \\
&= \int \frac{d^D Q Y_3^\mu}{N_1 N_2 N_3 N_4} \quad (\text{A.61})
\end{aligned}$$

As Y_3^μ has a term without any Q dependence, and N_1, N_2, N_3, N_4 (see Eq. A.60), we

¹⁰The last equality can be found following the same procedure as in Eq. A.59 using s_1 instead of Q .

can write the Eq. A.61 in terms of box and triangle scalar integrals, as was also found in the Passarino-Veltman technique in Eq. A.40. If we decompose the deltas, here we should get exactly what we got in the Passarino-Veltman technique. But computing these deltas directly is more suitable to handle numerical instability problem as that ensures less number of cancellation between scalar integrals which are also potential source of a numerical instability besides the dual vectors [66].

rank-two Box integral

Here we will use underline notation to mean integration over loop momenta. For example, $D^{\mu\nu}(1,2,3,4) = \int \frac{d^D Q}{N_1 N_2 N_3 N_4} \underline{Q}^\mu \underline{Q}^\nu = \underline{Q}^\mu \underline{Q}^\nu$.

$$\begin{aligned} \underline{Q}^\mu \underline{Q}^\nu &= \underline{Q}^\mu (Y_3^\nu + w_Q^\nu) \\ &= \underline{Q}^\mu Y_3^\nu + \underline{Q}^\mu w_Q^\nu \\ &= \underline{Q}^\mu Y_3^\nu + \underline{Y_3^\mu w_Q^\nu} + \underline{w_Q^\mu w_Q^\nu} \end{aligned} \tag{A.62}$$

Let's start from $Y_3^\mu w_Q^\nu$

$$\begin{aligned} \underline{Y_3^\mu w_Q^\nu} &= \frac{1}{2} \left(\sum_{i=1}^3 u_i^\mu f_i + (N_4 u_3^\mu + N_3 u_2^\mu + N_2 u_1^\mu) - N_1 (u_3^\mu + u_2^\mu + u_1^\mu) \right) w_Q^\nu \\ &= \frac{1}{2} \left(\sum_{i=1}^3 u_i^\mu f_i D^\alpha(1,2,3,4) + (u_3^\mu C^\alpha(1,2,3) + u_2^\mu C^\alpha(1,2,4) + u_1^\mu C^\alpha(1,3,4)) \right. \\ &\quad \left. - (u_3^\mu + u_2^\mu + u_1^\mu) (C^\alpha(2,3,4) - q_1^\alpha C_0(2,3,4)) \right) w_\alpha^\nu \\ \Rightarrow \underline{Y_3^\mu w_Q^\nu} &= 0 \end{aligned} \tag{A.63}$$

The last line follows from the tensor structure of rank-one tensors (see Eq. A.35, Eq. A.11)

and using property of projective tensor (see Eq. A.52). As the last derivation did not depend on μ and ν (alternatively, interchanging μ and ν in Eq. A.63), we have $\underline{Y_3^\nu w_Q^\mu} = 0$.

Now we will evaluate $\underline{w_Q^\mu w_Q^\nu}$ in Eq. A.62,

$$\begin{aligned}
\underline{w_Q^\mu w_Q^\nu} &= \underline{w_{\alpha 1}^\mu w_{\alpha 2}^\nu Q^{\alpha 1} Q^{\alpha 2}} \\
&= w_{\alpha 1}^\mu w_{\alpha 2}^\nu \underline{Q^{\alpha 1} Q^{\alpha 2}} \quad [\text{as } w_{\alpha 1}^\mu \text{ and } w_{\alpha 2}^\nu \text{ do not depend on } Q] \\
&= w_{\alpha 1}^\mu w_{\alpha 2}^\nu D^{\alpha 1 \alpha 2} \\
&= w_{\alpha 1}^\mu w_{\alpha 2}^\nu D_{00} g^{\alpha 1 \alpha 2} \quad [\text{using Eq. A.36 and Eq. A.52}] \\
&= D_{00} w_{\alpha 1}^\mu w^{\alpha 1 \nu} \\
&= D_{00} w_{\alpha 1}^\mu w_\sigma^{\alpha 1} g^{\sigma \nu} \\
\Rightarrow \underline{w_Q^\mu w_Q^\nu} &= D_{00} w^{\mu \nu} \quad (A.64)
\end{aligned}$$

So, using Eq. A.58 and Eq. A.64, Eq. A.62 can be written as

$$\underline{Q^\mu Q^\nu} = \underline{Q^\mu Y_3^\nu} + D_{00} w^{\mu \nu} \quad (A.65)$$

Although D_{00} as found in Passarino-Veltman technique could be used, but everything is expressed here in terms of Y and hence we will determine it also in terms of Y .

We will start from Eq. A.65

$$\begin{aligned}
\underline{Q}^\mu \underline{Q}^\nu &= \underline{Q}^\mu Y_3^\nu + D_{00} w^{\mu\nu} \\
\Rightarrow \underline{Q}^\mu \underline{Q}_\nu &= \underline{Y}_3^\mu Y_3^\nu + D_{00} w^{\mu\nu} \quad [\text{as } \underline{w}_Q^\mu Y_3^\nu = 0 \text{ (see Eq. A.63)}] \\
\Rightarrow \underline{Q}^\mu \underline{Q}_\mu &= \underline{Y}_3^\mu Y_{3\mu} + D_{00} w_\mu^\mu \quad [\text{contracting with } g_{\mu\nu}] \\
\Rightarrow \underline{Q}^2 &= \underline{Y}_3^2 + D_{00}(D-3) \\
\Rightarrow D_{00} &= \frac{1}{D-3} \underline{Q}^2 - \underline{Y}_3^2
\end{aligned} \tag{A.66}$$

So Eq. A.65 can be written as

$$\underline{Q}^\mu \underline{Q}^\nu = \underline{Q}^\mu Y_3^\nu + \frac{w^{\mu\nu}}{D-3} \underline{Q}^2 - \underline{Y}_3^2 \tag{A.67}$$

Using Eq. A.60, we can write $\underline{Q}^\mu Y_3^\nu$ in terms of rank-one box integral and four rank-one triangle integrals. In one of the triangle integrals in which N_1 is not present in the denominator, the loop momentum Q needs to be shifted so that the standard reduction formula can be used. Then all these integrals can be written in terms of master scalar integrals.

Now we will find $\underline{Q}^2 - \underline{Y}_3^2$. Let's first find \underline{Q}^2 first,

$$\begin{aligned}
\underline{Q^2} &= \int \frac{d^D Q Q^2}{N_1 N_2 N_3 N_4} \\
&= \int \frac{d^D Q (N_1 + m_1^2)}{N_1 N_2 N_3 N_4} \\
&= \int \frac{d^D Q (N_1 + \delta_{s_1}^{s_1})}{N_1 N_2 N_3 N_4} \\
&= \int \frac{d^D Q}{N_2 N_3 N_4} + \int \frac{d^D Q \delta_{s_1}^{s_1}}{N_1 N_2 N_3 N_4}
\end{aligned}
\tag{A.68}$$

Next we will find $\underline{Y_3^2}$,

$$\begin{aligned}
\underline{Y_3^2} &= \int \frac{d^D Q Y_3^2}{N_1 N_2 N_3 N_4} \\
&= \int \frac{d^D Q Y_{3\mu} Y_3^\mu}{N_1 N_2 N_3 N_4} \\
&= \int \frac{d^D Q Y_{3\mu} \frac{1}{2} \left(\sum_{i=1}^3 u_i^\mu f_i + (N_4 u_3^\mu + N_3 u_2^\mu + N_2 u_1^\mu) - N_1 (u_3^\mu + u_2^\mu + u_1^\mu) \right)}{N_1 N_2 N_3 N_4} \\
&= \frac{1}{2} \left(\sum_{i=1}^3 u_i^\mu f_i \right) \int \frac{d^D Q Y_{3\mu}}{N_1 N_2 N_3 N_4} + \frac{1}{2} \int \frac{d^D Q Y_{3\mu} (N_4 u_3^\mu + N_3 u_2^\mu + N_2 u_1^\mu)}{N_1 N_2 N_3 N_4} \\
&\quad - \frac{1}{2} \int \frac{d^D Q Y_{3\mu} N_1 (u_3^\mu + u_2^\mu + u_1^\mu)}{N_1 N_2 N_3 N_4} \\
&= \frac{1}{2} \left(\sum_{i=1}^3 u_i^\mu f_i \right) \int \frac{d^D Q Y_{3\mu}}{N_1 N_2 N_3 N_4} + \frac{1}{2} \int \frac{d^D Q Q_\mu (N_4 u_3^\mu + N_3 u_2^\mu + N_2 u_1^\mu)}{N_1 N_2 N_3 N_4} \\
&\quad - \frac{1}{2} \int \frac{d^D Q Q_\mu N_1 (u_3^\mu + u_2^\mu + u_1^\mu)}{N_1 N_2 N_3 N_4} \quad [\text{as } Y_{3\mu} = Q_\mu - w_\mu^Q \text{ and } w_\mu^Q u_i^\mu = 0]
\end{aligned}
\tag{A.69}$$

Let's calculate second part of the above equation

$$\begin{aligned}
& \int \frac{d^D Q Q_\mu (N_4 u_3^\mu + N_3 u_2^\mu + N_2 u_1^\mu)}{N_1 N_2 N_3 N_4} \\
&= u_3^\mu \int \frac{d^D Q Q_\mu}{N_1 N_2 N_3} + u_2^\mu \int \frac{d^D Q Q_\mu}{N_1 N_2 N_4} + u_1^\mu \int \frac{d^D Q Q_\mu}{N_1 N_3 N_4} \\
&= u_3^\mu C_\mu(q1, q2; 1, 2, 3) + u_2^\mu C_\mu(q1, q3; 1, 2, 4) + u_1^\mu C_\mu(q2, q3; 1, 3, 4) \\
&= u_3^\mu (C_1(1, 2, 3)q_{1\mu} + C_2(1, 2, 3)q_{2\mu}) + u_2^\mu (C_1(1, 2, 4)q_{1\mu} + C_2(1, 2, 4)q_{3\mu}) \\
&\quad + u_1^\mu (C_1(1, 3, 4)q_{2\mu} + C_2(1, 3, 4)q_{3\mu}) \\
&= 0 \quad [\text{as } u_i \cdot q_j = \delta_{ij}] \tag{A.70}
\end{aligned}$$

Let's calculate third part of Eq. A.69

$$\begin{aligned}
& \int \frac{d^D Q Q_\mu N_1 (u_3^\mu + u_2^\mu + u_1^\mu)}{N_1 N_2 N_3 N_4} \\
&= \int \frac{d^D Q Q_\mu (u_3^\mu + u_2^\mu + u_1^\mu)}{N_2 N_3 N_4} \\
&= \int \frac{d^D Q (Q_\mu - q_{1\mu})(u_3^\mu + u_2^\mu + u_1^\mu)}{(Q^2 - m_2^2)((Q + q2 - q1)^2 - m_3^2)((Q + q3 - q1)^2 - m_4^2)} \\
&= \int \frac{d^D Q (Q_\mu - q_{1\mu})(u_3^\mu + u_2^\mu + u_1^\mu)}{(Q^2 - m_2^2)((Q + q2 - q1)^2 - m_3^2)((Q + q3 - q1)^2 - m_4^2)} \\
&= \int \frac{d^D Q Q_\mu (u_3^\mu + u_2^\mu + u_1^\mu)}{(Q^2 - m_2^2)((Q + q2 - q1)^2 - m_3^2)((Q + q3 - q1)^2 - m_4^2)} \\
&\quad - \int \frac{d^D Q}{(Q^2 - m_2^2)((Q + q2 - q1)^2 - m_3^2)((Q + q3 - q1)^2 - m_4^2)} \quad [\text{as } u_i \cdot q_j = \delta_{ij}] \\
&= C_\mu(q2 - q1, q3 - q1; 2, 3, 4)(u_3^\mu + u_2^\mu + u_1^\mu) \\
&\quad - \int \frac{d^D Q}{N_2 N_3 N_4} \quad [\text{shifting } Q \text{ in the last integral by } +q_1] \\
&= (C_1(2, 3, 4)(q_{2\mu} - q_{1\mu}) + C_2(2, 3, 4)(q_{3\mu} - q_{1\mu}))(u_3^\mu + u_2^\mu + u_1^\mu) - \int \frac{d^D Q}{N_2 N_3 N_4} \\
&= (C_1(2, 3, 4)(1 - 1) + C_2(2, 3, 4)(1 - 1))(u_3^\mu + u_2^\mu + u_1^\mu) - \int \frac{d^D Q}{N_2 N_3 N_4} \quad [\text{as } u_i \cdot q_j = \delta_{ij}] \\
&= (0)(u_3^\mu + u_2^\mu + u_1^\mu) - \int \frac{d^D Q}{N_2 N_3 N_4}
\end{aligned}$$

$$= - \int \frac{d^D Q}{N_2 N_3 N_4} \quad (\text{A.71})$$

So using Eq.A.70 and Eq.A.71, Eq. A.69 becomes

$$\begin{aligned}
& \underline{Y_3^2} \\
&= \frac{1}{2} \left(\sum_{i=1}^3 u_i^\mu f_i \right) \int \frac{d^D Q}{N_1 N_2 N_3 N_4} Y_{3\mu} + \frac{1}{2} \int \frac{d^D Q}{N_2 N_3 N_4} \\
&= \frac{1}{2} \left(\sum_{i=1}^3 u_i^\mu f_i \right) \int \frac{d^D Q \frac{1}{2} \left(\sum_{j=1}^3 u_{j\mu} f_j + (N_4 u_{3\mu} + N_3 u_{2\mu} + N_2 u_{1\mu}) - N_1 (u_{3\mu} + u_{2\mu} + u_{1\mu}) \right)}{N_1 N_2 N_3 N_4} \\
&\quad + \frac{1}{2} \int \frac{d^D Q}{N_2 N_3 N_4} \\
&= \left(\sum_{i=1}^3 u_i^\mu s_1 \cdot q_i \right) \times \\
&\quad \int \frac{d^D Q \left(\sum_{j=1}^3 u_{j\mu} s_1 \cdot q_j + \frac{1}{2} (N_4 u_{3\mu} + N_3 u_{2\mu} + N_2 u_{1\mu}) - \frac{1}{2} N_1 (u_{3\mu} + u_{2\mu} + u_{1\mu}) \right)}{N_1 N_2 N_3 N_4} \\
&\quad + \frac{1}{2} \int \frac{d^D Q}{N_2 N_3 N_4} \quad [\text{as } f_i = 2s_1 \cdot q_i] \\
&= \int d^D Q \frac{(s_1 \cdot q_i)(s_1 \cdot q_j u_j \cdot u_i)}{N_1 N_2 N_3 N_4} + \frac{1}{2} \int d^D Q \frac{(s_1 \cdot q_i)(u_i \cdot u_3)}{N_1 N_2 N_3} + \frac{1}{2} \int d^D Q \frac{(s_1 \cdot q_i)(u_i \cdot u_2)}{N_1 N_2 N_4} \\
&+ \frac{1}{2} \int d^D Q \frac{(s_1 \cdot q_i)(u_i \cdot u_1)}{N_1 N_3 N_4} - \frac{1}{2} \int d^D Q \frac{(s_1 \cdot q_i)(u_i \cdot u_3 + u_i \cdot u_2 + u_i \cdot u_1) - 1}{N_2 N_3 N_4} \quad (\text{A.72})
\end{aligned}$$

So using Eq. A.68 and Eq. A.72, we can write

$$\begin{aligned}
& \underline{Q^2 - Y_3^2} \\
&= \int d^D Q \frac{\delta_{s_1}^{s_1} - (s_1 \cdot q_i)(s_1 \cdot q_j u_j \cdot u_i)}{N_1 N_2 N_3 N_4} - \frac{1}{2} \int d^D Q \frac{(s_1 \cdot q_i)(u_i \cdot u_3)}{N_1 N_2 N_3} - \frac{1}{2} \int d^D Q \frac{(s_1 \cdot q_i)(u_i \cdot u_2)}{N_1 N_2 N_4} \\
&- \frac{1}{2} \int d^D Q \frac{(s_1 \cdot q_i)(u_i \cdot u_1)}{N_1 N_3 N_4} + \frac{1}{2} \int d^D Q \frac{(s_1 \cdot q_i)(u_i \cdot u_3 + u_i \cdot u_2 + u_i \cdot u_1) + 1}{N_2 N_3 N_4} \quad (\text{A.73})
\end{aligned}$$

Before calculating Eq. A.73, let us derive dot product of dual vectors

$$\begin{aligned}
u_1 \cdot u_1 &= u_1^\mu u_{1\mu} \\
&= u_1^\mu \frac{\delta_{\mu q_2 q_3}^{q_1 q_2 q_3}}{\Delta_3} \\
&= \frac{u_1^\mu (q_{1\mu} \delta_{q_2 q_3}^{q_2 q_3} - q_{2\mu} \delta_{q_2 q_3}^{q_1 q_3} + q_{3\mu} \delta_{q_2 q_3}^{q_1 q_2})}{\Delta_3} \\
&= \frac{\delta_{q_2 q_3}^{q_2 q_3}}{\Delta_3}
\end{aligned}$$

Similarly $u_2 \cdot u_1 = -\frac{\delta_{q_2 q_3}^{q_1 q_3}}{\Delta_3}$ and $u_3 \cdot u_1 = \frac{\delta_{q_2 q_3}^{q_1 q_2}}{\Delta_3}$. $u_2 \cdot u_2 = u_2^\mu \frac{\delta_{q_1 \mu q_3}^{q_1 q_2 q_3}}{\Delta_3} = \frac{\delta_{q_1 q_3}^{q_1 q_3}}{\Delta_3}$ and $u_3 \cdot u_2 = -\frac{\delta_{q_1 q_3}^{q_1 q_2}}{\Delta_3}$. $u_3 \cdot u_3 = u_3^\mu \frac{\delta_{q_1 q_2 \mu}^{q_1 q_2 q_3}}{\Delta_3} = \frac{\delta_{q_1 q_2}^{q_1 q_2}}{\Delta_3}$. So dual vectors are neither orthogonal nor normalized.

The same is true for q_1, q_2, q_3 .

After having calculated the dot products of dual vectors, let's compute the numerators of Eq. A.73,

$$\begin{aligned}
&(s_1 \cdot q_i)(u_i \cdot u_3) \\
&= s_1 \cdot q_1 u_1 \cdot u_3 + s_1 \cdot q_2 u_2 \cdot u_3 + s_1 \cdot q_3 u_3 \cdot u_3 \\
&= s_1 \cdot q_1 \frac{\delta_{q_2 q_3}^{q_1 q_2}}{\Delta_3} + s_1 \cdot q_2 \left(-\frac{\delta_{q_1 q_3}^{q_1 q_2}}{\Delta_3}\right) + s_1 \cdot q_3 \frac{\delta_{q_1 q_2}^{q_1 q_2}}{\Delta_3} \\
&= \frac{\delta_{q_1}^{s_1} \delta_{q_2 q_3}^{q_1 q_2}}{\Delta_3} - \frac{\delta_{q_2}^{s_1} \delta_{q_1 q_3}^{q_1 q_2}}{\Delta_3} + \frac{\delta_{q_3}^{s_1} \delta_{q_1 q_2}^{q_1 q_2}}{\Delta_3} \\
&= \frac{\delta_{q_1 q_2 q_3}^{s_1 q_1 q_2}}{\Delta_3}
\end{aligned}$$

Similarly,

$$(s_1 \cdot q_i)(u_i \cdot u_2) = -\frac{\delta_{q_1}^{s_1} \delta_{q_2 q_3}^{q_1 q_3}}{\Delta_3} + \frac{\delta_{q_2}^{s_1} \delta_{q_1 q_3}^{q_1 q_3}}{\Delta_3} - \frac{\delta_{q_3}^{s_1} \delta_{q_1 q_2}^{q_1 q_3}}{\Delta_3} = -\frac{\delta_{q_1 q_2 q_3}^{s_1 q_1 q_3}}{\Delta_3}$$

and

$$(s_1 \cdot q_i)(u_i \cdot u_1) = \frac{\delta_{q_1}^{s_1} \delta_{q_2 q_3}^{q_2 q_3}}{\Delta_3} - \frac{\delta_{q_2}^{s_1} \delta_{q_1 q_3}^{q_2 q_3^2}}{\Delta_3} + \frac{\delta_{q_3}^{s_1} \delta_{q_1 q_2}^{q_2 q_3}}{\Delta_3} = \frac{\delta_{q_1 q_2 q_3}^{s_1 q_2 q_3}}{\Delta_3}$$

Using above equations, we have

$$\begin{aligned} & \delta_{s_1}^{s_1} - (s_1 \cdot q_i)(s_1 \cdot q_j u_j \cdot u_i) \\ &= \delta_{s_1}^{s_1} - (s_1 \cdot q_1)(s_1 \cdot q_j u_j \cdot u_1) - (s_1 \cdot q_2)(s_1 \cdot q_j u_j \cdot u_2) - (s_1 \cdot q_3)(s_1 \cdot q_j u_j \cdot u_3) \\ &= \frac{\delta_{s_1}^{s_1} \Delta_3 - (s_1 \cdot q_1) \delta_{q_1 q_2 q_3}^{s_1 q_2 q_3} + (s_1 \cdot q_2) \delta_{q_1 q_2 q_3}^{s_1 q_1 q_3} - (s_1 \cdot q_3) \delta_{q_1 q_2 q_3}^{s_1 q_1 q_2}}{\Delta_3} \\ &= \frac{\delta_{s_1}^{s_1} \delta_{q_1 q_2 q_3}^{q_1 q_2 q_3} - \delta_{s_1}^{q_1} \delta_{q_1 q_2 q_3}^{s_1 q_2 q_3} + \delta_{s_1}^{q_2} \delta_{q_1 q_2 q_3}^{s_1 q_1 q_3} - \delta_{s_1}^{q_3} \delta_{q_1 q_2 q_3}^{s_1 q_1 q_2}}{\Delta_3} \\ &= \frac{\delta_{s_1 q_1 q_2 q_3}^{s_1 q_1 q_2 q_3}}{\Delta_3} \end{aligned} \tag{A.74}$$

Similarly,

$$\begin{aligned} & (s_1 \cdot q_i)(u_i \cdot u_3 + u_i \cdot u_2 + u_i \cdot u_1) + 1 \\ &= \frac{\delta_{q_1 q_2 q_3}^{s_1 q_1 q_2}}{\Delta_3} - \frac{\delta_{q_1 q_2 q_3}^{s_1 q_1 q_3}}{\Delta_3} + \frac{\delta_{q_1 q_2 q_3}^{s_1 q_2 q_3}}{\Delta_3} + 1 \\ &= \frac{\delta_{q_1 q_2 q_3}^{s_1 q_1 q_2} - \delta_{q_1 q_2 q_3}^{s_1 q_1 q_3} + \delta_{q_1 q_2 q_3}^{s_1 q_2 q_3} + \Delta_3}{\Delta_3} \\ &= \frac{-\delta_{q_1 q_2 q_3}^{s_1 q_1 (q_3 - q_2)} + \delta_{q_1 q_2 q_3}^{(s_1 + q_1) q_2 q_3}}{\Delta_3} \\ &= \frac{-\delta_{q_1 q_2 q_3}^{s_1 q_1 (q_3 - q_2)} + \delta_{q_1 q_2 q_3}^{s_2 q_2 q_3}}{\Delta_3} \quad [\text{where } s_2 = s_1 + q_1] \\ &= \frac{\delta_{q_1 q_2 q_3}^{s_2 q_2 q_3} - \delta_{q_1 q_2 q_3}^{s_1 q_1 (q_3 - q_2)}}{\Delta_3} \end{aligned}$$

Using all the above expressions in Eq. A.73, we have

$$\begin{aligned}
& \underline{Q^2 - Y_3^2} \\
&= \int d^D Q \frac{\delta_{s_1}^{s_1} - (s_1 \cdot q_i)(s_1 \cdot q_j) u_j \cdot u_i}{N_1 N_2 N_3 N_4} - \frac{1}{2} \int d^D Q \frac{(s_1 \cdot q_i)(u_i \cdot u_3)}{N_1 N_2 N_3} - \frac{1}{2} \int d^D Q \frac{(s_1 \cdot q_i)(u_i \cdot u_2)}{N_1 N_2 N_4} \\
&- \frac{1}{2} \int d^D Q \frac{(s_1 \cdot q_i)(u_i \cdot u_1)}{N_1 N_3 N_4} + \frac{1}{2} \int d^D Q \frac{(s_1 \cdot q_i)(u_i \cdot u_3 + u_i \cdot u_2 + u_i \cdot u_1) + 1}{N_2 N_3 N_4} \\
&= \frac{1}{\Delta_3} \int d^D Q \frac{\delta_{s_1 q_1 q_2 q_3}^{s_1 q_1 q_2 q_3}}{N_1 N_2 N_3 N_4} - \frac{1}{2\Delta_3} \int d^D Q \frac{\delta_{q_1 q_2 q_3}^{s_1 q_1 q_2}}{N_1 N_2 N_3} + \frac{1}{2\Delta_3} \int d^D Q \frac{\delta_{q_1 q_2 q_3}^{s_1 q_1 q_3}}{N_1 N_2 N_4} \\
&- \frac{1}{2\Delta_3} \int d^D Q \frac{\delta_{q_1 q_2 q_3}^{s_1 q_2 q_3}}{N_1 N_3 N_4} + \frac{1}{2\Delta_3} \int d^D Q \frac{\delta_{q_1 q_2 q_3}^{s_2 q_2 q_3} - \delta_{q_1 q_2 q_3}^{s_1 q_1 (q_3 - q_2)}}{N_2 N_3 N_4} \tag{A.75}
\end{aligned}$$

So, all the terms in Eq. A.67 can be reduced to scalar integrals.

rank-three Box integral

$$\begin{aligned}
\underline{Q^\mu Q^\nu Q^\sigma} &= \underline{Q^\mu Q^\nu (Y_3^\sigma + w_Q^\sigma)} \\
&= \underline{Q^\mu Q^\nu Y_3^\sigma} + \underline{Q^\mu Q^\nu w_Q^\sigma} \\
&= \underline{Q^\mu Q^\nu Y_3^\sigma} + \underline{Y_3^\mu Y_3^\nu w_Q^\sigma} + \underline{Y_3^\mu w_Q^\nu w_Q^\sigma} + \underline{Y_3^\nu w_Q^\mu w_Q^\sigma} + \underline{w_Q^\mu w_Q^\nu w_Q^\sigma} \tag{A.76}
\end{aligned}$$

In the above equation $\underline{Y_3^\mu Y_3^\nu w_Q^\sigma}$ and $\underline{w_Q^\mu w_Q^\nu w_Q^\sigma}$ are zero. To show it for $\underline{Y_3^\mu Y_3^\nu w_Q^\sigma}$, we can use $q_i \cdot Q u^{i\mu}$ and $u_j \cdot Q q^{j\nu}$ for Y_3^μ and Y_3^ν , respectively. The resulting three rank box integral must be zero as projective tensor, w , either contracts with q_i or u_i . Showing $\underline{w_Q^\mu w_Q^\nu w_Q^\sigma} = 0$ is very easy as at least one projective tensor contracts with q_i 's.

So Eq. A.76 becomes

$$\underline{Q^\mu Q^\nu Q^\sigma} = \underline{Q^\mu Q^\nu Y_3^\sigma} + \underline{Y_3^\mu w_Q^\nu w_Q^\sigma} + \underline{Y_3^\nu w_Q^\mu w_Q^\sigma} \tag{A.77}$$

We evaluate $\underline{Y_3^\mu w_Q^\nu w_Q^\sigma}$

$$\begin{aligned}
\underline{Y_3^\mu w_Q^\nu w_Q^\sigma} &= \underline{q_i^\mu u_{i\alpha 1} w_{\alpha 2}^\nu w_{\alpha 3}^\sigma Q^{\alpha 1} Q^{\alpha 2} Q^{\alpha 3}} \\
&= \underline{q_i^\mu u_{i\alpha 1} w_{\alpha 2}^\nu w_{\alpha 3}^\sigma Q^{\alpha 1} Q^{\alpha 2} Q^{\alpha 3}} \\
&= q_i^\mu u_{i\alpha 1} w_{\alpha 2}^\nu w_{\alpha 3}^\sigma D_{00j} g^{[\alpha 1 \alpha 2} q_j^{\alpha 3]} \\
&= q_i^\mu u_{i\alpha 1} w_{\alpha 2}^\nu w_{\alpha 3}^\sigma (D_{001} g^{\alpha 2 \alpha 3} q_1^{\alpha 1} + D_{002} g^{\alpha 2 \alpha 3} q_2^{\alpha 1} + D_{003} g^{\alpha 2 \alpha 3} q_3^{\alpha 1}) \quad [\text{as } w_{u_i}^\nu = 0] \\
&= w_{\alpha 2}^\nu w_{\alpha 3}^\sigma g^{\alpha 2 \alpha 3} (D_{001} q_1^\mu + D_{002} q_2^\mu + D_{003} q_3^\mu) \quad [\text{as } u_i \cdot q_j = \delta_{ij}] \\
&= w^{\nu \sigma} (D_{001} q_1^\mu + D_{002} q_2^\mu + D_{003} q_3^\mu) \tag{A.78}
\end{aligned}$$

Using above, we can write Eq. A.77 as

$$\begin{aligned}
\underline{Q^\mu Q^\nu Q^\sigma} &= \underline{Q^\mu Q^\nu Y_3^\sigma} + w^{\nu \sigma} (D_{001} q_1^\mu + D_{002} q_2^\mu + D_{003} q_3^\mu) \\
&\quad + w^{\mu \sigma} (D_{001} q_1^\nu + D_{002} q_2^\nu + D_{003} q_3^\nu) \tag{A.79}
\end{aligned}$$

We want to replace the unknown D_{00i} in terms of integrals. For that we contract ν and σ in the above equation

$$\begin{aligned}
\underline{Q^\mu Q^2} &= \underline{Q^\mu Q^\nu Y_{3\nu}} + w^{\nu \nu} (D_{001} q_1^\mu + D_{002} q_2^\mu + D_{003} q_3^\mu) \quad [\text{as } w^{\mu \nu} q_{i\nu} = 0] \\
\Rightarrow \underline{Q^\mu Q^2} &= \underline{Q^\mu Q^\nu Y_{3\nu}} + (D - 3)(D_{001} q_1^\mu + D_{002} q_2^\mu + D_{003} q_3^\mu) \quad [\text{as } w^{\mu \nu} q_{i\nu} = 0] \\
\Rightarrow \underline{(Y_3^\mu + w_Q^\mu) Q^2} &= \underline{Q^\mu (Y_3^\nu + w_Q^\nu) Y_{3\nu}} + (D - 3)(D_{001} q_1^\mu + D_{002} q_2^\mu + D_{003} q_3^\mu) \\
\Rightarrow \underline{Y_3^\mu Q^2} &= \underline{Q^\mu Y_3^\nu Y_{3\nu}} + (D - 3)(D_{001} q_1^\mu + D_{002} q_2^\mu + D_{003} q_3^\mu) \\
&\quad [\text{as } Y_3^\nu w_{\nu Q} = q_i \cdot Q u_i^\nu w_{\nu Q} = 0 \text{ and } \underline{w_Q^\mu Q^2} = \underline{w_Q^\mu (N_1 + m_1^2)} = 0]
\end{aligned}$$

$$\Rightarrow \underline{Y_3^\mu Q^2} = \underline{Y_3^\mu Y_3^\nu Y_{3\nu}} + (D-3)(D_{001}q_1^\mu + D_{002}q_2^\mu + D_{003}q_3^\mu)$$

$$[\text{as } \underline{w_Q^\mu Y_3^\nu Y_{3\nu}} = 0 \text{ as } \underline{Y_3^\mu Y_3^\nu w_Q^\sigma} = 0]$$

So, we have $(D_{001}q_1^\mu + D_{002}q_2^\mu + D_{003}q_3^\mu) = \frac{1}{D-3}Y_3^\mu(Q^2 - Y_3^2)$. Using this in Eq. A.79, we have

$$\boxed{\underline{Q^\mu Q^\nu Q^\sigma} = \underline{Q^\mu Q^\nu Y_3^\sigma} + w^{\nu\sigma} \frac{1}{D-3} Y_3^\mu (Q^2 - Y_3^2) + w^{\mu\sigma} \frac{1}{D-3} Y_3^\nu (Q^2 - Y_3^2)} \quad (\text{A.80})$$

The reduction of the first part of RHS of Eq. A.80 is straightforward. We use Eq. A.60 for Y^σ . Then we will have rank-two four-point and rank-two three-point functions, the expressions for which can be used to reduce it further. The reduction of the second part and third part follows exactly same procedure. Let's take second part for illustration. When A.60 is used for Y_3^μ , we will have four-point integrals and three-point integrals with $Q^2 - Y_3^2$ in the numerator for of them. For four-point integral we can use Eq. A.75. For three-point integrals, it is better to have $Q^2 - Y_2^2$ in the numerator, where Y_2 plays the same role for triangle integrals as what Y_3 plays for box integrals.

$$\begin{aligned} \int d^D Q \frac{Q^2 - Y_3^2}{N_1 N_2 N_3} &= \int d^D Q \frac{w_{3Q} Q}{N_1 N_2 N_3} \quad [\text{Squaring } Q^\mu = Y_3^\mu + w_3^\mu \text{ and noting } Y_3^\mu w_{3\mu} = 0] \\ &= \int d^D Q \frac{w_{3\alpha 1 \alpha 2} Q^{\alpha 1} Q^{\alpha 2}}{N_1 N_2 N_3} \\ &= w_{3\alpha 1 \alpha 2} C_{00}(q1, q2; 1, 2, 3) g^{\alpha 1 \alpha 2} \\ &= (D-3) C_{00}(q1, q2; 1, 2, 3) \\ C_{00}(q1, q2; 1, 2, 3) &= \frac{1}{(D-3)} \int d^D Q \frac{Q^2 - Y_3^2}{N_1 N_2 N_3} \end{aligned} \quad (\text{A.81})$$

Following the same way as above for Y_2 in place of Y_3 , we have

$$\begin{aligned}
\int d^D Q \frac{Q^2 - Y_2^2}{N_1 N_2 N_3} &= \int d^D Q \frac{w_{2QQ}}{N_1 N_2 N_3} \quad [\text{Squaring } Q^\mu = Y_2^\mu + w_2^\mu \text{ and noting } Y_2^\mu w_{2\mu} = 0] \\
&= \int d^D Q \frac{w_{2\alpha 1\alpha 2} Q^{\alpha 1} Q^{\alpha 2}}{N_1 N_2 N_3} \\
&= w_{2\alpha 1\alpha 2} C_{00}(q1, q2; 1, 2, 3) g^{\alpha 1\alpha 2} \\
&= (D-2) C_{00}(q1, q2; 1, 2, 3) \\
C_{00}(q1, q2; 1, 2, 3) &= \frac{1}{(D-2)} \int d^D Q \frac{Q^2 - Y_2^2}{N_1 N_2 N_3} \tag{A.82}
\end{aligned}$$

Equating $C_{00}(q1, q2; 1, 2, 3)$ of Eq. A.81 and Eq. A.82, we have

$$\begin{aligned}
\frac{1}{(D-3)} \int d^D Q \frac{Q^2 - Y_3^2}{N_1 N_2 N_3} &= \frac{1}{(D-2)} \int d^D Q \frac{Q^2 - Y_2^2}{N_1 N_2 N_3} \\
\Rightarrow \int d^D Q \frac{Q^2 - Y_3^2}{N_1 N_2 N_3} &= \frac{D-3}{D-2} \int d^D Q \frac{Q^2 - Y_2^2}{N_1 N_2 N_3} \tag{A.83}
\end{aligned}$$

This completes reduction of three rank four point function. The reduction of four rank four point function does not require any new technique. It can be derived using the same tricks we have used so far. Reduction of lower point integrals are also similar. Details can be found in Ref. [66].

A.4 Reduction of five point and higher point functions

For five-point function, we will have q_1, q_2, q_3 , and q_4 . For reduction of more than five point functions also, the number of basis vectors will again be four. This is because of the fact that we are doing the reduction in four dimension and hence there are only four inde-

pendent vectors. For example for 7-point functions we will have q_1, q_2, q_3, q_4, q_5 , and q_6 . We can choose any four vectors from these six vectors to define our basis. Let's work with q_1, q_2, q_3 , and q_4 . In all these cases, the dimension of the physical space is 4 and that of transverse space is 0.

Here $w_V^\mu = \frac{\delta_{q_1 q_2 q_3 q_4}^{\mu}}{\delta_{q_1 q_2 q_3 q_4}^V} = 0$ which follows from the anti-symmetry under the interchange

of any two indices and in four dimension the indices can take only four values.

Again $w_V^\mu = \delta_V^\mu - u_i^\mu q_{iV} = \delta_V^\mu - q_i^\mu u_{iV}$. So, $\delta_V^\mu = u_i^\mu q_{iV} = q_i^\mu u_{iV}$. Therefore, Q^μ can be written as $Q^\mu = u_i^\mu q_i \cdot Q = q_i^\mu u_i \cdot Q = Y_4^\mu$.

This Y_4 can be written in terms of denominator factors

$$\begin{aligned} Y_4^\mu &= u_i^\mu q_i \cdot Q \\ &= \frac{1}{2} \sum_{i=1}^4 u_i^\mu f_i + \frac{1}{2} (N_5 u_4^\mu + N_4 u_3^\mu + N_3 u_2^\mu + N_2 u_1^\mu) - \frac{1}{2} N_1 (u_4^\mu + u_3^\mu + u_2^\mu + u_1^\mu) \quad (\text{A.84}) \end{aligned}$$

So using Eq. A.84, rank-one five-point function can be written as one five-point scalar function and five four-point scalar functions with different denominator factors. Similarly, for rank-two five-point functions, we can replace one of the Q in the numerator by the above Y_4 . We will have one rank-one five-point functions and five rank-one four-point functions with different denominator factors. We can use appropriate formula to further reduce these tensor integrals to scalar integrals. This way we can reduce five-rank five-point functions as well, where using one Y_4 we will have one rank-four five-point functions and five rank-four four-point functions with different denominator factors.

For the reduction of more than five point functions also, we can use Y_4 . As for example for six point function, Y_5 is not well defined as u_i would be $u_i = \frac{0}{0}$ if we would have taken

five basis vectors q_1, q_2, q_3, q_4 and q_5 in four dimension. So we need to use Y_4 for five- and higher-point functions. In this case also, rank-one six-point function can be written as one six-point scalar function and five five-point scalar functions with different denominator factors. Similarly other higher-rank tensors can be reduced following the same procedure. So after all these, only task remaining will be to perform the reduction of scalar integral of more than four points to master scalar integrals. Below we discuss reduction of five- and higher-point scalar function.

higher-point scalar function

For five-point function, we will start from $Q^\mu = u_i^\mu q_i \cdot Q = q_j^\mu u_j \cdot Q$.

$$\begin{aligned}
Q^2 &= u_i \cdot q_j q_i \cdot Q u_j \cdot Q \\
\Rightarrow N_1 + m_1^2 &= q_i \cdot Q u_i \cdot Q \quad [\text{using } u_i \cdot q_j = \delta_{ij}] \\
&= \frac{1}{2} \sum_{i=1}^4 (N_{i+1} - N_1 + f_i) u_i \cdot Q \\
&= \frac{1}{2} \left(\sum_{i=1}^4 N_{i+1} u_i \cdot Q - N_1 \sum_{i=1}^4 u_i \cdot Q + \sum_{i=1}^4 f_i u_i \cdot Q \right) \\
\Rightarrow m_1^2 &= \frac{1}{2} \left(\sum_{i=1}^4 N_{i+1} u_i \cdot Q - N_1 (2 + \sum_{i=1}^4 u_i \cdot Q) \right. \\
&\quad \left. + \sum_{i=1}^4 f_i u_i \cdot \sum_{j=1}^4 u_j q_j \cdot Q \right) \\
&\quad [\text{using } Q^\mu = u_j^\mu q_j \cdot Q] \\
&= \frac{1}{2} \left(\sum_{i=1}^4 N_{i+1} u_i \cdot Q - N_1 (2 + \sum_{i=1}^4 u_i \cdot Q) \right. \\
&\quad \left. + \frac{1}{2} \sum_{i=1}^4 f_i u_i \cdot \sum_{j=1}^4 u_j (N_{j+1} - N_1 + f_j) \right)
\end{aligned}$$

$$\Rightarrow m_1^2 - \frac{1}{4} \sum_{i,j=1}^4 f_i u_i \cdot u_j f_j = \frac{1}{2} \left(\sum_{i=1}^4 N_{i+1} u_i \cdot Q - N_1 (2 + \sum_{i=1}^4 u_i \cdot Q) + \frac{1}{2} \sum_{i=1}^4 f_i u_i \cdot \sum_{j=1}^4 u_j (N_{j+1} - N_1) \right)$$

So we have

$$1 = \frac{1}{2(m_1^2 - \frac{1}{4} \sum_{i,j=1}^4 f_i f_j u_i \cdot u_j)} \times \left(\sum_{i=1}^4 N_{i+1} u_i \cdot Q - N_1 (2 + \sum_{i=1}^4 u_i \cdot Q) + \frac{1}{2} \sum_{i,j=1}^4 f_i u_i \cdot u_j (N_{j+1} - N_1) \right) \quad (\text{A.85})$$

So multiplying denominator factors with Eq. A.85 and integrating over loop momentum, we will get formula for scalar integration of five or more point functions. For the five-point scalar integral, the first two terms in the RHS of Eq. A.85 simplify a lot and five-point scalar integral can be easily reduced to four-point scalar integrals without having to use reduction of rank-one four-point functions for the first two terms. We will investigate them below.

The first part is given by

$$\begin{aligned} & \int \frac{d^D Q N_{i+1} u_i \cdot Q}{N_1 N_2 N_3 N_4 N_5} \\ &= \int \frac{d^D Q u_1 \cdot Q}{N_1 N_3 N_4 N_5} + \int \frac{d^D Q u_2 \cdot Q}{N_1 N_2 N_4 N_5} + \int \frac{d^D Q u_3 \cdot Q}{N_1 N_2 N_3 N_5} + \int \frac{d^D Q u_4 \cdot Q}{N_1 N_2 N_3 N_4} \\ &= u_{1\mu} (D_1 q_2^\mu + D_2 q_3^\mu + D_3 q_4^\mu) + \int \frac{d^D Q u_2 \cdot Q}{N_1 N_2 N_4 N_5} + \int \frac{d^D Q u_3 \cdot Q}{N_1 N_2 N_3 N_5} + \int \frac{d^D Q u_4 \cdot Q}{N_1 N_2 N_3 N_4} \\ &= 0 + \int \frac{d^D Q u_2 \cdot Q}{N_1 N_2 N_4 N_5} + \int \frac{d^D Q u_3 \cdot Q}{N_1 N_2 N_3 N_5} + \int \frac{d^D Q u_4 \cdot Q}{N_1 N_2 N_3 N_4} \quad [\text{as } u_i \cdot q_j = \delta_{ij}] \\ &= 0 \quad [\text{other integrals are also zero as } u_i \cdot q_j = \delta_{ij}] \end{aligned}$$

The second part is given by

$$\begin{aligned}
& \int \frac{d^D Q N_1 (2 + \sum_{i=1}^4 u_i \cdot Q)}{N_1 N_2 N_3 N_4 N_5} \\
&= \int \frac{d^D Q (2 + \sum_{i=1}^4 u_i \cdot Q)}{N_2 N_3 N_4 N_5} \\
&= \int \frac{d^D Q (2 + \sum_{i=1}^4 u_i \cdot (Q - q_1))}{(Q^2 - m_2^2)((Q + q_2 - q_1)^2 - m_3^2)((Q + q_3 - q_1)^2 - m_4^2)((Q + q_4 - q_1)^2 - m_5^2)} \\
&= \int \frac{d^D Q (1 + \sum_{i=1}^4 u_i \cdot Q)}{(Q^2 - m_2^2)((Q + q_2 - q_1)^2 - m_3^2)((Q + q_3 - q_1)^2 - m_4^2)((Q + q_4 - q_1)^2 - m_5^2)} \\
&\hspace{25em} [\text{as } u_i \cdot q_j = \delta_{ij}] \\
&= \int \frac{d^D Q}{(Q^2 - m_2^2)((Q + q_2 - q_1)^2 - m_3^2)((Q + q_3 - q_1)^2 - m_4^2)((Q + q_4 - q_1)^2 - m_5^2)} \\
&+ \sum_{i=1}^4 u_i \cdot (D_1(q_2 - q_1)^\mu + D_2(q_3 - q_1)^\mu + D_3(q_4 - q_1)^\mu) \\
&= \int \frac{d^D Q}{N_2 N_3 N_4 N_5} + (D_1(1 - 1) + D_2(1 - 1) + D_3(1 - 1)) \quad [\text{as } u_i \cdot q_j = \delta_{ij}] \\
&= \int \frac{d^D Q}{N_2 N_3 N_4 N_5}
\end{aligned}$$

The third term in Eq. A.85 does not have any Q dependence in the numerator, so it trivially becomes four-point scalar integral. Thus the five-point scalar integral can be reduced to four-point scalar integrals without having to use reduction of rank-one four-point functions.

However for six or more point scalar integral, for the first two terms in the RHS after multiplying the denominator factors, we need to use reduction of rank-one tensor integral of one less point function. For the third term, we need to use reduction of scalar integral of one less point function. For example, for the six-point scalar integral, we need to use reduction formula for rank-one five-point function for the first two terms and for the third term we

need reduction for five-point scalar integrals of various denominator factors. Similarly for seven-point scalar integral, we need to use reduction for rank-one six-point function for the first two terms and for the third term, we need reduction of six-point scalar integrals of various denominator factors. Other higher point scalar integrals can be reduced in exactly similar manner.

Appendix B

Miscellaneous

B.1 Loop Integrations

In this appendix, we list some formulae which frequently appear during loop integrations.

Feynman parameters can be used to combine denominator factors

$$\frac{1}{D_1 D_2 \cdots D_n} = \int_0^1 dx_1 dx_2 \cdots dx_n \delta(\sum x_i - 1) \frac{(n-1)!}{[x_1 D_1 + x_2 D_2 + \cdots + x_n D_n]^n} \quad (\text{B.1})$$

The denominator $[x_1 D_1 + x_2 D_2 + \cdots + x_n D_n]$ can be written as $Q^2 - \Delta + i\epsilon$ after a shift of integration variable under the integration over $\int d^D Q$.

The following formula, which can be derived using wick rotation, appears frequently in one loop calculation:

$$\int \frac{d^D Q}{(2\pi)^D} \frac{1}{(Q^2 - \Delta)^n} = \frac{(-1)^n i \Gamma(n - \frac{D}{2})}{(4\pi)^{\frac{D}{2}} \Gamma(n)} \left(\frac{1}{\Delta}\right)^{(n - \frac{D}{2})} \quad (\text{B.2})$$

Two expansions of Γ containing singularity, which appear in one loop scalar integral calculation:

$$\Gamma(\epsilon) = \frac{1}{\epsilon} - \gamma + O(\epsilon) \quad (\text{B.3})$$

$$\Gamma(-n + \epsilon) = \frac{(-1)^n}{n!} \left(\frac{1}{\epsilon} - \gamma + \sum_{i=1}^n \frac{1}{i} + O(\epsilon) \right) \quad (\text{B.4})$$

The following expansion is frequently needed in one-loop calculation

$$x^\varepsilon = e^{\log_e(x^\varepsilon)} = e^{(\varepsilon \log_e x)} = 1 + \varepsilon \log_e x + O(\varepsilon^2) \quad (\text{B.5})$$

Eq. B.2 diverges only for $n = 1, 2$. These two n values appear in tadpole and bubble scalar integrals, respectively. For other values of n , $D=4$ can be set from the beginning.

Some rearranging can be done in Eq. B.2 in order to separate divergent parts and finite parts as follows

$$\begin{aligned} \int \frac{d^D Q}{(2\pi)^D} \frac{1}{(Q^2 - \Delta)^n} &= \frac{(-1)^n i \Gamma(n - \frac{D}{2})}{(4\pi)^{\frac{D}{2}} \Gamma(n)} \left(\frac{1}{\Delta} \right)^{(n - \frac{D}{2})} \\ &= \frac{(-1)^n i}{(4\pi)^{2 - (2 - \frac{D}{2})}} \frac{\Gamma(n - 2 + 2 - \frac{D}{2})}{\Gamma(n)} \left(\frac{1}{\Delta} \right)^{(n - 2 + 2 - \frac{D}{2})} \\ &= \frac{i}{(4\pi)^2} \frac{(-1)^n \Delta^{(2-n)}}{\Gamma(n)} \left(\frac{4\pi}{\Delta} \right)^{(2 - \frac{D}{2})} \Gamma(n - 2 + 2 - \frac{D}{2}) \\ &= \frac{i}{(4\pi)^2} \frac{(-1)^n \Delta^{(2-n)}}{\Gamma(n)} \left(\frac{4\pi}{\Delta} \right)^\varepsilon \Gamma(n - 2 + \varepsilon) \quad [\text{using } D = 4 - 2\varepsilon] \end{aligned} \quad (\text{B.6})$$

For $n=1$, Eq. B.6 becomes

$$\begin{aligned} &\int \frac{d^D Q}{(2\pi)^D} \frac{1}{(Q^2 - \Delta)} \\ &= \frac{i}{(4\pi)^2} \frac{(-1)\Delta}{\Gamma(1)} \left(\frac{4\pi}{\Delta} \right)^\varepsilon \Gamma(-1 + \varepsilon) \\ &= \frac{i}{(4\pi)^2} \frac{(-1)\Delta}{\Gamma(1)} \left(1 + \varepsilon \log\left(\frac{4\pi}{\Delta}\right) + O(\varepsilon^2) \right) \frac{(-1)}{1} \left(\frac{1}{\varepsilon} - \gamma + 1 + O(\varepsilon) \right) \\ &= \frac{i}{(4\pi)^2} \frac{(-1)\Delta}{\Gamma(1)} \left(1 + \varepsilon \log\left(\frac{4\pi}{\Delta}\right) + O(\varepsilon^2) \right) \frac{(-1)}{1} \left(\frac{1}{\varepsilon} - \gamma + 1 + O(\varepsilon) \right) \\ &= \frac{i}{(4\pi)^2} \frac{(-1)\Delta}{\Gamma(1)} \frac{(-1)}{1} \left(\frac{1}{\varepsilon} - \gamma + 1 + \log\left(\frac{4\pi}{\Delta}\right) + O(\varepsilon) \right) \end{aligned}$$

$$= \frac{i}{(4\pi)^2} \Delta \left(\frac{1}{\varepsilon} - \gamma + 1 + \log\left(\frac{4\pi}{\Delta}\right) + O(\varepsilon) \right) \quad (\text{B.7})$$

For $n=2$, Eq. B.6 becomes

$$\begin{aligned} & \int \frac{d^D Q}{(2\pi)^D} \frac{1}{(Q^2 - \Delta)^2} \\ &= \frac{i}{(4\pi)^2} \frac{1}{\Gamma(2)} \left(\frac{4\pi}{\Delta} \right)^\varepsilon \Gamma(\varepsilon) \\ &= \frac{i}{(4\pi)^2} \frac{1}{\Gamma(2)} \left(1 + \varepsilon \log\left(\frac{4\pi}{\Delta}\right) + O(\varepsilon^2) \right) \left(\frac{1}{\varepsilon} - \gamma + O(\varepsilon) \right) \\ &= \frac{i}{(4\pi)^2} \frac{1}{\Gamma(2)} \left(1 + \varepsilon \log\left(\frac{4\pi}{\Delta}\right) + O(\varepsilon^2) \right) \left(\frac{1}{\varepsilon} - \gamma + O(\varepsilon) \right) \\ &= \frac{i}{(4\pi)^2} \frac{1}{\Gamma(2)} \left(\frac{1}{\varepsilon} - \gamma + \log\left(\frac{4\pi}{\Delta}\right) + O(\varepsilon) \right) \\ &= \frac{i}{(4\pi)^2} \left(\frac{1}{\varepsilon} - \gamma + \log\left(\frac{4\pi}{\Delta}\right) + O(\varepsilon) \right) \end{aligned} \quad (\text{B.8})$$

The Δ contains the Feynman parameters, which need to be integrated over. It is to be noted that Δ in Eq. B.7 or Eq. B.8 will be dictated by the denominator of the Eq. B.1.

All the master integrals regularized in dimensional regularization for ultraviolet, infrared, or collinear divergences with $D = 4 - 2\varepsilon$ can be found in [111].

B.2 Running of QCD coupling constant

The running of coupling constant is dictated by beta function of the underlying theory. The beta function is defined as

$$\beta(g) = \frac{\partial g}{\partial \ln \mu} \quad (\text{B.9})$$

where μ is the scale and g is the coupling constant which runs with the energy scale.

The QCD beta function, $\beta(g)$, at one loop is given by

$$\beta(g) = b_0 \frac{g^3}{16\pi^2} \quad (\text{B.10})$$

where b_0 is defined as $-(11 - \frac{2n_f}{3})$.

Using Eq. B.10 and Eq. B.9, we have

$$\begin{aligned} \frac{\partial g}{\partial \ln \mu} &= b_0 \frac{g^3}{16\pi^2} \\ \Rightarrow \frac{\partial g}{g^3} &= b_0 \frac{1}{16\pi^2} \partial \ln \mu \\ \Rightarrow \frac{1}{-2g^2} &= b_0 \frac{1}{16\pi^2} \ln \mu + \text{const} \\ \Rightarrow \frac{1}{\alpha} &= -b_0 \frac{1}{2\pi} \ln \mu + \text{const} \\ \Rightarrow \frac{1}{\alpha} - \frac{1}{\alpha_0} &= -b_0 \frac{1}{2\pi} \ln \frac{\mu}{\mu_0} \\ \Rightarrow \alpha &= \frac{\alpha_0}{1 - \alpha_0 b_0 \frac{1}{2\pi} \ln \frac{\mu}{\mu_0}} \end{aligned} \quad (\text{B.11})$$

B.3 Hadronic Cross-section

The cross section for production of final states $\{f\}$ in the collision of two hadrons A and B is given by

$$\sigma_{AB \rightarrow \{f\}} = \sum_{i,j} \int dx_1 dx_2 d\hat{t} f_{i/A}(x_1, Q_F^2) f_{j/B}(x_2, Q_F^2) \frac{d\hat{\sigma}_{ij \rightarrow \{f\}}(x_1, x_2, Q_R, Q_F)}{d\hat{t}},$$

where i, j are partons inside the hadrons. x_1, x_2 are the partonic momentum fractions. Q_R and Q_F are the renormalization and factorization scales. $f^{1,2}$ are parton distribution func-

tions, and $\hat{\sigma}_{ij \rightarrow \{f\}}$, the partonic cross section, is given by

$$d\hat{\sigma}_{ij \rightarrow \{f\}} = \frac{1}{(2E_i)(2E_j)|v_i - v_j|} d\Pi |\mathcal{M}|^2 \quad (\text{B.12})$$

In the last line, $d\Pi$, the Lorentz invariant phase space, is given by

$$d\Pi = \left(\prod_f \frac{d^3 p_F}{(2\pi)^3} \frac{1}{2E_f} \right) (2\pi)^4 \delta^4(p_i + p_j - \sum_f p_f)$$

B.4 Polarization

Massless spin-1 particle

The x and y polarizations of a massless spin-1 particle with momentum \vec{p} along z-direction can be written as

$$\epsilon_x = \begin{pmatrix} 0 \\ \text{sign of } p_z \\ 0 \\ 0 \end{pmatrix} \quad \text{and} \quad \epsilon_y = \begin{pmatrix} 0 \\ 0 \\ 1 \\ 0 \end{pmatrix}$$

.

For general momentum \vec{p} not confined only along z-direction, its two x and y polariza-

tions can be written as

$$\epsilon_x = \begin{pmatrix} 0 \\ \frac{p_x p_z}{p_T |\vec{p}|} \\ \frac{p_y p_z}{p_T |\vec{p}|} \\ -\frac{p_T}{|\vec{p}|} \end{pmatrix} \text{ and } \epsilon_y = \begin{pmatrix} 0 \\ -\frac{p_z}{p_T} \\ \frac{p_y}{p_T} \\ 0 \end{pmatrix},$$

where $p_T = \sqrt{p_x^2 + p_y^2}$.

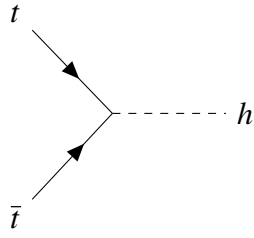
Massive spin-1 particle

For massive spin-1 particle of mass m , its polarizations can be written as

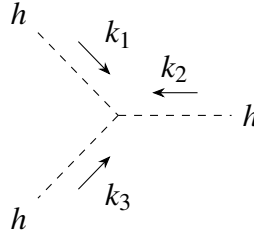
$$\epsilon_x = \begin{pmatrix} 0 \\ \frac{p_x p_z}{p_T |\vec{p}|} \\ \frac{p_y p_z}{p_T |\vec{p}|} \\ -\frac{p_T}{|\vec{p}|} \end{pmatrix}, \epsilon_y = \begin{pmatrix} 0 \\ -\frac{p_z}{p_T} \\ \frac{p_y}{p_T} \\ 0 \end{pmatrix}, \text{ and } \epsilon_z = \begin{pmatrix} \frac{|\vec{p}|}{m} \\ \frac{p_x E}{p_T m} \\ \frac{p_y E}{p_T m} \\ \frac{p_z E}{p_T m} \end{pmatrix}$$

Appendix C

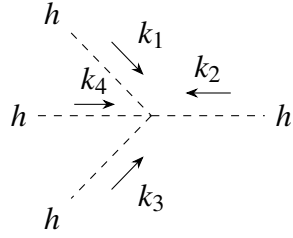
C.1 Feynman Rules for Chapter-IV



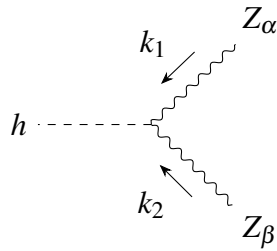
$$= -i \frac{m_t}{v} \left\{ (1 + \kappa_t) + i \tilde{\kappa}_t \gamma_5 \right\}$$



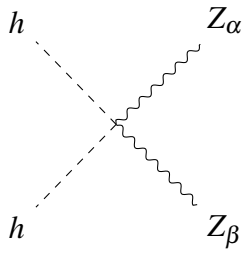
$$= -i \frac{3m_h^2}{v} \left\{ (1 + g_{3h}^{(0)}) - \frac{g_{3h}^{(1)}}{3m_h^2} \sum_{i < j}^3 k_i \cdot k_j \right\}$$



$$= -i \frac{3m_h^2}{v^2} \left\{ (1 + g_{4h}^{(0)}) - \frac{g_{4h}^{(1)}}{6m_h^2} \sum_{i < j}^4 k_i \cdot k_j \right\}$$



$$= i \frac{g M_Z}{c_W} \left\{ g^{\alpha\beta} (1 + g_{hZZ}^{(0)}) + \frac{g_{hZZ}^{(1)}}{M_Z^2} [g^{\alpha\beta} (k_1 \cdot k_2) - k_2^\alpha k_1^\beta] + \frac{g_{hZZ}^{(2)}}{M_Z^2} [g^{\alpha\beta} (k_1^2 + k_2^2) - (k_1^\alpha k_1^\beta + k_2^\alpha k_2^\beta)] \right\}$$



$$= i \frac{g M_Z}{c_W v} \left\{ g^{\alpha\beta} (1 + g_{hhZZ}^{(0)}) \right\}$$

Bibliography

- [1] *Neutral Higgs boson pair production at hadron colliders: QCD corrections*, S. Dawson, S. Dittmaier, and M. Spira, *Phys. Rev. D* **58** (1998) 115012 [[arXiv:hep-ph/9805244](#)].
- [2] *Top-quark mass effects in double and triple Higgs production in gluon-gluon fusion at NLO*, F. Maltoni, E. Vryonidou, and M. Zaro, *JHEP* **11** (2014) 079 [[arXiv:1408.6542](#)].
- [3] *Observation of a new particle in the search for the Standard Model Higgs boson with the ATLAS detector at the LHC*, **ATLAS** Collaboration, G. Aad *et. al.*, *Phys. Lett. B* **716** (2012) 1–29 [[arXiv:1207.7214](#)].
- [4] *Observation of a New Boson at a Mass of 125 GeV with the CMS Experiment at the LHC*, **CMS** Collaboration, S. Chatrchyan *et. al.*, *Phys. Lett. B* **716** (2012) 30–61 [[arXiv:1207.7235](#)].
- [5] *Review of Particle Physics*, **Particle Data Group** Collaboration, M. Tanabashi *et. al.*, *Phys. Rev. D* **98** (2018), no. 3 030001.
- [6] *A Theory of the Fundamental Interactions*, J. S. Schwinger, *Annals Phys.* **2** (1957) 407–434.
- [7] *Implications of the Intermediate Boson Basis of the Weak Interactions: Existence of a Quartet of Intermediate Bosons and Their Dual Isotopic Spin Transformation Properties*, T. D. Lee, and C.-N. Yang, *Phys. Rev.* **119** (1960) 1410–1419.

- [8] *Partial Symmetries of Weak Interactions*, S. L. Glashow, *Nucl. Phys.* 22 **(1961)** 579–588.
- [9] *Broken symmetries, massless particles and gauge fields*, P. W. Higgs, *Phys. Lett.* 12 **(1964)** 132–133.
- [10] *Broken Symmetries and the Masses of Gauge Bosons*, P. W. Higgs, *Phys. Rev. Lett.* 13 **(1964)** 508–509. [,160(1964)].
- [11] *Spontaneous Symmetry Breakdown without Massless Bosons*, P. W. Higgs, *Phys. Rev.* 145 **(1966)** 1156–1163.
- [12] *Broken Symmetry and the Mass of Gauge Vector Mesons*, F. Englert, and R. Brout, *Phys. Rev. Lett.* 13 **(1964)** 321–323. [,157(1964)].
- [13] *Global Conservation Laws and Massless Particles*, G. S. Guralnik, C. R. Hagen, and T. W. B. Kibble, *Phys. Rev. Lett.* 13 **(1964)** 585–587. [,162(1964)].
- [14] *A Model of Leptons*, S. Weinberg, *Phys. Rev. Lett.* 19 **(1967)** 1264–1266.
- [15] *Weak and Electromagnetic Interactions*, A. Salam, *Conf. Proc.* C680519 **(1968)** 367–377.
- [16] *Renormalization of Massless Yang-Mills Fields*, G. 't Hooft, *Nucl. Phys.* B33 **(1971)** 173–199.
- [17] *Renormalizable Lagrangians for Massive Yang-Mills Fields*, G. 't Hooft, *Nucl. Phys.* B35 **(1971)** 167–188. [,201(1971)].

- [18] *Observation of Neutrino Like Interactions Without Muon Or Electron in the Gargamelle Neutrino Experiment*, **Gargamelle Neutrino** Collaboration, F. J. Hasert *et. al.*, *Phys. Lett.* 46B **(1973)** 138–140. [,5.15(1973)].
- [19] *Experimental Observation of Isolated Large Transverse Energy Electrons with Associated Missing Energy at $s^{*}(1/2) = 540\text{-GeV}$* , **UA1** Collaboration, G. Arnison *et. al.*, *Phys. Lett.* B122 **(1983)** 103–116. [,611(1983)].
- [20] *Observation of Single Isolated Electrons of High Transverse Momentum in Events with Missing Transverse Energy at the CERN anti- p p Collider*, **UA2** Collaboration, M. Banner *et. al.*, *Phys. Lett.* B122 **(1983)** 476–485. [,7.45(1983)].
- [21] *Evidence for $Z^0 \rightarrow e^+ e^-$ at the CERN anti- p p Collider*, **UA2** Collaboration, P. Bagnaia *et. al.*, *Phys. Lett.* B129 **(1983)** 130–140. [,7.69(1983)].
- [22] *Experimental Observation of Lepton Pairs of Invariant Mass Around $95\text{-GeV}/c^{*2}$ at the CERN SPS Collider*, **UA1** Collaboration, G. Arnison *et. al.*, *Phys. Lett.* B126 **(1983)** 398–410. [,7.55(1983)].
- [23] *Isotopic Spin and New Unstable Particles*, M. Gell-Mann, *Phys. Rev.* 92 **(1953)** 833–834.
- [24] *Charge Independence for V-particles*, T. Nakano, and K. Nishijima, *Prog. Theor. Phys.* 10 **(1953)** 581–582.
- [25] *Symmetries of baryons and mesons*, M. Gell-Mann, *Phys. Rev.* 125 **(1962)** 1067–1084.

- [26] *The eightfold way: A theory of strong interaction symmetry*, M. Gell-Mann.
- [27] *Derivation of strong interactions from a gauge invariance*, Y. Ne'eman, *Nucl. Phys.* 26 (1961) 222–229. [,34(1961)].
- [28] *A Schematic Model of Baryons and Mesons*, M. Gell-Mann, *Phys. Lett.* 8 (1964) 214–215.
- [29] *An $SU(3)$ model for strong interaction symmetry and its breaking. Version 1*, G. Zweig.
- [30] G. Zweig, *An $SU(3)$ model for strong interaction symmetry and its breaking. Version 2*, in *DEVELOPMENTS IN THE QUARK THEORY OF HADRONS. VOL. 1. 1964 - 1978* (D. Lichtenberg, and S. P. Rosen, eds.), pp. 22–101. 1964.
- [31] *Three Triplet Model with Double $SU(3)$ Symmetry*, M. Y. Han, and Y. Nambu, *Phys. Rev.* 139 (1965) B1006–B1010. [,187(1965)].
- [32] *Spin and Unitary Spin Independence in a Paraquark Model of Baryons and Mesons*, O. W. Greenberg, *Phys. Rev. Lett.* 13 (1964) 598–602.
- [33] *Magnetic moments of baryons in the quark model*, B. Struminsky, *JINR-Preprint P-1939, Dubna, Russia, Submitted on January 7, 1965*.
- [34] *Advantages of the Color Octet Gluon Picture*, H. Fritzsch, M. Gell-Mann, and H. Leutwyler, *Phys. Lett.* 47B (1973) 365–368.
- [35] *Jet Analysis of the $\Upsilon(9.46)$ Decay Into Charged Hadrons*, **PLUTO** Collaboration, C. Berger *et. al.*, *Phys. Lett.* 82B (1979) 449–455.

- [36] *Topology of the Υ Decay*, **PLUTO** Collaboration, C. Berger *et. al.*, *Z. Phys.* C8 (1981) 101.
- [37] *Asymptotic Sum Rules at Infinite Momentum*, J. D. Bjorken, *Phys. Rev.* 179 (1969) 1547–1553.
- [38] *Very high-energy collisions of hadrons*, R. P. Feynman, *Phys. Rev. Lett.* 23 (1969) 1415–1417. [,494(1969)].
- [39] *The behavior of hadron collisions at extreme energies*, R. P. Feynman, *Conf. Proc.* C690905 (1969) 237–258.
- [40] *Ultraviolet Behavior of Nonabelian Gauge Theories*, D. J. Gross, and F. Wilczek, *Phys. Rev. Lett.* 30 (1973) 1343–1346. [,271(1973)].
- [41] *Reliable Perturbative Results for Strong Interactions?*, H. D. Politzer, *Phys. Rev. Lett.* 30 (1973) 1346–1349. [,274(1973)].
- [42] *Calculation of the Structure Functions for Deep Inelastic Scattering and $e^+ e^-$ Annihilation by Perturbation Theory in Quantum Chromodynamics.*, Y. L. Dokshitzer, *Sov. Phys. JETP* 46 (1977) 641–653. [Zh. Eksp. Teor. Fiz.73,1216(1977)].
- [43] *Deep inelastic $e p$ scattering in perturbation theory*, V. N. Gribov, and L. N. Lipatov, *Sov. J. Nucl. Phys.* 15 (1972) 438–450. [Yad. Fiz.15,781(1972)].
- [44] *Asymptotic Freedom in Parton Language*, G. Altarelli, and G. Parisi, *Nucl. Phys.* B126 (1977) 298–318.

- [45] *Weak Interactions with Lepton-Hadron Symmetry*, S. L. Glashow, J. Iliopoulos, and L. Maiani, *Phys. Rev. D* **2** (1970) 1285–1292.
- [46] *Experimental Observation of a Heavy Particle J*, **E598** Collaboration, J. J. Aubert *et. al.*, *Phys. Rev. Lett.* **33** (1974) 1404–1406.
- [47] *Discovery of a Narrow Resonance in e^+e^- Annihilation*, **SLAC-SP-017** Collaboration, J. E. Augustin *et. al.*, *Phys. Rev. Lett.* **33** (1974) 1406–1408. [*Adv. Exp. Phys.* **5**, 141 (1976)].
- [48] *Observation of a Dimuon Resonance at 9.5-GeV in 400-GeV Proton-Nucleus Collisions*, S. W. Herb *et. al.*, *Phys. Rev. Lett.* **39** (1977) 252–255.
- [49] *Observation of top quark production in $\bar{p}p$ collisions*, **CDF** Collaboration, F. Abe *et. al.*, *Phys. Rev. Lett.* **74** (1995) 2626–2631 [[arXiv:hep-ex/9503002](https://arxiv.org/abs/hep-ex/9503002)].
- [50] *Observation of the top quark*, **D0** Collaboration, S. Abachi *et. al.*, *Phys. Rev. Lett.* **74** (1995) 2632–2637 [[arXiv:hep-ex/9503003](https://arxiv.org/abs/hep-ex/9503003)].
- [51] *CP Violation in the Renormalizable Theory of Weak Interaction*, M. Kobayashi, and T. Maskawa, *Prog. Theor. Phys.* **49** (1973) 652–657.
- [52] *Decay Correlations of Heavy Leptons in $e^+e^- \rightarrow \text{Lepton}^+ \text{Lepton}^-$* , Y.-S. Tsai, *Phys. Rev. D* **4** (1971) 2821. [Erratum: *Phys. Rev. D* **13**, 771 (1976)].
- [53] *Evidence for Anomalous Lepton Production in e^+e^- Annihilation*, M. L. Perl *et. al.*, *Phys. Rev. Lett.* **35** (1975) 1489–1492. [,193(1975)].

- [54] *Review of final LEP results, or, A Tribute to LEP*, J. Drees, *Int. J. Mod. Phys. A* **17** (2002) 3259–3283 [[arXiv:hep-ex/0110077](#)]. [,349(2001)].
- [55] *Review of Physics Results from the Tevatron*, D. Bandurin et. al., *Int. J. Mod. Phys. A* **30** (2015), no. 06 1541001 [[arXiv:1409.4861](#)].
- [56] *Beyond the standard model*, R. N. Mohapatra, *Prog. Part. Nucl. Phys.* **26** (1991) 1–89. [,90(1990)].
- [57] C. Cs    ki, and P. Tanedo, *Beyond the Standard Model*, in *Proceedings, 2013 European School of High-Energy Physics (ESHEP 2013): Paradfurdo, Hungary, June 5-18, 2013*, pp. 169–268, 2015. [arXiv:1602.04228](#).
- [58] **CMS** Collaboration, *Search for supersymmetry in proton-proton collisions at 13 TeV in final states with jets and missing transverse momentum*, Tech. Rep. CMS-PAS-SUS-19-006, CERN, Geneva, 2019.
- [59] *Effective Lagrangian Analysis of New Interactions and Flavor Conservation*, W. Buchmuller, and D. Wyler, *Nucl. Phys. B* **268** (1986) 621–653.
- [60] *Dimension-Six Terms in the Standard Model Lagrangian*, B. Grzadkowski, M. Iskrzynski, M. Misiak, and J. Rosiek, *JHEP* **10** (2010) 085 [[arXiv:1008.4884](#)].
- [61] *Effective Lagrangian for a light Higgs-like scalar*, R. Contino, M. Ghezzi, C. Grojean, M. Muhlleitner, and M. Spira, *JHEP* **07** (2013) 035 [[arXiv:1303.3876](#)].

- [62] *Higgs Basis: Proposal for an EFT basis choice for LHC HXSWG*, A. Falkowski, and A. Falkowski.
- [63] *Scalar One Loop Integrals*, G. 't Hooft, and M. J. G. Veltman, *Nucl. Phys.* B153 (1979) 365–401.
- [64] *One-loop calculations in quantum field theory: from Feynman diagrams to unitarity cuts*, R. K. Ellis, Z. Kunszt, K. Melnikov, and G. Zanderighi, *Phys. Rept.* 518 (2012) 141–250 [[arXiv:1105.4319](https://arxiv.org/abs/1105.4319)].
- [65] *Production of two photons and a jet through gluon fusion*, P. Agrawal, and G. Ladinsky, *Phys. Rev. D* 63 (2001) 117504 [[arXiv:hep-ph/0011346](https://arxiv.org/abs/hep-ph/0011346)].
- [66] *New Algorithms for One Loop Integrals*, G. J. van Oldenborgh, and J. A. M. Vermaseren, *Z. Phys.* C46 (1990) 425–438.
- [67] *OneLOop: For the evaluation of one-loop scalar functions*, A. van Hameren, *Comput. Phys. Commun.* 182 (2011) 2427–2438 [[arXiv:1007.4716](https://arxiv.org/abs/1007.4716)].
- [68] *Combined measurements of Higgs boson production and decay using up to 80 fb^{-1} of proton–proton collision data at $\sqrt{s} = 13\text{ TeV}$ collected with the ATLAS experiment*, **ATLAS** Collaboration, T. A. collaboration.
- [69] *Generalized Furry’s Theorem for Closed Loops*, K. Nishijima, *Progress of Theoretical Physics* 6 (08, 1951) 614–615
[[arXiv:http://oup.prod.sis.lan/ptp/article-pdf/6/4/614/5419315/6-4-614.pdf](http://oup.prod.sis.lan/ptp/article-pdf/6/4/614/5419315/6-4-614.pdf)].

- [70] *Gluon fusion and $b\bar{b}$ corrections to HW^+W^-/HZZ production in the POWHEG-BOX*, J. Baglio, *Phys. Lett. B* 764 (2017) 54–59 [[arXiv:1609.05907](#)].
- [71] *QCD corrections to associated Higgs boson production with a W boson pair at the LHC*, M. Song, W.-G. Ma, R.-Y. Zhang, L. Guo, S.-M. Wang, and L. Han, *Phys. Rev. D* 79 (2009) 054016 [[arXiv:0903.2885](#)].
- [72] *Shape of Higgs Potential at Future Colliders*, P. Agrawal, D. Saha, L.-X. Xu, J.-H. Yu, and C. P. Yuan, [arXiv:1907.02078](#).
- [73] R. Contino, *The Higgs as a Composite Nambu-Goldstone Boson*, in *Physics of the large and the small, TASI 09, proceedings of the Theoretical Advanced Study Institute in Elementary Particle Physics, Boulder, Colorado, USA, 1-26 June 2009*, pp. 235–306, 2011. [arXiv:1005.4269](#).
- [74] *Is the Higgs Boson Associated with Coleman-Weinberg Dynamical Symmetry Breaking?*, C. T. Hill, *Phys. Rev. D* 89 (2014), no. 7 073003 [[arXiv:1401.4185](#)].
- [75] *Induced Electroweak Symmetry Breaking and Supersymmetric Naturalness*, J. Galloway, M. A. Luty, Y. Tsai, and Y. Zhao, *Phys. Rev. D* 89 (2014), no. 7 075003 [[arXiv:1306.6354](#)].
- [76] *Combination of searches for Higgs boson pairs in pp collisions at $\sqrt{s}=13$ TeV with the ATLAS detector*, ATLAS Collaboration, G. Aad *et. al.*, [arXiv:1906.02025](#).
- [77] *Electroweak Precision Tests of the Standard Model after the Discovery of the Higgs Boson*, J. Erler, and M. Schott, *Prog. Part. Nucl. Phys.* 106 (2019) 68–119 [[arXiv:1902.05142](#)].

- [78] *The Standard model*, M. Herrero, *NATO Sci. Ser. C* 534 (**1999**) 1–59
[[arXiv:hep-ph/9812242](#)].
- [79] *Extending the Standard Model Effective Field Theory with the Complete Set of Dimension-7 Operators*, L. Lehman, *Phys. Rev. D* 90 (**2014**), no. 12 125023
[[arXiv:1410.4193](#)].
- [80] *2, 84, 30, 993, 560, 15456, 11962, 261485, ...: Higher dimension operators in the SM EFT*, B. Henning, X. Lu, T. Melia, and H. Murayama, *JHEP* 08 (**2017**) 016
[[arXiv:1512.03433](#)]. [Erratum: *JHEP*09,019(2019)].
- [81] *Low-derivative operators of the Standard Model effective field theory via Hilbert series methods*, L. Lehman, and A. Martin, *JHEP* 02 (**2016**) 081
[[arXiv:1510.00372](#)].
- [82] *Renormalization Group Evolution of the Standard Model Dimension Six Operators III: Gauge Coupling Dependence and Phenomenology*, R. Alonso, E. E. Jenkins, A. V. Manohar, and M. Trott, *JHEP* 04 (**2014**) 159 [[arXiv:1312.2014](#)].
- [83] *The Strongly-Interacting Light Higgs*, G. F. Giudice, C. Grojean, A. Pomarol, and R. Rattazzi, *JHEP* 06 (**2007**) 045 [[arXiv:hep-ph/0703164](#)].
- [84] *Updated Global SMEFT Fit to Higgs, Diboson and Electroweak Data*, J. Ellis, C. W. Murphy, V. Sanz, and T. You, *JHEP* 06 (**2018**) 146 [[arXiv:1803.03252](#)].
- [85] *Better Higgs-CP Tests Through Information Geometry*, J. Brehmer, F. Kling, T. Plehn, and T. M. P. Tait, *Phys. Rev. D* 97 (**2018**), no. 9 095017
[[arXiv:1712.02350](#)].

- [86] *Angles on CP-violation in Higgs boson interactions*, F. U. Bernlochner, C. Englert, C. Hays, K. Lohwasser, H. Mildner, A. Pilkington, D. D. Price, and M. Spannowsky, *Phys. Lett. B* **790** (2019) 372–379 [[arXiv:1808.06577](#)].
- [87] *Effective theory analysis of precision electroweak data*, Z. Han, and W. Skiba, *Phys. Rev. D* **71** (2005) 075009 [[arXiv:hep-ph/0412166](#)].
- [88] *Towards the Ultimate SM Fit to Close in on Higgs Physics*, A. Pomarol, and F. Riva, *JHEP* **01** (2014) 151 [[arXiv:1308.2803](#)].
- [89] *Model independent constraints on four-lepton operators*, A. Falkowski, and K. Mimouni, *JHEP* **02** (2016) 086 [[arXiv:1511.07434](#)].
- [90] *Compilation of low-energy constraints on 4-fermion operators in the SMEFT*, A. Falkowski, M. González-Alonso, and K. Mimouni, *JHEP* **08** (2017) 123 [[arXiv:1706.03783](#)].
- [91] *Rosetta: an operator basis translator for Standard Model effective field theory*, A. Falkowski, B. Fuks, K. Mawatari, K. Mimasu, F. Riva, and V. Sanz, *Eur. Phys. J. C* **75** (2015), no. 12 583 [[arXiv:1508.05895](#)].
- [92] *Handbook of LHC Higgs Cross Sections: 4. Deciphering the Nature of the Higgs Sector*, **LHC Higgs Cross Section Working Group** Collaboration, D. de Florian *et. al.*, [arXiv:1610.07922](#).
- [93] *Low-energy effects of new interactions in the electroweak boson sector*, K. Hagiwara, S. Ishihara, R. Szalapski, and D. Zeppenfeld, *Phys. Rev. D* **48** (1993) 2182–2203.

- [94] *Pseudo-observables in Higgs decays*, M. Gonzalez-Alonso, A. Greljo, G. Isidori, and D. Marzocca, *Eur. Phys. J. C* **75** (2015) 128 [[arXiv:1412.6038](#)].
- [95] *A framework for Higgs characterisation*, P. Artoisenet *et. al.*, *JHEP* **11** (2013) 043 [[arXiv:1306.6464](#)].
- [96] *The Chiral approach to the electroweak interactions*, F. Feruglio, *Int. J. Mod. Phys. A* **8** (1993) 4937–4972 [[arXiv:hep-ph/9301281](#)].
- [97] *The Strongly interacting $W W$ system: Gold plated modes*, J. Bagger, V. D. Barger, K.-m. Cheung, J. F. Gunion, T. Han, G. A. Ladinsky, R. Rosenfeld, and C. P. Yuan, *Phys. Rev. D* **49** (1994) 1246–1264 [[arXiv:hep-ph/9306256](#)].
- [98] *Complete Electroweak Chiral Lagrangian with a Light Higgs at NLO*, G. Buchalla, O. Cata, and C. Krause, *Nucl. Phys. B* **880** (2014) 552–573 [[arXiv:1307.5017](#)].
[Erratum: *Nucl. Phys. B* **913**, 475(2016)].
- [99] *On the Power Counting in Effective Field Theories*, G. Buchalla, O. Cata, and C. Krause, *Phys. Lett. B* **731** (2014) 80–86 [[arXiv:1312.5624](#)].
- [100] *CP violation with a dynamical Higgs*, M. B. Gavela, J. Gonzalez-Fraile, M. C. Gonzalez-Garcia, L. Merlo, S. Rigolin, and J. Yepes, *JHEP* **10** (2014) 044 [[arXiv:1406.6367](#)].
- [101] *One-loop $W_L W_L$ and $Z_L Z_L$ scattering from the electroweak Chiral Lagrangian with a light Higgs-like scalar*, R. L. Delgado, A. Dobado, and F. J. Llanes-Estrada, *JHEP* **02** (2014) 121 [[arXiv:1311.5993](#)].

- [102] *Disentangling a dynamical Higgs*, I. Brivio, T. Corbett, O. J. P. ÑL'boli, M. B. Gavela, J. Gonzalez-Fraile, M. C. Gonzalez-Garcia, L. Merlo, and S. Rigolin, *JHEP* 03 (2014) 024 [[arXiv:1311.1823](#)].
- [103] *The Effective Chiral Lagrangian for a Light Dynamical "Higgs Particle"*, R. Alonso, M. B. Gavela, L. Merlo, S. Rigolin, and J. Yepes, *Phys. Lett.* B722 (2013) 330–335 [[arXiv:1212.3305](#)]. [Erratum: *Phys. Lett.* B726,926(2013)].
- [104] *A Higgs-Higgs bound state due to new physics at a TeV*, B. Grinstein, and M. Trott, *Phys. Rev.* D76 (2007) 073002 [[arXiv:0704.1505](#)].
- [105] *Electroweak chiral Lagrangian for neutral Higgs boson*, L.-M. Wang, and Q. Wang, *Chin. Phys. Lett.* 25 (2008) 1984 [[arXiv:hep-ph/0605104](#)].
- [106] *A Higgs or not a Higgs? What to do if you discover a new scalar particle*, C. P. Burgess, J. Matias, and M. Pospelov, *Int. J. Mod. Phys.* A17 (2002) 1841–1918 [[arXiv:hep-ph/9912459](#)].
- [107] *The Phenomenology of a nonstandard Higgs boson in $W(L) W(L)$ scattering*, V. Koulovassilopoulos, and R. S. Chivukula, *Phys. Rev.* D50 (1994) 3218–3234 [[arXiv:hep-ph/9312317](#)].
- [108] *The Standard Model as an Effective Field Theory*, I. Brivio, and M. Trott, *Phys. Rept.* 793 (2019) 1–98 [[arXiv:1706.08945](#)].
- [109] *Current and Future Constraints on Higgs Couplings in the Nonlinear Effective Theory*, J. de Blas, O. Eberhardt, and C. Krause, *JHEP* 07 (2018) 048 [[arXiv:1803.00939](#)].

- [110] *Effective Theory of a Dynamically Broken Electroweak Standard Model at NLO*,
G. Buchalla, and O. Cata, *JHEP* 07 (2012) 101 [[arXiv:1203.6510](#)].
- [111] *Scalar one-loop integrals for QCD*, R. K. Ellis, and G. Zanderighi, *JHEP* 02 (2008)
002 [[arXiv:0712.1851](#)].
- [112] *Collier: a fortran-based Complex One-Loop Library in Extended Regularizations*,
A. Denner, S. Dittmaier, and L. Hofer, *Comput. Phys. Commun.* 212 (2017)
220–238 [[arXiv:1604.06792](#)].
- [113] *Separation of soft and collinear singularities from one loop N point integrals*,
S. Dittmaier, *Nucl. Phys.* B675 (2003) 447–466 [[arXiv:hep-ph/0308246](#)].
- [114] *One Loop Corrections for $e^+ e^-$ Annihilation Into $\mu^+ \mu^-$ in the Weinberg Model*,
G. Passarino, and M. J. G. Veltman, *Nucl. Phys.* B160 (1979) 151–207.
- [115] *Reducing full one-loop amplitudes to scalar integrals at the integrand level*,
G. Ossola, C. G. Papadopoulos, and R. Pittau, *Nucl. Phys.* B763 (2007) 147–169
[[arXiv:hep-ph/0609007](#)].
- [116] *Numerical evaluation of six-photon amplitudes*, G. Ossola, C. G. Papadopoulos,
and R. Pittau, *JHEP* 07 (2007) 085 [[arXiv:0704.1271](#)].
- [117] *CutTools: A Program implementing the OPP reduction method to compute
one-loop amplitudes*, G. Ossola, C. G. Papadopoulos, and R. Pittau, *JHEP* 03
(2008) 042 [[arXiv:0711.3596](#)].

- [118] *Fusing gauge theory tree amplitudes into loop amplitudes*, Z. Bern, L. J. Dixon, D. C. Dunbar, and D. A. Kosower, *Nucl. Phys.* B435 (1995) 59–101
[arXiv:hep-ph/9409265].
- [119] *One loop n point gauge theory amplitudes, unitarity and collinear limits*, Z. Bern, L. J. Dixon, D. C. Dunbar, and D. A. Kosower, *Nucl. Phys.* B425 (1994) 217–260
[arXiv:hep-ph/9403226].
- [120] *On-Shell Methods in Perturbative QCD*, Z. Bern, L. J. Dixon, and D. A. Kosower, *Annals Phys.* 322 (2007) 1587–1634 [arXiv:0704.2798].
- [121] *Unitarity cuts and Reduction to master integrals in d dimensions for one-loop amplitudes*, C. Anastasiou, R. Britto, B. Feng, Z. Kunszt, and P. Mastrolia, *JHEP* 03 (2007) 111 [arXiv:hep-ph/0612277].
- [122] *D -dimensional unitarity cut method*, C. Anastasiou, R. Britto, B. Feng, Z. Kunszt, and P. Mastrolia, *Phys. Lett.* B645 (2007) 213–216 [arXiv:hep-ph/0609191].
- [123] *Direct extraction of one-loop integral coefficients*, D. Forde, *Phys. Rev.* D75 (2007) 125019 [arXiv:0704.1835].
- [124] *Recursive numerical calculus of one-loop tensor integrals*, F. del Aguila, and R. Pittau, *JHEP* 07 (2004) 017 [arXiv:hep-ph/0404120].
- [125] *Automatized one loop calculations in four-dimensions and D -dimensions*, T. Hahn, and M. Perez-Victoria, *Comput. Phys. Commun.* 118 (1999) 153–165
[arXiv:hep-ph/9807565].

- [126] *FeynCalc 9*, V. Shtabovenko, *J. Phys. Conf. Ser.* 762 (2016), no. 1 012064
[arXiv:1604.06709].
- [127] *Package-X 2.0: A Mathematica package for the analytic calculation of one-loop integrals*, H. H. Patel, *Comput. Phys. Commun.* 218 (2017) 66–70
[arXiv:1612.00009].
- [128] *HEPMath 1.4: A mathematica package for semi-automatic computations in high energy physics*, M. Wiebusch, *Comput. Phys. Commun.* 195 (2015) 172–190
[arXiv:1412.6102].
- [129] *New features of FORM*, J. A. M. Vermaseren, arXiv:math-ph/0010025.
- [130] *Two photons plus jet at LHC: The NNLO contribution from the $g g$ initiated process*, D. de Florian, and Z. Kunszt, *Phys. Lett. B* 460 (1999) 184–188
[arXiv:hep-ph/9905283].
- [131] *Gluon fusion contribution to $W^+W^- + \text{jet}$ production*, T. Melia, K. Melnikov, R. Rontsch, M. Schulze, and G. Zanderighi, *JHEP* 08 (2012) 115
[arXiv:1205.6987].
- [132] *Di-Vector Boson + Jet Production via Gluon Fusion at Hadron Colliders*, P. Agrawal, and A. Shivaji, *Phys. Rev. D* 86 (2012) 073013 [arXiv:1207.2927].
- [133] *Towards $pp \rightarrow VVjj$ at NLO QCD: Bosonic contributions to triple vector boson production plus jet*, F. Campanario, *JHEP* 10 (2011) 070 [arXiv:1105.0920].

- [134] *Production of $\gamma Z g$ and associated processes via gluon fusion at hadron colliders*, P. Agrawal, and A. Shivaji, *JHEP* 01 (2013) 071 [[arXiv:1208.2593](#)].
- [135] *ZZ+jet production via gluon fusion at the LHC*, F. Campanario, Q. Li, M. Rauch, and M. Spira, *JHEP* 06 (2013) 069 [[arXiv:1211.5429](#)].
- [136] A. K. Shivaji, *Gluon Fusion Processes at One-loop within the Standard Model and Beyond*. PhD thesis, Bhubaneswar, Inst. Phys., 2013. [arXiv:1305.4926](#).
- [137] *Interference effects for Higgs boson mediated Z-pair plus jet production*, J. M. Campbell, R. K. Ellis, E. Furlan, and R. R  ntschi, *Phys. Rev. D* 90 (2014), no. 9 093008 [[arXiv:1409.1897](#)].
- [138] *Gluon Fusion Contribution to VHj Production at Hadron Colliders*, P. Agrawal, and A. Shivaji, *Phys. Lett. B* 741 (2015) 111–116 [[arXiv:1409.8059](#)].
- [139] *Higgs and Z boson associated production via gluon fusion in the SM and the 2HDM*, B. Hespel, F. Maltoni, and E. Vryonidou, *JHEP* 06 (2015) 065 [[arXiv:1503.01656](#)].
- [140] *Automated event generation for loop-induced processes*, V. Hirschi, and O. Mattelaer, *JHEP* 10 (2015) 146 [[arXiv:1507.00020](#)].
- [141] *Asking for an extra photon in Higgs production at the LHC and beyond*, E. Gabrielli, B. Mele, F. Piccinini, and R. Pittau, *JHEP* 07 (2016) 003 [[arXiv:1601.03635](#)].

- [142] *Higgs pair production at the LHC with NLO and parton-shower effects*,
R. Frederix, S. Frixione, V. Hirschi, F. Maltoni, O. Mattelaer, P. Torrielli,
E. Vryonidou, and M. Zaro, *Phys. Lett. B* **732** (2014) 142–149 [[arXiv:1401.7340](#)].
- [143] *The quartic higgs coupling at hadron colliders*, T. Plehn, and M. Rauch, *Phys. Rev. D* **72** (2005) 053008 [[arXiv:hep-ph/0507321](#)].
- [144] *Multi-Higgs boson production in the Standard Model and beyond*, T. Binoth,
S. Karg, N. Kauer, and R. Ruckl, *Phys. Rev. D* **74** (2006) 113008
[[arXiv:hep-ph/0608057](#)].
- [145] *Triple Higgs boson production at a 100 TeV proton-proton collider*,
A. Papaefstathiou, and K. Sakurai, *JHEP* **02** (2016) 006 [[arXiv:1508.06524](#)].
- [146] *Scrutinizing the Higgs quartic coupling at a future 100 TeV proton-proton collider
with taus and b-jets*, B. Fuks, J. H. Kim, and S. J. Lee, *Phys. Lett. B* **771** (2017)
354–358 [[arXiv:1704.04298](#)].
- [147] *New Physics in multi-Higgs boson final states*, W. Kilian, S. Sun, Q.-S. Yan,
X. Zhao, and Z. Zhao, *JHEP* **06** (2017) 145 [[arXiv:1702.03554](#)].
- [148] *Production of HHH and HHV ($V = \gamma, Z$) at the hadron colliders*, P. Agrawal,
D. Saha, and A. Shivaji, *Phys. Rev. D* **97** (2018), no. 3 036006
[[arXiv:1708.03580](#)].
- [149] *JaxoDraw: A Graphical user interface for drawing Feynman diagrams. Version 2.0
release notes*, D. Binosi, J. Collins, C. Kaufhold, and L. Theussl, *Comput. Phys.
Commun.* **180** (2009) 1709–1715 [[arXiv:0811.4113](#)].

- [150] *Search for Higgs boson pair production in the $\gamma\gamma b\bar{b}$ final state in pp collisions at $\sqrt{s} = 13$ TeV*, CMS Collaboration, A. M. Sirunyan *et. al.*, *Phys. Lett. B* **788** (2019) 7–36 [[arXiv:1806.00408](#)].
- [151] *Search for Higgs boson pair production in the $\gamma\gamma b\bar{b}$ final state with 13 TeV pp collision data collected by the ATLAS experiment*, ATLAS Collaboration, M. Aaboud *et. al.*, *JHEP* **11** (2018) 040 [[arXiv:1807.04873](#)].
- [152] *Complete Higgs Sector Constraints on Dimension-6 Operators*, J. Ellis, V. Sanz, and T. You, *JHEP* **07** (2014) 036 [[arXiv:1404.3667](#)].
- [153] *A Minimal set of top-Higgs anomalous couplings*, J. A. Aguilar-Saavedra, *Nucl. Phys. B* **821** (2009) 215–227 [[arXiv:0904.2387](#)].
- [154] *Effects of genuine dimension-six Higgs operators*, V. Barger, T. Han, P. Langacker, B. McElrath, and P. Zerwas, *Phys. Rev. D* **67** (2003) 115001 [[arXiv:hep-ph/0301097](#)].
- [155] *Anomalous Higgs couplings*, M. C. Gonzalez-Garcia, *Int. J. Mod. Phys. A* **14** (1999) 3121–3156 [[arXiv:hep-ph/9902321](#)].
- [156] *Testing anomalous gauge couplings of the Higgs boson via weak boson scatterings at the CERN LHC*, B. Zhang, Y.-P. Kuang, H.-J. He, and C. P. Yuan, *Phys. Rev. D* **67** (2003) 114024 [[arXiv:hep-ph/0303048](#)].
- [157] *Feyn Arts: Computer Algebraic Generation of Feynman Graphs and Amplitudes*, J. Kublbeck, M. Bohm, and A. Denner, *Comput. Phys. Commun.* **60** (1990) 165–180.

- [158] *The Renormalization of the axial anomaly in dimensional regularization*, S. A. Larin, *Phys. Lett. B* **303** (1993) 113–118 [[arXiv:hep-ph/9302240](#)].
- [159] *The automated computation of tree-level and next-to-leading order differential cross sections, and their matching to parton shower simulations*, J. Alwall, R. Frederix, S. Frixione, V. Hirschi, F. Maltoni, O. Mattelaer, H. S. Shao, T. Stelzer, P. Torrielli, and M. Zaro, *JHEP* **07** (2014) 079 [[arXiv:1405.0301](#)].
- [160] *Evidence for the associated production of the Higgs boson and a top quark pair with the ATLAS detector*, **ATLAS** Collaboration, M. Aaboud *et. al.*, *Phys. Rev. D* **97** (2018), no. 7 072003 [[arXiv:1712.08891](#)].
- [161] *Observation of $t\bar{t}H$ production*, **CMS** Collaboration, A. M. Sirunyan *et. al.*, *Phys. Rev. Lett.* **120** (2018), no. 23 231801 [[arXiv:1804.02610](#)].
- [162] *Combination of searches for Higgs boson pair production in proton-proton collisions at $\sqrt{s} = 13$ TeV*, **CMS** Collaboration, A. M. Sirunyan *et. al.*, *Phys. Rev. Lett.* **122** (2019), no. 12 121803 [[arXiv:1811.09689](#)].
- [163] *Search for resonant and non-resonant Higgs boson pair production in the $b\bar{b}\tau^+\tau^-$ decay channel in pp collisions at $\sqrt{s} = 13$ TeV with the ATLAS detector*, **ATLAS** Collaboration, M. Aaboud *et. al.*, *Phys. Rev. Lett.* **121** (2018), no. 19 191801 [[arXiv:1808.00336](#)]. [Erratum: *Phys. Rev. Lett.* **122**, no. 8, 089901 (2019)].
- [164] *Search for pair production of Higgs bosons in the $b\bar{b}b\bar{b}$ final state using proton-proton collisions at $\sqrt{s} = 13$ TeV with the ATLAS detector*, **ATLAS** Collaboration, M. Aaboud *et. al.*, *JHEP* **01** (2019) 030 [[arXiv:1804.06174](#)].

- [165] *Search for Higgs boson pair production in the $WW^{(*)}WW^{(*)}$ decay channel using ATLAS data recorded at $\sqrt{s} = 13$ TeV*, **ATLAS** Collaboration, M. Aaboud *et. al.*,
Submitted to: *JHEP* (**2018**) [[arXiv:1811.11028](#)].
- [166] *Search for Higgs boson pair production in the $b\bar{b}WW^*$ decay mode at $\sqrt{s} = 13$ TeV with the ATLAS detector*, **ATLAS** Collaboration, M. Aaboud *et. al.*, *JHEP* 04 (**2019**) 092 [[arXiv:1811.04671](#)].
- [167] *Search for Higgs boson pair production in the $\gamma\gamma WW^*$ channel using pp collision data recorded at $\sqrt{s} = 13$ TeV with the ATLAS detector*, **ATLAS** Collaboration, M. Aaboud *et. al.*, *Eur. Phys. J. C* 78 (**2018**), no. 12 1007 [[arXiv:1807.08567](#)].
- [168] *Search for the $HH \rightarrow b\bar{b}b\bar{b}$ process via vector boson fusion production using proton-proton collisions at $\sqrt{s} = 13$ TeV with the ATLAS detector*, **ATLAS** Collaboration, T. A. collaboration.
- [169] *Next-To-Leading Order QCD Corrections to Associated Production of a SM Higgs Boson with a Pair of Weak Bosons in the POWHEG-BOX*, J. Baglio, *Phys. Rev. D* 93 (**2016**), no. 5 054010 [[arXiv:1512.05787](#)].
- [170] *$HZ\gamma$ production at 14 TeV LHC in next-to-leading order QCD*, S.-J. Xiong, W.-G. Ma, L. Guo, R.-Y. Zhang, C. Chen, and M. Song, *J. Phys. G* 42 (**2015**), no. 6 065006 [[arXiv:1505.03226](#)].
- [171] *tWH associated production at the LHC*, F. Demartin, B. Maier, F. Maltoni, K. Mawatari, and M. Zaro, *Eur. Phys. J. C* 77 (**2017**), no. 1 34 [[arXiv:1607.05862](#)].

- [172] *NLO QCD corrections to $WWbb$ production at hadron colliders*, A. Denner, S. Dittmaier, S. Kallweit, and S. Pozzorini, *Phys. Rev. Lett.* 106 (2011) 052001 [[arXiv:1012.3975](#)].
- [173] *W^+W^- Production at Hadron Colliders in Next to Next to Leading Order QCD*, T. Gehrmann, M. Grazzini, S. Kallweit, P. Maierhöfner, A. von Manteuffel, S. Pozzorini, D. Rathlev, and L. Tancredi, *Phys. Rev. Lett.* 113 (2014), no. 21 212001 [[arXiv:1408.5243](#)].
- [174] *NLO QCD corrections to $W^+W^-b\bar{b}$ production with leptonic decays in the light of top quark mass and asymmetry measurements*, G. Heinrich, A. Maier, R. Nisius, J. Schlenk, and J. Winter, *JHEP* 06 (2014) 158 [[arXiv:1312.6659](#)].
- [175] *Anomalous Higgs-boson coupling effects in $HW+W\tilde{L}\tilde{S}$ production at the LHC*, E. Gabrielli, M. Heikinheimo, L. Marzola, B. Mele, C. Spethmann, and H. Veermae, *Phys. Rev. D* 89 (2014), no. 5 053012 [[arXiv:1312.4956](#)].
- [176] *LHC HXSWG interim recommendations to explore the coupling structure of a Higgs-like particle*, **LHC Higgs Cross Section Working Group** Collaboration, A. David, A. Denner, M. Duehrssen, M. Grazzini, C. Grojean, G. Passarino, M. Schumacher, M. Spira, G. Weiglein, and M. Zanetti, [arXiv:1209.0040](#).
- [177] *NLO Higgs effective field theory and $\hat{I}\tilde{Z}$ -framework*, M. Ghezzi, R. Gomez-Ambrosio, G. Passarino, and S. Uccirati, *JHEP* 07 (2015) 175 [[arXiv:1505.03706](#)].

- [178] *Di-vector boson production in association with a Higgs boson at hadron colliders*, P. Agrawal, D. Saha, and A. Shivaji, [arXiv:1907.13168](#).
- [179] *Multidimensional integration in a heterogeneous network environment*, S. Veseli, *Comput. Phys. Commun.* 108 (1998) 9–19 [[arXiv:physics/9710017](#)].
- [180] G. P. Lepage, *VEGAS - an adaptive multi-dimensional integration program*, Tech. Rep. CLNS-447, Cornell Univ. Lab. Nucl. Stud., Ithaca, NY, Mar, 1980.
- [181] A. Geist, A. Beguelin, J. Dongarra, W. Jiang, R. Manchek, and V. Sunderam, *PVM: Parallel Virtual Machine: A Users' Guide and Tutorial for Networked Parallel Computing*. MIT Press, Cambridge, MA, USA, 1994.
- [182] *New parton distribution functions from a global analysis of quantum chromodynamics*, S. Dulat, T.-J. Hou, J. Gao, M. Guzzi, J. Huston, P. Nadolsky, J. Pumplin, C. Schmidt, D. Stump, and C. P. Yuan, *Phys. Rev. D* 93 (2016), no. 3 033006 [[arXiv:1506.07443](#)].
- [183] *HIGGS BOSON PAIR PRODUCTION VIA GLUON FUSION*, E. W. N. Glover, and J. J. van der Bij, *Nucl. Phys.* B309 (1988) 282–294.
- [184] *Probing the Higgs selfcoupling at hadron colliders using rare decays*, U. Baur, T. Plehn, and D. L. Rainwater, *Phys. Rev. D* 69 (2004) 053004 [[arXiv:hep-ph/0310056](#)].
- [185] *Examining the Higgs boson potential at lepton and hadron colliders: A Comparative analysis*, U. Baur, T. Plehn, and D. L. Rainwater, *Phys. Rev. D* 68 (2003) 033001 [[arXiv:hep-ph/0304015](#)].

- [186] *Higgs self-coupling measurements at the LHC*, M. J. Dolan, C. Englert, and M. Spannowsky, *JHEP* 10 **(2012)** 112 [[arXiv:1206.5001](#)].
- [187] *The measurement of the Higgs self-coupling at the LHC: theoretical status*, J. Baglio, A. Djouadi, R. Grober, M. M. Muhlleitner, J. Quevillon, and M. Spira, *JHEP* 04 **(2013)** 151 [[arXiv:1212.5581](#)].
- [188] *Higgs boson pair production at the LHC in the $b\bar{b}W^+W^-$ channel*, A. Papaefstathiou, L. L. Yang, and J. Zurita, *Phys. Rev. D* 87 **(2013)**, no. 1 011301 [[arXiv:1209.1489](#)].
- [189] *Higgs Boson self-coupling measurements using ratios of cross sections*, F. Goertz, A. Papaefstathiou, L. L. Yang, and J. Zurita, *JHEP* 06 **(2013)** 016 [[arXiv:1301.3492](#)].
- [190] *Higgs-Pair Production and Measurement of the Triscalar Coupling at LHC(8,14)*, V. Barger, L. L. Everett, C. B. Jackson, and G. Shaughnessy, *Phys. Lett. B* 728 **(2014)** 433–436 [[arXiv:1311.2931](#)].
- [191] *Di-Higgs final states augmented – selecting hh events at the high luminosity LHC*, A. J. Barr, M. J. Dolan, C. Englert, and M. Spannowsky, *Phys. Lett. B* 728 **(2014)** 308–313 [[arXiv:1309.6318](#)].
- [192] *Probe Higgs boson pair production via the $3\ell 2j + \cancel{E}$ mode*, Q. Li, Z. Li, Q.-S. Yan, and X. Zhao, *Phys. Rev. D* 92 **(2015)**, no. 1 014015 [[arXiv:1503.07611](#)].

- [193] *Standard model Higgs boson pair production in the $(b\bar{b})(b\bar{b})$ final state*, D. E. Ferreira de Lima, A. Papaefstathiou, and M. Spannowsky, *JHEP* 08 (2014) 030 [[arXiv:1404.7139](#)].
- [194] *Can We Discover Double Higgs Production at the LHC?*, A. Alves, T. Ghosh, and K. Sinha, *Phys. Rev. D* 96 (2017), no. 3 035022 [[arXiv:1704.07395](#)].
- [195] *Revisiting the non-resonant Higgs pair production at the HL-LHC*, A. Adhikary, S. Banerjee, R. K. Barman, B. Bhattacharjee, and S. Niyogi, *JHEP* 07 (2018) 116 [[arXiv:1712.05346](#)].
- [196] *Higgs boson pair production at future hadron colliders: From kinematics to dynamics*, D. Goncalves, T. Han, F. Kling, T. Plehn, and M. Takeuchi, *Phys. Rev. D* 97 (2018), no. 11 113004 [[arXiv:1802.04319](#)].
- [197] *Probing the scalar potential via double Higgs boson production at hadron colliders*, S. Borowka, C. Duhr, F. Maltoni, D. Pagani, A. Shivaji, and X. Zhao, *JHEP* 04 (2019) 016 [[arXiv:1811.12366](#)].
- [198] *Measurement of the Triple Higgs Coupling at a HE-LHC*, S. Homiller, and P. Meade, *JHEP* 03 (2019) 055 [[arXiv:1811.02572](#)].
- [199] *Probing the Triple Higgs Self-Interaction at the Large Hadron Collider*, J. H. Kim, K. Kong, K. T. Matchev, and M. Park, *Phys. Rev. Lett.* 122 (2019), no. 9 091801 [[arXiv:1807.11498](#)].

- [200] *Probing the trilinear Higgs boson coupling in di-Higgs production at NLO QCD including parton shower effects*, G. Heinrich, S. P. Jones, M. Kerner, G. Luisoni, and L. Scyboz, *JHEP* 06 (2019) 066 [[arXiv:1903.08137](#)].
- [201] *Report from Working Group 2*, M. Cepeda *et. al.*, *CERN Yellow Rep. Monogr.* 7 (2019) 221–584 [[arXiv:1902.00134](#)].
- [202] *Portraying Double Higgs at the Large Hadron Collider*, J. H. Kim, M. Kim, K. Kong, K. T. Matchev, and M. Park, [arXiv:1904.08549](#).
- [203] *Effects of the anomalous Higgs couplings on the Higgs boson production at the Large Hadron Collider*, S. Kanemura, and K. Tsumura, *Eur. Phys. J. C* 63 (2009) 11–21 [[arXiv:0810.0433](#)].
- [204] *Anomalous Couplings in Double Higgs Production*, R. Contino, M. Ghezzi, M. Moretti, G. Panico, F. Piccinini, and A. Wulzer, *JHEP* 08 (2012) 154 [[arXiv:1205.5444](#)].
- [205] *Resolving the degeneracy in top quark Yukawa coupling with Higgs pair production*, G. Li, L.-X. Xu, B. Yan, and C. P. Yuan, [arXiv:1904.12006](#).
- [206] *Resolving the Degeneracy in Single Higgs Production with Higgs Pair Production*, Q.-H. Cao, B. Yan, D.-M. Zhang, and H. Zhang, *Phys. Lett. B* 752 (2016) 285–290 [[arXiv:1508.06512](#)].
- [207] *Double Higgs production at the 14 TeV LHC and a 100 TeV pp collider*, Q.-H. Cao, G. Li, B. Yan, D.-M. Zhang, and H. Zhang, *Phys. Rev. D* 96 (2017), no. 9 095031 [[arXiv:1611.09336](#)].

- [208] *Double take on new physics in double Higgs boson production*, C.-R. Chen, and I. Low, *Phys. Rev. D* **90** (2014), no. 1 013018 [[arXiv:1405.7040](#)].
- [209] *Combined analysis of double Higgs production via gluon fusion at the HL-LHC in the effective field theory approach*, J. H. Kim, Y. Sakaki, and M. Son, *Phys. Rev. D* **98** (2018), no. 1 015016 [[arXiv:1801.06093](#)].
- [210] *Corrections to di-Higgs boson production with light stops and modified Higgs couplings*, P. Huang, A. Joglekar, M. Li, and C. E. M. Wagner, *Phys. Rev. D* **97** (2018), no. 7 075001 [[arXiv:1711.05743](#)].
- [211] *Showcasing HH production: Benchmarks for the LHC and HL-LHC*, P. Basler, S. Dawson, C. Englert, and M. Muhlleitner, *Phys. Rev. D* **99** (2019), no. 5 055048 [[arXiv:1812.03542](#)].
- [212] *Enhanced Di-Higgs Production in the Two Higgs Doublet Model*, K. S. Babu, and S. Jana, *JHEP* **02** (2019) 193 [[arXiv:1812.11943](#)].
- [213] *Effective field theory analysis of double Higgs boson production via gluon fusion*, A. Azatov, R. Contino, G. Panico, and M. Son, *Phys. Rev. D* **92** (2015), no. 3 035001 [[arXiv:1502.00539](#)].
- [214] *What's in the loop? The anatomy of double Higgs production*, S. Dawson, A. Ismail, and I. Low, *Phys. Rev. D* **91** (2015), no. 11 115008 [[arXiv:1504.05596](#)].
- [215] *Composite Higgs Boson Pair Production at the LHC*, R. Grober, and M. Muhlleitner, *JHEP* **06** (2011) 020 [[arXiv:1012.1562](#)].

- [216] *Higgs Low-Energy Theorem (and its corrections) in Composite Models*, M. Gillioz, R. Grober, C. Grojean, M. Muhlleitner, and E. Salvioni, *JHEP* 10 **(2012)** 004 [[arXiv:1206.7120](#)].
- [217] *Signs of Composite Higgs Pair Production at Next-to-Leading Order*, R. Grober, M. Muhlleitner, and M. Spira, *JHEP* 06 **(2016)** 080 [[arXiv:1602.05851](#)].
- [218] *$SU(2) \times U(1)$ Breaking by Vacuum Misalignment*, D. B. Kaplan, and H. Georgi, *Phys. Lett.* 136B **(1984)** 183–186.
- [219] *Composite Higgs Scalars*, D. B. Kaplan, H. Georgi, and S. Dimopoulos, *Phys. Lett.* 136B **(1984)** 187–190.
- [220] *Anatomy of a Composite Higgs Model*, M. J. Dugan, H. Georgi, and D. B. Kaplan, *Nucl. Phys.* B254 **(1985)** 299–326.
- [221] *The Composite Nambu-Goldstone Higgs*, G. Panico, and A. Wulzer, *Lect. Notes Phys.* 913 **(2016)** pp.1–316 [[arXiv:1506.01961](#)].
- [222] *Composite Higgses*, B. Bellazzini, C. Csaki, and J. Serra, *Eur. Phys. J.* C74 **(2014)**, no. 5 2766 [[arXiv:1401.2457](#)].
- [223] *Radiative Corrections as the Origin of Spontaneous Symmetry Breaking*, S. R. Coleman, and E. J. Weinberg, *Phys. Rev.* D7 **(1973)** 1888–1910.
- [224] *Radiative Electroweak Symmetry Breaking Model Perturbative All the Way to the Planck Scale*, D. Chway, T. H. Jung, H. D. Kim, and R. Dermisek, *Phys. Rev. Lett.* 113 **(2014)**, no. 5 051801 [[arXiv:1308.0891](#)].

- [225] *Minimal conformal extensions of the Higgs sector*, A. J. Helmboldt, P. Humbert, M. Lindner, and J. Smirnov, *JHEP* 07 (2017) 113 [[arXiv:1603.03603](#)].
- [226] *Discriminative phenomenological features of scale invariant models for electroweak symmetry breaking*, K. Hashino, S. Kanemura, and Y. Orikasa, *Phys. Lett. B* 752 (2016) 217–220 [[arXiv:1508.03245](#)].
- [227] *Phenomenology of Induced Electroweak Symmetry Breaking*, S. Chang, J. Galloway, M. Luty, E. Salvioni, and Y. Tsai, *JHEP* 03 (2015) 017 [[arXiv:1411.6023](#)].
- [228] *Prospects for HH measurements at the HL-LHC*, CMS Collaboration, *CMS-PAS-FTR-18-019* (2018).
- [229] *Measurement prospects of the pair production and self-coupling of the Higgs boson with the ATLAS experiment at the HL-LHC*, ATLAS Collaboration, *ATL-PHYS-PUB-2018-053* (Dec, 2018).
- [230] *EFTs meet Higgs Nonlinearity, Compositeness and (Neutral) Naturalness*, H.-L. Li, L.-X. Xu, J.-H. Yu, and S.-H. Zhu, [arXiv:1904.05359](#).
- [231] *Probing triple-Higgs productions via $4b2\hat{s}$ decay channel at a 100 TeV hadron collider*, C.-Y. Chen, Q.-S. Yan, X. Zhao, Y.-M. Zhong, and Z. Zhao, *Phys. Rev. D* 93 (2016), no. 1 013007 [[arXiv:1510.04013](#)].
- [232] *Probing Higgs self-interactions in proton-proton collisions at a center-of-mass energy of 100 TeV*, B. Fuks, J. H. Kim, and S. J. Lee, *Phys. Rev. D* 93 (2016), no. 3 035026 [[arXiv:1510.07697](#)].

- [233] *Constraints on the quartic Higgs self-coupling from double-Higgs production at future hadron colliders*, W. Bizon, U. Haisch, and L. Rottoli, [arXiv:1810.04665](#).
- [234] *Probing the quartic Higgs boson self-interaction*, T. Liu, K.-F. Lyu, J. Ren, and H. X. Zhu, *Phys. Rev. D* **98** (2018), no. 9 093004 [[arXiv:1803.04359](#)].
- [235] *Multi-Higgs Production and Unitarity in Vector-Boson Fusion at Future Hadron Colliders*, W. Kilian, S. Sun, Q.-S. Yan, X. Zhao, and Z. Zhao, [arXiv:1808.05534](#).
- [236] *Constraining the Higgs self-couplings at e^+e^- colliders*, F. Maltoni, D. Pagani, and X. Zhao, *JHEP* **07** (2018) 087 [[arXiv:1802.07616](#)].
- [237] *Self Coupling of the Higgs boson in the processes $pp \rightarrow ZHHH + X$ and $pp \rightarrow WHHH + X$* , D. A. Dicus, C. Kao, and W. W. Repko, *Phys. Rev. D* **93** (2016), no. 11 113003 [[arXiv:1602.05849](#)].